

Magnetic and electromagnetic field induced kinetic effects on aqueous solutions with a focus on the iodine clock reaction

A thesis submitted in fulfillment for the requirements of

Master of Research

Institute for Sustainable Industries and Livable Cities

Victoria University

By

Andrew John McNaughton

July 2022

Abstract

Chemical and physical phenomena arising from the exposure of aqueous solutes to magnetic and electromagnetic fields have been widely researched and the associated scientific literature consistently reports physical, chemical, and kinetic effects across a wide variety of experimental settings. However, no consensus has been forthcoming regarding underlying mechanisms, with inconsistency in replication being a major issue. An extensive review of this research area has been conducted and forms a major part of this thesis.

In regard to this area of research, an experimental program has been designed and carried out, albeit within the constraints of the COVID-19 pandemic, to explore the effect of magnetic and electromagnetic fields on the rate aspects of a well-known chemical reaction. Thus, this project utilizes the bromate-iodine clock reaction, whereby selected chemical reactants have been exposed to both a 0.3T static magnetic field and the pulsed electromagnetic field (PEMF) of a previously characterized water treatment device. A major focus in terms of experimental design was placed upon temperature control and UV-Vis absorbance analysis techniques, incorporating appropriate software and inputs, to accurately track kinetic reaction rates relative to controls.

The data for these experiments reflect the relative rates of appearance of the maximum blue coloration (352 nm) due to triiodide/starch complexation under different magnetic and PEMF exposures for selected reactants. The two sets of aqueous reagents that have been exposed to 0.3T magnetic and PEMF treatments (both 180 min) are: “A” - consisting of sodium iodide (5.984×10^{-1} mM), sodium thiosulfate (1.493×10^{-1} mM) and starch indicator (1.995×10^{-1} mg) and “B” - containing sodium bromate (1.236 mM) and hydrochloric acid (1.545 mM). Due to time constraints all combinations of exposure were not possible, but the following results have been established. A (no exposure)/B (magnetic) – no significant difference in rate; A (magnetic)/ B (no exposure) – no significant difference in rate; A (PEMF)/B (no exposure) – significant (SE) *increase* in rate.

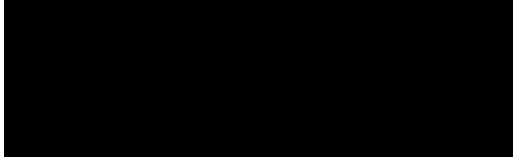
An attempt has been made to explain the observed increase in the rate of appearance of the blue triiodide/starch complex, upon PEMF exposure of reagent A, with reference to relevant theory in the literature. Thus, it is proposed that the starch amylose double helices are partially or completely disassociated by PEMF exposure, thereby facilitating a faster reaction rate due to a higher proportion of single stranded amylose being available for triiodide complexation.

Declaration

“I, Andrew John McNaughton, declare that the Master of Research thesis entitled “*Magnetic Fields and Chemical Reaction Kinetics*” is no more than 50,000 words in length including quotes and exclusive of tables, figures, appendices, bibliography, references and footnotes. This thesis contains no material that has been submitted previously, in whole or in part, for the award of any other academic degree or diploma. Except where otherwise indicated, this thesis is my own work”.

“I have conducted my research, in alignment with the Australian Code for the Responsible Conduct of Research and Victoria University’s Higher Degree by Research Policy and Procedures.”

Signature

A large black rectangular redaction box covering the area where a signature would normally be placed.

Date: 1/7/2022

Table of Contents

Title	i
Abstract	ii
Declaration	iv
Table of Contents	v
Abbreviations	ix
Symbols	xii
List of Figures	xiv
List of Tables	xvii
Acknowledgements	xix
Introduction	21
Research development flowchart	25
Chapter 1: Literature Review	27
1.1. Applications of magnetic fields (Introduction).....	27
1.1.1. Magnetic treatment of scale (CaCO_3 and Biofilms)	28
1.1.2. Magnetic fields in electrochemistry applications	34
1.1.3. Magnetic fields and environmental applications	37
Comments on sub chapters 1.1.1., 1.1.2. and 1.1.3.....	40
1.1.4. Magnetic fields in plant and microbial applications (Introduction).....	42
Comments on sub chapter 1.1.4.....	48
1.1.5. Magnetic field applications in mammalian medical research (Introduction).....	51
Comments on sub chapter 1.1.5.....	59
1.2. Water (H_2O) (Introduction).....	62
1.2.1. H_2O Hydrogen bonding	63
1.2.2. H_2O cluster geometry and binding energies.....	64
1.2.3. H_2O Ionization.....	67
1.2.4. H_2O Isomers and nuclear spin states.....	69
1.3. H_2O and magnetic fields (Introduction).....	73
1.3.1. H_2O and static magnetic fields.....	73
1.3.2. H_2O and dynamic magnetic fields.....	77
1.3.3. H_2O and magnetic field computer simulations.....	86
1.4. Ions and molecules in aqueous solution (Introduction).....	89

1.4.1. Solvation.....	89
1.4.2. Ion hydration clusters.....	90
1.4.3. Hydrated ionic diffusion.....	91
1.4.4. H ₂ O residence time in ionic hydration shells.....	94
1.4.5. Proton transfer.....	95
1.4.6. H ₂ O and ionic nucleation	99
1.5. Hydrated ions and magnetic fields (Introduction).....	101
1.5.1. Hydrated ions in static magnetic fields	102
1.5.2. Hydrated ions in dynamic magnetic fields	112
1.5.3. Proton transfer in magnetic fields.....	120
1.5.4. Hydrated ions and magnetic field computer simulations.....	124
1.6. Magnetic water devices: Quackery and critiques (Introduction).....	127
1.6.1. Domestic magnetic water devices and absurd claims.....	127
1.6.2. Critiques of magnetic field induced aqueous research	128
1.7. Literature review summation (sub chapters 1.1.1. to 1.6.2.).....	131
1.8. Clock reactions (Introduction).....	131
1.8.1. The bromate-iodine clock reaction	133
1.8.2. Properties of bromate-iodide reaction chemicals and ions.....	134
1.8.3. Starch, amylose, and amylopectin.....	135
Comments on sub chapters 1.8.....	138
1.9. UV-Vis Spectrophotometry (Introduction).....	138
1.9.1. UV-Vis Spectrophotometry and temperature.....	139
1.9.2. UV-Vis Spectrophotometry polyiodide and iodine analysis.....	139
1.9.3. UV-Vis Spectrophotometry and iodine-iodide starch complexation.....	146
1.9.4. UV-Vis Spectrophotometry and bromate analysis.....	147
1.10. Research design and method modelling.....	148
Chapter 2: Experimental Design and Method trials (flowchart).....	150-151
2.1. The development of the clock reaction methodology.....	151
2.1.1. Reactant compositions, concentrations, dilutions, and initial ambient temperature/time trials.....	151
2.2. Clock reaction and temperature factors.....	152
2.2.1. Clock reaction and water bath trials.....	152
2.2.2. Clock reaction and Scanvac water bath trials.....	153
2.3. Experimental UV-Vis kinetic analysis trials.....	156

2.3.1. UV-Vis Spectrophotometry application in this research.....	157
2.3.2. Reaction UV-Vis Kartell cuvette baseline calibration.....	158
2.3.3. Reaction temperature control and UV-Vis kinetic trials.....	158
2.3.4. Scanvac temperature control and UV-Vis kinetic results.....	160
2.4. Experimental ambient temperature measurement.....	162
2.4.1. The 0.3T rare earth magnet experimental design.....	162
2.4.2. 0.3T magnet exposure and ambient temperature monitoring.....	163
2.5. Investigating the Dolphin 3000 PEMF device.....	165
2.5.1. The Dolphin 3000 PEMF device temperature investigation.....	167
2.5.2. The Dolphin 3000 PEMF device electrical engineer report.....	168
2.5.3. Scanvac water bath and Dolphin 3000 PEMF trial.....	170
2.5.4. Dolphin 3000 PEMF thermocouple and reaction vessel design.....	171
2.5.5. Dolphin 3000-thermocouple-irrigation system design trial.....	172
2.5.6. The thermocouple/PEMF/Scanvac water bath trials.....	174
2.6. Experimental 0.3T static magnet design trial.....	177
2.6.1. Experimental 0.3T static magnet exposure/control trials.....	177
2.6.2. An approximation of the 0.3T magnetic flux density.....	178
2.7. Summary of trial experiments.....	179
Chapter 3: Experimental research.....	180
3.1. Analyte A/B (0.3T x 180 min) exposure methodology.....	180
3.2. 0.3T magnet corresponding control analyte preparation.....	181
3.3. Magnet (0.3T x 180 min.)/control analyte UV-Vis methodology.....	181
3.4. Analyte A (0.3T x 180 min.) vs control UV-Vis data.....	183
3.5. Analyte B (0.3T x 180 min.) vs control UV-Vis data.....	184
3.6. Analyte A (PEMF/180 min) exposure methodology.....	185
3.7. Analyte A (PEMF x 180 min x 5)/control UV-Vis methodology.....	187
3.7.1. Analyte A (PEMF x 180 min) exposure temperature control.....	188
3.7.2. Analyte A (PEMF x 180 min) vs control UV-Vis kinetic data.....	188
3.8. ICP-MS analysis of PEMF thermocouple/analyte integrity data.....	189
Chapter 4: Results and Discussion.....	191
4.1. Extrapolation of Scanvac water bath UV-Vis analysis.....	191
4.2. Analyte A (0.3T x 180 min.) vs control UV-Vis kinetic results.....	194
4.3. Analyte B (0.3T x 180 min.) vs control UV-Vis kinetic results.....	197
4.4. Analyte A/B (0.3T x 180 min.) and temperature discussion.....	202

4.5.	Analyte A (PEMF x 180 min.) vs control UV-Vis kinetic results.....	204
4.6.	Analyte A (PEMF and 0.3T magnet) discussion.....	210
4.7.	Atmospheric gasses and this research.....	210
4.8.	The Piyadasa hypothesis.....	211
4.9.	Analyte A magnetic susceptibility factors.....	214
4.10.	ICP-MS analysis of PEMF thermocouple/analyte results.....	214
Chapter 5: Conclusions.....		215
5.1.	Factors to consider for analyte A PEMF/static magnet differential kinetics... 5.1.1. Analyte A (PEMF and 0.3T) exposure: A hypothetical mechanism.....	215 218
5.1.2.	Analyte A magnetic field exposure: Conclusion.....	219
5.2.	Analyte B (0.3T x 180 min) UV-Vis kinetic analysis.....	220
5.2.1.	Temperature alignments of Analyte B and Control kinetics.....	220
5.2.2.	H ₂ O cluster geometry and hydrogen bond energy revisited.....	223
5.2.3.	H ₃ O ⁺ and H ₂ O proton transfer revisited.....	223
5.2.4.	HCl and proton transfer under magnetic field exposure.....	224
5.2.5.	Factors to consider for analyte B magnet differential kinetics.....	225
5.2.6.	Analyte B (0.3T x 180 min) exposure: A hypothetical mechanism.....	225
5.2.7.	Analyte B magnetic field exposure: Conclusion.....	226
5.3.	Analyte A/ B (0.3T x 180 min) magnet exposure vs control displacement differentials.....	227
5.3.1.	Analyte A/B (0.3T) magnet exposure: Conclusion.....	227
Chapter 6: Future Research.....		228
References.....		230

Abbreviations

AIMD: ab initio molecular dynamics computer simulation

α-CD: alpha-cyclodextrin

atm: Atmosphere (1 atmosphere = 101.325 kPa)

C.I.: Confidence Interval

cm: Centimetre (1×10^{-2} metre)

cm⁻¹: per centimetre or wavelength (10,000nm)

CEC: Cation Exchange Capacity

DF: Degrees of freedom

DFT: Density Functional Theory computer simulation

DFT-CM: Density Functional Theory–Quantum chemical cluster Model simulation

DNA: Deoxyribonucleic acid

DoE: Design of Experiments

DO: Dissolved Oxygen

D₂O: Deuterium Oxide (heavy water)

EC: Electrical Conductivity

ESI-MS: Electrospray Ionization Mass Spectrometry

EMF: Electromagnetic Field

fs: femtoseconds (10^{-15} seconds)

g: gram

μg: microgram (10^{-6} grams)

GC: Gas Chromatography

GHG: Greenhouse Gas

GMF: Geomagnetic Field (earth geographic magnetic field)

Hz: Hertz (EMF wave cycles per second)

ICR: Ion Cyclotron Resonance

ICP: Inductively Coupled Plasma

ICP-MS: Inductively Coupled Plasma Mass Spectrometry

INDO CI: Intermediate Neglect of Differential Overlap Configuration Interaction

IR: Infra-red (700nm-1mm EMF wavelength)

k: kelvin ($K = {}^\circ C \pm 273.15K$)

kHz: kilohertz (10^3 Hertz)

kPa: kilopascals (10^3 pascals)

km: kilometers (10^3 meters)

kJ: kilojoules (10^3 joules)

kcal: kilocalories (10_3 calories)

L: Litre (10^3 millilitres)

LC: Liquid Chromatography

LQT: Linear-Quadrupole ion Trap

µl: microlitres (10^{-6} litres)

m²: square metres

M, M⁻¹ or mol, mol⁻¹: Mole weight

MF: Magnetic Field

MGMT: O⁶ – methylguanine-DNA-methyltransferase (human DNA repair enzyme)

MHz: Megahertz (10^6 Hertz)

miRNA: micro ribonucleic acid

mm: millimetres (10^{-3} meters)

MRT: Mean Residence Time

MWT: Magnetic Water Treatment

min.: minute/s

mL: millilitres (10^{-3} litres)

MDS: Molecular Dynamic Simulation (computational)

MHD: Magnetohydrodynamic

m/s: metres per second

mM: millimole (10^{-3} moles)

µm or µmol: micromole (10^{-6} moles)

mg: milligram (10^{-3} grams)

M.P.: Melting Point

MPa: Megapascals (10^6 pascals), Pascal (Pa: S.I. basic pressure unit, $\text{kg}\cdot\text{m}^{-1}\cdot\text{s}^{-2}$)

mm²: square millimetres

m⁻¹: per meter

mU: milli units

nm: nanometers (10^{-9} meters)

nmol: nanomoles

NMR: Nuclear Magnetic Resonance

ns: nanosecond (10^{-9} seconds)

nT: nanotesla (10^{-9} Tesla)

NTU: Nephelometric Turbidity Units

OPR: ortho to para ratio (proton nuclear spin ratio)

ORP: Oxidation Reduction Potential (change in redox properties)

PEMF: Pulsed Electromagnetic Field

pg: picograms (10^{-12} grams)

pH: potential of hydrogen

ppm: parts per million

ps: picosecond (10^{-12} seconds)

RNA: Ribonucleic Acid

rRNA: ribosomal ribonucleic acid

ROS: Reactive Oxygen Species

s or sec.: second

s⁻¹: per second

SEM: Scanning Electron Microscope

μs: microsiemens (10^{-6} siemens, electrical conductance units)

SMF: Static Magnetic Field

S/N: Signal to Noise ratio

SD: Standard Deviation

SE: Standard Error

SEM: Standard Error of the Mean

T: Tesla (S.I. units for magnetic field strength, $1 \text{ kg}\cdot\text{s}^{-2}\cdot\text{A}^{-1}$)

TDS: Total Dissolved Solids

TOF-MS: Time of Flight Mass Spectrometry

μL: microliters (10^{-6} liters)

μm: micrometre (10^{-6} metres)

μT: microtesla (10^{-6} Tesla)

mT: millitesla (10^{-6} Tesla)

U: Units

UV: Ultraviolet (100-400nm EMF wave length)

UV-Vis: Ultraviolet-Visible (100nm-1mm EMF wave length)

V: Volt (unit of electromotive force over 2 points, metres x kilograms x seconds)

w/v: weight to volume ratio

XRD: X-Ray Diffraction

Symbols

α : alpha

\AA : angstrom (1nm in S.I. units)

\AA^2 : angstrom square area

B : B coefficient (solute concentration and viscosity correlations)

β : beta

$^\circ\text{C}$: Celsius (S.I. units for temperature)

R^2 : coefficient of determination

j : current density

$^\circ$: Degrees (angular)

χ_α : Diamagnetic susceptibility (molar = - m³/mol @ $^\circ\text{C}/\text{kPa}$)

ϵ : Dielectric constant (a materials ability to store an electric charge)

D : diffusion coefficient (movement of particles in a given region, M²/s)

D_0 : diffusion at infinite temperature

E : electrical field wave

$T\Delta S$: Entropy calculation (T = temperature, ΔS = entropy gained or lost)

K_{eq} : Equilibrium constant (reaction time when all reactants and products are in equilibrium relative to temperature)

f : frequency of cycles per second

K_w : ionic equilibrium constant for H₂O (pH)

λ : Lambda (a materials absorbance response to photons)

λ_{max} : Lambda maximum (a materials maximum absorbance response to photons)

F_L : Lorentz Force ($\vec{F} = q\vec{V} \times \vec{B}$)

B : magnetic field wave

\vec{B} : magnetic field interacting with matter

$\vec{\zeta}$: magnetic gradient

\mathbf{Br} : Magnetic remanence (magnetism retained when magnetic field is removed)

χ : Magnetic susceptibility (molar = \pm m³/mol @ $^\circ\text{C}/\text{kPa}$)

m/z : mass to charge ratio (the mass number of an ion divided by its charge)

$M\Omega$: Megaohm (10⁶ ohms, units of electrical resistance)

p : pressure in grams per centimetre

$\bullet\uparrow + \bullet\downarrow$: radical singlet

$\bullet\uparrow + \bullet\uparrow$: radical triplet

σ : standard deviation

\bar{x} : statistical mean

\tilde{x} : statistical median

σ^2 : statistical variance

\rightleftharpoons : system equilibrium

List of Figures

Figure 1-1: Lorentz Force mechanism initiating MHD and micro-MHD vortices.....	35
Figure 1-2: A flavin - tryptophan molecule and aliphatic linkage.....	43
Figure 1-3: Cryptochrome light and dark induced redox cycle.....	44
Figure 1-4: Light intensity, regimes and static 500 μ T cry1 phosphorylation	45
Figure 1-5: Microbial N ₂ O evolution and accumulation.....	47
Figure 1-6: Mice Ehrlich carcinoma/mortality 100 μ T PEMF/6 μ T SMF exposure.....	54
Figure 1-7: miR-21-5p expression in Temozolomide and PEMF treatment.....	56
Figure 1-8: The Cisplatin 1,2 intra-strand DNA cross linkage mechanism.....	57
Figure 1-9: A2780 and A2780-CP culture Cisplatin dosage and 15 mT.....	58
Figure 1-10: Ehrlich carcinoma: Cisplatin, PEMF and Cisplatin- PEMF outcome.....	59
Figure 1-11: MDS of H ₂ O (donor) and H ₂ O (acceptor) low energy configuration.....	63
Figure 1-12: Hydrogen bonded tetrahedral H ₂ O configuration.....	64
Figure 1-13: MDS Pentagonal dodecahedron cluster (H ₂ O) ₂₀	65
Figure 1-14: Various MDS H ₂ O cluster configurations.....	66
Figure 1-15: (left) Eigen cation H ₉ O ₄ ⁺ and (right) Zundel cation H ₅ O ₂ ⁺	68
Figure 1-16: Magnetic field separation methodology of ortho and para H ₂ O.....	70
Figure 1-17: (left) Caged H ₂ O endohedral fullerene.....	71
Figure 1-17: (right) Temperature dependence and ortho and para-H ₂ O.....	71
Figure 1-18: Spectroscopic ortho and para D ₂ O and D ₂ O H ₂ O ratios.....	72
Figure 1-19: H ₂ O and magnetic field diamagnetic “Moses Effect”.....	74
Figure 1-20: Dissolved oxygen (DO) and pH magnetic field exposure.....	75
Figure 1-21: Electrical resistivity-conductivity of H ₂ O/magnetic field strength.....	76
Figure 1-22: PEMF and SMF H ₂ O conductivity and absorbed gasses.....	79
Figure 1-23: H ₂ O ICR (H ₃ O ⁺) and pH response.....	81
Figure 1-24: EMF frequency (500 kHz -1 MHz) and H ₂ O magnetic response.....	83
Figure 1-25: EMF voltage (1MHz/0.1 - 2.5V) and H ₂ O magnetic response.....	84
Figure 1-26: 135MHz EMF and in situ pH electrode integrity.....	85
Figure 1-27: Simulation magnetic field gradient coordinates of the H1 atom.....	87
Figure 1-28: Cation and anion H ₂ O hydration shell arrangements.....	91
Figure 1-29: Hofmeister series and Jones-Dole B coefficient correlations.....	94
Figure 1-30: MDS HCl ionization and proton transfer mechanism.....	96

Figure 1-31: Classical and non-classical CaCO_3 nucleation mechanisms.....	101
Figure 1-32: Water treatment static magnetic field configurations.....	102
Figure 1-33: Diametric static magnetic configuration.....	104
Figure 1-34: Diametric static magnetic field measurement.....	105
Figure 1-35: Axial static magnetic field configuration.....	106
Figure 1-36: Axial static magnetic field measurement.....	106
Figure 1-37: Axial static magnetic field MHD induction zone manipulation.....	107
Figure 1-38: $\text{C}_6\text{H}_{12}\text{O}_6$ (0.9M) control and 0.9T m^2 ORP reduction (70 mins).....	109
Figure 1-39: Control vs 1T exposure hydrated salt viscosity effects.....	110
Figure 1-40: (left) Control 5mM CaCO_3 nucleation turbidity/time.....	112
Figure 1-40: (right) PEMF 5mM CaCO_3 nucleation turbidity/time.....	112
Figure 1-41: (left) Control 5mM CaCO_3 nucleation UV-Vis /time.....	113
Figure 1-41: (right) PEMF 5mM CaCO_3 nucleation UV-Vis/time.....	113
Figure 1-42: ESI-MS 5mM Na_2CO_3 control Na^+ spectra.....	114
Figure 1-43: ESI-MS 5mM Na_2CO_3 PEMF (10 minutes) Na^+ spectra.....	114
Figure 1-44: ESI-MS 5mM $\text{Ca}(\text{NO}_3)_2$ control Ca^{2+} spectra.....	115
Figure 1-45: ESI-MS 5mM $\text{Ca}(\text{NO}_3)_2$ PEMF Ca^{2+} spectra.....	115
Figure 1-46: Dolphin 3000 vs control and scale inhibition over 800 hours.....	116
Figure 1-47: PEMF SEM $\beta\text{-CoC}_2\text{O}_4\cdot2\text{H}_2\text{O}$ morphology.....	117
Figure 1-48: PEMF SEM $\beta\text{-CoC}_2\text{O}_4\cdot2\text{H}_2\text{O}$ XRD diffraction.....	118
Figure 1-49: Starch desorption design and 20-190mT magnetic field gradient.....	119
Figure 1-50: "Superimploder" vortex and magnetic water treatment device.....	128
Figure 1-51: MBC DN10 industrial static magnetic water treatment device.....	130
Figure 1-52: hydrated α -amylose helix molecular configuration.....	134
Figure 1-53: Linear (α 1 \rightarrow 4) and branched (α 1 \rightarrow 6) starch molecule.....	136
Figure 1-54: helical amylose with hydrophilic and hydrophobic intensities.....	137
Figure 1-55: UV-Vis absorbance for I_2 (459nm) and I_3^- (288 and 352nm).....	142
Figure 1-56: UV-Vis absorbance $\text{KI} + \text{I}_2 + \alpha\text{-CD} \rightarrow \text{I}_3^-$ increase.....	143
Figure 1-57: UV-Vis absorbance $\alpha\text{-CD}\cdot\text{I}_3^-$ complex and I_3^- (288 and 352nm).....	143
Figure 1-58: UV-Vis absorbance $\alpha\text{-CD}\cdot\text{I}_3^-$ complex stoichiometric analysis.....	144
Figure 1-59: UV-Vis absorbance $\alpha\text{-CD}\cdot\text{I}_3^-$ complex temperature analysis.....	144
Figure 2-1: Scanvac water bath and reagent temperature control method.....	154
Figure 2-2: Gresinger G-1700 digital thermometer (± 0.01 sensitivity).....	155

Figure 2-3: Temperature control experimental design layout.....	155
Figure 2-4: Shimadzu UV1900 Milli Q blank baseline spectra (352nm).....	158
Figure 2-5: Temperature control UV-Vis λ_{\max} (20.0 - 26.0°C).....	161
Figure 2-6: Alpha magnetics scientific 0.3T neodymium magnet device.....	163
Figure 2-7: Stainless steel alloys and correlated magnetic field response	164
Figure 2-8: Dolphin 3000 PEMF oscilloscope waveform.	165
Figure 2-9: Dolphin 3000 control box and connected PEMF reaction coil.....	166
Figure 2-10: Engineer oscilloscope report of Dolphin 3000 wave output.....	168
Figure 2-11: Engineer oscilloscope report of Dolphin 3000 single pulse.....	169
Figure 2-12: Scanvac water bath and Dolphin 3000 temperature calibration.....	171
Figure 2-13: Reaction vessel, thermocouple and GL14 cap design.....	172
Figure 2-14: Sealed reaction vessel/thermocouple and reagent A	172
Figure 2-15: (left) Scanvac water bath Y piece/hose.....	173
Figure 2-15: (right) Y piece/thermocouple lead (yellow) to data logger.....	173
Figure 2-16: Overall thermocouple/reaction vessel configuration	173
Figure 2-17: PEMF/Scanvac/data logger overall experimental design layout.....	174
Figure 2-18: Dolphin 3000 PEMF coil reaction vessel insertion point.....	175
Figure 2-19: Analyte A/B (0.3T x 180 mn) experimental exposure method.....	177
Figure 2-20: Research static rod magnet ζ gradient	178
Figure 2-20: Approximate magnetic gradient in the 0.3T experimental design.....	178
Figure 4-1: Extrapolation of Figure 3-1 incorporating 0.2°C gradient intervals.....	193
Figure 4-2: Analyte A (0.3T x 180 mins) vs Control kinetics and error.....	195
Figure 4-3: Analyte A (0.3T x 180 mins) exposure increased differential rate.....	196
Figure 4-4: Analyte B (0.3T x 180 mins) vs Control kinetics and error.....	199
Figure 4-5: Analyte B (0.3T x 180 mins) vs Control kinetics and error.....	200
Figure 4-6: Analyte B (0.3T x 180 mins) vs Control increased differential rate.....	201
Figure 4-7: Analyte A (PEMF x 180 mins) vs Control kinetics and error.....	206
Figure 4-8: Analyte A (PEMF x 180 mins) vs Control kinetics and error.....	207
Figure 4-9: Analyte A (PEMF x 180 mins) vs Control kinetics and error.....	208
Figure 4-10: Analyte A (PEMF x 180 mins) exposure increased differential rate....	209
Figure 5-1: Glucose molecule.....	215
Figure 5-2: Analyte B (0.3T x 180 mins) exposure λ_{\max} (0.02°C variation).....	222

List of Tables

Table 1-1: <i>Celosia argentea</i> and 100mT SMF exposure Cd ⁺ ion sequestration.....	38
Table 1-2: <i>Celosia argentea</i> and 100mT SMF exposure Cd ⁺ ion ICP analysis.....	39
Table 1-3: PEMF phase and time design for gene response.....	52
Table 1-4: PEMF phase and time regime gene response	52
Table 1-5: Cytokine response to combined PEMF and SMF regimes.....	53
Table 1-6: MDS (H ₂ O) _n hydrogen bond kinetic fragmentation stability.....	66
Table 1-7: H ₃ O ⁺ ICR frequencies and isotopic D ₂ O-H ₂ O exchange.....	82
Table 1-8: MDS (H ₂ O) _n hydrogen bond response to magnetic fields	86
Table 1-9: H ₂ O Ionic diffusion coefficients at infinite dilution (D ₀) @ 25.0°C.....	92
Table 1-10: H ₂ O and 0.001M-1.0M salt diffusion coefficients (D ₀) /25.0°C.....	92
Table 1-11: Piyadasa-McNaughton research anion diffusion/hydrodynamic radii....	93
Table 1-12: Ion-H ₂ O 1 st hydration shell mean residence times.....	94
Table 1-13: Ion hydration shell H ₂ O entropy (298K/101.325kPa).....	95
Table 1-14: MDS H ₃ O ⁺ (H ₂ O) _n cluster size and geometry bonding energies.....	98
Table 1-15: Chemical engineering induced crystallisation methods.....	100
Table 1-16: H ₂ O- Cu ²⁺ salt concentration and paramagnetic response.....	102
Table 1-17: H ₂ O- CuCH ₃ (COO) ₂ concentration and magnetic response.....	103
Table 1-18: Pascal's constants for analyte A diamagnetic susceptibilities.....	104
Table 1-19: CaCO ₃ and static magnet configuration precipitation.....	106
Table 1-20: SrSO ₄ and 1T nucleation kinetic retention and particulate size.....	111
Table 1-21: PEMF vs Control CaCO ₃ morphology (SEM).....	113
Table 1-22: Potato starch control vs magnetic exposure desorption.....	120
Table 1-23: 0.23T HCl variable molarity, flow, temperature, and pH analysis.....	121
Table 1-24: Taguchi experimental design components.....	122
Table 1-25: Experimental design factors with DoE statistical significance.....	122
Table 1-26: 3.8M HCl and 0.3T N80 steel corrosion.....	123
Table 1-27: MDS solvent control vs (1.1T) diffusion coefficient and density.....	126
Table 1-28: Bromate-iodine clock reaction chemical properties.....	135
Table 1-29: Bromate-iodine clock reaction ionic properties.....	135
Table 1-30: Temperature impact on solvent UV coefficients (5 - 33°C).....	139
Table 1-31: Iodine species UV-Vis (180-600nm) absorbance spectra.....	145

Table 1-32: Various reported starch + I ₂ H ₂ O UV-Vis absorbance (λ_{\max}).....	146
Table 1-33: Various reported starch + I ₂ H ₂ O UV-Vis absorbance (λ_{\max}).....	147
Table 2-1: Temperature controlled UV-Vis kinetic absorbance statistics.....	160
Table 2-2: Electrical engineers report of PEMF device thermal analysis.....	167
Table 2-3: PEMF - water bath/thermocouple temperature control trial.....	176
Table 3-1: Analyte A (0.3T) and control UV-Vis kinetics and temp.....	184
Table 3-2: Analyte B (0.3T) and control UV-Vis kinetics and temp.....	185
Table 3-3: Analyte A (PEMF) and post PEMF exposure UV-Vis analysis time.....	188
Table 3-4: Analyte A (PEMF) and (0.3T) respective control series UV-Vis absorbance commencement, λ_{\max} and displacement comparisons	189
Table 3-5: ICP-MS Ca(NO ₃) ₂ PEMF and control Cr and Ni ion analysis.....	190
Table 4-1: Extrapolated temperature control UV-Vis upper/lower 95% C.I.....	192
Table 4-2: Analyte A (0.3T x 180 min. x 15) and control (x 15) temperature control statistical comparison correlated with λ_{\max} and temperature.....	194
Table 4-3: Analyte B (0.3T x 180 min. x 15) and control (x 15) and temperature control statistical comparison correlated with λ_{\max} and temperature.....	198
Table 4-4: Analyte A/B (0.3T) and control series analysis.....	202
Table 4-5: Analyte A (0.3T x 180 min.) and temperature-controlled differential kinetic rate comparison (100-136 seconds).....	203
Table 4-6: Analyte A/B (0.3T x 180 min.) and control comparisons.....	204
Table 4-7: Analyte A (PEMF x 180 min. x 20) and control (x 20) and temperature control kinetic statistical data comparisons*.....	205
Table 4-8: Analyte A (PEMF) and (0.3T) and respective control series UV-Vis absorbance commencement, λ_{\max} and displacement duration.....	210
Table 5-1: Analyte A (0.3T) and (PEMF) UV-Vis analysis and temperature.....	220
Table 5-2: Analyte B (0.3T x 180 min) and control $\pm 0.2^{\circ}\text{C}$ UV-Vis.....	221

Acknowledgements

I would like to express my gratitude to Professor John Orbell and Dr. Tom Yeager for seeing a potential in me that would warrant their support in giving me this opportunity to expand my education under their supervision.

I would further wish to acknowledge the appreciation of the assistance given to me by the Footscray Park campus laboratory staff, Nishantha Illangantilaka and Chathuri Piyadasa for their day to day assistance, Miroslav Radev and Don Elmeri in the electrical engineering department, whose assistance was crucial in getting the PEMF device temperature calibration facilitated, Stacy Lloyd for her efficient professionalism with obtaining laboratory perishables in the knowledge that the clock was a consistent enemy during the COVID-19 pandemic, and finally Larruceo “Larry” Bautista, for his assistance and training with the UV-Vis spectrophotometry and ICP-MS instruments.

I would not have achieved anything without all your valuable support and assistance throughout the arduous and unforeseen circumstances of 2020 and 2021.

I would finally like to thank my family for their love, patience, and assistance throughout this period. It is never taken for granted.

Introduction

This research thesis has set out to address a plethora of commentary in the scientific literature pertaining to static, electromagnetic, and pulsed electromagnetic field (PEMF) interactions with molecular and ionic aqueous reaction processes. The genesis of the inspiration for this research path emerged in my 3rd year undergraduate BSc. studies which investigated “*The effects of electromagnetic fields on crystal polymorphism*” in semester one of 2019, which was well received by my supervisor.

This 2019 paper identified the shortcomings in the classical theoretical understanding regarding polymorphology, and claims that magnetic, electromagnetic and PEMF's did have the capacity to effect molecular structures was an accepted phenomena in scientific circles, however, poor experimental replication is a consistently reported factor, mainly due to the bulk of the research incorporating relatively unique variables in chemical species, concentrations, temperature conditions and instrument integrity issues.

Therefore, this research set out investigate static and electromagnet applications with analytes that did not incorporate the significant complexities that exist with crystal nucleation, by subjecting individual aqueous analyte combinations to both static and PEMF's and focusing on reactions whereby the resulting products remain in a soluble state, which is free of the complications that can arise with incorporating the analytical aspects of the research during magnetic exposures. The analytical focus for this research is concentrated on post magnetic field exposure analytes in comparison to controls, at equimolar concentrations, dilutions and with the intention to keep temperature variability to a bare minimum to scrutinise magnetic field effects at the soluble ionic and molecular level.

The questions driving this research thesis were:

- Do static and electromagnet fields applied to aqueous reactants alter the rate of experimental kinetic rates and product formation?

- If so, does magnetic exposure impact ionic hydration, molecular hydration, ionic-molecular complexation, or overall bulk H₂O molecular factors?
- How sensitive are ionic hydration, ionic complexation, molecular hydration, ionic-molecular complexation, and overall H₂O molecular factors to the application of static and electromagnet fields?
- Can UV-Vis spectroscopy incorporating kinetic rate software applications measure the initial identification of the reaction blue starch-triiodide complex, the kinetic rate curve during complexation and the reactions completion to give conclusions about the roles individual halide, oxyhalide and molecular starch analytes have undertaken in any phenomena detected?
- Are the reported claims of static and electromagnetic field applications incorporated in scientific research and industry, actually feasible?

The layout of this thesis takes in a broad literature review in order to identify the impact which the applications of magnetic fields with various isolated and combinatorial molecular and ionic species typically identified as being of interest in irrigation and agricultural, electrochemical, industrial, and environmental remediation, before the review delves deeper in to biological research focusing on plant and microbial gene transcription, then mammalian medical research. Further commentary related to aspects of research in these field is as commentaries at the end of these sections.

The review then scrutinises the independent role that water plays, as it is the common participant in most of the previously outlined research, by examining widely accepted theoretical underpinnings of its properties in isolation, then follows up with an investigation of the research utilised exclusively with H₂O and a variety of incorporated magnetic field regimes.

Attention then shifts to delving in to the research examining ions under aqueous conditions, and a variety of theories behind these unique analytical conclusions and the theoretical underpinnings applied to this research, then also focuses on a selection of scientific literature focusing magnetic field exposures with aqueous ionic and molecular experiments, incorporating computer simulation modelling, and a variety of analytical applications and their associated conclusions.

The Literature research section then reviews some of the critiques that accompany magnetic exposure phenomena, prior to commenting on, “clock reactions”, also known as the Landolt reactions, which were chosen as our experiments of choice, due to its well established use over a long period of time in academia, these reactions incorporate aqueous ions and molecules, which are common to the majority of magnetic field chemistry research, as this choice meets the criteria set out in our initial research aims. The reactions are based upon the simple fundamentals of chemistry kinetics, incorporating concentration and temperature independent factors under stoichiometric batch reactor conditions, and can be prepared to facilitate consistent kinetic lag time in the slow rate determining step of the reaction, followed by a consistent induction period when formed polyiodide species undergo rapid complexation with molecular starch in the reaction solution to facilitate the emergence of a vivid blue starch-iodide complex. Once consistent replication was established according to chemical concentration, overall reaction dilution and temperature, then it was anticipated that these reactions would be excellent candidates for magnetic exposure and control experiments.

The bromate – iodide variation of these clock reactions was chosen because it has been also well researched in the literature, could be utilised as identical cationic salts, thereby limiting “*spectator ions*” issues, and featured two differing sodium halides, two differing sodium oxyhalides and starch in an acidic reaction, leaving all remaining reactants and products in a soluble state.

A series of experiments with combinations of aqueous NaI, NaBrO₃, Na₂S₂O₃, HCl and starch were conducted, and then analysed in combinations of respective concentrations and dilutions utilising basic thermometer measurements to identify whether consistent rate determining, and complexation reaction kinetics could be visually established. Then an accompanying series of experiments employing magnetic stirring were also undertaken and no significant variation in the rate determining and complexation kinetics were noted utilising our selected concentrations and dilutions, and stirring protocols were then abandoned.

The outcome of this initial research identified that temperature fluctuation due to the North facing window arrangements of the laboratory contributed to inconsistent results, and initial generic laboratory water bath experiments were conducted to insulate the reactants from this temperature fluctuation prior to quickly blending them together batch reactor conditions, however, precision was still not deemed to be suitable for research purposes.

A high precision refrigerated water bath was identified at another university campus and after this was obtained a series of experiments with clock reactants A and B immersed in this bath, which resulted in excellent precision and replication in the visually observed and timed setting.

Analytical research utilised a Shimadzu UV-1900 spectrophotometer incorporating Lab Solutions 1.03 kinetic rate absorbance software in its program selections and a series of experiments to calibrate the parameters of the instrument software kinetic absorbance until suitable data inputs were obtained to measure the initiation, then second by second incremental rate increase in absorbance, and the completion of the triiodide starch complex, which returned excellent precision, sensitivity and replication results.

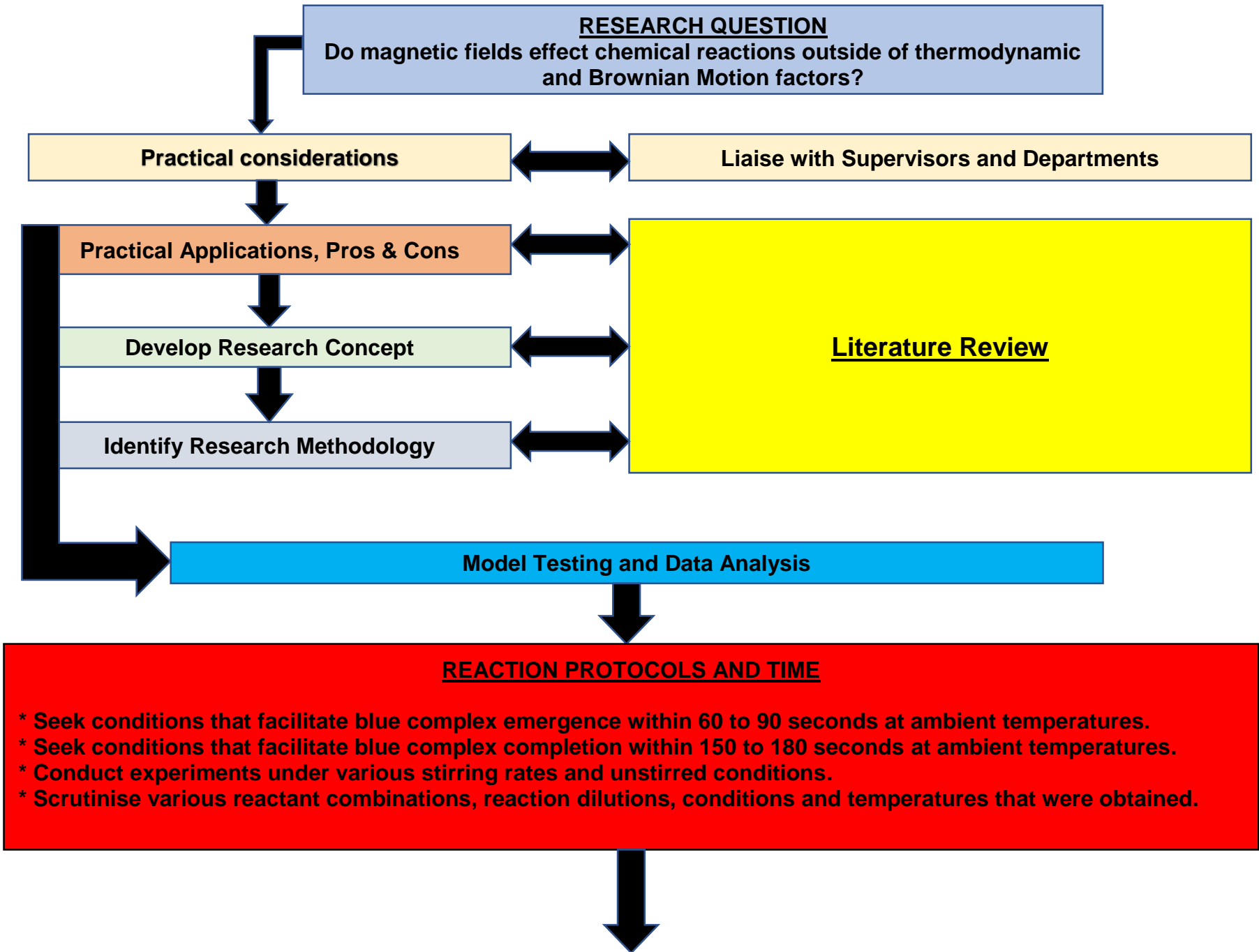
The design focus then shifted to modifying significant temperature rises identified in water measurements inside the aperture of the Dolphin 3000 PEMF instrument with thermocouples of high temperature sensitivity consisting of alloys that were totally resistant to electromagnetic fields, and measurements were gathered on a second by second basis incorporating temperature measurement software on a scientific data logger computer system.

The refrigerated water bath was now incorporated as the recirculating irrigation system of the PEMF instrument, and this was found to insulate temperature fluctuation to a level of high precision, and an identical thermocouple was incorporated with the same data logger computer system to measure identical laboratory ambient temperature reading to calibrate the refrigerated water bath and Dolphin 3000 PEMF instrument under working conditions. This ambient temperature

measuring arrangement was also utilised to record temperatures at the time of exposure and control UV-Vis analysis in order to facilitate temperature consistency.

The 0.3T static magnet exposure method was devised utilising a simple design of a dedicated clean beaker containing a volume of either reactant A or B, with the cylindrical section of the rare earth magnet covered smaller dedicated clean beakers acting as sheaths as the magnet was inserted in to each analyte and located centrally.

Static and PEMF magnetic field exposure experiments were then undertaken in replicate form, and the respective kinetic absorbance initiation times, complexation rates and completion times were measured and compared with equimolar control reaction, whilst carefully scrutinising and employing respective experimental and control temperature correlations, in order to identify conclusions that corresponded with our research aims.



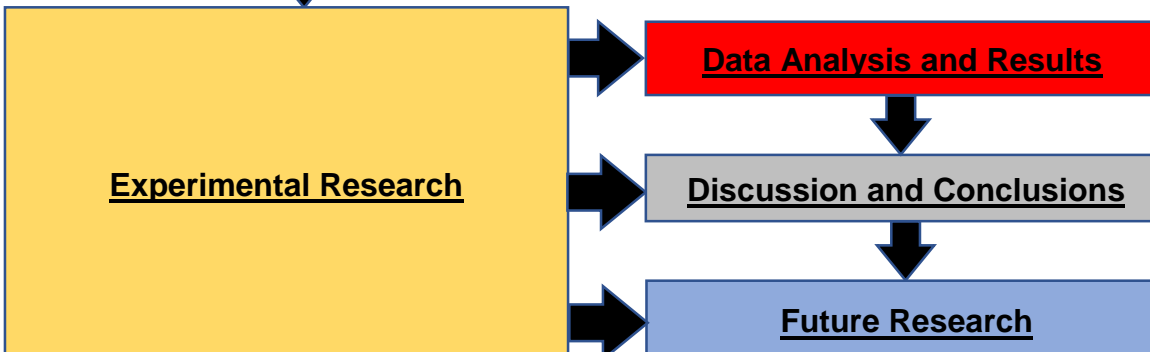
TEMPERATURE

- * Conduct temperature measurements of Dolphin 3000 PEMF under previous research protocols.
- * Conduct initial temperature stabilised experiments with water bath for temperature dependant replicability.
- * Conduct refrigerated water bath experiments to improved temperature stabilisation and replicability.
- * Conduct thermocouple- data logger experiments for ambient aqueous control/static magnet suitability.
- * Design and conduct trial of thermocouple-reactant vessel- Dolphin 3000 PEMF temperature experiments.
- * Design and conduct trial of thermocouple-reactant vessel- Dolphin 3000 PEMF- refrigerated water bath experiments



UV-Vis SUITABILITY & DATA ANALYSIS

- * Conduct initial replicate refrigerated water bath temperature stabilised reactant A & B reactions utilising the Shimadzu UV-1900 incorporating Lab Solutions kinetic software (version 1.03) to identify Instrument sensitivity, and suitable experimental data input regimes for the purposes of incremental reaction measurement, high precision replication and the impact of real time temperature variation during kinetic absorbance measurements.
- * Initiate laboratory temperature stabilisation conditions to mitigate temperature drift throughout the day in the area of the UV-1900 Spectrophotometer, and identify best times for UV-Vis analysis.



Chapter 1: Literature Review

1.1. Applications of magnetic fields

Introduction

The first recorded use of magnetic water treatment (MWT) devices in industrial and irrigation practices can be traced back to the late 1860's when renowned inventor and resident of Iowa, U.S.A., Abram Hay undertook an investigation into the causes of steam boiler explosions which were a dangerous frequent occurrence in the formative years of U.S. industrialization. Gallaher (1947) recounts that Hay eventually arrived at the conclusion that "*foul water*" was the underlying cause of this problem, and that the solution required a focus on the treatment of boiler waters and went on to patent an electromagnetic device "*for the application of a direct circuit of electricity to steam boilers as a protective against corrosion and incrustation*" (pp. 199-200, Gallaher 1947).

Mr Edward Martin (1872), reporting to the Nottingham Institution of Mechanical Engineers, reports that 219 incidents of boiler explosions resulted in 315 people being killed and another 450 injured, concluding in his report that 28 of these fatality and injury incidents were directly related to scale formation, commenting further that scale accumulation had been responsible for 144 steam boiler explosion investigated in the period prior to June 1870.

Abram Hay was later lauded with having an acute understanding "*into the mysterious elements of the world, such as electricity and magnetism, and all those forces comprised of the grand cosmos which have engaged the attention of profoundest philosophers of all ages*" (p.204, Gallaher, 1947).

The historical record reveals that Hay's invention pertaining to magnetic water treatment (MWT), and boiler maintenance was absorbed throughout United States

industry, “*wherever boilers were used*” (p.199, Gallaher, 1947), and this timing was particularly fortuitous during the emergence of the United States railway system.

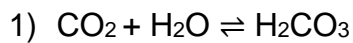
The scientific literature assigns the first recorded claims of a MWT process in Europe to a Belgian inventor, Theodore Vermeiren, who devised and patented an electromagnetic process that was claimed to combat “foul water” and “calcareous incrustation” (Vermeiren, 1958) by means of a treatment pipe which was encased in a magnetic field generated perpendicular to the water flow

.
The focus of research prior to commencing this thesis identified common themes throughout the scientific literature pertaining to magnetic field applications with aqueous solutions consisting of dissolved ions, undissolved salts, the interplay of microbial biofilms and ions, irrigation water treatments and plant responses, and dissolved metals, either in isolation or in combinations. It is with this in mind that the selection of related literature in sub chapters 1.1.1., 1.1.2., and 1.1.3. were of interest.

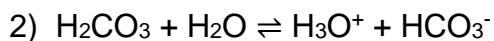
1.1.1. Magnetic treatment of scale (CaCO_3 and Biofilms)

Many ionic species are involved in the process of various scale formations, particularly the bivalent cations calcium (Ca^{2+}), magnesium (Mg^{2+}), ferrous (Fe^{2+}) and barium (Ba^{2+}) along with their scale forming anions carbonate (CO_3^{2-}), sulfate (SO_4^{2-}) and phosphate (PO_4^{3-}), and the most prominently studied of these compounds is the sparingly soluble, calcium carbonate (CaCO_3), which exists as three crystalline salts listed as the decreasing thermodynamically stable polymorphs, Calcite, Aragonite and Vaterite, as outlined by Amjad and Demadis (2015). They go on to state that the precipitation of CaCO_3 is a complex process triggered by variations in pH typically effected by the rise and loss of water absorbed carbon dioxide (CO_2), which in further is result of temperature variation, the population, and types of ions present, leading to a state of supersaturation and the availability of adhesion surfaces, which gives rise to nucleation sites that facilitate the initiation and continuing growth of the CaCO_3 crystallisation process.

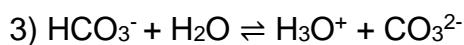
Typically, the process of CaCO_3 formation in the natural environment is the production of carbonic acid (H_2CO_3) from CO_2 dissolved in water (H_2O):



The formed H_2CO_3 then further disassociates to form the aqueous bicarbonate (HCO_3^-) anion and a hydronium cation (H_3O^+):



Which then depending upon pH and temperature can then further go on to form the carbonate CO_3^{2-} anion



* If the concentration of H^+ rises, the products in steps 2 and 3 will shift towards the left. (Dobersek & Giricanec, 2014, p.56).

When the thermodynamic factors are in place to facilitate supersaturation and nucleation then CO_3^{2-} anions engage in ionic bonding with available Ca^{2+} cations and precipitate as the sparingly soluble CaCO_3 :



* If the concentration of CO_2 rises then the reaction will shift towards the left. (Dobersek & Giricanec, 2014, p.56).

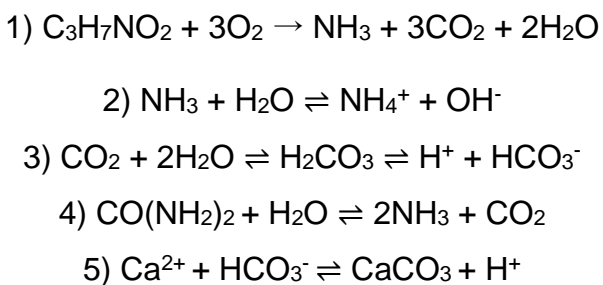
Alotaibi and Bukhari (2021) describe biofilms as singular or multiple microbial communities that adhere to surfaces where favourable water, light temperature, pH, nutrient and mineral conditions are available, allowing for the growth of colonies and the formation of an “*extracellular polymeric matrix*” (p. 617, Alotaibi and Bukhari , 2021).

The development of biofilms follows 5 stages:

- 1) The conditioning layer (reversible): This comprises of organic and/or inorganic matter substrate consisting of optimal conditions utilised to form the base for the bacterial biofilm production, then bacterial adhesion to the substrate.
- 2) Irreversible adhesion: Microbial adhesion has overcome any repulsive factors and established the suitable hydrophobic/hydrophilic surface conditions for biofilm production.
- 3) Maturation (I): The microbial population increases thereby establishing a microcolony allowing for the transport of nutrients and minerals the extracellular polymeric matrix.
- 4) Maturation (II): Rapid microbial population rise, further biological processes are facilitated, and intercellular adhesion polymers and divalent cations contribute to the strengthening the mechanical stability of the intercellular matrix.
- 5) Dispersal: The biofilm population reaches a critical mass respective to location and available nutrients and microbes disperse to generate and colonise other biofilms.

According to Liu et al. (2021), the mechanism of the co-accumulation of biofilm and scale (CaCO_3) has been sparsely researched up until this point in time with biofilm scale accumulations researched respectively as separate microbiological and chemical research disciplines, however new research is emerging integrating these fields with the interplay between microbes, divalent cations such as Ca^{2+} and the formation of scales. This group utilised *Sphingobium limneticum* cultures in sterilised tap water containing $\text{Ca}^{2+} + \text{HCO}_3^- (\rightleftharpoons \text{H}^+ + \text{CO}_3^{2-})$ below supersaturation levels and identified two distinct mechanisms of CaCO_3 formation. In the experiments, analogous culture populations were placed in the tap waters and monitored for cellular growth, pH, and ammonium and calcium ions over identical time periods. The outcomes determined that the *S. limneticum* population (6.0×10^6 cells/mL) had increased at 62 hours in cellular growth, with ammonium (NH_4^+) levels increasing significantly from ~10 milligrams per millilitre (mg/mL) to ~50mg/mL, correlating with a pH increase from 6.5 to 7.2, and that the available Ca^{2+} ions had dropped from

~550 mg/mL to ~360 mg/mL. The microbially induced crystals present in the colonies biofilm at 96 hours were subjected to scanning electron microscope (SEM) and X-ray diffraction (XRD) analysis that revealed rhombohedral structures similar to that found in calcite. The researchers then summarised the experiments, by hypothesising that the bacterial cellular surfaces facilitated CaCO_3 nucleating sites as they grew in the presence of the complimentary increased ammonia production, as an ammonification mechanism via the deamination of amino acids took place (alanine used in mechanism):



Sarker and Hossen (2013) conducted experimental research in Bangladesh utilising a commercial static magnetic water treatment system in a laboratory setting and subjected industrial wastewater sourced from two textile plants and reported that total dissolved salts (TDS) were reduced from 109.2mg/L to 96.8mg/L (~ 11%), water hardness determined respective to Ca^{2+} ion content measurements lowered from 2.193 mg/L to 1.814 mg/L (~17%), combined with a shift in pH from 6.63 to 7.01.

This methodology incorporated several design protocols of importance:

- 1) The movement of the aqueous analyte must be 90° perpendicular to the magnetic field in order to maximise the “shear force”.
- 2) Aqueous analytes should first interact with the field of the magnetic south pole.
- 3) Aqueous analytes then traverse wider and stronger alternating magnetic poles.
- 4) Aqueous analytes finally exit through a chamber consisting of a magnetic North pole field only.
- 5) Water must move through the magnetic fields under pressure, but with as little turbulence as possible.

Alternating magnetic field experiments (0 - 0.026T, orthogonal to waterflow) were conducted by Latva et al. (2016) with surface drinking water collected in Rauma, Finland. The H₂O samples were placed into a stainless-steel storage tank, and two differing independent 25 litre networks consisting of high density polyethylene and copper pipes were set up as the irrigation systems, then the experiments were subjected to monthly temperature, pH, dissolved oxygen, redox, conductivity and chemical composition measurements over an ongoing 9 month period, whilst under identical flow rate regimes. The outcomes identified that the MWT lowered the precipitation of CaCO₃ in both pipe materials, with the significant finding exhibited in copper piping (1.31 and 0.48 µg/cm²) in comparison with their non-exposure experimental controls (1.53 and 0.57 µg/cm²).

After the completion of the MF treatment irrigation experiments, sections of all pipes utilised in the research were isolated and subjected to surface Ca²⁺ analysis, and it was further identified that Ca²⁺ was approximately 15% less prevalent in the pipe samples that were incorporated in the alternating field systems. It was also noted with the copper piping systems that oxygen (% and mg/ml) had diminished in comparison to the incoming water and exiting control measurements which remained relatively consistent. Further FE-SEM analysis on the copper piping system identified that the CaCO₃ morphology was less densely compacted in the copper pipe-AMF samples compared to the control samples and concluded that the magnetic field induced changes in typical morphology due to impacting with typical pipe surface and oxidation reactions.

MWT research of scale inhibition was undertaken by Simonic and Urbanci (2017) at a Slovenian water pumping station, incorporating alternately arranged permanent Neodymium magnets of differing strengths (0.60 & 1.44T), then subjected recirculating water at 1.3 metres per second (m/s) to 1-, 2-, 3- and 4-hour exposure times. Scanning electron microscope (SEM), and X-ray diffraction (XRD) morphology analysis identified that the CaCO₃ deposits from the samples subjected to 2–4-hour treatments contained significantly higher amounts of needle type aragonite morphology in comparison to cuboidal calcite crystals present the control morphologies. Microbiological and physico-chemical analyses of the treatment and

control analytes remained unchanged, and these researchers concluded that the magnetic treatments altered the kinetics of CaCO₃ nucleation.

Controlled laboratory experiments with magnetic fields by Putro and Endarko (2016) were embarked upon to gain a greater insight into underlying MWT mechanisms, by conducting experiments with two differing sets of permanent magnets (0.05T and 0.1T) and incorporating both alternating and inverted design arrangements. A recirculating system containing high alkaline hard water (500 mg/L containing Ca²⁺ and CO₃²⁻ ions) was set at a flow rate of 375 mL/min, and the magnetic water analyte was also subjected to electron discharge (plasma) utilising SS 304 electrodes, to induce the rupture of the ion hydration shells. This research was conducted over 10-, 20-, 30-, 45-, 60-, 80-, 100- and 120-minutes exposure times, and identified that analytes subjected to the 0.1T exposure and plasma treatment over 40 minutes induced an increase in CaCO₃ precipitation of approximately a 75%, with the initial pH 11.37 and conductivity of 1180 microsiemens (μ s) measurements decreasing to pH 10.51, and 363 μ s in conductivity).

Putro and Endarko (2016) concluded that both symmetrical and asymmetrical north and south pole magnetic field configurations utilised without plasma discharge impacted CaCO₃ nucleation, however the asymmetrical arrangement facilitated a twofold effect, and both arrangements were assisted by incorporating plasma discharge. They concluded that the Lorentz force arising from the magnetic field applications, assisted by plasma discharge, impacted on Ca²⁺ and/or CO₃²⁻ hydration cluster characteristics which altered the typical CaCO₃ nucleation kinetics identified in their control analytes.

El-Shamy et al. (2021) analysed static MWT (1.45 ± 0.05T) with saline ground water (200 L/940ppm) under two different recycling flow rates (12.32 and 52.16 L/min), and measured for electrical conductivity (EC), TDS and pH, in comparison to controls, noting that after 75 minutes of MWT at 52.16 L/min flow rate, the EC had reduced by 13.83%, TDS by 14.89% and the pH had dropped from ~8.57 to ~ 8.23. These researchers also incorporated Density Functional Theory (DFT) computational simulations with their work, and concluded that the magnetic field had impacted with

bulk water cluster arrangements rather than ionic modifications, and that this led to the resulting shifts in EC, TDS and analyte pH.

Keyword search: Nonchemical Methods to Control Scale, Boiler explosions scale, Magnetic waste water, Magnetic field brackish water, Magnetic water treatment, Magnetic water calcium carbonate, Magnetic field calcium carbonate, Mineral scales, Magnetic water scale, Microbial bacteria calcium carbonate, Bacterial Biofilm Formation, Magnetic field irrigation water plants

1.1.2. Magnetic fields in electrochemistry applications

According to Monzon and Coey (2014), Gatard, Deseure and Chatenet (2020), and Li and Chen (2021), magnetic fields applied to reagents undergoing electrochemical processes induce “magnetohydrodynamics” (MHD) (p.38, Monzon and Coey, 2014) and have become a topic of much interest in relation to electrolysis, electrodeposition, and chirality research. These research teams have incorporated magnetic fields to create convective forces in electrolysis applications via calibration of the Lorentz Force effect ($F_L = j \times B$), which involves a generated magnetic field \vec{B} interacting with the current density in an electrolysis cell j , that results in vortices that promote improved electrode gas diffusion and mass transport, dependent upon the relative configurations of B to j , noting that a perpendicular design arrangement affords maximum effects compared to a parallel layout which exhibits zero force.

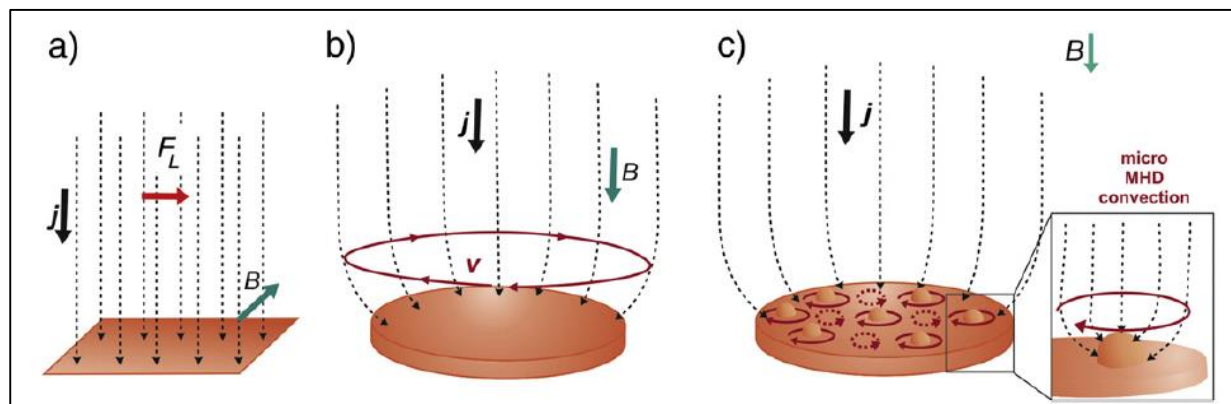


Figure 1-1: Depiction of the Lorentz Force mechanism initiating MHD and micro-MHD vortices
(Monzon, L.M. and Coey, J.M.D., 2014.)

It was further confirmed that a secondary effect of MHD vortices occurs at the sporadic non-uniform protuberances that are formed at the electrode surface, are referred to as “*micro-MHD’s*” (p.97, Gatard, Deseure and Chatenet, 2020), and the modification and control of these factors can induce effects which allow for mechanical manipulation which typical mixing and stirring protocols cannot provide, such as a higher control of Lithium ion (Li^+) dendritic orientation in electroplating processes, resulting in improved mechanical and electrochemical performance.

The chemical and gas manufacturing industries have also begun to take advantage of aqueous magnetic field treatments, in conjunction with electrocatalytic processes, with Pan et al. (2019) engaging in investigative research into the generation of the very useful compound formic acid (HCOOH) derived from the greenhouse gas carbon dioxide (CO_2). They utilised an electrode of copper mesh coated with catalytic tin (Sn) nanoparticles, in conjunction with 25 mL CO_2 and NO_2 saturated 0.3M potassium bicarbonate (KHCO_3) electrolytes (pH 7.56 vs pH 9.27) in electrolysis experiments. Varying reduction potentials -0.8 to -1.7 Volts (V) and static magnetic field strengths (0-0.1T) were incorporated for periods of 30 minutes, whilst monitoring the reduction of CO_2 via UV-Vis spectrophotometry (210-360nm). The outcome of these experiments identified the generation of a CO_2 radical anion (235nm @-1.7V/0.9T), that was not identified in the NO_2 saturated analyte subjected under identical conditions. Post treatment analysis of the collected gas and liquid samples were conducted utilising gas chromatography (GC) and Nuclear Magnetic Resonance (NMR), which revealed that the CO_2 in the 0.3M $\text{CO}_2/\text{KHCO}_3$ analyte was reduced by 89.6%, and the yield of formic acid was increased by 99.90%, when compared to identical control analytes that were not subjected to the magnetic field.

This research concluded that the manipulation of generated spin radicals was the controlling mechanism, providing substantial results that have potentially significant environmental implications.

Research into the electrolysis rotational control of micro-MHD and chiral manipulation has also been undertaken with chiral copper (Cu) “*magnetoelectrodeposited*” (p.1, Mogi and Watanabe, 2011) films, when 20mM solutions of L-alanine and D-alanine and 0.1Molar sodium hydroxide (NaOH)

undergoing exposures with strong magnetic fields (+ and -5T), that were arranged perpendicular to the working design electrodes (~0.7V).

The researchers noted that enantioselective oxidation current for the L-isomer was greater in the +5T field and that the opposite effect was exhibited by the D-isomer undergoing the -5T reversed magnetic field. These researchers further undertook experiments with the enantiomers of phenylalanine, which did not result in chiral selectivity, and concluded this was the result of steric effects related to that compounds benzyl group (-CH₂C₆H₅). They additionally researched aspartic acid, glutamic acid, arginine, and lysine under identical conditions, noting that magnetoelectrodeposited film treatments exhibited chiral recognition for aspartic acid and glutamic acids, and no recognition was exhibited with the other analytes, and concluded that the carboxyl groups (-COOH) on the enantioselective compounds were involved in the recognition process.

Similar investigations conducted by Mishra et al. (2020) into anodic corrosion, by reacting nickel (Ni) in combination with L and D tartaric acid resulted in the formation of the chiral deposition of enantiopure Ni-LTA or Ni-DTA working electrodes, slightly differing with the magnetic field and electrode perpendicular methodology claims noting that a slightly modified rake angle arrangement gave maximal performance.

Keyword search: *Magnetic field electrochemistry, Magnetic field electrochemistry CO₂, Magnetic field electrochemistry amino*

1.1.3. Magnetic fields and environmental applications

Global ecological agricultural deterioration has reached the point where the United Nations Food and Agricultural Organization (FAO and UNEP, 2021) has declared it “one of the major global challenges facing humanity” (p XVIII, FAO and UNEP, 2021) citing the “industrial, mining, waste treatment and agriculture” (p XVIII, FAO and UNEP, 2021) sectors as the main sources contributing to soil pollution, with trace elements which incorporate heavy metals being a significant issue. According to Rebello et al. (2021) many of these metals are highly resistant to degradation and

bioaccumulate in the tissues of aquatic and land-based organisms, and transport down the food chain, triggering reproductive, cardiovascular, neuronal, immunological, and mutagenic disorders. Indonesian researchers, Mahardiono et al. (2016) scrutinised the influence of a PEMF water treatment device (9.1mT) upon heavy metal contaminated water obtained from a lake in Kolong in the Bangka Belitung Islands, which had received runoff from tin mining practices and was utilised by 45,000 people as a freshwater supply. The scientists focused on modifications to heavy metal precipitation and changes in pH over 2 hours at a flow rate of 16.2L/min under EMF treatment, reporting that the replicate experiments revealed a mean shift in pH from 4.84 at 1 hour to 5.25 at 20 hours and a dark brown precipitate emerging in the initially clear pre-treatment samples, consisting of various Ba⁺, Fe⁺, Mn⁺, Zn⁺, Cu⁺, Cd⁺ and Pb⁺ salts.

Phytoremediation is another low cost sustainable ecological restoration practice encouraged by Saxena and Bharagava (2020) and is gaining attention as a means to address heavy metal pollution in soil by harnessing natural and engineered plant and plant microbially assisted metabolic processes in order to extract highly toxic cadmium ions (Cd⁺) from soils, which has also attracted combination treatments with water magnetic treatment protocols, such as that conducted by Chinese research group Niu et al. (2021) regarding de-ionised irrigation water subjected to SMF pre-treatment (100mT @ 3 x 10s cycles @ 300L/min) with 50 day old plumed cockscomb seedlings (*Celosia argentea*) that had been subjected to 0, 10, 25 and 33% root pruning protocols, and irrigated with SMF treated and non-treated deionised water on a 3 day schedule, measuring for soil pH, organic matter (OM), cation exchange capacity (CEC), chlorophyll and carotenoid content, enzyme activities, Cd⁺ uptake, and final biomass weight, , then subjected their measurements to a two way analysis of variance (ANOVA), and after obtaining a necessary p value of < 0.05, the data was further resolved by applying Fisher's protected least significant difference analysis which factored, magnetised water, identical non-exposed water, which derived the following conclusions (see Tables 1-1 and 1-2).

Table 1-1: *Celosia argentea* and 100mT SMF exposure Cd⁺ ion sequestration

Pruning	pH	OM (g/kg ⁻¹)	CEC (cmolc kg ⁻¹)	Biomass (shoots/mg)	Cd ⁺ (µg 1 x 10 ⁵)
Initial	6.1 ± 0.4	23.7 ± 3.9	13.6 ± 3.9		3.5 ± 0.5
	Shift (%)	Shift (%)			Cd ⁺ (µg)
Control 0%	- 3.3	+ 5.3	- 2.9	300	21.40
Control 10%	- 9.8	+ 7.7	- 6.6	600	74.20
SMF 10%	- 11.2	+ 9.2	- 5.9	900	138.10
Control 25%	- 8.2	+ 6.3	- 5.2	500	57.00
SMF 25%	- 9.2	+ 8.1	- 5.5	700	83.10
Control 33%	- 3.3	+ 4.9	- 3.9	400	31.60
SMF 33%	- 3.5	+ 6.9	- 4.2	500	43.50

Calculations were undertaken after organic matter was subjected to ICP analysis to determine the overall Cd⁺ bioremediation by calculating the combined accumulation factor (AF) in roots, shoots and leaves, and the translocation factor of above and below ground material as a measure of in mobilisation of plant transpiration, which revealed the following soil absorbance quantities according to respective cutting and water treatments.

Table 1-2: *Celosia argentea* and 100mT SMF exposure Cd⁺ ion ICP analysis.

Samples	AF (µg)	SMF (±)
Control	21.40	
Control 10%	74.20	
SMF 10%	138.10	+ 60.20%
Control 25%	57.00	
SMF 25%	83.10	+ 37.26%
Control 33%	31.60	
SMF 33%	43.50	+ 31.69%

Accompanying UV-Vis spectroscopy analysis confirmed that the 10% pruning and SMF treatment irrigation water exhibited higher levels of the enzymes catalase, ascorbic peroxidase and guaiacol peroxidase which counter the generation of reactive oxygen species (ROS) which are generated as *Celosia argentea* goes

through the process of sequestering Cd+ ions from soil, leading to the higher Cd+ uptake identified in the SMF samples.

According to Thornley and Adams (2018) the dominant human induced GHG identified with global warming is carbon dioxide (CO₂), with van Oss (2018) reporting that CO₂ increase with cement production reported to have surpassed 4 billion tons worldwide in and is claimed to be the source of 7-8% of the total man-made output of CO₂ over the past century.

Concrete related research conducted by Zhao et al. (2021) focused on MWT with cement in a variety of concrete composition, alternating voltages, MF field strengths and exposure flow rates, determining that the fluidity (workability) of concrete improved after 280mT water exposure, as well as compressive strength (27%), flexural strength (31%) after 2 x 280mT exposure cycles, and most importantly, that the mechanical strength of this MWT regime was preserved when the concrete ratio was reduced by 6.9%.

Keyword search: *Pulsed electromagnetic fields heavy metals water, Magnetic field irrigation water phytoremediation, magnetic water treatment cement*

Comments on sub chapters 1.1.1., 1.1.2. and 1.1.3.

Consistency in static magnetic field - TDS, EC and pH phenomena

The literature which is presented has agreement with regard static magnetic field exposure to aqueous analytes of varying compositions, with Sarker and Hossen (2013), Putro and Endarko (2016) and El-Shamy et al. (2021) all identifying reduction in TDS, EC and a neutralising effect with regards to pH regardless of acidic or alkaline experimental commencement measurements, even though the experimental magnetic field design method utilised by all three research groups differed in configuration and magnetic field strengths applied.

A PEMF field application to water consisting of significant heavy metal pollution (Mahardiono et al., 2016) also identified a tendency towards pH neutralisation in a highly acidic environment and the precipitation of a variety of heavy metal salts.

Varying hypotheses

Sarker and Hossen (2013) hypothesised that magnetic exposure design and analyte flow characteristics to maximise “*shear force*” were crucial aspects of their outcomes.

Putro and Endarko (2016) concluded that both symmetrical and asymmetrical north and south pole magnetic field configurations utilised without plasma discharge impacted CaCO₃ nucleation, however the asymmetrical arrangement facilitated a twofold effect, and both arrangements were assisted by incorporating plasma discharge. They concluded that the Lorentz force arising from the magnetic field applications, assisted by plasma discharge, impacted on Ca²⁺ and/or CO₃²⁻ hydration cluster characteristics which altered the typical CaCO₃ nucleation kinetics identified in their control analytes.

As with Sarker and Hossen (2013), El-Shamy and colleagues (2021) were in agreement regarding the significance of flow rates, and their accompanying DFT computer modelling was somewhat in agreement with the alteration of typical cluster kinetics being impacted under static magnetic field exposures, however they concluded that the H₂O cluster binding arrangements under magnetic field exposure was the predominant driving aspect of their experimental findings.

Mahardiono et al. (2016) concluded that their experimental observations arose to the applied PEMF magnetic force displacing excess H⁺ ions in their acidic analyte driving a shift in heavy metal cation precipitation kinetics.

Contradiction

These combined findings of static magnetic field exposure experimented were contradicted by Latva et al. (2016) who utilised an asymmetrical static magnetic field (AMF) in a perpendicular experimental design configuration with copper piping,

which identified no change in cation measurements over 11 months, and a minor shift in pH moving away from neutralisation. Their hypothesis concluded that AMF induced changes in typical morphology due to impacting with typical Copper pipe surface corrosion and oxidation reactions. Cu⁺ ions were identified as precipitated products in the research of Mahardiono et al. (2016), however the research of Latva et al. (2016) was conducted with alkali analytes (pH 8.17) which rose over 11 months (pH 8.41) but was accompanied by no increase in cationic products.

Magnetic field water irrigation and plants

Niu et al. (2021) employed a regime of static magnetic field exposures with “double de-ionised” irrigation water and root pruning protocols with Celosia argentea in Cd+ ion soil sequestration experiments, and noted that enzymes which catalyse ROS products generated by Cd⁺ plant uptake toxicity were present in higher amounts in the samples irrigated with magnetic field waters, which facilitated significantly higher amounts of Cd+ phytoremediation.

Criticism

No analysis of magnetic field exposed or control “double de-ionised” irrigation water was tabled in the research paper.

Magnetic fields and microbial manipulation?

Liu et al. (2021), reported the mechanism of the co-accumulation of biofilm and scale (CaCO₃) resulted from nucleating sites on bacterial cellular in the presence of the increased ammonia production, however, no magnetic field applications were involved in this research.

Contradiction

Research conducted by Simonic and Urbanci (2017) utilising an asymmetrical north and south pole configuration of static magnets monitored microbiological and physico-chemical properties and reported no change in Coliform, E. coli or Enterococcus populations. Likewise, chemical analysis also remained unchanged.

Hypotheses

Simonic and Urbanci (2017) were in agreement with Sarker and Hossen (2013) and El-Shamy et al. (2021) that magnetic field applications impacted a shift in typical CaCO₃ aqueous cluster kinetics.

The contradictions presented in this short presentation related to microorganism and plant biology under magnetic field exposure briefly outlined in sub chapters 1.1.1, 1.1.2., and 1.1.3. will be further investigated in sub chapter 1.1.4.

1.1.4. Magnetic fields in plant and microbial applications

Introduction

This section of the thesis is dedicated to expanding on the claims that were briefly discussed in the previous comments outlined in pages 40-42.

Sherrard et al. (2018) describe cryptochromes as a class of evolutionary conserved photoreceptor proteins, which modulate plant germination, growth, and flowering processes via the mediation of blue light responses in the 400-500 nanometres (nm) range, and are claimed act as “magnetosensors” according to multiple scientific researchers, including Landler and Keays (2018), Vanderstraeten, Gailly and Malkemper, (2018), Pooam et al. (2019), and Palayam et al., (2021).

Liu et al, (2011) in their work with *Arabidopsis thaliana* reported that blue light induces an electron transfer chain reaction with circadian transcription regulators (*Cry1*, *Cry 2*, *Cry 3*), whereby *Cry 1* recruits molecular O₂ to induce a reactive oxygen species (ROS) redox cycle via three resident tryptophan residues (*try1*, *try2*, *try3*) connected by an aliphatic linkage, which is further connected to a flavin adenine dinucleotide (FAD) residue (see Figure 1-2).

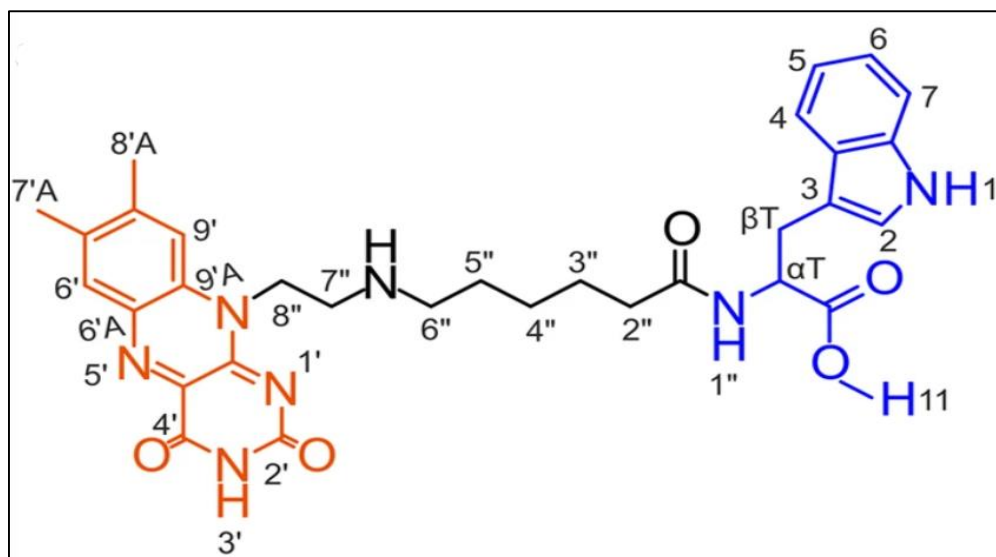


Figure 1-2: Flavin molecule (orange), an aliphatic linkage (black) , tryptophan (blue)
(Paul et al., 2017.)

EI-Esawi et al. (2017) additionally reports that tryptophan electron transfer associated with *Arabidopsis* results in FAD reduction, and the formation of neutral radicals ($\text{FAD}_{\text{ox}} \rightarrow \text{FADH}^{\circ}$ and FADH^{\cdot}) generating conformational changes in cryptochrome resulting in further biological processes, and in the absence of light the complex returns to the oxidised ground state (see Figure 1-3) and was later confirmed by Tweedy et al. (2019).

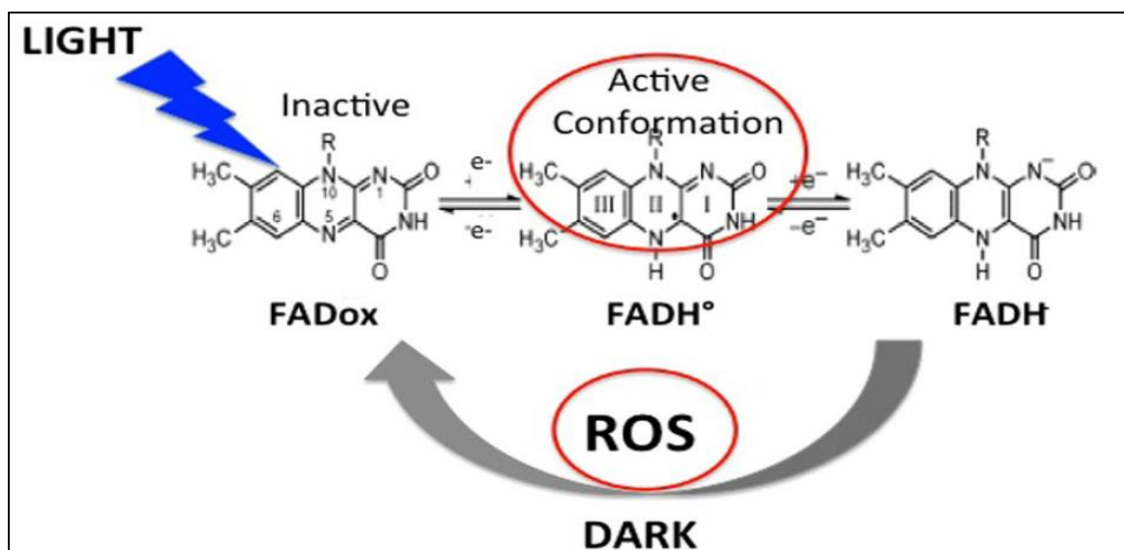


Figure 1-3: Cryptochrome light and dark induced redox cycle (EI-Esawi et al., 2017).

The thale cress (*Arabidopsis thaliana*) is a plant species that has attracted significant interest regarding cryptochrome (*Cry*) and magnetic field mechanism studies, with research conducted by Pooam et al. (2019) focusing on an *Arabidopsis thaliana* wild type strain and transgenic *cryptochrome 1* modified lines, in conjunction with a combination of blue light intensities (448nm x 10-120 $\mu\text{mol/m}^{-2}\text{s}^{-1}$) under 500 μT static magnetic exposure, then compared to control replicates (60 $\mu\text{mol m}^{-2}\text{s}^{-1}$). Phosphorylation assays were conducted on the modified and wild type strains to determine which had the better response to mitigating metabolic phytochrome interference and settled on the modified strains, which were utilised for static 500 microtesla (μT) exposures in conjunction with complimentary exposure and control light regimes of 10, 30, 60 and 120 ($\mu\text{mol/m}^{-2}\text{s}^{-1}$) over 30 minutes. The resulting phosphorylation assays determined that the most significant 500 μT vs control differential increases were identified in the 60 $\mu\text{mol/m}^{-2}\text{s}^{-1}$ and 500 μT magnetic exposure samples, further noting that the variation of light intensity had no significant impact on the control seedlings (see Figures 1-4).

Furthermore, they conducted similar assays on seeds that underwent 500 μT exposures conducted in darkness, with 500 μT exposures conducted under an intermittent light and darkness regime (5min 60 $\mu\text{mol m}^{-2}\text{s}^{-1}$ /10 min dark cycles), with the MF only applied during dark cycles (@T-10sec), then compared the phosphorylation profiles with identical controls, and identified a 19% increase in the 500 μT /total darkness samples and their controls, compared with the 500 μT light and dark intermittent samples and it's controls. The outcomes prompted these researchers to hypothesise that the magnetic fields can induce changes in free radicals which contribute to the cryptochrome generated *Arabidopsis* light cycle.

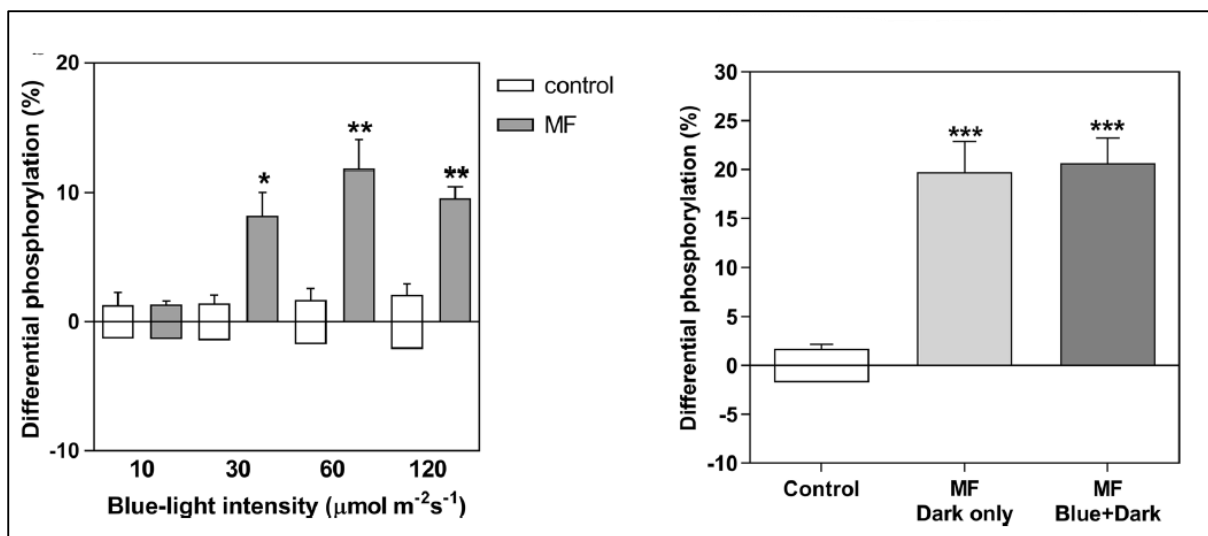


Figure 1-4: (left) Light intensity and static 500 μT cry1 phosphorylation (* $p < 0.05$, ** $p < 0.01$)

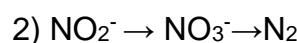
Figure 1-4: (right) Control, SMF light/dark, and SMF dark cry1 phosphorylation (***($p < 0.001$)

(Pooam et al., 2014).

The issue of global warming and atmospheric pollution are of great significance to all of us, and a class of atmospheric gasses of considerable concern are Nitrous oxides (NO_x), which are predominately generated in the natural environment by the microbial metabolism of marine, soil and water borne bacteria, and according to Thakur and Medhi, (2019), this involves an enzyme driven 2 step process which can generate Nitrogen (N_2), first involves the oxidation of ammonium ions by β -proteobacteria, which is converted to nitrite ions:



Then α -proteobacteria sequester the generated nitrite ions to form intermediary nitrate ions and ultimately the formation of N_2 .



However, when conditions of O_2 scarcity arise in the β -proteobacteria environment, nitrous oxide gasses are generated (N_2O and NO) at the (NH_2OH) and (NO_2^-) metabolic phases, resulting the highest generating source of atmospheric N_2O .

The mitigation of atmospheric N₂O has drawn the attention microbial scientists, with Xu et al. (2020) employing both static magnetic field strategies (30mT) with microbial sequencing batch reactors, incorporating synthesised wastewater and integrating microbial sludge inoculations sourced from a Xioanlin wastewater plant (3000mg/L). Replicate microbial control and 30mT exposure cultures were kept under otherwise identical treatment protocols for 124 days at below 10°C temperatures, and experimental analysis monitored for chemical oxygen demand (COD), N₂O emission, total nitrogen removal (TN), enzyme expression, gene expression (qPCR) and overall microbial population analysis via 16S rRNA sequencing.

The analytical outcomes reported that SMF exposure decreased ammonium (NH₄⁺) by 39.5% and total nitrogen by 22.4%, thereby lowering the N₂O conversion rate by an overall 34.3%. The 30mT exposure microbial population exhibited increased expression of *nosZ* genes which encodes for N₂O reductase and *nirS* and *nirK* which contribute to nitrite reductase generation, with gene sequencing revealing a 25.67% culture increase in the denitrifying bacterial species *Zoogloea*, concluding that SMF treatment facilitated microbial denitrification processes.

The incorporation of PEMF exposure in microbial N₂O reduction analysis was undertaken by Wu et al. (2021) by formulating a combinatorial chicken and human manure compost with moisture contents maintained at 56.82 ± 0.37%, then exposing one compost reactor to dynamic magnetic field (0.005T/50Hz) and comparative analysis with an identical control protocol over 48 days, measuring for generated N₂O fluctuations, physicochemical aspects, microbial communities and related NH₄⁺/NO₃⁻/NO₂⁻ → N₂O functional genes and enzymes. The outcomes revealed that the dynamic MF after 240 minutes of exposure exhibited lower values for NH₄⁺ (14 mg/L) compared with controls (32 mg/L), indicating that more nitrogen was retained in this compost, however, the MF microbial counts vs controls revealed a reductions in both the nitrification (<2% vs 8.5%) and denitrification (3.5% vs 9.5%) microbe populations.

The genetic analysis identified that the functional nitrification gene for was inhibited (*amoA* - 96%) in the exposure cultures, resulting in a lower formation of NO₃⁻ and

NO_2^- and a suppression of the ammonium-oxidation pathway, whilst the *narG* expression which contributes to denitrification processes was 83.7% lower, along with both *nirS* and *norB* also significantly lower by ratios of 64:1 and 324:1 respectively. The gene which encodes for the reduction of N_2O to N_2 is *nosZ*, which fluctuated in the MF and control samples throughout the 42 day cycle of measurements, but overall was found to be higher in the MF sample (36.5%), genes encoding for NO_2^- to NO conversion are the reductases *nirK* and *nirS*, which utilise differing pathways and in combination with *nosZ* these genes calculate the metabolic constraint of N_2O production ($\text{nosZ}/[\text{nirK} + \text{nirS}]$) which correlated well with the total accumulated release of N_2O in the MF treatment colony being a significant 39.8% lower than that produced in the control sample (see Figure 1-5).

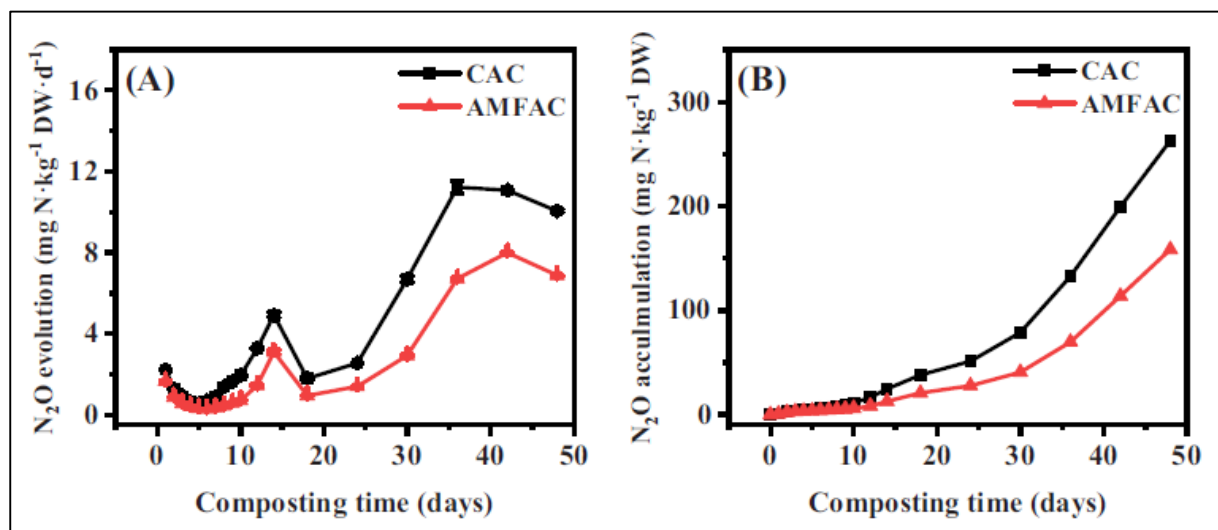


Figure 1-5: Microbial N_2O evolution and accumulation (Wu et al., 2021)

Luo, Zhang and Zhang (2021) mused that *Chlorella vulgaris* is a species of microalga that can engage in a symbiotic relationship with bacteria such as *Bacillus licheniformis* to metabolise aqueous nitrogen and phosphorous waste generated by cultural eutrophication, with the added advantage of reducing water absorbed atmospheric CO_2 due to carbon fixation requirement of the *C. vulgaris* photosynthetic requirements, and design a research model focusing on symbiosis utilising cultures of *C. vulgaris* and *B. licheniformis*, a species resident in the microbial population of the nearby Rihu Lake, and sewerage outlet water taken from that same lake, and incorporating differing SMF exposure regimes of 40, 80 and 150mT. The team established identical and treatment control cultures and the test samples were

subjected were taken from the incubator for 2 hours a day, over 4 days of PEMF treatment, then placed back in incubation after exposure (22 hours @ $28 \pm 1^\circ\text{C}$ / $120 \text{ m}^{-2} \text{ s}^{-1}$ @ 12 hours on off cycles).

The team formulated a method design to scrutinize how SMF exposure may have impacted bound and soluble extracellular polysaccharide excretions (B and S-EPS), enzyme expressions, respective microbial population responses and phycospheric sequestration of total carbon (TOC), nitrogen (TN including $[\text{NO}_2/\text{NH}_4^+]$ composition), and phosphorous (TP). Results from this work ascertained that although the mitigation of N, NO_2^- , and $/\text{NH}_4^+$ was not significant across the range of analytes, the 150mT SMF exposure culture consortium exhibited the highest removal rate, a 56.01% higher cell count compared to controls, Increased S-EPS formation, the highest representation of combinatorial *B. licheniforis*, the lowest pH fluctuation (Base 8.48 ± 0.4 : 150 mT 9.48 vs control 10.04 ± 0.05) and a significantly higher rate of phosphorous removal (82.21%) in comparison to the control cultures.

Comments on sub chapter 1.1.4.

Magnetic field application and *Arabidopsis thaliana*

There is strong agreement in the botanical scientific literature supporting the notion that the blue light activated photoreceptor protein cryptochrome also acts as a “*magnetosensor*”, and functions via a redox switching mechanism that recruits molecular oxygen and creates ROS activate the ground state dark cycle upon interaction with the blue light spectrum.

Pooam et al. (2019) investigated *Arabidopsis thaliana* seedlings under SMF and control conditions with correlating light and dark exposure regimes, and identified that their light intensity regime played no role in phosphorylation expression.

Kusakina and Dodd (2012) inform that phosphorylation assaying is a widely utilised method for identifying gene regulation and signal transduction, particularly in relation to the functioning of circadian cycles. The outcomes of the Pooam research team in

their assays identified that SMF exposure seedlings exhibited higher levels of phosphorylation, and this finding was also present when the SMF exposure seedlings were subjected to total darkness, then compared with controls subjected to a typical light and dark blue lighting regime.

Hypothesis

The Pooam research team concluded that SMF exposure induced free radical generation which upregulated the typical cryptochrome photoreceptor response to blue light activation.

Contradiction

If we return to the experimental findings of Niu et al. (2021) who employed a stronger static magnetic field to irrigation water only (100mT vs 500 μ T) in their Celosia argentea and Cd⁺ soil sequestration experiments (p. ?), they identify an increase in Catalase (CAT), Ascorbate peroxidase (APX), Guaiacol peroxidase (GPX) in their plants subjected to SMF water, resulting in the mitigation of free radical reactive oxygen species, as their hypothesis. Research conducted by Kidwai, Ahmad, and Chakrabarty (2020), Oliveira et al., (2019) and the National Centre for Biotechnology Information inform that CAT, APX, and GPX are ubiquitous in *Arabidopsis thaliana*, yet Pooam et al. (2019) reasonably claim that ROS was increased in their findings, logically infers that CAT, APX, and GPX did not play a mitigating ROS role in their research.

Magnetic field applications and microbial responses

The research of Xu et al. (2020), and Wu et al. (2021) employed differing magnetic field applications on microbial populations, yet found agreement in the reduction of generated N₂O, NH₄⁺, increased expression of the nosZ gene, which is involved in N₂O reductase transcription, leading to an overall suppression of the ammonium-oxidation pathway.

Contradiction

Xu et al. (2020) identified an increase in the nirS gene which is involved in the expression of nitrite reductase in their SMF research analysis, whilst Wu et al. (2021)

noted a decrease in nirS in their SMF research analysis.

Luo, Zhang and Zhang (2021), on the other hand, noted that their work with *Bacillus licheniformis* and SMF exposure resulted in no significant change in N, NO₂⁻, and NH₄⁺ analysis, but reported significant removal of aqueous phosphorous in their symbiotic microalga and bacteria research.

Hypothesis

The research of Xu et al. (2020) reported an increase in the nirS gene which correlated with a marked increase in the denitrifying bacteria *Zoogloea* present in their aqueous analyte, and concluded that SMF exposure facilitated increased microbial denitrification

The AMF exposure experiments conducted by Wu et al. (2021) were undertaken in an environment which consisted of less water, and under consistent moisture control, that identified a significant decrease in AMF amoA gene involved in the nitrification process which lowered the formation of NO₃⁻ and NO₂⁻ as well as the narG and nirS genes which are crucial in the denitrification pathways, resulting in a hypothesis that nosZ was enhanced as a result, and the combination of AMF induced nitrification and denitrification microbial gene expression was responsible for their findings.

These findings raise the question of whether magnetic field applications could impact with immunological and medicinal responses in higher animals, and will be addressed in sub chapter 1.1.5.

Keyword search: *plant cryptochrome, plant cryptochrome magnetic, Phosphorylation in the plant circadian system, nitrous oxide processes water, nitrous oxide magnetic, nitrous oxide magnetic 2021, nitrogen phosphorus bacteria magnetic 2021, Arabidopsis class III peroxidase, National Centre for Biotechnology Information Catalase (CAT), National Centre for Biotechnology Information Ascorbate peroxidase (APX), National Centre for Biotechnology Information Guaiacol peroxidase (GPX)*

1.1.5. Magnetic field applications in mammalian medical research

Introduction

The research outlined in sub chapters 1.1.1., 1.1.2. and 1.1.3. identified that magnetic field applications impacted upon dissolved aqueous ions, via shifts in typical ion-H₂O and H₂O cluster dynamics, which in some instances impacted ionic nucleation kinetics and resulting morphologies. Magnetic field exposure impacting typical oxidation processes was also presented. A range of associated magnetic field strengths, experimental designs, and methods were also presented and phenomena was reported for all research presentations. Literature provided in sub chapter 1.1.4. delved deeper in to magnetic field phenomena associated with plants and microbes, which consistently reported changes in gene expression when incorporating a variety of designs and methods, then analysed against the respective control samples. This section of the thesis now looks at magnetic field applications utilised in mammalian medical research.

The science of magnetic research into neuronal molecular and cellular responses to low intensity pulsed electromagnetic fields (PEMF 13mT/1- 100 Hz) was conducted by Grehl et al. (2015) on cell cultures isolated from pooled cortex samples gathered from mice. The administration of five varying pulse regimes (see Table 1-3) was incorporated daily for 10 minutes under in vitro incubation over 4 days (37°C/5% CO₂ + 95% air), whilst real time Ca⁺ cellular analysis was conducted during the treatment period, in order to identify any mechanisms, then correlate survival and morphology findings. This work identified that three PEMF protocols induced a rise in cellular Ca⁺ by 13.4 ± 2.3%, 15.0 ± 2.6% and 15.1 ± 2.0% respectively, concluding that the extracellular Ca⁺ was not significantly affected, but increases were due to neuronal intracellular Ca⁺.

Table 1-3: PEMF phase and time design for gene response		
Frequency (Hz)	Pulse phase	Pulse total (10 min)
1	Uniform	600
10	Uniform	6000
100	Uniform	60,000
cTBS	3 @ 50Hz then 3 @ 5 Hz	7000
BHFS	20 x 62.6ms @ 9.75 Hz	120,000

The researchers then conducted a further series of analyses on a variety of selected human gene cultures and determined the following PEMF induced responses (see Table 1-4), concluding that intracellular calcium flux had impacted gene expression under low intensity repetitive magnetic stimulation (Table 1-4).

Table 1-4: PEMF phase and time regime gene response.				
Gene	1 Hz*/#	10 Hz*/#	BHFS Hz*/#	Function
Brca1	-	Up	Down	Breast cancer 1 trnscrp. regulator
Cdk5	-	-	Up	cytoskeleton nuclear kinase
Cga	-	-	Down	cell survival hormone
Crh	Down	Down	Down	cell survival cytokine
Cyr61	-	-	Down	cytoskeletal protein
Eno2	Down	Down	Down	cell survival cytoplasm enzyme
Hk2	Up	-	Down	cell survival cytoplasm kinase
Hspa4	-	-	Down	cytoplasm protein
Pmaip1	-	Up	Down	apoptosis cytoplasm protein
TNF	-	Down	Down	cell survival cytokine

* p value relative to controls, # Fold change (log)

According to Klimov (2019) cytokines are six classes of cellular secreted proteins which promote immunomodulatory functions in the recruitment or suppression of other cytokines and cellular interactions via specialized cellular receptors, with Dembic (2015) further noting that combinatorial cytokines can induce anti-cancer effects include Interferon-gamma (IFN- γ), Interleukins 2 and 3 (IL-2, IL-3) and Tumor Necrosis Factor alpha (TNF- α), which is a fundamental cytokine in carcinogenic processes. Magnetic field research has been incorporated with gene regulation to investigate the potential modification of cytokine expression on tumor regulation.

Novoselova et al. (2019) embarked on an investigation to identify how cytokine expression and related oncogenic aspects were affected by static and dynamic magnetic field exposure, with a further focus placed on the significance of the role the geomagnetic field (GMF) plays a role in cytokine expression and immunity function.

The research conducted experiments accounting for the local GMF (30µT), then incorporated a further range of SMF's (42, 60, 2 x 65 and 150 µT) in conjunction with 100 µT and 200 µT plus 65 µT PEMF/SMF regimes of varying frequencies (Hz) on 60 mice injected with Ehrlich carcinoma cell cultures (2×10^5). The 14 day exposure groups consisted of 30 mice subjected to the 5 different PEMF + SMF regimes, and a 30 mice control group that was subjected to an induced field synchronized with the local geomagnetic field. Upon the elapse of these 14 day protocols, blood, splenic T-lymphocytes, and peritoneum macrophages (abdominal lining) samples were isolated, and ELISA analysis focusing on respective IFN- γ , TNF- α , IL-2 and IL-3 profiling was undertaken. The conclusions revealed that the 100 µT PEMF/60 µT SMF analytes exhibited the highest prevalence of all 4 cytokines in comparison with controls, with the 100 µT PEMF in combination 150 SMF treatments results revealing negligible impacts upon all cytokine analytical profiles. Notably, the 200 µT PEMF/65 µT SMF samples revealed a higher expression of IFN- γ , TNF- α , whereas a comparable expression of IL-2 and IL-3 was seen in the controls (see Table 1-5). As expected, no effects were observed in the cytokine profiles of the 30 µT GMF control samples.

Table 1-5: Cytokine response to combined PEMF and SMF regimes									
Cytokine	PEMF	SMF	Macrophage (pg/ml)		T-Lymphocyte (pg/ml)		Blood plasma (pg/ml)		
	(µT)	(µT)	Control	MT	Control	MT	Control	MT	
TNF-α	100*	60	14 ±0.9	52±4.8	11±0.9	39±4.0	4.1±0.3	20±2.4	
IFN-γ	100*	60	37±4.1	101±8.9	37±4.1	128±11.9	8±0.3	25±1.0	
IL-2	100*	60	-	-	85±9.6	126±10.5	26±3.1	59±5.4	
IL-3	100*	60	-	-	67±7.1	125±12.0	17±2.4	47±2.9	

* 6 frequency: 5.10; 5.26; 5.91; 6.26; 6.31; 6.98 Hz

The combined 100 μ T PEMF/60 μ T SMF regime was then further utilized in combination with Ehrlich carcinoma induced mice (x 30) and compared with control subjects (x 30) to monitor tumor growth progression over 35 days and mortality over 70 days and identified that the exposure treatment population had slower tumor progression from 17 days onward and was maintained until the analysis concluded at 35 days. The exposure population also exhibited a later onset of mortality (45 vs 27 days) and had a greater life expectancy at 70 days (~30%), whereas the control populations were all deceased by day 55. These researchers concluded that low intensity pulsed magnetic fields induced immunostimulatory effects, and further reinforced a hypothesis that the GMF influenced biological processes (Figures 1-6).

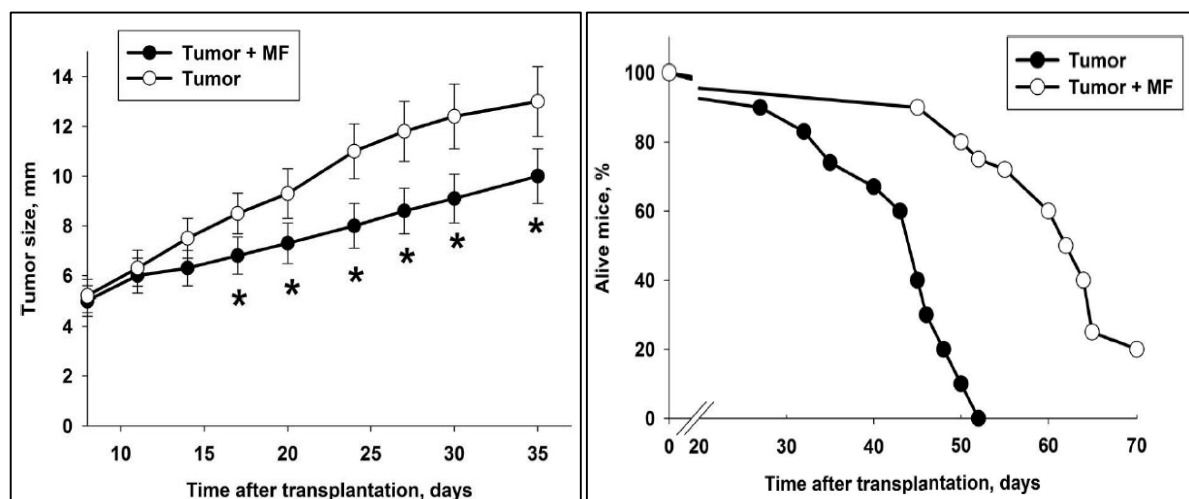


Figure 1-6: Mice Ehrlich carcinoma size and mortality 100 μ T PEMF/60 μ T SMF (* $p < 0.05$)
(Novoselova et al., 2019)

Natural Killer cells (NK) make up 10-15% of human leukocytes according to Dembic (2015) and are innate immune cells which mediate the first phase in tumor cell recognition and collaborate with cytotoxic T cells and B cells as an adaptive immune tumor response. Shu-Li Lin et al. (2019) undertook research to determine the impacts of SMF exposure (0.4T/4, 48 and 72 hours) under incubation (5%CO₂/37°C/100% humidity) with cultured human NK cells (NK92-MI) to measure cytotoxic correlations on human erythroleukemic breast cancer cells (K562). Cellular viability, membrane integrity, and the feasibility of impacts upon DAG/IP3, ERK, JNK, p38 and STAT 3 signaling pathways by utilizing inhibitors to selectively isolate each cascade were analysed, and the results reported that NK cells proliferated at a 1.28-

fold increase compared with controls, noting the inhibited STAT3 signal pathway had played no role on SMF NK cells. Conversely, the ERK, JNK, p38 inhibitors reduced SMF enhancements, whilst no statistical relevance was identified with the DAG/IP3 inhibitor treatments.

Cytotoxicity evaluations identified the pre-treatment of NK92-MI with 0.4T SMF for 48 hours prior to exposure to the K562 cells, and a final post treatment of 4 hours exposure contributed to a $74.03 \pm 9.95\%$ ($p<0.01$) increase in K562 cell neutralization, whilst SMF 0.4T/48 hours exposures with K562 control cultures in isolation did not exhibit any neutralization effects. Shu-Li Lin et al. (2019) concluded that NK cell proliferation and a correlating increased activation of the MAPK signaling pathway explained their findings. No significant promotion or inhibition of any research of their initial signaling pathways was identified.

Glioblastoma multiforme is an incurable affliction that contributes to 50% of adult brain tumours, with Gesundheit et al. (2020) revealing the depressing statistics of a median survival rate of 15 months, and a 5-year survival rate below 10%, due to this illness being generally impervious to most radiotherapy and chemotherapy treatments. Horton et al., (2009) summarised that the condition is commonly treated with Temozolomide, a drug belonging to the class of imidazotetrazine compounds which acts as a cytotoxic agent, particularly with early detection, by delivering methylating payloads to targeted zones and impair oncological growth by depleting the demethylation repair protein MGMT.

Unfortunately, *Glioblastoma multiforme* has also attained evolutionary tumor resistance pathways which downregulate the drug's effectiveness. Kirstein, Schmid, and Combs (2020) further add that micro-RNA's (miRNA's) are a class of non-coding RNA's (19-22 nucleotides) which compliment messenger RNA regulation via cleavage and translational suppression, with over 2000 variants currently identified in the human genome, that are also frequently identified as upregulated in cancers, with miR-21 claimed as playing a role in blocking the activation of *Glioblastoma* apoptosis and enabling mechanisms such as MGMT to intervene in favour of oncogenic proliferation. Italian researchers Pasi et al. (2016) subjected chemotherapy resistant *Glioblastoma* cell line (T98G) to a combination of

Temozolomide and PEMF treatments (2mT/75Hz) in silico, then monitored for epigenetic mediation in *miRNA* proteins. The method exposed the treatment cultures to 60 minutes of PEMF exposure, then further incubation for 24 hours before subsequently administering 10 µg of Temozolomide to PEMF treatment and control samples. Analysis of *miRNA* expression was conducted over the following 8 days and the research outcome noted that the apoptic index increased to between 5 to 8% for the Temozolomide- PEMF treatment in comparison to Temozolomide only controls ($p<0.05$), adding that whilst all cultures displayed little variation in their actual *miRNA*-21 cellular mechanism, the protein was significantly downregulated in the combination Temozolomide and PEMF treatment cultures (Figure 1-7, $*p< 0.05$).

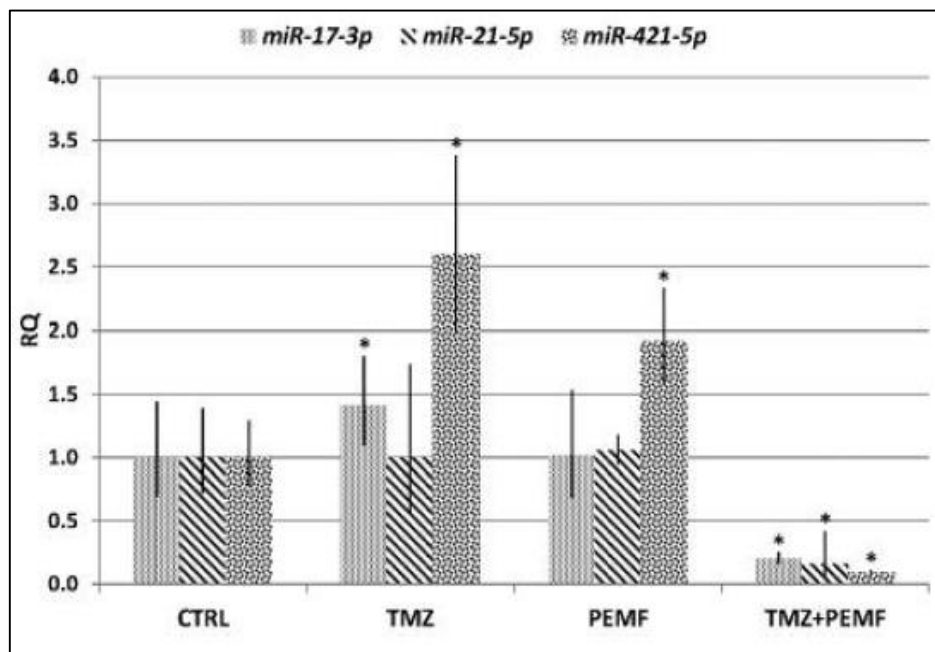


Figure 1-7: Downregulation of miR-21-5p in Temozolomide/PEMF treatment (Pasi et al., 2016)

An extensive compendium by Lippert (2009) related to Cisplatin ($\text{Cl}_2\text{H}_6\text{N}^2\text{Pt}$) states that it is a class of platinum containing compounds first identified in 1969 as a significant cancer treatment and is considered the “*first line*” (p. 39, Lippert, 2009) treatment for a wide range of sarcoma, carcinoma, and lymphoma tumours. The molecule consists of a platinum (Pt) centre, bonded to two inert ammonia (NH_3) ligands, and two chloride (Cl) ligands (see Figure 1-8).

The chloride ligands act as *in vivo* leaving groups, eliciting a mode of action via intracellular hydrolysis that further initiates Pt positive charge activation, thereby

inducing covalent bonding at DNA guanine regions and resulting in cross linkages which disrupt tumour replication and transcription, ultimately leading to cell cycle arrest and apoptosis.

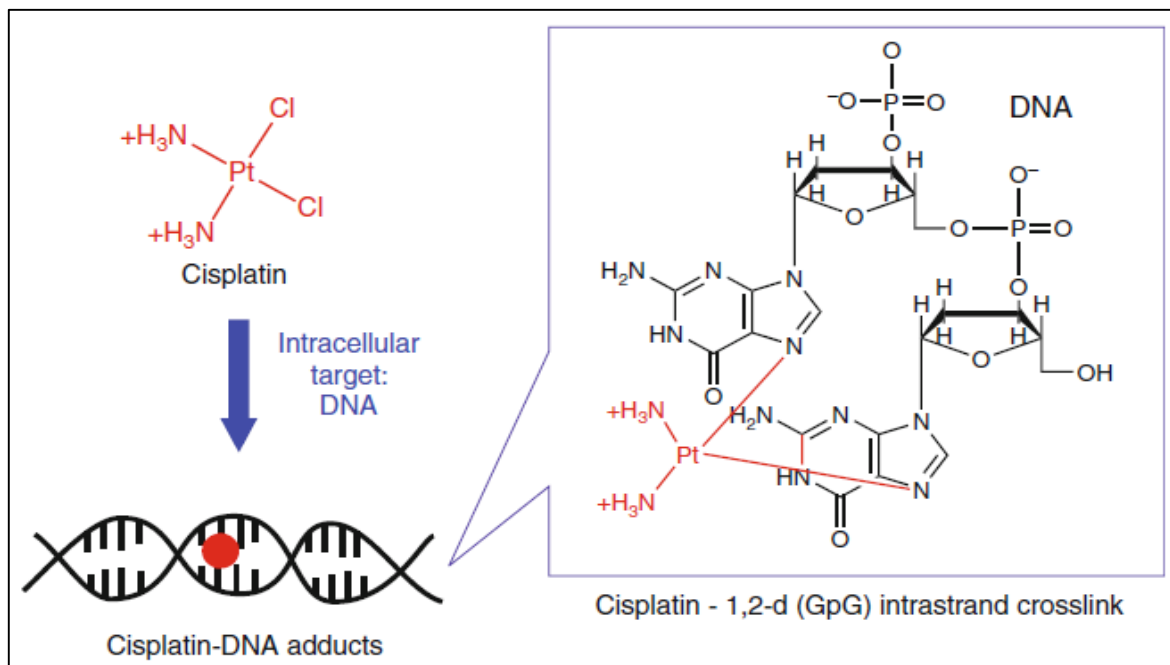


Figure 1-8: The Cisplatin 1,2 intra-strand DNA cross linkage mechanism (Schwab, 2017)

A variety of toxicity issues have arisen over time with use of the drug, and additionally many variations of cancer cells have evolved strategies to inhibit its efficacy, therefore alternative combinatorial therapies including magnetic field treatment research have been incorporated with this treatment. Jalali et al. (2019) set out to identify the impact on two differing cultures of human ovarian carcinoma cells that were sensitive (A2780) and resistant (A2780-CP) to Cisplatin treatment to analyse responses with a combinatorial regime of Cisplatin dosages (1, 10, 20, 50, 100 and $500\mu\text{l}$), PEMF strengths (10, 15 and 25mT) and exposure times (24, 48 and 96 hours).

The experimental outcomes reported negligible variation with PEMF treatment alone and the increased dosage and time correlations afforded a predictably conspicuous correlation between the sensitive and resistant strains, however, the incorporation of PEMF treatment and Cisplatin resulted in a significant decrease in overall carcinoma cell viability. The PEMF strengths utilised in this research did not identify any

significant difference in cellular cisplatin uptake, but a significant PEMF exposure time correlation did appear in the data sets (see Figures 1-9).

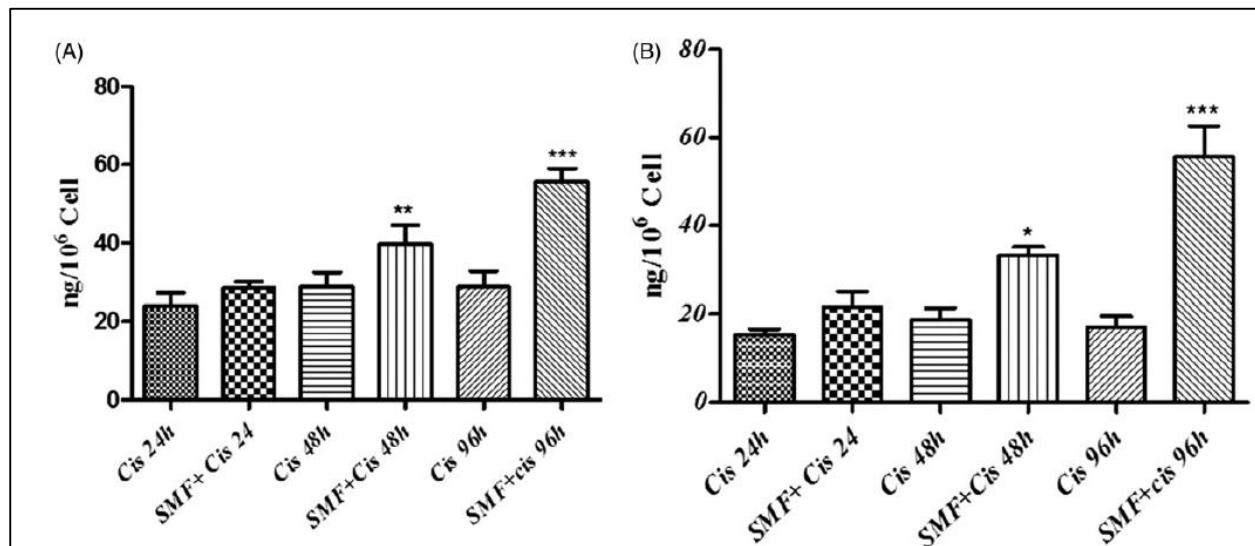


Figure 1-9: ICP analysis of A2780 (left) and A2780-CP (right) cisplatin uptake of combined SMF and exposure regimes vs cisplatin only treatments
(mean \pm SD, * $p\leq.05$, ** $p\leq.01$, *** $p\leq.001$) (Jalali et al., 2019)

The oncogenic cellular resistance to Cisplatin treatment is not the sole focus of research, with MF treatments related to dosage and toxicity being undertaken to determine whether magnetic combination treatments can mitigate outcomes and prolong treatments, such as that undertaken focusing on kidneys, which according to Shinde et al. (2021), is a major issue for Cisplatin related nephrotoxicity and affects approximately 20% of related patients. Rageh, El-Garhy, and Mohamad (2020) undertook a combination of low dosage Cisplatin (3 and 6 mg/kg) with and without PEMF exposures (50mT @ 50/60Hz/30 min/12 days) on mice induced with Ehrlich carcinoma, focusing their analysis on oxidative stress (SOD/MDA/GSH), microscope histopathology, and comet assays to scrutinise tumour and kidney tissue morphology.

These research findings announced that the 3mg Cisplatin and PEMF combination exhibited higher tumour and kidney cell malondialdehyde levels than 6mg Cisplatin alone (3.3 ± 0.2 vs 3.3 ± 0.2 nmol/ml), along with reduced superoxide dismutase (56 ± 2 vs 78 ± 5 U/g), and glutathione levels (0.6 vs 0.9 ± 0.1 mU/ml) in comparison to controls and 3mg Cisplatin treatment, and concluded that lower levels of cisplatin

combined with PEMF exposure reduced tumour size, whilst mitigating mitochondrial nephrotoxicity and the associated over production of reactive oxygen species (ROS) (see Figure 1-10).

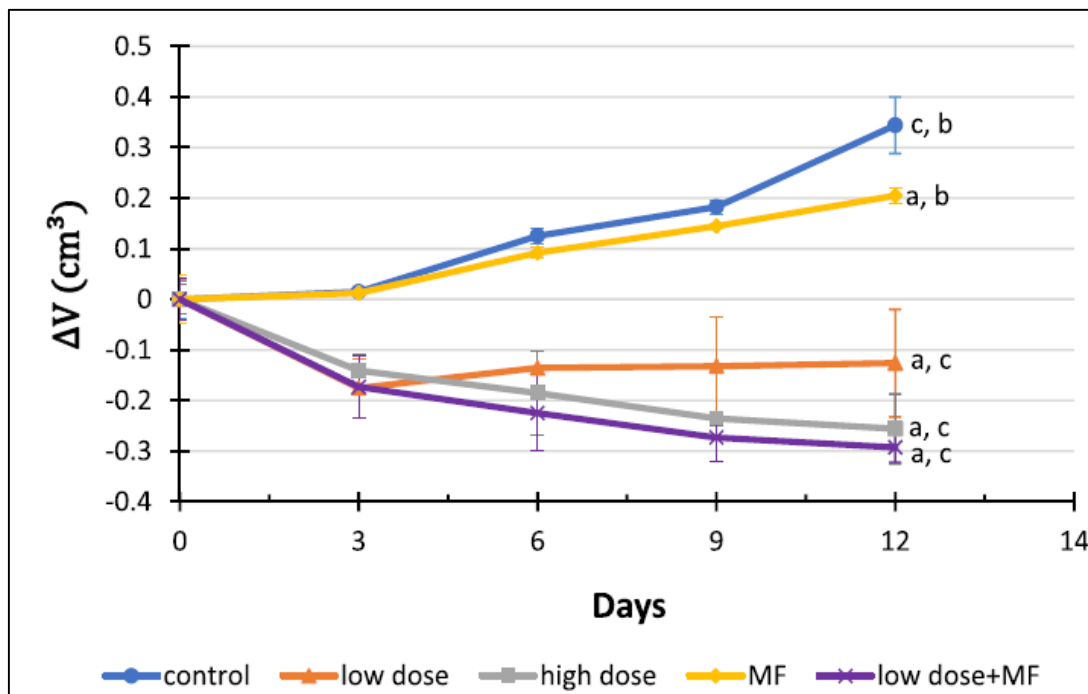


Figure 1-10: Ehrlich tumour volume over 12 days (a) $p < 0.05$ compared with control group, (b) $p < 0.05$ compared with low dose of cisplatin group, (c) $p < 0.05$ compared with MF group

Comments on sub chapter 1.1.5.

Correlations identified in this research

A total of 19 PEMF exposure protocols were employed in the aforementioned research, with 17 outcomes deemed to have statistical relevance in the manipulation of gene expression, and 2 affording negligible results. There were also 3 differing time related SMF methods employed, which concluded with 2 outcomes having significant results in NK cell proliferation which would implicitly correlate with altered cytokine and gene responses. All of the research presented here reported magnetic field exposure phenomena outside of their respective control experiments.

Grehl et al. (2016) and Novoselova et al. (2019) both utilised PEMF regimes in their experiments which impacted upon cytokine expression.

Pasi et al. (2016), Jalali et al. (2019) and Rageh, El-Garhy, and Mohamad (2020) all reported significant results in their research with PEMF exposures in combination with drug treatments and human tumour cell lines, Jalali et al. (2019) and Rageh, El-Garhy, and Mohamad (2020) both incorporating cisplatin.

Hypotheses

Grehl et al. (2015) presented the view that pulsed electromagnetic exposure frequency and phase regimes with mice neuronal cultures, impacted upon intracellular neuronal Ca⁺ mobilization, which further gave no response in gene expression or variations of up and down gene regulation depending upon the specific electromagnetic frequency and phase application.

Novoselova et al. (2019) arrived at a very broad conclusion that low intensity pulsed electromagnetic fields can induce immunostimulatory effects in mice inoculated with Ehrlich Carcinoma, which inhibits tumor progression and increases mortality. They further claimed that the geomagnetic field also plays a role in typical terrestrial immunity responses.

The research with Temozolomide and PEMF's in combatting Glioblastoma multiforme in silico by focusing on miRNA analysis undertaken by Pasi et al. (2016) theorized that whilst the miRNA-21 cellular mechanism appeared to remain unaffected by the combinatorial treatment, miRNA-21 expression was still significantly mitigated in the Temozolomide + PEMF experiments compare with Temozolomide controls.

Jalali et al. (2019) concluded that cisplatin dosage identified typical responses with sensitive and resistant cultured of human ovarian carcinoma cells, and that their range of applied PEMF strengths had a negligible impact, but identified a strong correlation between combinatorial cisplatin and PEMF time exposure in comparison to cisplatin only controls.

Research in to associated cisplatin dosage and nephrotoxicity with mice induced with Ehrlich carcinoma, and incorporating PEMF applications, conducted by Rageh,

El-Garhy, and Mohamad (2020), proposed that lower dosage cisplatin combined with PEMF exposure reduced tumour size with the comparable effects of higher dosage cisplatin, by inhibiting the toxicity associated production of reactive oxygen species (ROS), thereby mitigating mitochondrial nephrotoxicity.

Shu-Li Lin et al. (2019) experiments with SMF exposures, cultured human NK cells (NK92-MI) and human erythroleukemic breast cancer cells (K562) in silico, recognized that the SMF exposure had no impact the K562 cultures, but had induced proliferation of the NK92-MI cultures when compared with controls. This facilitated a ~65-85% increase in K562 cell neutralization when the culture was combined with the PEMF exposure NK92-MI cultures, revealing that the NK92-MI MAPK signal pathway had also been significantly enhanced by PEMF exposure

Contradictions

The reports of Grehl et al. (2016) PEMF and Novoselova et al. (2019) PEMF /SMF accounting for GMF reported differing cytokine responses with respective mice neuronal and blood, spleen and abdominal analyses. Grehl et al. (2016) identified that gene expression and cytokines can be either unaffected, upregulated, or downregulated dependent upon PEMF frequency and phase, whilst Novoselova et al. (2019) identified either negligible or significant upregulated expression. The important anti-cancer cytokine TNF was deemed unaffected or downregulated by the Grehl et al. (2016) research team, whilst Novoselova et al. (2019) noted significant increased expression of TNF- α in their blood, spleen, and abdominal analyses by ~370%, ~350% and ~500% respectively.

Jalali et al. (2019) identified a strong time correlation of PEMF exposure and cisplatin with ovarian carcinoma cultures (96 hours), whereas Rageh, El-Garhy, and Mohamad (2020) reported significant results with a linear short PEMF exposure method (30 mins) over a longer time frame (12 days) in conjunction with cisplatin applications with Ehrlich carcinoma.

Keyword search: *human cell magnetic cryopreservation, basic immunology, cytokines immune system, cellular molecular change magnetic field, cytokines*

magnetic field, magnetic field tumour NK cells, Encyclopaedia of Cancer, Glioblastoma multiforme treatment survival 2020, temozolomide mechanism of action, Glioblastoma multiforme miRNA, magnetic field glioblastoma, pulsed electromagnetic field glioblastoma, cisplatin chemistry cancer drug, magnetic field tumour cisplatin

1.2. Water (H_2O)

Introduction

The impacts of magnetic field exposures and interactions with ions and molecules in aqueous environments was consistent throughout chapter 1.1., and the single common factor in all of the prior scientific literature has been water. The focus of this work now turns to investigating the literature pertaining to the properties of water in isolation, with Lupis et al. (2013) report that in isolation, or in combination with various organic and/or inorganic factors, there has been extensive research undertaken, resulting in a multitude of reported outcomes and hypothesized mechanisms, which is at first appearance intuitively at odds considering the simplicity of water molecules.

The literature reveals that this simple, abundant compound exhibits a myriad of complexities, many of which still defy detailed understanding to this day. This section of the thesis investigates various theoretical aspects of the chemistry of water, examining its structure, hydrogen bonding, intramolecular hydrogen bonding cluster arrangements and how these respective geometries correlate to hydrogen bond binding energies, autoionization, and will conclude with research related to the respective ortho and para H_2O isomer properties arising from their associated H atom spin states.

This platform of theoretical understanding will then be examined with regard any possible significance with respect to the interaction of magnetic and electromagnetic fields, in order to gain insight into the role that it might play in the reported phenomena. The magnetic field and H_2O research section (1.3.) will not contain a

final combined comment summary, but is accompanied by brief comments related to the respective mechanism conclusions associated with the presented research.

1.2.1. H₂O Hydrogen bonding

The polarity arising from the imbalance in the H₂O molecule's electron distributions facilitates hydrogen bonding between the two oxygen atoms on adjacent H₂O molecules which are bridged by a resident donor hydrogen atom on one of the H₂O participants at the lone pair of electrons on the acceptor oxygen atom of the other molecule, as described by Stefanutti (2017), forming a weak bond calculated at 23 kJ/mol at acceptor O and donor H distance of ~1.7 Å and an acceptor O and donor H-O distance of ~2.7 Å (Figure 1-11). The redistribution of acceptor and donor H₂O charges arising from hydrogen bond interactions facilitates further charge specific attractions and repulsions throughout the H₂O network, further elaborating that the intermolecular structure exhibits low energy stabilisation as a tetrahedral geometry (Figure 1-12), however, these bonds are strongly influenced by thermal factors, and highly dynamic in nature with lifetimes in the order of picoseconds.

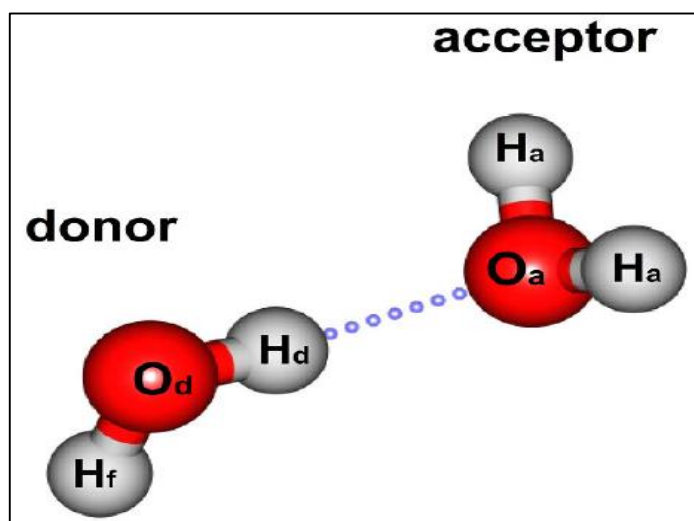


Figure 1-11: MDS of H₂O (donor) and H₂O (acceptor) low energy configuration (Stefanutti, 2017)

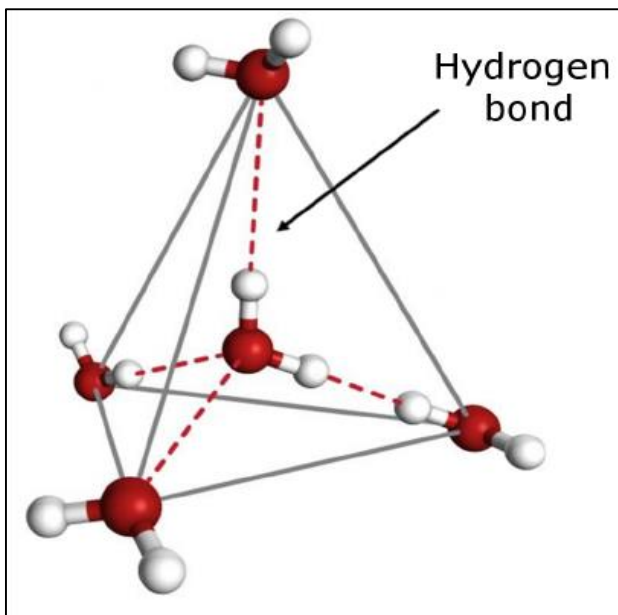


Figure 1-12: Hydrogen bonded tetrahedral H_2O configuration (Stefanutti, 2017)

1.2.2. H_2O cluster geometry and binding energies

The nature of the combined electronic charge transfers of hydrogen bond interactions, are referred to as non-additive effects, which according to van der Lubbe and Guerra (2019), are the result of two or more hydrogen bonds in a cluster arrangement by either strengthening (cooperativity), which facilitates a stronger cluster binding energy than the same number of contributions occurring individually and is usually associated with directional factors, or conversely, weakening hydrogen bond associations (anti-cooperativity) relating to charge transfer interactions that tend to weaken the overall hydrogen bonding network in a given H_2O cluster.

Castor-Villegas et al. (2020) reported that cooperative arrangements could increase hydrogen bond formation energy by up to $\approx 65\%$ in H_2O clusters, whilst anti-cooperative contributions could reduce structural H bonding by $\approx 25\%$. These researchers utilised a novel quantum topology and interacting atom computer simulation method (QTAIM) and identified that tri-coordinated H bonds were surprisingly stronger contributors than tetracoordinated species in a selection of $(\text{H}_2\text{O})_{n=11-17}$ clusters, however, that tetra-coordination was favoured in large water clusters due to the reduction of anti-cooperativity associated with double HB donors and acceptors and conferring to higher overall favourable interactions.

Computer simulation modelling conducted by Kirov, Fanourgakis and Xantheas (2008) investigating hydrogen bond kinetics beyond dimeric H₂O- H₂O interactions was utilising cooperative (trans) and anti-cooperative (cis) dimer contributions in a pentagonal dodecahedron cluster (H₂O)₂₀ structure (see Figure 1-13) to calculate all of the 30 possible H bond arrangements representing 30,026 isomeric configurations, and identified that the most energetically favoured arrangement consisted of 18 cooperative *trans* components and 12 anti-cooperative *cis* geometries concluding that H₂O- H₂O and H₂O neighbouring molecules contributed to the overall stabilization of the energetically favoured cluster.

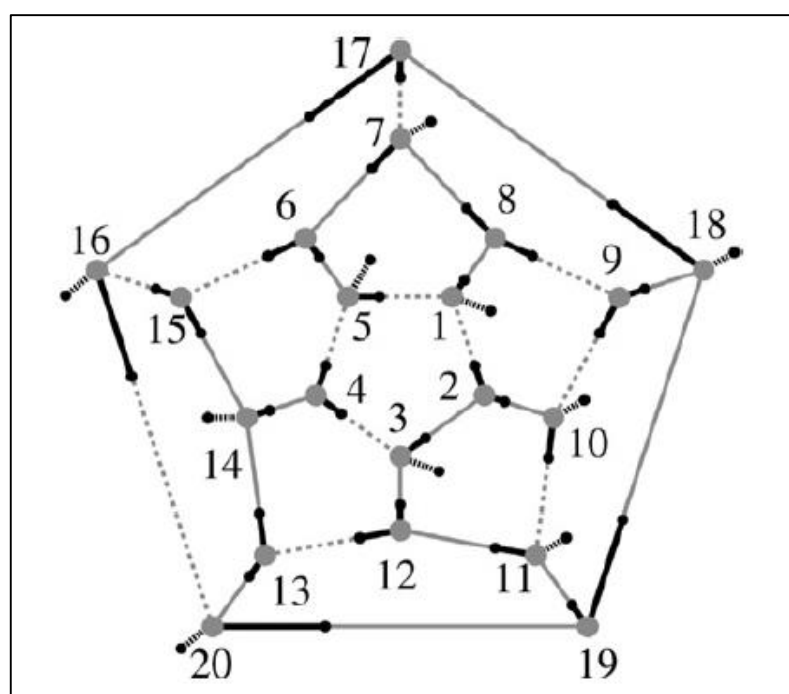


Figure 1-13: MDS Pentagonal dodecahedron cluster (H₂O)₂₀
(Kirov, Fanourgakis and Xantheas, 2008)

The Infra-red (IR) spectroscopic studies of Fujii and Misuze (2013) state that H₂O in the bulk phase arranges into a variety of structures, with the most prominently reportedly being tetrahedral arrangements where oxygen atom lone pairs of electrons form attachments with the weakly electropositive hydrogen atoms on neighboring H₂O molecules, however a significant variety of constituent molecule ranges and geometries have been experimentally identified (see Figure 1-14).

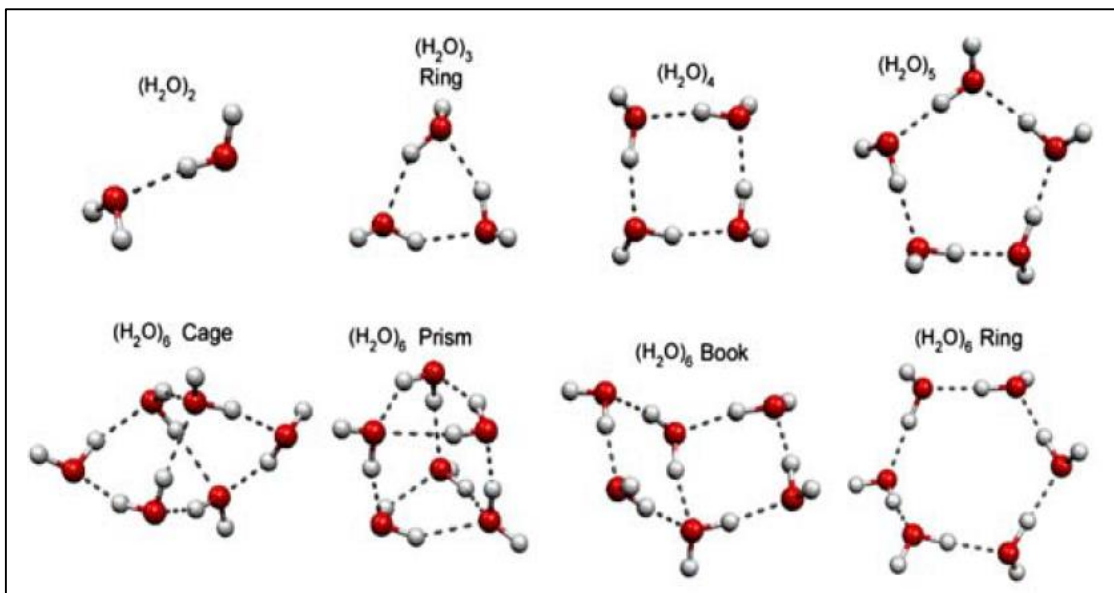


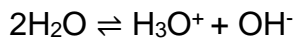
Figure 1-14: Various MDS H_2O cluster configurations (Fujii and Misuze, 2013)

Liu, Wang and Ho (2011) conducted computer simulations focusing on the calculated hydrogen bond energies of $(\text{H}_2\text{O})_{2-30}$ arranged in ring, multi ring and caged geometries exhibiting the lowest energy cluster arrangements, and then focused on the kinetic fragmentation profiles according to each arrangement (Table 1-6). The outcome of this work identified that the most kinetically favorable disassociation fragments in a step-by-step process were H_2O monomers ($\sim 11.53 \text{ kcal/mol}$)

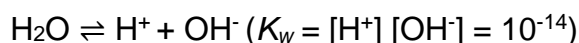
Table 1-6: MDS $(\text{H}_2\text{O})_n$ hydrogen bond kinetic fragmentation stability					
$(\text{H}_2\text{O})_n$	Geometry	1 st Fragment	kcal/mol	2 nd Fragment	kcal/mol
$(\text{H}_2\text{O})_2$	Dimer	Monomer	6.09	-	-
$(\text{H}_2\text{O})_3$	Ring planar	Monomer	11.71	-	-
$(\text{H}_2\text{O})_4$	Ring planar	Monomer	13.53	Dimer	19.15
$(\text{H}_2\text{O})_5$	Ring planar	Monomer	10.26	Dimer	17.70
$(\text{H}_2\text{O})_{6a}$	Book	Monomer	10.17	Dimer	14.33
$(\text{H}_2\text{O})_{6b}$	Trigonal prism	"	"	Trimer	16.16
$(\text{H}_2\text{O})_8$	Box	Monomer	16.37	Tetramer	15.74
$(\text{H}_2\text{O})_{10}$	Pentamer box	Monomer	12.86	Dimer	18.03
$(\text{H}_2\text{O})_{11}$	-	Monomer	9.98	Trimer	16.32
$(\text{H}_2\text{O})_{12}$	Tetramer prism	Monomer	15.51	Tetramer	18.32
$(\text{H}_2\text{O})_{15a}$	Pentamer prism	Monomer	13.35	Dimer	20.61
$(\text{H}_2\text{O})_{15b}$	Pentamer prism	"	"	Trimer	21.11

1.2.3. H₂O Ionization

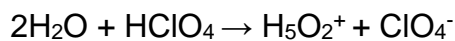
Kubik (2019) describes the autoionization of H₂O is typically represented by the following equation:



The ionization constant of water (K_w) is further extrapolated to represent pH calculations in classical chemistry as:



Dahms et al. (2016) informs that two characteristic hydronium structures have been the major focus of autoprotolysis research and proton transfer, the Eigen cation and the Zundel cation, both of which are implicated in the intermolecular transfer of an excess proton in the picosecond to femtosecond time range and have been experimentally identified in d by spectroscopic analysis of H₂O clusters (see Figures 1-15). This research group set out to analyse the characteristics of the Zundel cation (H₅O₂⁺) via femtosecond spectroscopy focusing in the 1500 to 4000 cm⁻¹ spectral range to ascertain distinctive correlating vibrational aspects. This was enabled by diluting 0.26 M perchloric acid (HClO₄) 0.88M H₂O and combining the solution in Trideuteroacetonitrile (CD₃CN) to produce and isolate the typically elusive H₅O₂⁺ species for extended time scales:



Initial analysis of the reaction identified superfluous H₂O species consisting mostly of monomers, and some residual H₃O⁺ in a ratio of less than 1:10 in comparison to H₅O₂⁺. The outcome of this work revealed that rapid proton transfer fluctuations in ambient temperature ranges, typically occurs in ≤100 femtosecond time scales, and the researchers further remarked that long-range structural fluctuations in bulk H₂O were transferred to the local hydrogen bond networks and were a necessary component in determining the molecular arrangements and motility of the H₃O⁺ species in bulk water. The researchers further identified that degrees of proton

transfer inhibition at one specific H₂O molecule (H₃O⁺ --- OH₂) could only be arise when the correlating oxygen atoms were separated by more than 2.60 Å.

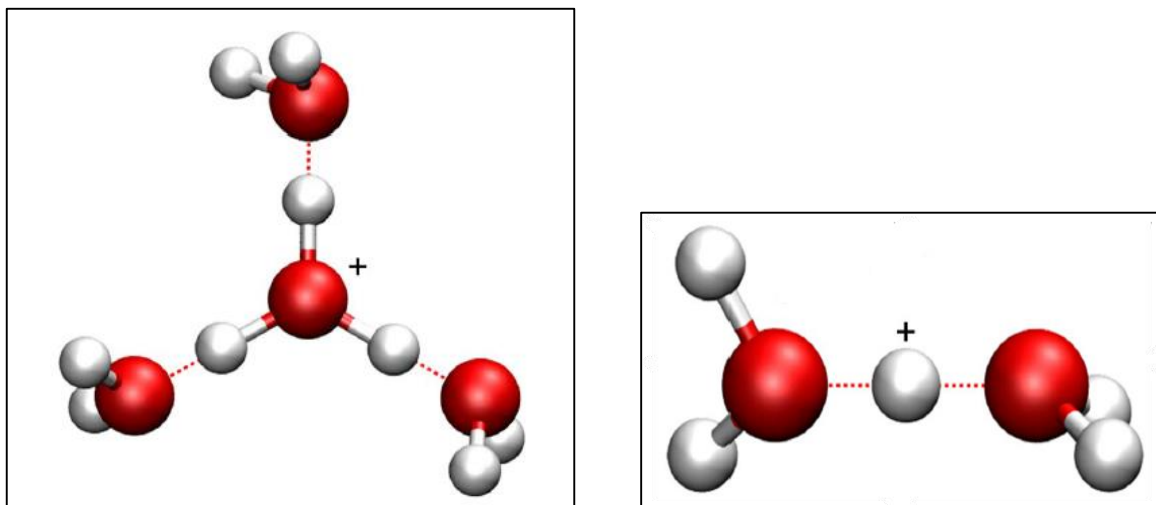


Figure 1-15: (left) Eigen cation (H₉O₄⁺), (right) Zundel cation (H₅O₂⁺) (Dahms et al., 2016)

Artemov et al. (2015) delved deeper into the ongoing debate of H₂O autoprotolysis from a primary hypothesis that the analytical ionization constant (*K_w*) reported in the research literature was determined by conductivity frequencies at or below 10⁷ Hz, questioning whether this was sensitive enough to determine the true dynamics and population of H₂O → H⁺ protons. The investigation incorporated 10¹¹ Hz analysis of pure H₂O over a variety of temperature ranges between 0 to 400 °C, and revealed that conductivity was not in fact temperature dependent, as is widely understood, and that H₂O electrodynamics arises from H₃O⁺ ⇌ OH⁻ proton exchange with non-protonated or hydroxide bound H₂O, rather than autoionization, and that the ionization constant (and pH) is represented by this H₃O⁺(H₂O) and OH⁻ (H₂O) “thermoactivation” (p.4, Artemov et al., 2015).

Later accompanying research conducted by Artemov, Volkov and Sysoev (2016) challenged the earlier and broadly accepted view that pure H₂O proton populations were exceedingly rare, claiming that they were identified by this novel 10¹¹ Hz analytical method as being present at levels “7 orders higher” (p.4, Artemov et al., 2016) than the typical representation (pH = 7) at a concentration of approximately 1% of the bulk H₂O. The group further declared that the classically accepted claims

of the Eigen research relating to the stable lifetime of a H₂O molecule at ~ 10 hours @ 25 °C, and an approximate 1 picosecond (ps) lifetime of molecular stability.

1.2.4. H₂O Isomers and nuclear spin states

Water exists as two isomeric forms relative to the spin properties of the constituent hydrogen protons which arising from the combination of rotational and nuclear spin states, *ortho* which has three symmetrical spin states ($I = 1$), and the antisymmetric *para* isomer where the spin states are in opposite directions and a total spin state of zero ($I = 0$), as described by Kilaj et al. (2018). The ratio of these isomeric spin states (OPR) differs dependent upon collisions, which are influenced by external factors such as chemical, temperature, electrical and magnetic contributions, however, in the singular H₂O molecule state, the laws of physics deem ortho-para conversion to be forbidden, as spin states are conserved even when external factors are applied.

Tikhonov and Volkov (2002) calculate the OPR ratio on earth to be 3:1 varying to 1:10 in interstellar clouds, and the investigation of the nature of ortho and para H₂O, and the phenomena surrounding its conversion process has revealed that these isomers exhibit relatively extended time periods of up to 26 minutes, and has been of significant interest to astrophysicists studying the formation of interstellar H₂O, surface H₂O research and spin chemistry, the hypothetical outcomes of which still attract contentious discussions. The research into ortho-para H₂O conversion realised a landmark moment when Tikhonov and Volkov (in 2002), configured experimental correlations with hydrogen gas, then set out to utilise chromatographic adsorption and separation of H₂O isomers in the vapor phase, based upon their respective rotational states. Their work utilised charcoal, alumina, silica gel and zeolite adsorbents and scrutinised the doublet for H₂O isomers at 36.60 cm⁻¹ (ortho) and 37.14 cm⁻¹ (para) identifying conspicuous time correlations (ortho 10:1/1-3 hours @ ~500µL, para 1:2/ > 4-5 hours @ ~100µL). This research remarked that the widely held view of that time was that ice spin modified conversion of ortho-para H₂O to the 3:1 ratio identified at ambient conditions was estimated to take several months to achieve, were startled by their calculated findings of the gas to liquid metastable lifetimes for ortho- H₂O was 55 ± 5 minutes, and para- H₂O was 26 ± 5 minutes,

concluding that this was 10^6 faster than that proposed for bulk liquid H₂O, and proposed this mechanism for the formation of H₂O, via H₂ and O₂ adsorption with interstellar dust.

Pershin and Bunkin (2009) focused upon the rotational transition states of ortho-para H₂O in the gas state, utilising four photon laser spectroscopy in the 10¹¹-10¹² Hz range with distilled H₂O and identified after multiple experiments that the ortho-para ratio of the condensed H₂O at ambient temperature had decreased from 3:1 by a factor of 2.0 to 2.5 (1.75:1-1.5:1), concluding that temperature increase and cavitation collapse of distilled H₂O revealed to them that “any action on water” (p.5, Pershin and Bunkin, 2009) could impact ortho-para H₂O ratios towards equilibrium.

Kilaj et al. (2018) contemplated the different properties ortho-para H₂O molecular isomers and nuclear spins and conducted research focusing how the respective isomer symmetrical properties impacted upon chemical reactivity and transition states. Drawing on the recent work of Chang et al. (2015), who in turn drew inspiration from the famous Stern-Gerlach experiments, these researchers set out to manipulate H₂O isomers utilising electrostatic fields utilising specific coordinates to selectively deflect para and ortho species, then direct the separated isomers at diazenylium (N₂H⁺) reactant ions trapped in a linear-quadrupole ion trap (LQT). The ortho and para H₂O and N₂H⁺ reactants were then ejected into a time of flight mass spectrometer (TOF-MS) to determine quantitative and mass aspects of the experiments (see Figure 1-16).

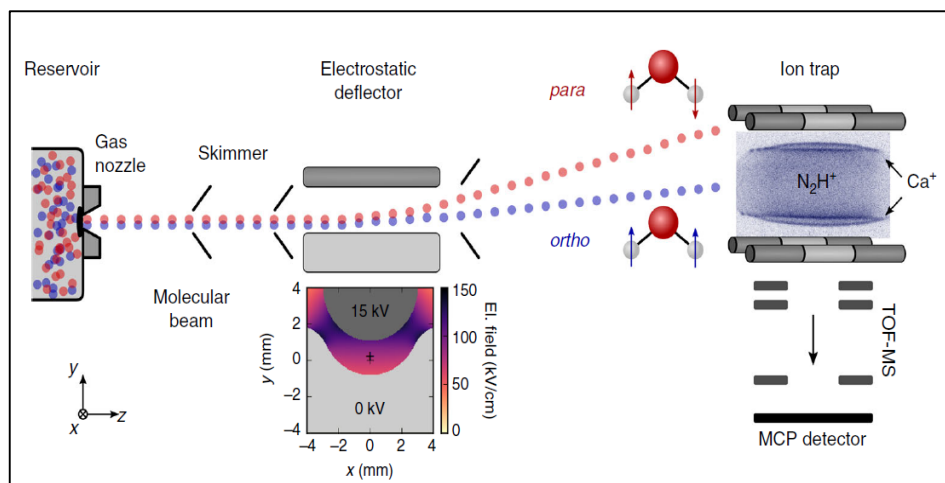


Figure 1-16: Magnetic field separation methodology of ortho and para H₂O (Chang et al. , 2015)

The investigation of the experimental data identified what they defined as a “*barrierless reaction*” (p.5, Kilaj et al., 2018), where no transition states were identified and that the reactions proceeded via the intermediate complexation of a singular hydrogen atom binding the N_2H^+ and H_2O moieties. Ab initio computations informed that the altered centrifugal interactions of N_2H^+ and H_2O were “*rotationally adiabatic*” (p.5, Kilaj et al., 2018), with the para nuclear-spin isomers acquiring a higher reactivity rate with N_2H^+ due to a smaller degree of rotational averages compared to the ortho-species. In conclusion, these researchers emphasized the involvement of nuclear-spins and rotational symmetries in aqueous chemical reactions, claiming this research as a first where “*rotationally state-selected polyatomic neutral molecules have been reacted with ions*” (p.6, Kilaj et al., 2018).

Experiments designed to encapsulate and isolate singular ortho- H_2O and para- H_2O isomers with ^{16}O and ^{17}O isotopic configurations inside “endohedral fullerenes” (C_{60}) and subjecting the samples to varying temperatures ranging between 5 and 40 kelvin, where conducted by Meier et al. (2018) at the University of Southampton, U.K. the work focused on identifying temperature dependent aspects of spin conversion outside of molecular collision factors with regard to the two isotopologies, and NMR ^1H analysis identified a minor quantity of ortho- H_2O persisting even after 40 hours @ 5 kelvin, contrary to previous studies, then they slowly raised temperatures measuring the bulk dielectric constants to detect thermal impacts on spin conversion processes (Figure 1-17).

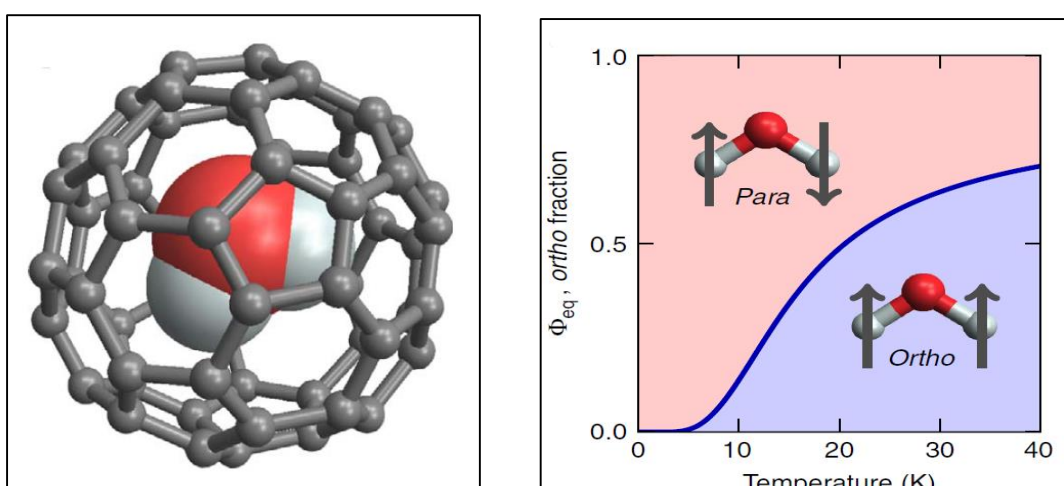


Figure 1-17: (left) Caged H_2O endohedral fullerene, (right) Temperature/ortho-para H_2O ratio (Meier et al., 2018)

The conclusions from NMR signal dynamics identified in this work that the $\text{H}_2^{16}\text{O}@\text{C}_{60}$ species temperature shift facilitated a slow shift in signal respective to $\text{H}_2^{17}\text{O}@\text{C}_{60}$, which was respectively identified by a uniquely weak signal. The calculated thermal time constant for each isotopic para to ortho isomer spin conversion at 30 ± 4 seconds for the H_2^{16}O species, and 16 ± 3 seconds for the H_2^{17}O species, with significant conversion occurring at approximately 15K, concluding that faster spin conversion of H_2^{17}O was associated with $^1\text{H}-^{17}\text{O}$ dipole-dipole interactions, and the lowest rotational energies calculated at $\leq 53\text{K}$ for para and $\leq 60\text{K}$ for the ortho species.

Analysis of ortho-para D_2O and $\text{D}_2\text{O}-\text{H}_2\text{O}$ properties (1:1) in the gas phase by Maity et al. (2021) employing cavity ring-down spectroscopy, a method which according to Picarro Inc. (n.d.), utilises an optical cavity correlating a laser light source which is first measured as decay time inside the empty cavity, and then again when a desired gas phase species is injecting in to the cavity, and high precision quantitative measurements can be drawn from the ring down absorbance correlations in the parts per million range, independent of light intensity fluctuations and power. The research group utilised a quantum cascade laser set to the $7.8 \mu\text{m}$ wavelength, which allowed them to focus on the “rovibrational” spectra (p.2, Maity et al., 2021) of isomeric D_2O (99.99% purity) and $\text{D}_2\text{O}-\text{H}_2\text{O}$ (Milli Q), after dropping the cavity pressure to ~ 0.02 Torr to vaporise $0.4\mu\text{L}$ of the respective reagents in the cavity, which was thermally stabilised at 45°C ($\pm 0.01^\circ\text{C}$) with an external heating jacket.

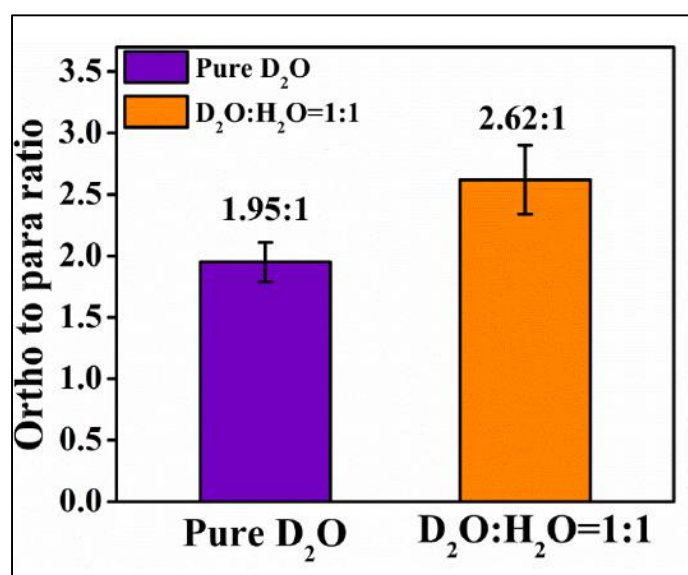


Figure 1-18: Spectroscopic ortho and para D_2O and $\text{D}_2\text{O}-\text{H}_2\text{O}$ ratios (Maity et al., 2021)

This research further experimentally established the ring down rotational transitions of *ortho* - D₂O at 135.9 ← 126.6 and *para* - D₂O 133.10 ← 132.11 at the v2 vibrational-rotational IR spectrum (@~ 7.8 μM), or the D₂O interference-free isomeric profiles. The respective ratios drawn from the quantitative analysis identified the OPR of D₂O spin isomer at 1.95 ± 0.16 at ambient temperature, which was in strong correlation to prior research of lesser comparative precision, and further reported a preliminary observation of potential thermodynamic interactions of *ortho* and *para* nuclear spin exchanges process between D₂O and H₂O spin states, noting a deviation of approximately 13% in comparison to established *ortho-para* H₂O measurements at ambient temperature (see Figure 1-18).

Keyword search: *Water hydrogen bond, water donor acceptor, water cluster geometry, water cluster binding energy, water cluster fragmentation, water ionization, Eigen cation, Zundel cation, water isomers, para ortho water, para ortho water spin states.*

1.3. H₂O and magnetic fields

Introduction

This section follows up on research related to H₂O and a variety of magnetic field research applications. No summary concludes this section, as the individuals summaries of the research literature are addressed individually by identifying the reported underlying mechanisms responsible for identified phenomena.

1.3.1. H₂O and static magnetic fields

Bormashenko (2019) describes the Moses Effect as a phenomenon where a nearby static magnetic field of requisite strength induces a “well” (p.4, Bormashenko, 2020) in a body of water due to diamagnetic repulsion (see Figure 1-19), and informing that the surface of diamagnetic H₂O exhibits repulsion due to weak electron field repulsion opposing the magnetic field which can be determined by the equation:

$$F_{\text{mag}} \approx \Delta_x V (\vec{B} \cdot \nabla) \vec{B} / \mu_0$$

Δ_x = variable change

V = H₂O volume

\vec{B} = Magnetic flux

μ_0 = vacuum magnetic constant ($4\pi \times 10^{-7}$ H/m)

∇ = divergence (field curve)

The literature reported that when $\vec{B} \geq 0.5$ T up to 10 T is applied at the surface of H₂O, the height (h) of repulsion is depressed $h \approx 10$ to $10^4 \mu\text{m}$ at the well centre, in proportion to the H₂O level prior to exposure, and that soap bubbles and floating diamagnetic materials on H₂O surfaces can be propelled due to interactions with \vec{B} forces ≈ 0.5 T and larger.

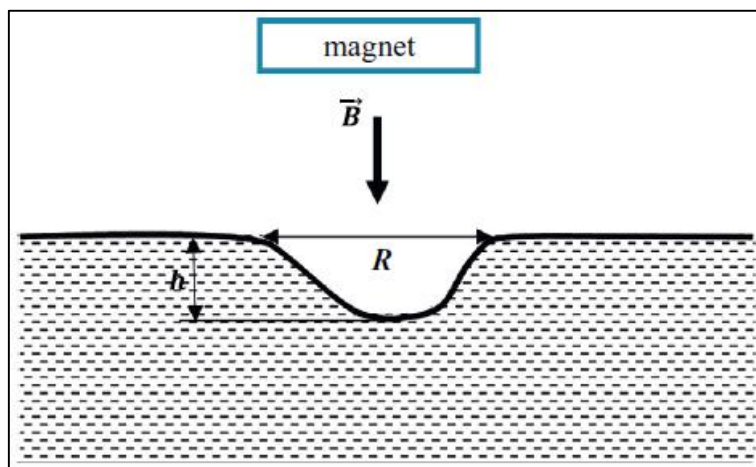


Figure 1-19: H₂O and magnetic field diamagnetic “Moses Effect” (Bormashenko, 2019)

Mechanism: Diamagnetic H₂O is repelled by static magnetic fields

The literature reported that when $\vec{B} \geq 0.5$ T up to 10 T is applied at the surface of H₂O, the height (h) of repulsion is depressed $h \approx 10$ to $10^4 \mu\text{m}$ at the well centre, in proportion to the H₂O level prior to exposure, and that soap bubbles and floating diamagnetic materials on H₂O surfaces can be propelled due to interactions with \vec{B} forces ≈ 0.5 T and larger magnetic fields.

Lee et al. (2013) focused on gaseous/H₂O interaction undergoing SMF treatments (24 hours/1T @ 50mL/min) under strict temperature protocols (25 ± 0.01°C), utilizing pre-treatment sonification (30 min) and noted that both dissolved oxygen (DO) comparatively decreased for the SMF exposure analytes at 24 hours (7.74 ± 0.06 - 7.43 ± 0.02 mg/L), based on a series of 30 minute in situ measurements, and was accompanied by a negligible rise in pH measurements (see Figure 1-20).

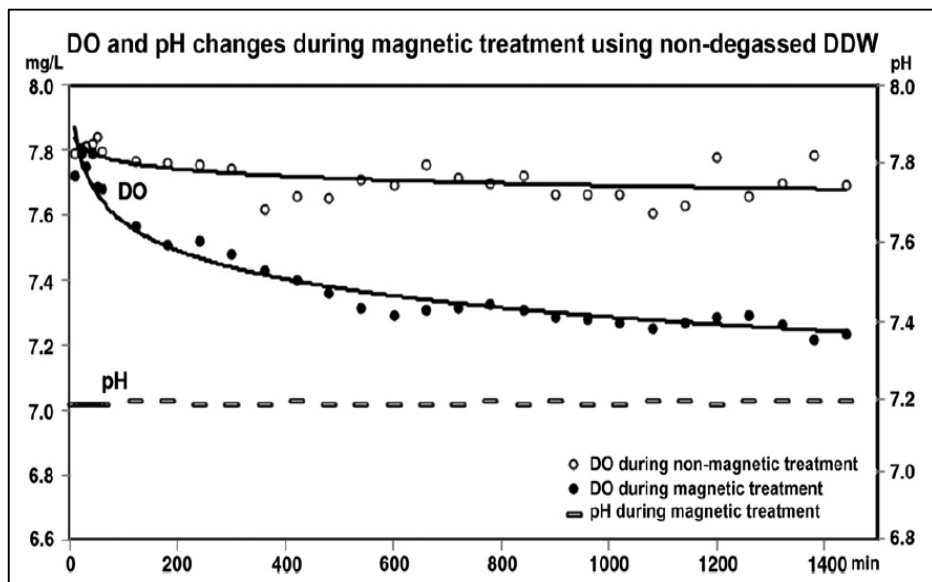


Figure 1-20: Dissolved oxygen (DO) and pH control with magnetic field exposure (Lee et al., 2013)

Mechanism: The reliability of static magnetic field H₂O analysis DO

The researchers concluded that the application of the 1T magnetic fields conclusively reduced conductivity levels in the exposed H₂O samples, and the correlations with the levels of dissolved oxygen present in the H₂O analytes impacted the way H₂O behaves in magnetic fields.

Presenting conflicting results to that outlined by the Lee research team, Shcherbakov et al. (2020), subjected deionized H₂O (18 MΩ @ 25°C) to a range of 0, 1, 2, 3, 5 and 7T static magnetic fields and detected no significant alteration in aqueous oxygen level and minimal fluctuation in pH, although changes in resistivity were identified at 1T and tending to stabilize at 3T (see Figure 1-21).

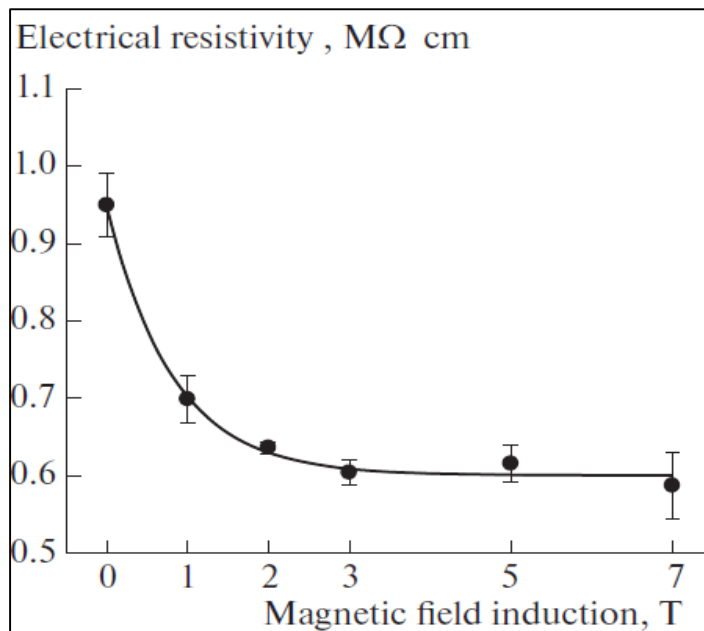


Figure 1-21: Electrical resistivity/conductivity of H₂O and MF (Shcherbakov et al., 2020)

Mechanism: Static magnetic field strength and CO₂ impact H₂O kinetics

Shcherbakov and his colleagues concluded that the shift in H₂O resistivity under the effect of the static fields was a result of an interaction with the population and mobility in the samples representation of charge carries, impacting the kinetics of H₂O in the presence of impurities, arising from absorbed atmospheric carbon dioxide.

1.3.2. H₂O and dynamic magnetic fields

Colic and Morse (1999) were pioneers in investigating claims of water and magnetic field exposures inducing a phenomena reported as “*magnetic memory*” (p.167, Colic and Morse, 1999) by conducting their own experimental investigations, consisting of EMF effects with surface tension, silica-H₂O dissolution, and gas solubility where they established that outgassing was occurring in MF treated H₂O analytes, then conducted pre-exposure degassing procedures prior to treatments and identified the absence of prior observations. Spectroscopic analysis supported their hypothesis that EMF treatment acting on absorbed gasses and the in situ atmospheric-H₂O interface promoted CO₂ and noble gas “*clathrate like structuring*” (p.171, Colic and Morse, 1999) facilitating a protracted effect which instigated changes in pH and the generation of reactive oxygen species (ROS).

Mechanism: The dynamic magnetic field impacts H₂O gas exchange kinetics

Colic and Morse forwarded a speculative hypothesis based upon their own research and careful scrutinization of the related literature, that the retention of dynamic magnetic field effects on H₂O analytes resulted from the induced shift in the kinetics of the atmospheric gas absorbance and H₂O molecular interface regarding, and the formation of clathrate like nanobubbles.

These revelations set in motion a series of further investigations, with Valee et al. (2005) undertaking a series of high precision experiments with highly purified water (18.2 MΩ *cm @ 25°C) which was degassed (20 min @ 1.6 x 10³ Pa) and then subjected to PEMF treatments (6 hours/10-500 Hz/ ≈1mT) under strict external magnetic and temperature mitigation protocols (< 0.01°C), then incorporated an analysis of “*dynamic light scattering*” (p.2295, Valee et al., 2005) to investigate the generation of gas nanobubbles. The results determined that there was a reduction of 27% of identified nanobubbles in the non-degassed H₂O subjected to 6 hours PEMF in comparison to the degassed sample under identical treatment, and an accompanying analysis on the same samples was conducted 12 days post treatment both analytes had reached equilibrium. Furthermore, there was a 22% reduction of degassed scattering spectra which was not subjected to 6 hours PEMF in

comparison to the MF treatment analytes. The group concluded with a hypothesis that MF Lorentz forces were inducing deformation of atmospherically absorbed gasses prior to treatment and/or at the atmospheric-H₂O interface during PEMF exposure, which destabilized gaseous bubbles at the ion- H₂O electric double layer as frequently expressed in aqueous colloidal research.

Mechanism: The Lorentz Force deforms the atmospheric-H₂O interface

The group concluded with a hypothesis that the PEMF induced Lorentz Force resulted in deformations of atmospherically absorbed gasses at the atmospheric-H₂O interface and destabilized the resident gas bubbles at the ion- H₂O electric double layer.

Further experiments focusing on dissolved oxygen - H₂O interactions to PEMF exposures (1-24 hours/0-0.08T/7Hz) under strict temperature protocols ($25 \pm 0.01^\circ\text{C}$) was carried out by Lee et al. (2013), combining pre-treatment sonification (30 min), which resulted in DO decrease for the PEMF exposure (x10) in comparison to correlating control replicates (7.43 ± 0.02 vs 7.74 ± 0.06 mg/L). H₂O conductivity was analyzed and it was demonstrated that non-degassed sampled subjected to PEMF exhibited increases compared with non-exposed controls (0.62 ± 0.017 vs 0.68 ± 0.036 $\mu\text{S}/\text{cm}$), , and surface tension was significantly lowered in the sonicated MF analytes when compared to the non-degassed samples (67.69 ± 0.301 dyn/cm vs 71.28 ± 0.318 dyn/cm) contributed to the theory that dissolved gasses had been a contributor to previously espoused MF- H₂O findings (see Figure 1-22).

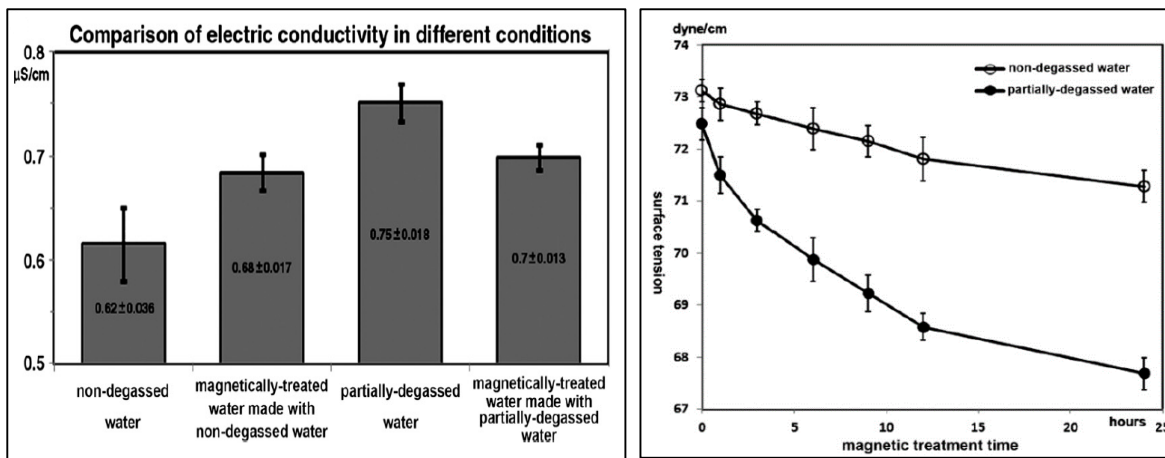


Figure 1-22: PEMF and SMF H_2O conductivity (left) and absorbed gasses (right)
(Lee et al., 2013)

Mechanism: Absorbed oxygen impacts H_2O dynamic magnetic field kinetics

The researchers identified that the application of the 0.6 – 0.8T oscillating magnetic field increased in the standard atmospheric gas samples conductivity, and reduced in the partially degassed samples conductivity levels, and decreased surface tension in the partially degassed analytes, compared with the solutes that had both undergone 24 hour PEMF exposure, concluding that the correlations with the levels of dissolved oxygen present in the H_2O analytes impacted the way H_2O behaves in magnetic fields.

The incorporation of a novel laser induced dynamic speckle spectroscopic analysis to investigate the cluster kinetics of H_2O under alternating magnetic field exposure (50mT/1-22 Hz/60 mins) was undertaken by Usanov et al. (2016), who let the MF exposed H_2O analytes settle for 60 minutes post treatment to eliminate “hydrodynamic perturbations” (p. 83, Usanov et al., 2016), then scrutinized exposure and control cluster populations, size, geometries, and velocities to determine respective cluster durations and spatial variations. The outcome of these findings was an increase of approximately 2.8:1 for magnetic field exposed H_2O (~56 to 20/1.7mL) and noted that clusters up to 200 μm in size were detected in the control analytes.

Mechanism: Dynamic magnetic fields increase smaller H₂O cluster populations

The variation in alternating electromagnetic wave amplitudes increased the number of visible H₂O cluster populations as determined by optical dynamic speckle spectroscopy, revealing that H₂O clusters have a spatially dynamic populations, structures, and lifetimes in the presence of dynamic magnetic fields.

Chirkova, Sharlaeva and Stas (2019) scrutinized the cohesive and adhesive aspects of deionized H₂O with EMF's ranging between 100 and 200 MHz (22°C), identifying that exposed H₂O samples exhibited increased temperatures of evaporation over the range (~6.5%), increased cohesion from 72.75 to 82.20 ± 1.50 mJ/m² @ 22 °C (130 MHz/60 mins) and decreased adhesion from 105.0 to 94.9 mJ/m².

Mechanism: Hydrogen bonding of H₂O PEMF is time and frequency dependent.

H₂O exposed to pulsed electromagnetic fields, exhibited increased surface tensions and rates of evaporation, as well as an increase in measured surface wetting angles, concluding that increased cohesion arised from the strengthening of both the supramolecular and intermolecular hydrogen bonding, and was dependent upon frequency and exposure time.

The effects of magnetic fields upon H₂O with regard to autocatalytic hydroxide (OH⁻) and hydronium (H₃O⁺) generation has been the focus of significant research, particularly with regard to pH variation and transfer kinetics, with D'Emilia et al. (2015) focusing on ion cyclotron resonance and the mass to charge ratio of H₃O⁺ (33.7Hz/42µT) oscillations in purified H₂O analytes (18.2 MΩ under N₂) with regard to first analyzing pH variation over 10 minutes (see Figure 1-23).

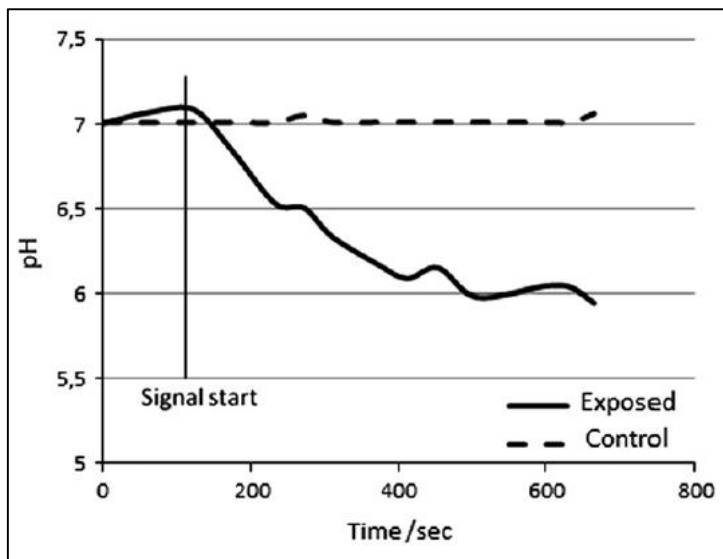
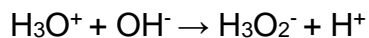


Figure 1-23: H_2O ion cyclotron resonance (H_3O^+) and pH response (D'Emilia et al., 2015)

The researchers reported that they utilized identical experimental conditions with a 35 Hz sinusoidal EMF field and detected no alteration in control H_2O pH measurements, and commented that the following reaction had taken place:



This progressed to a further series of experiments with another correlating MF for H_3O^+ (7.83Hz/9.7 μT) generated along a perpendicular axis (z-direction), combined with either a 50 Hz or a neodymium magnet of unspecified field strength, as “decoherence” (p.372, D'Emilia et al., 2015) fields inside a special MF shielded room containing no internal electronic controls, then exposed purified water samples (10 mins) again, and remotely detected sustained post exposure oscillations in the frequency spectrum at decreasing strength after the decoherence fields were removed, when no other magnetic field was detected inside the room. Identical experiments with a 35 Hz EMF did not detect any phenomena.

Mechanism: Resonance frequencies induce charged domains and oscillations

The scientists finalized their paper by stating that ICR fields tuned to H_3O^+ restructure exposed H_2O at ambient temperatures and emit lasting oscillations of domains after being subjected to decoherence fields. These domains were

conceptualized as populations of negatively charged spinning spheres consisting of populations of H₂O molecules with random arrangements of one of the two possible spin states, that are aligned in the presence of certain magnetic field frequencies and induce oscillation which is retained once the field is removed, then decays over time relative to the systems thermal kinetics.

D'Emilia et al. (2017) later headed up another H₃O⁺ ion cyclotron another research team, expanding the investigation to isotopic factors (H₂O, D₂O and H₂O:D₂O), which detected an extra resonance spike at lower frequency (2.04 Hz) identifying a unique structure with a mass 4.1 times greater than the hydronium ion, which was reasoned to be a protonated tetrahedral hydronium configuration. Similar effects were revealed in the pure D₂O analytes; however, it was noted that the absorption peak downshifted to 6.75 Hz, which correlates well with the hypothetical larger mass of the D₃O⁺ ion in comparison to H₃O⁺ (22:19 = 1.16, 7.84: 6.75 Hz = 1.16). The 50:50 H₂O and D₂O experiments produced perplexing results which they assigned structures (see Table 1-7), surmising that resonating H₃O⁺ ions transform H₂O in to "bound water" (p. 60, D'Emilia et al., 2017).

Table 1-7: H ₃ O ⁺ ICR frequencies and theorised isotopic D ₂ O-H ₂ O exchange						
ICR (Hz)	7.85	7.45	7.09	6.78	2.04	1.82
Ionic species	H ₃ O ⁺	DH ₂ O ⁺	D ₂ HO ⁺	D ₃ O ⁺	3H ₂ O - H ₃ O ⁺	3D ₂ O - D ₃ O ⁺

Mechanism: ICR frequencies generates tetrahedral H₂O- H₃O⁺ and 3D₂O - D₃O⁺

This research team had again confirmed their earlier ICR- H₃O⁺ experimental results and expanded upon that by identifying further phenomena in weaker 10 nT magnetic fields, which was again further confirmed as isotopically consistent in D₂O experiments. They further hypothesized that there was no feasible reason that their findings could not apply to interfacial H₂O mechanisms in biological macromolecules and ionic transport, including the elusive kinetics associated with proton hopping, conceiving that much of the still unresolved kinetics encountered chemical and biological processes could involve a subtle electromagnetically Lorentz Force induced transport of tetrameric H₃O⁺-H₂O clusters.

In the knowledge that H₂O is a bulk diamagnetic molecule due to its negative magnetic susceptibility (-9 x 10⁻⁶), Mexican scientists, Gutierrez-Mejia and Ruiz-Suarez (2012) undertook experiments examining how the magnetic responses of H₂O are affected by temperature and magnetic field frequency. The researchers subjected samples of pure H₂O (Milli-Q, 18.2 MΩ cm) at a range of frequencies between 1kHz up to 1MHz (2.5V), and stabilised temperatures of 37°C, 25°C and -1°C, utilising self-inductance spectroscopy, which according to Valenzuela (1993), is also known as Impedance spectroscopy or Electrochemical Impedance Spectroscopy (EIS) described as a “*non-destructive, rapid and precise method*” (p.193, Valenzuela, 1993) to analyse the magnetic polarization of materials, by measuring the time-constants of individual atomic domain spin rotations.

The research outcomes identified that as frequency increased past 400KHz the magnetic susceptibility of H₂O shifted and registered as paramagnetic (χ' positive) at approximately 500 KHz, taking on higher paramagnetic susceptibility as the frequency climbed to 1MHz (see Figure 1-24), and the accompanying temperature experiments revealed that the magnetic effect was temperature related with frequency correlating higher induced paramagnetism at 37°C, a moderate increase at 25°C and no measurable shift in the -1°C analytes, which contradicted previous research outcomes.

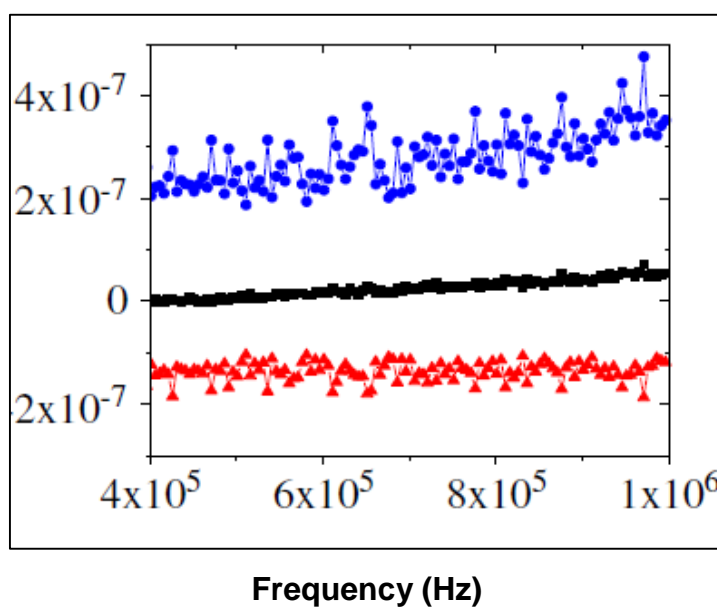


Figure 1-24: EMF frequency (500 kHz - 1 MHz) and H₂O paramagnetic response.
(Gutierrez-Mejia and Ruiz-Suarez, 2012)

Gutierrez-Mejia and Ruiz-Suarez hypothesised that paramagnetism arises due to oscillating magnetic fields inducing “*perturbations*” (p.1131, Gutierrez-Mejia and Ruiz-Suarez, 2012) in the typical formations of bonded supramolecular H₂O molecular electron clouds, which is not present in static magnetic field H₂O exposure, due to the respective field linearity balancing out respective spins in the H₂O volume, and further determined that the retention of diamagnetism in the ice like 1°C H₂O analytes was a result of the more rigid molecular structuring being able to resist the oscillating perturbations. A further series of experiments were conducted under 1MHz between a range of different voltages (0.1 - 2.5V) to measure amplitude induction on perturbation ($\Delta L/L$), which concluded that the voltage/amplitude correlation induced incrementally higher disruption in the bulk H₂O electron ground state, resulting in higher correlating paramagnetism (see Figure 1-25).

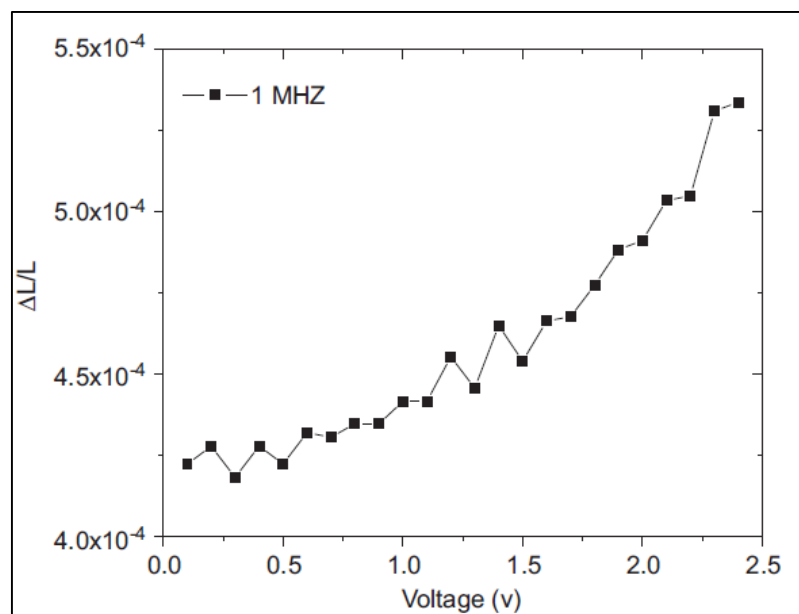


Figure 1-25: EMF voltage (1MHz/0.1 - 2.5V) and H₂O paramagnetic response (Gutierrez-Mejia and Ruiz-Suarez, 2012)

Mechanism: Dynamic magnetic fields impact H₂O hydrogen spin conservation

The scientists hypothesised that paramagnetism arises due to oscillating magnetic fields inducing perturbations in the typical formations of bonded supramolecular H₂O molecular electron clouds, which is not present in static magnetic field H₂O exposure, due to the respective field linearity balancing out respective spins in the

H_2O volume, and further determined that the retention of diamagnetism in the ice like 1°C H_2O analytes was a result of the more rigid molecular structuring being able to resist the oscillating perturbations.

Veselinovic and Velikic (2016) subjected new and used glass pH electrodes to both purified H_2O and a variety of buffer analytes (pH 4.0, 7.0 and 10.0) whilst employing a variety of electromagnetic fields (20-200MHz) exposures and analyzing electrode performance integrity factors. The pH electrodes were stabilized in the respective analytes for 2-3 minutes prior to EMF exposure to provide control readings, with all experiments were conducted under strict temperature protocols ($< 0.01^\circ\text{C}$), and the resulting evaluation of their data identified consistent EMF induced pH fluctuations at 95, 117, 122 and 135 MHz frequencies in all glass electrodes of varying combinations, age, and prior usage. Furthermore, this frequency response was identically observed in all buffer analytes, and the most significant pH fluctuation detected in distilled and double distilled H_2O exposed to the EMF field, highlighting that ionic makeup also played a role in the way EMF's affected ionic factors at the glass electrode interface. The researchers concluded that EMFs had a significant impact upon glass pH electrodes during experimentation, which may have merit as a possible explanation to poor replicability of experiments conducted under similar EMF real time analysis which incorporates glass pH electrodes (see Figure 1-26).

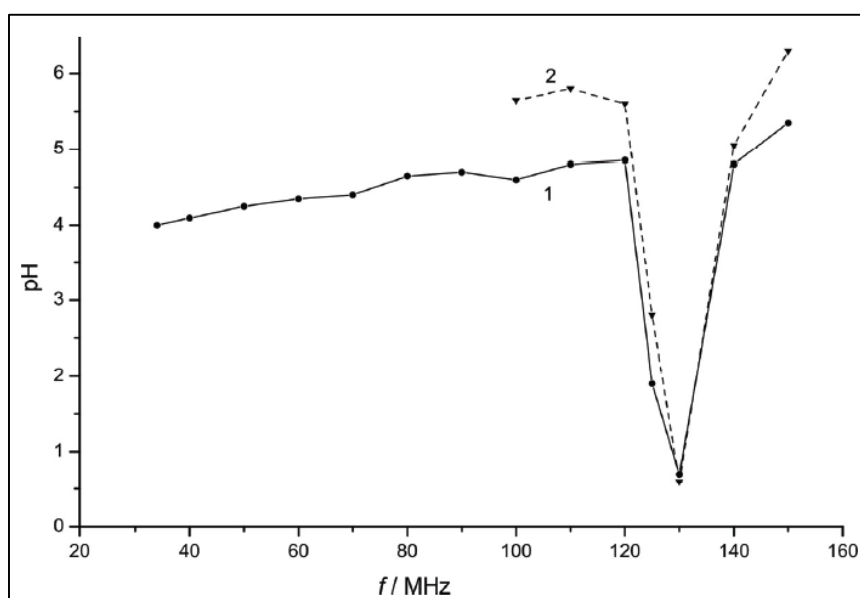


**Figure 1-26: 135MHz electromagnetic field and in situ pH electrode integrity
(Veselinovic and Velikic, 2016)**

Comment

Research incorporating in situ pH analysis in the presence of magnetic fields should be viewed with caution!

1.3.3. H₂O and magnetic field computer simulations

The incorporation of experimental and computational analysis with regard to static magnetic field effects (45–65 mT/21.85°C/180 mins) on H₂O by Toledo, Ramalho and Magriots (2008), focused on surface tension, viscosity and combined enthalpy of vaporization calculations, reporting respective experimental increases (3.23 ± 0.60 mN/m⁻¹, 32.23 ± 5.61 µPa/s and 18.00 ± 0.95 kJ mol⁻¹), whilst DFT computational data relating to a series of SMF's ranging between 0 and 34T correlated to (H₂O)₂₋₁₅ cluster geometries, identified intra-cluster H₂O binding energies (kcal/mol) that either increased or reduced various cluster cohesions, noting that stability in the hydrogen bond binding of molecular arrangements exhibited geometrical relationships. This team then put forth a hypothesis that magnetic fields weaken H bonds resulting in a rise in paramagnetic susceptibility, and a resulting breakdown of larger clusters to more stable smaller species.

Table 1-8: MDS (H₂O)_n hydrogen bond response to magnetic fields				
(H ₂ O) _n	Geometry	0.00T kcal/mol	0.688T kcal/mol	1.370T kcal/mol
(H ₂ O) ₂	Dimer	-2.8955	-2.8017	-2.6847
(H ₂ O) ₃	Planar ring	-6.1710	-6.1734	-6.1723
(H ₂ O) ₄	Planar ring	-7.9834	-7.9881	-7.9885
(H ₂ O) ₅	Planar ring	-8.2923	-8.3024	-8.3042
(H ₂ O) ₈	Box octamer	-10.4687	-10.4710	-10.4714
(H ₂ O) ₁₁	-	-10.3896	-10.3799	-10.3678
(H ₂ O) ₁₅	pentamer	-11.3319	-11.3079	-11.2817

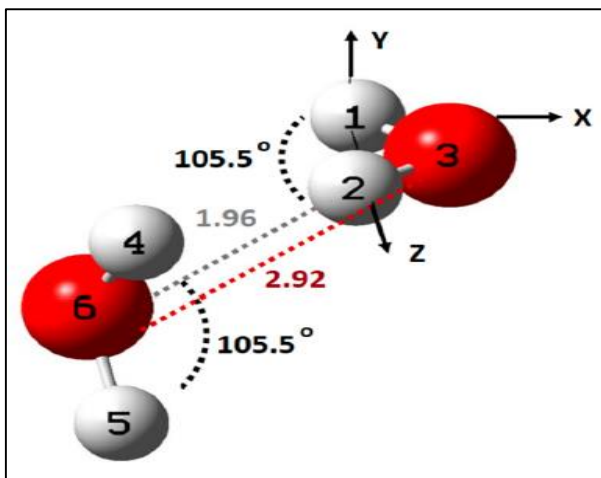


Figure 1-27: Simulation magnetic field gradient cartesian coordinates of the H1 atom
 (Toledo and Ramalho, 2021)

Mechanism: Static magnetic field strength impacts $(\text{H}_2\text{O})_n$ geometry

The intermolecular H_2O hydrogen bond geometry arrangements have specific correlations with external magnetic field applications.

Recent H_2O dimer and external magnetic field computer simulations were undertaken by, utilized a wide variety of static magnetic field strength inputs (0-100T) focusing on the x, y, z cartesian coordinates of the H_2O dimers relative to the magnetic field directed at a single gradient of the H1 atom (see Figure 1-27), then analyzing how the respective coordinate hydrogen bond energy and dipole moments were impacted.

The calculated H_2O dimer dipole moment and hydrogen bond energy at 0T was computationally calculated at 2.66 Debye and 3.44 kcal/mol respectively, and significant gradient fluctuation was identified with the dipole moment decreasing to 0.19 Debye when the magnetic field of approximately 75T was applied in the opposite direction of the H1-y axis and increased to ~4.50 Debye when a field strength of ~40T was applied in the direction of the x axis. The hydrogen bond energy also increased to ~4.80 kcal/mol at ~40T applied in the direction of the H1-x axis and decreased by a similar factor to 2.50 kcal/mol when the H1-x field gradient direction was reversed.

Mechanism: H₂O- H₂O bond strength is dictated relative to magnetic gradient

The research conclusion stated that H₂O monomer positions in H₂O dimer configurations are altered according to the magnetic field gradient, and the dimer intra-cluster hydrogen binding energy is either strengthened or weakened relative to the magnetic field gradient and respective atom position to that gradient.

Moosavi and Gholizadeh (2014) incorporating a 1.1T static magnetic field on a variety of solvents at 298.15K and noted that the H₂O molecular diffusion rates decreased in the order of 99.97% along the ζ gradient of the applied field scanned over the course of 1,000,000fs with the highest responses elicited by solvents incorporating hydrogen bonding, aligning with the field gradient with intra clustering bond energy becoming stronger and neighbouring hydrogen bonding molecules becoming interactive species collaborating in the decreasing of molecular diffusion.

A series of more contemporary DFT molecular dynamic simulations were carried out by Moosavi and Gholizadeh (2014) on H₂O (TIP3P) and various other solvents focusing on static magnetic fields (1.1T @ 298.15K) parallel to molecules in order to determine Lorentz effects (ζ -direction) and determined that the SMF influenced the charge distributions in the H₂O structure impacting the number of H bonds and overall supramolecular structure by aligning the molecules with the ζ -direction, creating smaller stronger hydrogen bonding and lowering H₂O diffusion

Mechanism: The DFT magnetic field lowers H₂O diffusion relative to gradient

The 1.1T static field influenced the charge distributions in the H₂O molecules, strengthening the hydrogen bonding and impacting the number of bonds and overall supramolecular structure by aligning the molecules with the z-direction. Molecular mobility and rate diffusion are significantly decreased as a result, and the molecular density increased.

Keyword search: *water magnetic field, Moses effect, water static magnetic field, water electromagnetic field, water pulsed electromagnetic field, water magnetic field computer simulation, water magnetic field gasses, water clusters magnetic field,*

water magnetic field evaporation, water magnetic field hydronium, water magnetic susceptibility, water magnetic field pH, water magnetic field diffusion.

1.4. Ions and molecules in aqueous solution.

Introduction

An examination of the phenomena reported in chapter 1.1., some of the fundamentals properties pertaining to water in chapter 1.2., and the response of water under the influences of magnetic field exposures have laid some of the groundwork in forming the conceptual reasoning of the research that is to follow. The thesis now moves on to an investigation of the scientific literature related to the phenomena of water interacting with ions and molecules, looking at solvation and how, how the clustering arrangements of H₂O with dissolved salts are configured according to respective charges and their diffusion according to concentration, H₂O residence time outlining the fluctuations of water molecules in the ion hydration cluster, and finally the mysterious phenomenon of proton transfer. This section will then conclude with a brief contribution related to nucleation theory.

After establishing an analysis of aqueous ion and molecule hydration in chapter 1.4., the thesis will then focus on aqueous ion and molecule research incorporating magnetic fields, which will again be accompanied by brief comments related to the respective mechanism conclusions corelated to the individual research.

1.4.1. Solvation

Solvents are arranged in categories according to complement properties that are of protic (easily donates H atoms), aprotic (unable or resistant to H donation), polar (dipole moment) and non-polar (no dipole moment), and these arrangements impact the solvation of ionic and molecular compounds, states Khapoor (2015), who further elaborates that the majority of chemical reactions take place in solvents, and solubility incorporates a critical aspect of physical chemistry that accompanies a classical dictum for polar and non-polar substances, “like dissolves like”, and the

polar molecule water (H_2O) is a major focus of dissolution chemistry (hydration), due to its ubiquitous nature regarding chemistry and life on earth, facilitated by the high dielectric constant (ϵ) of its polar nature. The dielectric constant measures a respective solvent molecules bond strength, which corresponds with its dipole moment, whilst the electronegativity properties correlate with the molecules atomic components determines and the scale of smaller to larger dipole moments and how well this solvent scale can overcome ionic bond energies to dissolve ionic solids or certain covalently bonded molecules and form charged hydrated species.

1.4.2. Ion hydration clusters

At given concentrations and temperatures, ionic hydration is customarily analysed by three main factors, the average number of H_2O molecules binding to a particular species $(\text{H}_2\text{O})_n$, referred to as shells or clusters, the diffusion coefficient (D) of ions in aqueous solutions and the mean residence times (MRT) of independent H_2O molecules as they exchange in ionic hydration shells.

Upon ionic hydration H_2O dipoles coordinate ions into shells or clusters relative to cationic $\text{M}^+(\text{H}_2\text{O})_n$ and anionic $\text{M}^-(\text{H}_2\text{O})_n$ charges, state Helm and Merbach (2019), elucidating further that positively charged cations induce close electronegative oxygen ($\text{O}^{\delta-}$) atoms, and negatively charged anions conversely drawing in electropositive hydrogen atoms ($\text{H}^{\delta+}$) to facilitate what is commonly known as the first hydration shell. This shift in H_2O molecular charges in the 1st shell can further impact bordering H_2O molecules and give rise secondary and tertiary H_2O shells dependent upon ionic charge, radius, hydrated configuration, and the aqueous concentration characteristics of the ions and dictates the solutes overall features. This ionic induced shift in H_2O molecular charge dissipates in energy creates a domino effect moving outward from the hydrated ion surface, until ultimately the water making up the bulk $\text{H}_2\text{O}-\text{H}_2\text{O}$ environment is unaffected from ionic charge interactions. These ionic hydration shells do not engage in typical ionic or covalent bonding where charges are shared with H_2O molecules in the classical sense, but they do distort the pre-existing $\text{H}_2\text{O}-\text{H}_2\text{O}$ network.

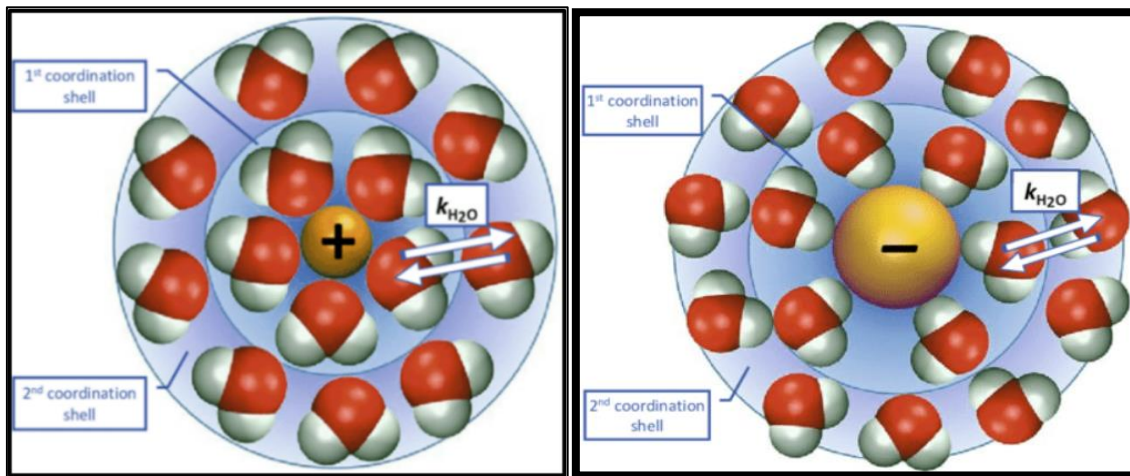


Figure 1-28: (left) Cation and (right) anion hydration shell H_2O arrangements
 (Helm and Merbach, 2019)

1.4.3. Hydrated ionic diffusion

Another important aspect of ion hydration is their rate of diffusion and how the ionic salts transfer their neutral charge across H_2O upon dissolution that facilitates gradient shift in respective ionic electric potentials, that in turn drives the movement of ions due to differing hydrated ionic radii, instigating diffusion coefficients where cation and anion simple salt pairs separates, as outlined by Dane, Topp and Campbell (2002), further declaring that ionic H_2O diffusion is impacted by solute concentrations (see Tables 1-9 and 1-10).

The diffusion coefficient of electrolytes, can be given as:

$$D_0 = \frac{D_1 D_2 (z_1^2 C_1 + z_2^2 C_2)}{D_1 z_1^2 C_1 + D_2 z_2^2 C_2}$$

D_1 and D_2 = diffusion coefficients for individual ions

C_1 and C_2 = respective ionic concentrations

z_1 and z_2 = respective ionic valences

Table 1-9: Ionic diffusion coefficients at infinite dilution (D_0) / 25.0°C			
Cations	D_0 (10 ⁻⁹ m ² s ⁻¹)	Anions	D_0 (10 ⁻⁹ m ² s ⁻¹)
H ⁺	9.311	OH ⁻	5.273
Li ⁺	1.029	F ⁻	1.475
Na ⁺	1.334	Cl ⁻	2.032
K ⁺	1.957	Br ⁻	2.080
Rb ⁺	2.072	I ⁻	2.045
Mg ²⁺	0.706	BrO ₃ ⁻	1.145
Ca ²⁺	0.792	SO ₃ ²⁻	1.064
Ba ²⁺	0.847	CO ₃ ²⁻	0.923

Table 1-10: H ₂ O and 0.001M-1.0M salt diffusion coefficients (D_0) / 25.0°C				
	(0.001M)	(0.01M)	(0.1M)	(1.0M)
Solute	10 ⁻⁹ m ² s ⁻¹			
LiCl	1.345	1.312	1.269	1.302
NaCl	1.585	1.545	1.483	1.484
KCl	1.964	1.917	1.844	1.892
CsCl	2.103	1.958	1.871	1.902
CaCl ₂	1.263	1.188	1.110	1.203

Dane, Topp and Campbell (2002) also outline that temperature and pressure significantly impact diffusion coefficients as the following example explains:

$$\text{KCl (D)} = 1.994 \times 10^{-9} \text{ m}^2 \text{ s}^{-1} @ 25.0^\circ\text{C}/1\text{atm} (298.15\text{K}) \rightarrow 35^\circ\text{C}/1\text{atm} = 308.15 \text{ K}$$

D(T) = diffusion coefficient @ 308.15 K

T₀ = reference temperature 298.15K

$\mu(T)$ = dynamic viscosity H₂O @ 308.15 K = 0.719 mpa s

$\mu(T_0)$ = dynamic viscosity H₂O @ 298.15K = 0.890 mpa s

D(T₀) = 1.994 × 10⁻⁹ m² s⁻¹ @ 25.0°C (298.15K)

$$0.1\text{M KCl} @ 35^\circ\text{C}/1\text{atm} = \frac{(298.15)(0.890)}{(298.15)(0.719)} \times 1.994 \times 10^{-9} \text{ m}^2 \text{ s}^{-1}$$

$$= 265.35/214.37 = \sim 1.238 \times 1.994 \times 10^{-9} \text{ m}^2 \text{ s}^{-1}$$

$$0.1\text{M KCl} @ 35^\circ\text{C}/1\text{atm} = 2.468 \times 10^{-9} \text{ m}^2 \text{ s}^{-1}$$

$$0.1\text{M KCl @ } 25.0^\circ\text{C}/1\text{atm} = 1.994 \times 10^{-9} \text{ m}^2 \text{ s}^{-1}$$

$$0.1\text{M KCl @ } 35.0^\circ\text{C}/1\text{atm} = 2.468 \times 10^{-9} \text{ m}^2 \text{ s}^{-1}$$

A rise of 10.0°C in temperature has increased the diffusion coefficient by 23.77%

A reference selection of diffusion coefficients and hydrodynamic radii that are of interest in this research are tabled below (Esteso et al., 2021)

Table 1-11: Piyadasa and McNaughton research anion diffusion and hydrodynamic radii		
Anion (H_2O)	$D (10^{-9} m^2 s^{-1})$	Hydrated radius ($10^{-9} m$)
NO_3^-	1.900	0.127
CO_3^{2-}	0.922	0.265
Anion (H_2O)	$D (10^{-9} m^2 s^{-1})$	Hydrated radius ($10^{-9} m$)
I^-	2.045	0.118
$S_2O_3^{2-}$	1.162	0.208

Another method examining the kinetics of aqueous ions was first postulated by Grinnell Jones and Malcolm Dole (1929), who were investigating a range of barium chloride water solutions (0.0005 and 1.000 g/molal @ 25.0°C), with regards to effects on resulting viscosities, and this work culminated in the “*Jones-Dole viscosity B-coefficient*” equation, relating to specific ion solvation characteristics at moderate concentrations (≤ 0.1 M) as follows:

$$\eta/\eta_0 = 1 + Ac/2 + Bc$$

η = viscosity of an aqueous salt solution @ fixed temperature & pressure

η_0 = viscosity of H_2O at correlating η temperature & pressure

A = ionic charge interactions on H_2O solute viscosity (Debye-Hückel theory)

B = strength of ion–water interactions standardised to H_2O

c = concentration of strong electrolyte solute

The implications of these equations determined that a positive viscosity B coefficient is derived from stronger H₂O hydration binding energies relative to H₂O – H₂O binding associations, with negative coefficients identifying weaker hydration relative to H₂O – H₂O binding energies (see Figure 1-29).

Cations	B	Anions	B
Mg ²⁺	0.385	PO ₄ ³⁻	0.590
Ca ²⁺	0.285	CH ₃ CO ₂ ⁻	0.250
Ba ²⁺	0.22	SO ₄ ²⁻	0.208
Li ⁺	0.150	F ⁻	0.10
Na ⁺	0.086	HCO ₃ ⁻	0.052
K ⁺	-0.007	Cl ⁻	-0.007
NH ₄ ⁺	-0.007	Br ⁻	-0.032
Rb ⁺	-0.030	NO ₃ ⁻	-0.046
Cs ⁺	-0.045	ClO ₄ ⁻	-0.061
		I ⁻	-0.068
		SCN ⁻	-0.103

Figure 1-29: Hofmeister series and Jones-Dole B coefficient correlations (Collins, 2019)

1.4.4. H₂O residence time in ionic hydration shells

Marcus (2015) reports that two analytical methods are employed in measurements of ion- H₂O hydration dynamics, dielectric relaxation spectroscopy, and Nuclear Magnetic Resonance (NMR) which have divulged good information pertaining to H₂O mean residence times in the 1st ion hydration shell (see Table 1-12).

Table 1-12: Ion-H ₂ O 1 st hydration shell mean residence times (MRT) 25.0°C					
H ₂ O/M ⁺	MRT (sec.)	H ₂ O/M ²⁺	MRT (sec.)	H ₂ O/M ⁻	MRT (sec.)
Li ⁺	54.0 x 10 ⁻¹²	Mg ²⁺	92.0 x 10 ⁻⁵	F ⁻	24.0 x 10 ⁻¹²
Na ⁺	22.0 x 10 ⁻¹²	Ca ²⁺	49.1 x 10 ⁻¹²	Cl ⁻	17.0 x 10 ⁻¹²
K ⁺	14.0 x 10 ⁻¹²	Sr ²⁺	43.1 x 10 ⁻¹²	Br ⁻	13.0 x 10 ⁻¹²
Rb ⁺	12.0 x 10 ⁻¹²	Ba ²⁺	14.6 x 10 ⁻¹²	I ⁻	14.0 x 10 ⁻¹²
Cs ⁺	14.0 x 10 ⁻¹²				
H ₂ O	5.6 x 10 ⁻¹²				

Computer simulations analysing hydration energy and entropy focusing on H₂O and ion hydration was undertaken by Saha and Mukherjee in 2016 which focused on the translational and rotational entropy's ($T\Delta S$) of H₂O in the 1st and 2nd hydration shells related to various cation and anion species, including sodium and calcium cations. It was identified that the Ca²⁺ (H₂O)_n thermodynamic kinetics exhibit ~16% less translational entropy in the 1st hydration shell whilst maintaining comparable 1st shell rotational entropy with Na⁺ (H₂O)_n kinetics. Likewise, the 2nd shell translational entropy is basically identical relative to (H₂O)_n configurations, but approximately 35% more H₂O molecules are to some extent fixed in the rotational state of the Ca²⁺ cation over this 50ns scan. This analysis also conducted calculations of various hydrated anions and noted that the H₂O entropy exhibited in divalent anions was similar to that identified in monovalent cation entropy kinetics.

The research concluded that modulation of thermodynamics arising from respective ion-(H₂O)_n species impacts molecular interactions in their vicinity, the 1st hydration shells of ion-(H₂O)_n ~70-80%, and the 2nd hydration shells of ion-(H₂O)_n ~20-25% of the energy to mitigate entropy (Table 1-13).

Table 1-13: Ion hydration shell H ₂ O entropy (TIP4P 298K/101.325kPa)						
	1 st shell			2 nd shell		
M ⁺	(H ₂ O)n	TΔS Trans %	TΔS Rot %	(H ₂ O)n	TΔS Trans %	TΔS Rot %
Na ⁺	6	40.3	39.2	16	10.6	7.0
Ca ²⁺	6	33.8	33.3	14	10.6	9.9
Cs ⁺	9	41.2	40.8	21	3.5	14.1
M-						
Cl ⁻	6	11.4	61.4	24	8.4	18.8
I ⁻	7	14.0	57.3	26	12.3	16.4
SO ₄ ²⁻	12	33.8	46.2	55	4.8	15.2

1.4.5. Proton transfer

Tachikawa (2017) utilized ab initio molecular dynamics (AIMD) computations to calculate the ionization of HCl and the (H₂O)₁₋₅ cluster geometry criteria correlated to

the rate of proton transfer and identified that “*proton transfer was strongly dependent on cluster size ($n=1-5$)*” (p.5242, Tachikawa, 2017). The kinetic data determined the following:

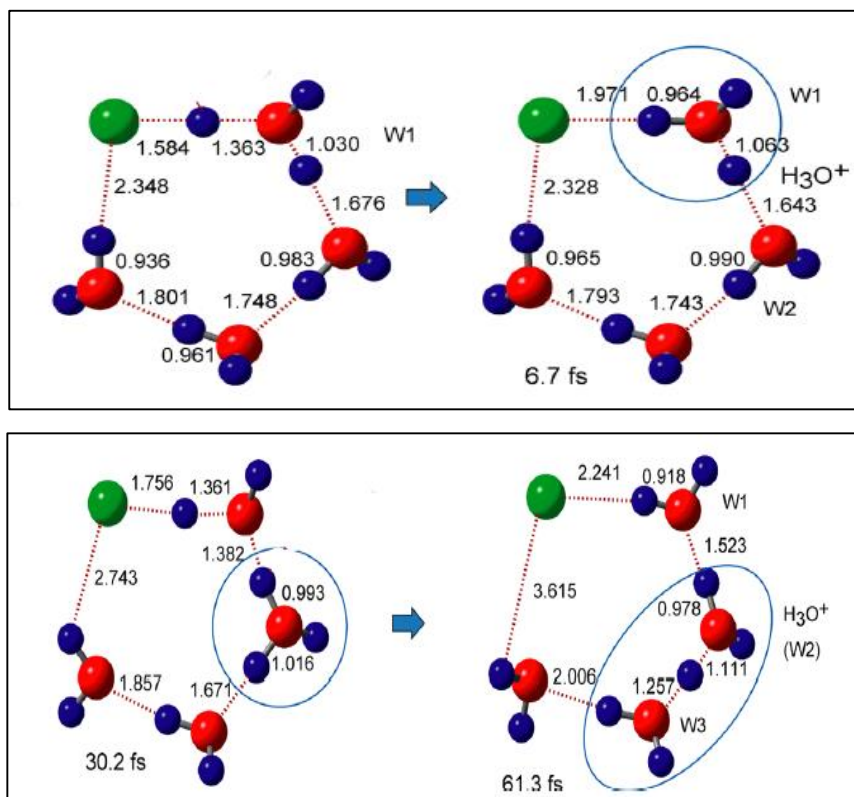


Figure 1-30: MSD of HCl-H₂O proton transfer (Tachikawa, 2017)

- 1) The 1st ionization-transfer occurred in ~7fs, the Cl(H₃O⁺) radical intermediate was established at 9.4fs, and at 14.3fs the H₂O acceptor was protonated (H₃O⁺).
- 2) The H₃O⁺-H₂O requires the approach of another H₂O molecule to initiate the 1st phase transfer, and the interplay of a 3rd further H₂O molecule to stabilize the resulting Zundel cation at 30fs.
- 3) The 2nd phase transfer occurs as the proton shifts between the 1st phase acceptor H₂O molecule and the 3rd stabilizing H₂O molecule, with the initial ionizing H₂O molecule and a 4th H₂O molecule stabilizing the protonated complex at 61.3fs and lowering the energy barrier to facilitate further proton transfer.

These simulation models were taken a further step by Dong and Bi (2019), who identified that computational proto transfer models were flawed, and the defect in the

modelling was that proton transfer of singular “*proton hopping*” (p5536, Fischer and Gunlycke, 2019) events did not filter out proton translocations whereby the hydrated proton initially transferred to neighbouring H₂O molecules, and then returned back to the originating Zundel cation H₂O position due to overall energetically preferable conditions in a process they titled as “*proton rattling*” (p5537, Fischer and Gunlycke, 2019). The computations extrapolated by these researchers declared that the numbers of reversible protons rattles occurred on approximately 55% of occasions when tetramer chain neighboring H₂O molecules interacted with the Zundel cation, and that proton rattling increased to approximately 70% when bordering trimer chains of H₂O initiated proton transfer, due to a lowered energy capacity to stabilize proton hydration and transfer.

Dong and Bi (2019) disputed the validity of Grotthuss mechanism type proton transfer, conducting density functional theory–quantum chemical cluster model (DFT-CM) computer simulations, first investigating cis and trans Zundel cation, (H₂O)₃ - H⁺ - (H₂O)₃ and (H₂O)₄ - H⁺ - (H₂O)₄ clusters with a view to identifying how the rotation aspects of these geometries transferred from the energetically optimal configurations to the transition states that were optimal for proton transfer, determining that the rotating migration of the H₃O⁺ cation was a better representation of the 3 dimensional aspects of the mechanism, whereby:

- 1) A cavity is required in bulk H₂O to facilitate a rotation reaction channel.
- 2) The kinetic transfer event requires an accompanying translocation and rotation of H₂O molecules in the cavity, as well as the correlated breaking of hydrogen bonds.
- 3) This interplay allows for the diffusion of the hydronium ion through the bulk water complex.

This ensemble of events combines to facilitate overall proton transfer kinetics. Perez deTudela and Marx (2020) recently undertook extensive computational simulation investigations of the temperature dependency of HCl and H₂O ionization, which had been an issue of some contention for researchers and identified that 6 H₂O molecules were required at room temperatures (300K) to facilitate HCl

disassociation, and that the mechanism followed a classical $(\text{H}_2\text{O})_6$ internal charge pathway. After ionization the lone Cl^- anion weakly complexes with H_2O electropositive hydrogen atoms to form an ion hydration cluster arrangement, whilst the H_2O bound hydronium undergoes proton transfer, and has been a core focus of all chemistry disciplines.

Specific protonated hydration arrangements impact upon chemical reaction rates relative to their cluster arrangements, as calculated by the computer simulations conducted by Diaz-Tinoco et al. (2013). These H_2O bound H^+ configurations identify how respective geometries can impact upon reaction kinetics, with proton hydration binding energies increasing at varying differentials respective to size, and exhibiting favorable stabilities, such as that identified for the Eigen cation (bold, Table 1-14).

Table 1-14: MSD $\text{H}_3\text{O}^+(\text{H}_2\text{O})_n$ cluster size and geometry bonding energies			
$\text{H}^+(\text{H}_2\text{O})_n$	Lower kJ/mol ⁻¹	Upper kJ/mol ⁻¹	\pm kJ/mol ⁻¹
H_3O^+	652.94	652.94	0.00
$\text{H}_3\text{O}^+(\text{H}_2\text{O})$	859.70	921.65	61.95
$\text{H}_3\text{O}^+(\text{H}_2\text{O})_2$	1029.63	1075.25	45.62
$\text{H}_3\text{O}^+(\text{H}_2\text{O})_3$	1148.50	1153.52	4.08
$\text{H}_3\text{O}^+(\text{H}_2\text{O})_4$	1189.52	1257.74	68.22
$\text{H}_3\text{O}^+(\text{H}_2\text{O})_5$	1213.38	1333.50	120.12
$\text{H}_3\text{O}^+(\text{H}_2\text{O})_6$	1172.36	1247.28	74.92

Experiments with proton diffusion of HCl under nanoconfined conditions were undertaken by van der Loop et al. (2017) which noted that proton diffusion rates decreased significantly in comparison with bulk water when subjected to a dynamic magnetic field, the researchers concluding that it required the collaboration of 15 H_2O in bulk water conditions to facilitate proton transfer, noting a correlation between decreased H_2O reorientation rate and proton transfer arising from the restriction of water molecules in confined arrangements impacting H^+ proton diffusion due to the limitation of typically kinetically more favorable available $\text{H}_2\text{O}-\text{H}_2\text{O}$ bond arrangements.

1.4.6. H₂O and ionic nucleation

Interactions between ions in aqueous solutions typically result in redox reactions, complexations with molecules, or other ionic species, the latter of which results in the formation of salts via crystallisation, which according to Myerson, Erdemir and Lee (2019), is a very convoluted process that is still not fully understood. Classical nucleation theory informs that when a solution of dissolved ions in a state of chemical equilibrium shifts thermodynamically to non-equilibrium conditions, a metastable state can arise where a solution can shift to overcome hydration and reach a point of supersaturation, thereby inducing higher collision rates whereby cationic and anionic species can overcome their respective hydration states and aggregate. If the metastable state is further driven toward supersaturation, cationic and anionic crystal nuclei can arise as phase transition points of origin for further salt crystallisation and precipitation.

Primary nucleation is classically explained by two theoretical process referred to as "*homogenous nucleation*" (p.77, Myerson, Erdemir and Lee, 2019) who define this as a system where a concentration of pure salt ions in H₂O oscillates until the solute system concentration and thermodynamics reaches a uniform state that triggers nucleation. The other major concept of classical crystallisation is "*heterogenous nucleation*" (p.95-96, Myerson, Erdemir and Lee, 2019), whereby external factors contribute to the germinal phase of nucleation, such as surfaces, mechanical agitation, magnetic and electric fields and crystal seeding where an existing salt crystal is introduced to the metastable state. These factors influence the outcome of the resulting salt particle sizes, structures (morphology), which can also incorporate foreign non-ionic or counterionic species which impact salt purity of the final crystal lattice. Non-ionic or counterionic factors can also impact homogenous nucleation as it moves to the initial growth accumulation stage, in a process known as "*secondary nucleation*" (p.96-98, Myerson, Erdemir and Lee, 2019).

Overall classical nucleation theory (CNT) characterises the homogenous process in values referred to as "*Gibbs free energy (ΔG)*" (p.77-78, Myerson, Erdemir and Lee,

2019) which coincides with the onset of supersaturation, and the initiation of the critical nuclei particle size, as follows:

$$\Delta G = \frac{RT}{2} \ln SR$$

R = Universal gas constant

T = Temperature (Kelvin)

SR = Supersaturation ratio

The theoretical description of crystallisation in a non-pure, heterogenous state describes that the external interplay with foreign factors induce the lowering of the nucleation activation barrier in the pre-nucleation surface states, by lowering the crystallisation metastable region, and many scientific and industrial practices are incorporated to induce this process.

Table 1-15: Chemical engineering induced crystallisation methods

Heterogenous factor	Nucleation	Impact
Heating solution	Primary	Reduce solvent area
“ “	Secondary	Increase salt surface area
Cooling solution	Primary	Heat dissipation
Mixing	Primary	Dissipate supersaturation
Mixing	Secondary	Increase nucleation surface area
Impeller collisions	Secondary	Determine crystal size

The many shortcomings identified in classical crystallisation experimental outcomes and modelling led Gebauer, Volkel and Colfen (2008) to undertake research which closely scrutinised the manner in which calcium carbonate (CaCO_3) supersaturation, nucleation, crystal growth and morphology arose from H_2O solutions via the slow addition of aqueous calcium chloride (CaCl_2) solutions to carbonate pH stabilised solutions, whilst measuring Ca^{2+} ions with a specialised ion electrode, and identified that the concentration of Ca^{2+} ions reduced prior to CaCO_3 nucleation as “*prenucleation clusters*” (p.1819, Gebauer, Volkel and Colfen, 2008) where approximately 35% of available Ca^{2+} ions had reduced in solution and “*bound*” (p.1820, Gebauer, Volkel and Colfen, 2008) at pH 9.00, whilst 75% of Ca^{2+} ions in solution exhibited a similar intermediary phase at pH 10.00, prior to further rise in pH,

the evolution of CaCO_3 nuclei and classical crystal precipitation, with the researchers ascertaining that pre nucleation clusters arose via autonomous pH equilibrium states (see Figure 1-31).

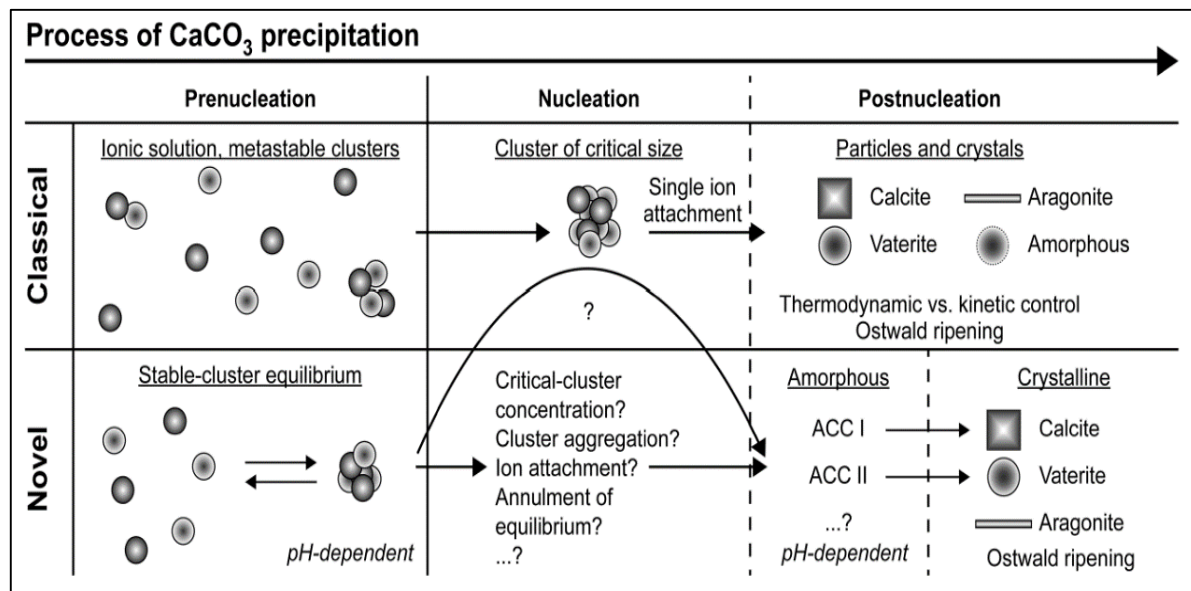


Figure 1-31: Classical and non-classical CaCO_3 nucleation mechanisms
(Gebauer, Volkel and Colfen, 2008)

Keyword search: *ion hydration, ion water hydration, ion water solvation, ion water diffusion, ion water clusters, hydrodynamic radii, Hofmeister series, ion water cluster residence time, water proton transfer, ion magnetic susceptibility, Grotthuss mechanism, ionic nucleation.*

1.5. Hydrated ions and magnetic fields

Introduction

The orientation of the magnetic north and south pole, and magnetic field strength experimental design arrangements are prevalent throughout the scientific literature in a plethora of domestic, agricultural, industrial and research applications, as reported by Al Helal et al. (2017), further noting that the generated flux density generated by the permanent magnet composition was crucial for suitability in these applications (Figure 1-32).

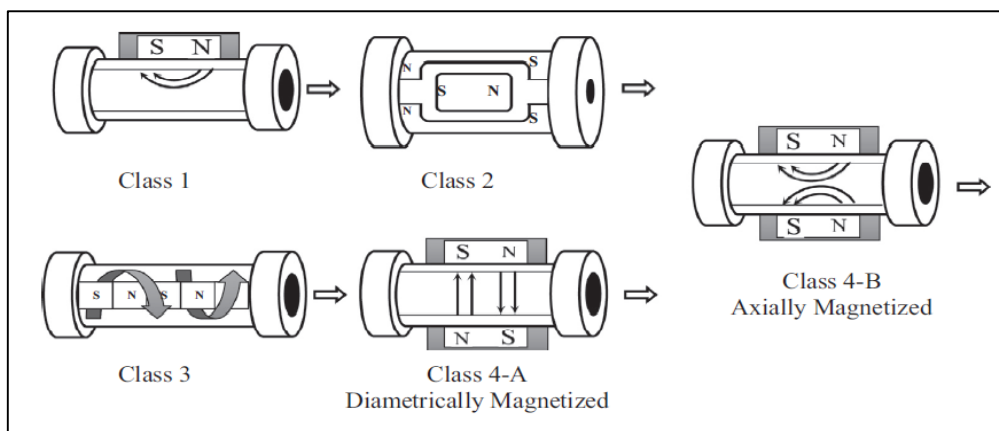


Figure 1-32: Water treatment static magnetic field configurations (Al Helal et al., 2017)

1.5.1. Hydrated ions in static magnetic fields

Ikeda and Sueoka (1970), subjected various copper salts to a range of static magnetic fields and investigated viscosities to deduce how the strength of the field impacted the specific Cu^{2+} and complimentary anionic components over a series of concentrations. The chosen reagents were cupric acetate ($\text{CH}_3[\text{COO}]_2$), cupric chloride (CuCl_2), cupric nitrate ($\text{Cu}[\text{NO}_3]_2$) and cupric sulfate (CuSO_4) and utilising the Ostwald Viscometry method they focused on the flow and time aspects of the magnetic susceptibility responses, as the susceptibility calculations of the Cu^{2+} paramagnetic response (see Tables 1-16 and 1-17).

Table 1-16: H_2O - Cu^{2+} salt concentration and paramagnetic response						
MW	1.8M	3.0M	1.1M	1.9M	0.93M	1.1M
Reagent	CuCl_2		$\text{Cu}(\text{NO}_3)_2$		CuSO_4	
Cu^{2+} (χ)	(B.M)		(B.M)		(B.M)	
\vec{B} (T)						
0.000	-	-	-	-	-	-
0.820	1.94	1.94	2.20	2.20	1.97	1.97
1.227	1.94	1.94	2.24	2.21	1.92	1.93
1.605	1.93	1.93	2.23	2.23	1.94	1.92
1.905	1.93	1.93	2.24	2.20	1.91	1.94
2.015	1.93	1.93	2.22	2.21	1.91	1.93
χ (\bar{X})	1.93		2.22		1.93	

The diamagnetic components were then calculated for the χ values of the chloride (-28.0), nitrate (-23.5), sulfate (-38.0) and acetate (-52.0) components, and reported that the magnetic exposure with the chloride, nitrate, and sulfate aqueous analytes were all consistent with the “*Wiedemann Law*” (p.1275, Ikeda and Sueoka, 1970).

Kuchel et al. (2003) articulates that “*Wiedemann’s Law of Magnetic Additivity*” (p.63, Kuchel et al., 2006) describes the sum of χ in a mixture, which is typically a solution, as the mass sum of the χ components, scaled according to their relative volume susceptibilities ($\chi V, i$):

$$\chi_{\text{mixture}} = \sum_{i=0}^n V_i \chi_i / \sum_{i=0}^n V_i$$

V : Volume of mixture

i : Substance

χ_i : Magnetic susceptibility value for i

The researchers concluded that the Cu(NO₃)₂ measurements were ~15% higher and therefore inconsistent with the scientific literature, despite identifying an Fe impurity in the reagent which could only account for $\leq 10\%$ of the identified error margin. The CuCH₃(COO)₂ analyte χ values were found to be consistent with the literature (1.95 B.M.) in the lower concentrations (0.113 and 0.169M) of exposure.

Table 1-17: H ₂ O- CuCH ₃ (COO) ₂ concentration and magnetic response (25.0°C)						
MW	0.113	0.169	0.224	0.279	0.347	0.516
Cu ²⁺ (χ)	B.M.	B.M.	B.M.	B.M.	B.M.	B.M.
(T)						
0.000	-	-	-	-	-	-
1.227	1.94	1.94	1.75	1.75	1.81	
1.605	2.01	1.96	1.85	1.85	1.67	1.55
1.905	1.97	1.93	1.83	1.78	1.65	
2.015	1.95	1.95	1.80	1.77	1.65	1.54

Mechanism: Crystalline formation is related to concentration.

The χ values decreased with increasing solute concentrations towards the literature χ measurements for CuCH₃(COO)₂ associated with the crystalline state (1.42 B.M.), deducing that the weak Cu-Cu dimeric bonds in the CuCH₃(COO)₂ crystal lattice were facilitating the observable phenomena in the increasing concentrations of the aqueous solutes.

Some of the respective diamagnetic susceptibilities for ions utilised in this research are assembled for reference purposes in Table 1-18 (Bain and Berry, 2008):

Table 1-18: Pascal's constants for analyte A diamagnetic susceptibilities					
Molecule/ion	H ₂ O	H+	Na+	I-	S ₂ O ₃ ²⁻
X (10 ⁻⁹ x m ³ mol ⁻¹ @ 298K)	-13.0 (ligand)	0	-6.8	-50.6	-46.0

Fathi et al. (2016) utilized an extended version of the diametrically magnetized arrangement depicted above (see Figure 1-33), applying five pairs of permanent magnets in opposing north and south pole arrangements with the reactant flowing through a magnet encased pipe with a measured field of 0.16T in the center position, when investigating the impacts of magnetic field exposures upon Ca²⁺ and HCO₃⁻ → CaCO₃ nucleation kinetics and morphology, noting this design generated higher salts of aragonite and calcite morphologies via homogeneous nucleation .

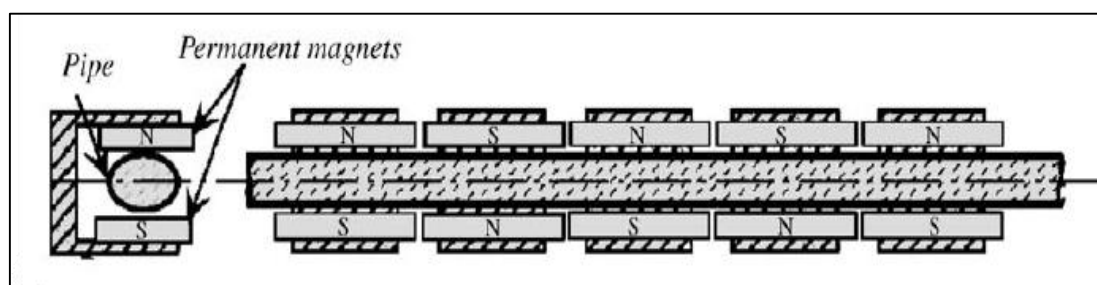


Figure 1-33: Diametric static magnetic configuration (Fathi et al., 2016)

This diametric arrangement was previously incorporated in the research of Gabrielli et al. (2001) who reported the waveform measurements acquired utilising a Hall probe revealed a consistent sinusoidal configuration of approximately ± 200mT over

the 200mm treatment chamber, when investigating CaCO_3 nucleation kinetics and morphology with an identical 0.16T field (see Figure 1-33 and 1-34).

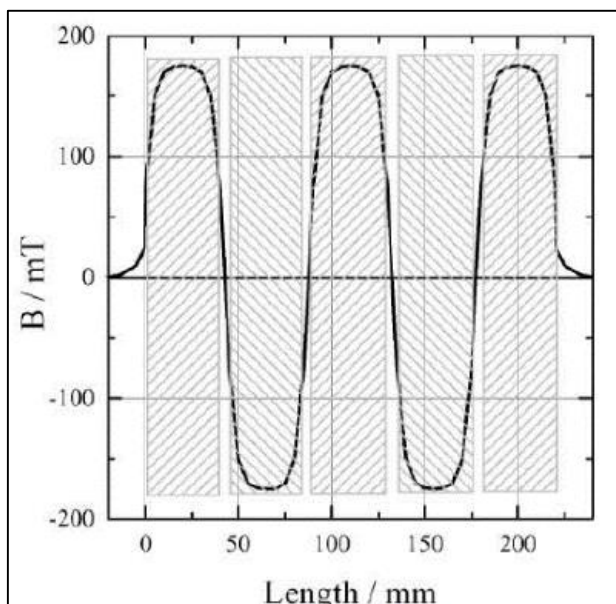


Figure 1-34: Diametric static magnetic field measurement (Gabrielli et al., 2001)

These scientists incorporated highly purified solutes generated from 5mM CaCO_3 in 1000 mL of deionized water, which was saturated with CO_2 to ensure the experimental solute contained only Ca^{2+} , CO_3^{2-} and HCO_3^- species, then measured the extent of scaling with a Ca^{2+} selective ion electrode over time (t_s), until the ion count was low enough to be considered negligible, and nucleation rates (t_n) via dissolved oxygen reduction and precipitated mass. The outcomes reported that this configuration had reduced nucleation rates by over 90% and scaling by 65% relative to time. The team then conducted a series of identical experiments, modifying only the permanent magnet positions to incorporate the axial configuration (see Figure 1-35), and the Hall probe measurements revealed a significantly smaller series of positive waveform oscillations in the 150 to 175 mT range (see Figure 1-36), with the experimental analysis informing superior rates of scaling and nucleation rates relative to control measurements, but lowered kinetics for both factors respective to the inverted magnetic layout (see Table 1-19).

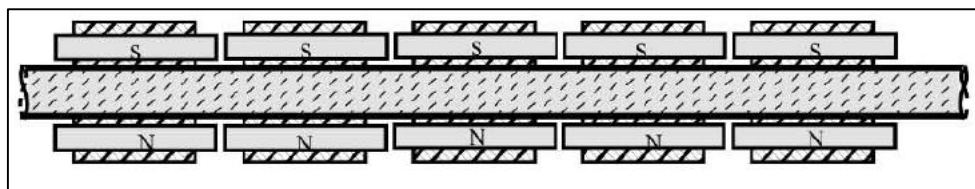


Figure 1-35: Axial static magnetic field configuration (Gabrielli et al., 2001)

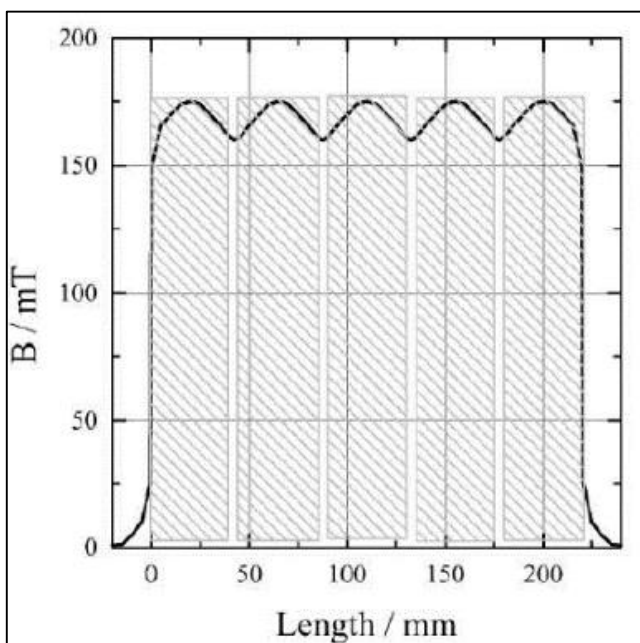


Figure 1-36: Axial static magnetic field measurement (Gabrielli et al., 2001)

Table 1-19: CaCO_3 and static magnet configuration precipitation		
CaCO_3	Nucleation (t_n): $\text{Ca}^{2+}/\text{mins}$	Scaling (t_s): $\text{DO} \rightarrow \text{mg/min}$
Control	5	75
0.16T diametric	60	215
0.16T axial	25	180

The axial configuration was reported by Russian scientists Ignatov and Mosin (2014) to be the optimal design to implement magnetohydrodynamic “zero induction zones” (p.77, Ignatov and Mosin, 2014) in flowing aqueous solutions encased in the arrangement below. The arrows depict the direction of the magnetic field inducing Lorentz force flows on cations (small dots) and anions (large dots), which collide at zero induction zones stipulated by the grey lines separating the four magnets depicted (see Figure 1-37), resulting in higher concentrations of oppositely charged species at increased rates of collisions, thereby inducing the faster formation of salt nucleation centers.

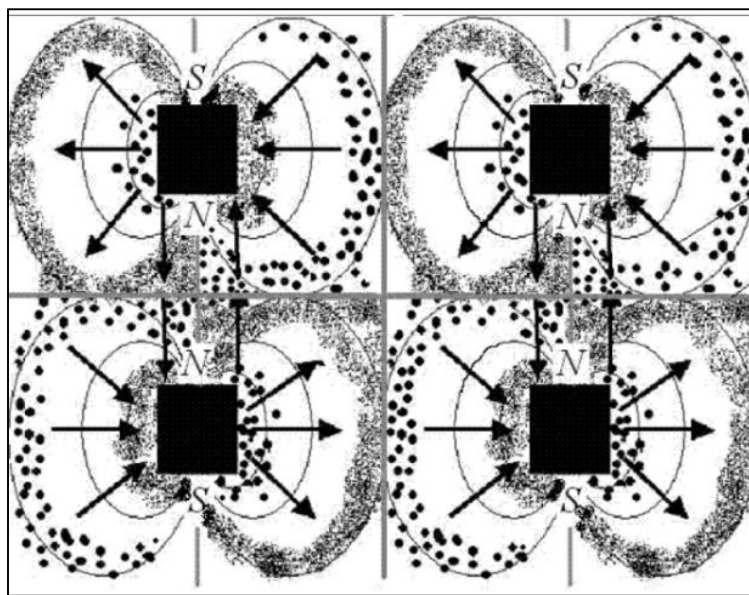


Figure 1-37: Axial static magnetic field MHD induction zone manipulation
 (Ignatov and Mosin, 2014)

Bozic, Lipus and Kokol (2008), committed to a series of experiments with reducing and oxidising agents exposed to a static magnetic field (0.9T m^2) to determine whether exposure could impact redox chemical performance in bleaching and dying processes of the textile industry. The research methodology focused on a range of concentrations of glucose as the reducing agent ($\text{C}_6\text{H}_{12}\text{O}_6$), and two commonly utilised oxidizing chemicals, hydrogen peroxide (H_2O_2) and sodium chlorate (NaClO), measuring ORP readings after exposures utilising a platinum electrode to measure the potentials and a reference Ag/AgCl electrode with KCl electrolyte, incorporating the Nernst equation:

$$\text{ORP} = E = E^\circ - \frac{RT}{nF} \ln \frac{\text{reduced}}{\text{oxidised}}$$

E° is the standard redox potential for the reference electrode ($\text{AgCl}(s) + e^- \Rightarrow \text{Ag}(s) + \text{Cl}^-(aq) = + 0.222\text{V}$ @ 25.0°C

R is the gas constant ($8.314 \text{ J}\cdot\text{K}^{-1}\cdot\text{mol}^{-1}$)

T is the temperature (K)

F is the Faraday constant (96485 C/mol^{-1})

n is the e^- transferred

The correlations of these equations is that as reduction increases relative to reference standards, the ORP values decreases, and as oxidation increases relative to the complimentary reference standards, the ORP values increases.

The aqueous C₆H₁₂O₆, H₂O₂ and NaClO₃ reagents were adjusted to pH 13, 10 and 11 respectively, commensurate to their common industrial applications, and then the ORP measurements were conducted on a minute-by-minute basis from 0 to 30-75 minutes, which identified an approximate increase of 10% in the reduction potential of the C₆H₁₂O₆ exposure analytes between ~ 15 to 30 minutes into the analysis, prior to tapering off (see Figure 1-38). The triplicate 0.06M H₂O₂/NaOH and 0.43M NaClO₃/NaOH control and exposure analytes both exhibited an increase of 20% and 15% in oxidation potential of the exposure respectively, which remained consistent for the 30 minutes of ORP.

Mechanism: The static magnetic field altered analyte hydration.

Bozic, Lipus and Kokol hypothesised that as all three molecules exhibited OH bonds, there was a tendency to form H bonds with H₂O molecules in solution, and the magnetic fields induced distortions and interrupted the typical hydration shell kinetics that were representative in controls, leading to deprotonation and increases in respective reduction and oxidation potentials. This group further surmised that a possible mechanism was correlated with oxidation facilitating “distortions” in the hydrogen bonded hydration shells associated with OH groups lining the glucose molecule, adding that a possible mechanism was correlated with oxidation facilitating “distortions” in the hydrogen bonding hydration associated with OH groups lining the glucose molecule.

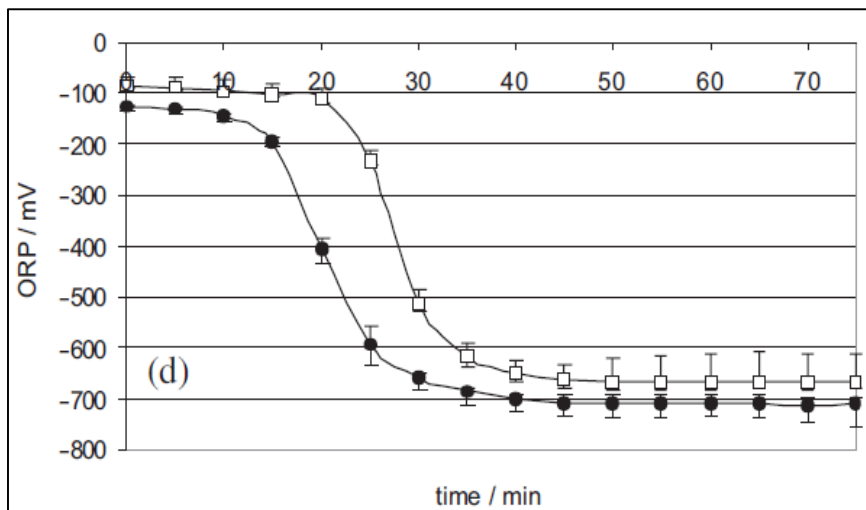
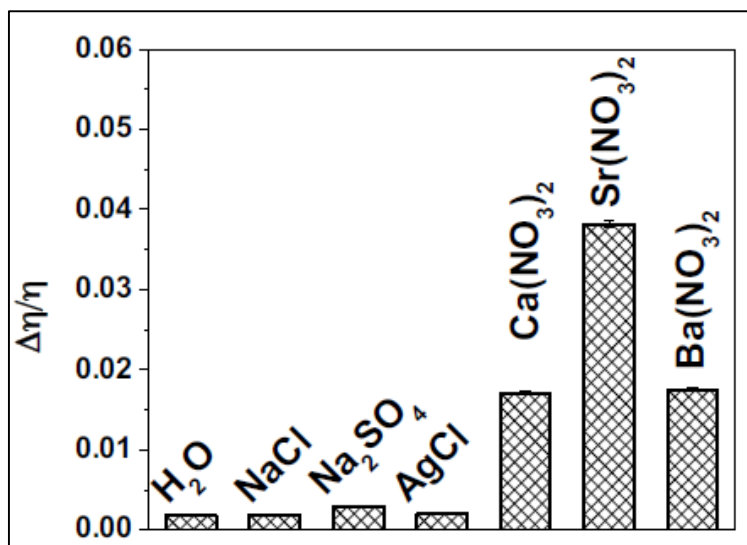


Figure 1-38: $\text{C}_6\text{H}_{12}\text{O}_6$ (0.9M) control and 0.9Tm^2 ORP reduction (70 mins)
(Bozic, Lipus and Kokol, 2008)

Igor Silva et al., Neto and Petri (2014) set out to investigate the ion hydration of a selection of 0.5M salts to induce low soluble sulfate scales, with regard to the impacts of a homogenous 1T static field under consistent flow rates (0.992 ms^{-1}), focusing on control and treatment viscosities utilising Ubbelohde capillary viscometers (calibrated constant = $0.009536 \text{ mm}^2/\text{s}^2$), monitoring colloidal kinetics with a separation analyser, rates of sedimentation utilising “*low angle laser light scattering*” (p.177, Silva, Neto and Petri, 2014), and XRD to visually scrutinise morphological aspects.

They chose barium nitrate ($\text{Ba}[\text{NO}_3]_2$), strontium nitrate ($\text{Sr}[\text{NO}_3]_2$), and calcium nitrate ($\text{Ca}[\text{NO}_3]_2$) as their source of divalent cations, and silver nitrate (AgNO_3) and sodium chloride (NaCl) as the monovalent selections, with sodium sulfate (Na_2SO_4) as their source for divalent and chlorides as the monovalent species. The salts were prepared as 0.5M solutions with Milli Q H_2O and adjusted to pH 6, and alternative cation and anion 1T field exposures were undertaken in a temperature stabilised setting ($24 \pm 1^\circ\text{C}$). The viscosity profiles noted that the divalent nitrates subjected to the 1T field exhibiting increased viscosity (Δn) relative to controls (n), and that the monovalent and anionic experiments afforded no changes (see Figure 1-39).



**Figure 1-39: Control vs 1T exposure hydrated salt viscosity effects
(Silva et al., Neto and Petri, 2014)**

The laser scattering data disclosed no shift in the exposure Ag⁺ ions settling rates ($\mu\text{m/s}^{-1}$) and mean particle diameter (μm), moderate effects with the Ba²⁺ and Ca²⁺ species, and a significant change in the Sr²⁺ parameters ($\geq 60\% \mu\text{m/s}^{-1}$ and $\leq 30\% \mu\text{m}$). Considering the strontium sulfate analytes had exhibited the most significant responses, this analyte was selected to conduct 1T field retention analysis. The samples subjected to XRD profiling were freeze dried overnight then analysed next day ($\lambda = 0.154 \text{ nm}$, $0.02^\circ/\text{min}$). The diffraction peak analysis of the \vec{B} field treatment salts in the $2\theta 28^\circ$ to 30° and 27° to 33° ranges revealed a significant decrease of approximately 45% at the characteristic 29.49° peak for BaSO₄, an increase at the 29.52° peak for CaSO₄, and decreases at both major Sr(NO₃)₂ that were not as significant, concluding that the atomic structures of the salt crystals only exhibited minor affects from the exposures, and the AgCl control and exposure analyses were consistent.

The Sr(NO₃)₂ solutions which had exhibited the most significant shifts in colloidal absorbance kinetics and particle nucleation were chosen as the retention effect “memory” (pp.176-182, 2014) cations, then blended with Na₂SO₄ as the anion source to generate SrSO₄ to again exposed to 1T fields under otherwise identical prior conditions. The sulfate control and exposure products were set aside in sealed flasks under identical temperature conditions and analysed for colloidal stability and particle size after 24, 48, 72 and 216 hours. The 1T exposure analytes were also subjected

to heating ($60^{\circ}\text{C}/20$ and 60 min), then cooled to lab temperature to identify any temperature related impacts on sustained magnetic phenomena, as outlined in the research literature.

Table 1-20: SrSO₄ and 1T nucleation kinetic retention and particulate size					
1T	Cation	Anion	Analysis (T)	60% nm/min	µm
Control	Sr ²⁺	SO ₄ ²⁻	Same day	2.2 ± 0.5	5.3 ± 0.5
Yes	Sr ²⁺	SO ₄ ²⁻	Same day	9.0 ± 2.0	3.6 ± 0.3
Yes	Sr ²⁺	SO ₄ ²⁻	+ 24 hours	10.5 ± 0.5	3.0 ± 0.5
Yes	Sr ²⁺	SO ₄ ²⁻	+ 48 hours	4.6 ± 0.5	4.7 ± 0.5
Yes	Sr ²⁺	SO ₄ ²⁻	+ 72 hours	2.2 ± 0.4	5.9 ± 0.6
Yes	Sr ²⁺	SO ₄ ²⁻	+ 216 hours	1.9 ± 0.5	8.1 ± 0.6

The results of the magnetic retention analysis declared that the magnetic field induced phenomena were still observed at least as strongly after 24 hours of analytical delay, and persisted relative to the controls at 48 hours, but had dissipated by 72 hours post exposure (see Table 1-20). The heating of the Sr(NO₃)₂ treatment analytes post exposure noted that $n/\Delta n$ viscosity had diminished after 20 minutes at 60°C and was at baseline with the control viscosities after 60 minutes at 60°C .

Mechanism: The static magnetic field induced divalent hydration.

This team concluded that the cationic charge densities of the divalent species experienced higher hydration in the 1T field, respective to the monovalent analytes and anions, and this increased hydration identified in the viscosity profiles lead to the nucleation of smaller particulates, and that the increased polarisation was a result of a combination of the 1T field induced Lorentz Force under flow increasing hydration and the divalent species having favoured orientation at gas/bubble interfaces. A memory effect was observed to support these factors were retained post treatment, were equally present after 24 hours, then slowly dissipated from that point up until 72 hours, and this retention phenomena is impacted by thermal kinetics.

1.5.2. Hydrated ions in dynamic magnetic fields

Research was carried out at Victoria University in Melbourne, Australia by Piyadasa et al. (2017) utilising two pulsed electromagnetic field (PEMF) water treatment devices on 5mM and 8mM Na₂CO₃ and Ca(NO₃)₂·4H₂O solutions utilised for CaCO₃ precipitation. The research goal was to determine kinetic and morphology aspects of the respective aggregates, and it was identified that one particular device, the Dolphin 3000 (230 V, 50/60Hz, 0-100 kHz), was reported to impart a significant change in the treatment precipitation profiles.

The Na₂CO₃ and Ca(NO₃)₂·4H₂O reagents were placed into 10 mL polypropylene screw cap graduated tubes, then placed inside the device opening inside the EMF reaction coil and exposed to PEMF for 180 minutes under dry conditions, and under static flow condition, with ~600 mL of H₂O in the system to insulate temperature effects, which were reported to rise to ~45°C then stabilise. The analysis focused on turbidity to measure colloidal aspects (NTU) and UV-Vis spectroscopy absorbance (350nm) to measure kinetic rates, both over 30 minutes at 2 minute intervals, and scanning electron microscope (SEM) to investigate the resulting CaCO₃ morphological characteristics and correlations (see Figures 1-40 and 1-41, D = PEMF solenoid under non-irrigated conditions, DWB = PEMF solenoid under water bath irrigation conditions).

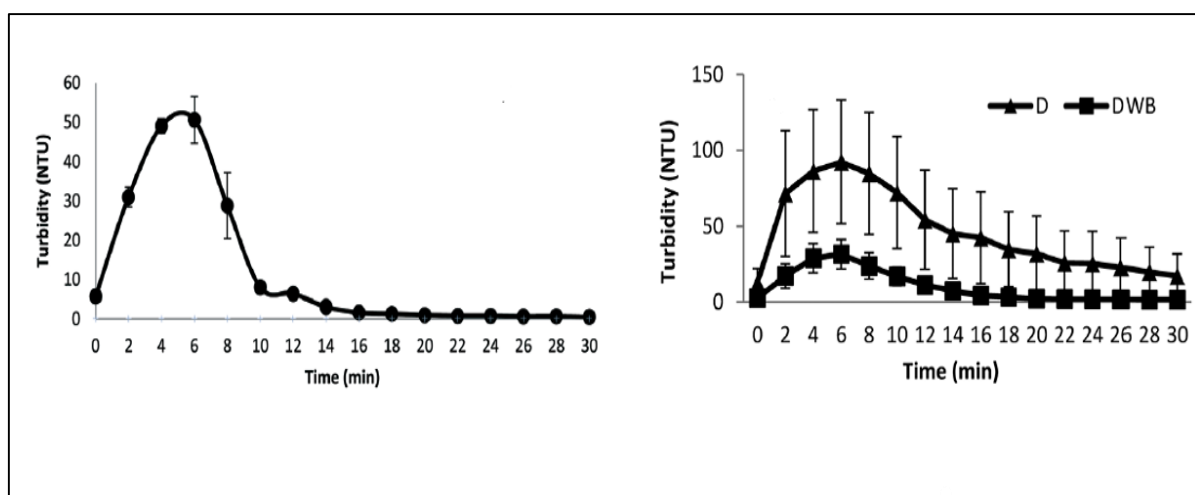


Figure 1-40 (left): Control 5mM CaCO₃ nucleation turbidity/time,

Figure 1-40 (right): PEMF (180 min) 5mM CaCO₃ nucleation turbidity/time

(Piyadasa et al., 2017)

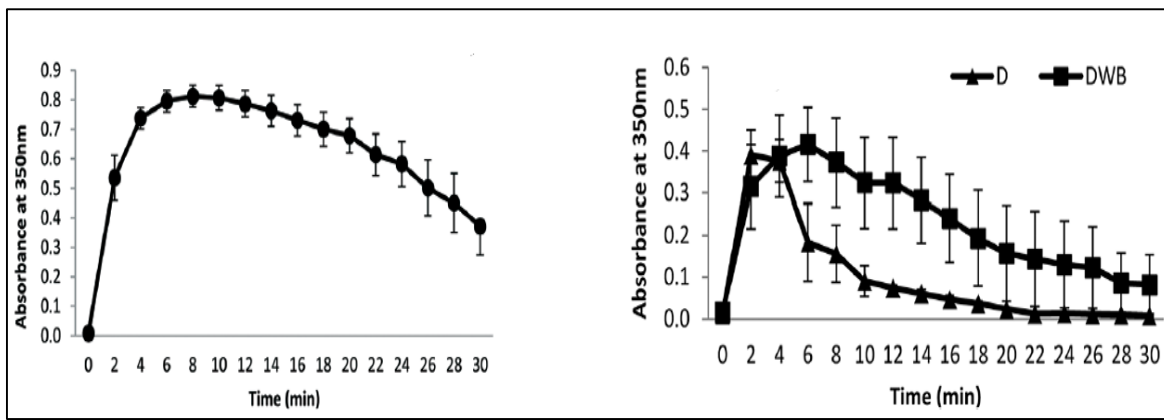


Figure 1-41 (left): Control 5mM CaCO_3 nucleation UV-Vis /time.

**Figure 1-41 (right): PEMF (180 min) 5mM CaCO_3 nucleation UV-Vis/time.
(Piyadasa et al., 2017)**

The SEM morphologies identified shifts correlated with the Dolphin 3000 PEMF exposures in the resulting crystal structures as Tabled in 1-21 below:

Table 1-21: PEMF vs Control CaCO_3 morphology (SEM)		
PEMF Analyte	PEMF Morphology	Control Morphology
$\text{Na}_2\text{CO}_3 + \text{Ca}(\text{NO}_3)_2 \cdot 4\text{H}_2\text{O}$	Cuboidal	Indiscernible
Na_2CO_3	Rod like	Indiscernible
$\text{Ca}(\text{NO}_3)_2 \cdot 4\text{H}_2\text{O}$	Plates/rods	Cuboidal

Complimentary unpublished electrospray ionisation mass spectroscopy (ESI-MS) positive ion mode analysis was undertaken as outlined in the thesis presented by Piyadasa et al. (2017), with 5mM Na_2CO_3 and $\text{Ca}(\text{NO}_3)_2 \cdot 4\text{H}_2\text{O}$ aqueous solutions that were exposed to the Dolphin 3000 PEMF field for 10 minutes to investigate H_2O cluster aspects. This analysis identified significantly increased smaller Na^+ (H_2O)_n clustering in the Na_2CO_3 exposure spectra in comparison with the controls, and the $\text{Ca}(\text{NO}_3)_2 \cdot 4\text{H}_2\text{O}$ ESI-MS analysis also revealed notable shifts in Ca^{2+} (H_2O)_n spectra clustering (Figures 1-42 to 1-45).

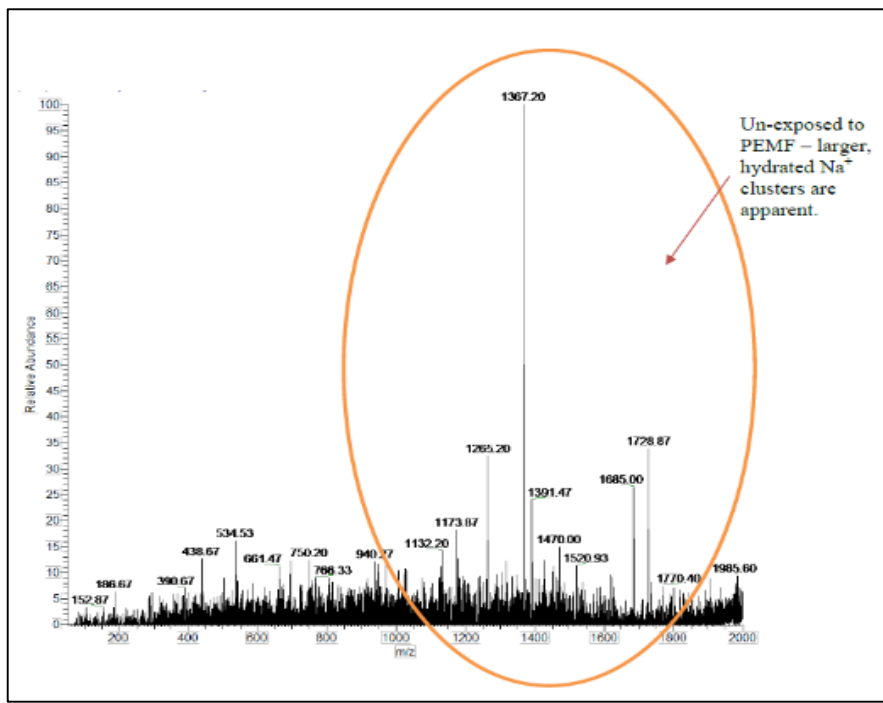


Figure 1-42: ESI-MS 5mM Na_2CO_3 control Na^+ spectra (Piyadasa et al., 2017)

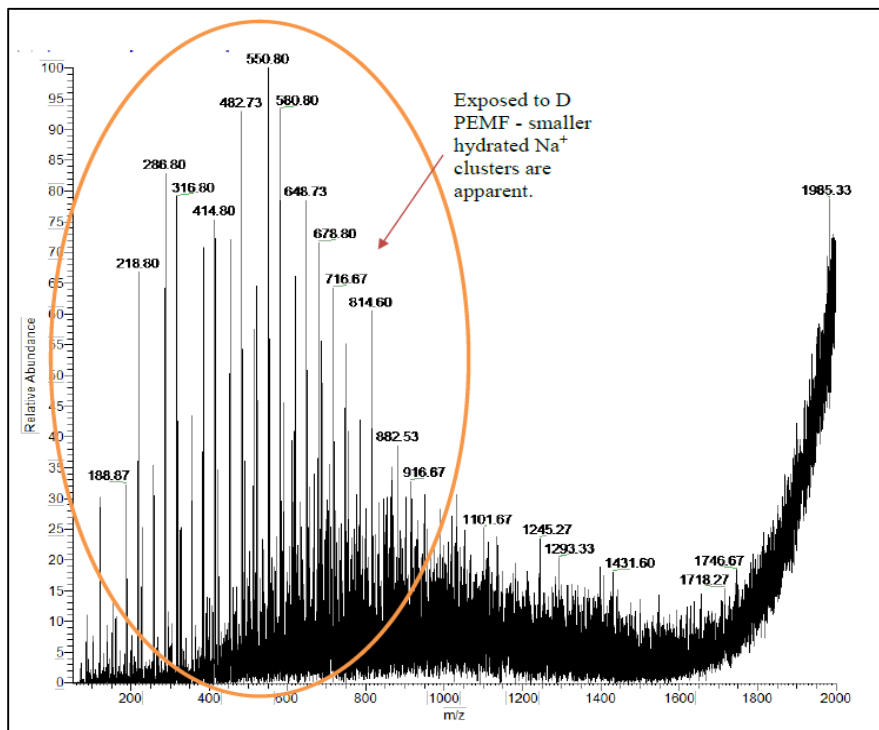


Figure 1-43: ESI-MS 5mM Na_2CO_3 PEMF (10 minutes) Na^+ spectra (Piyadasa et al., 2017)

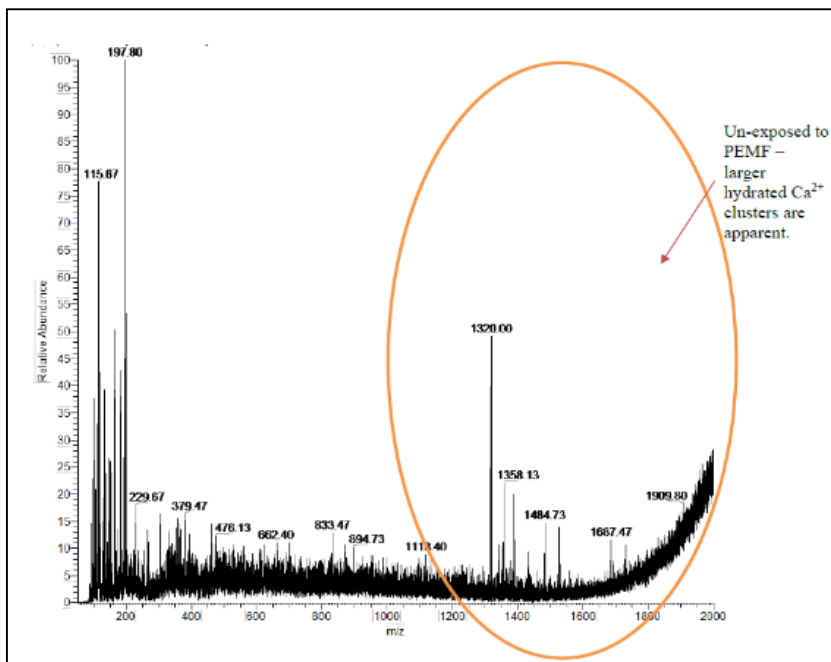


Figure 1-44: ESI-MS 5mM $\text{Ca}(\text{NO}_3)_2$ control Ca^{2+} spectra (Piyadasa et al., 2017)

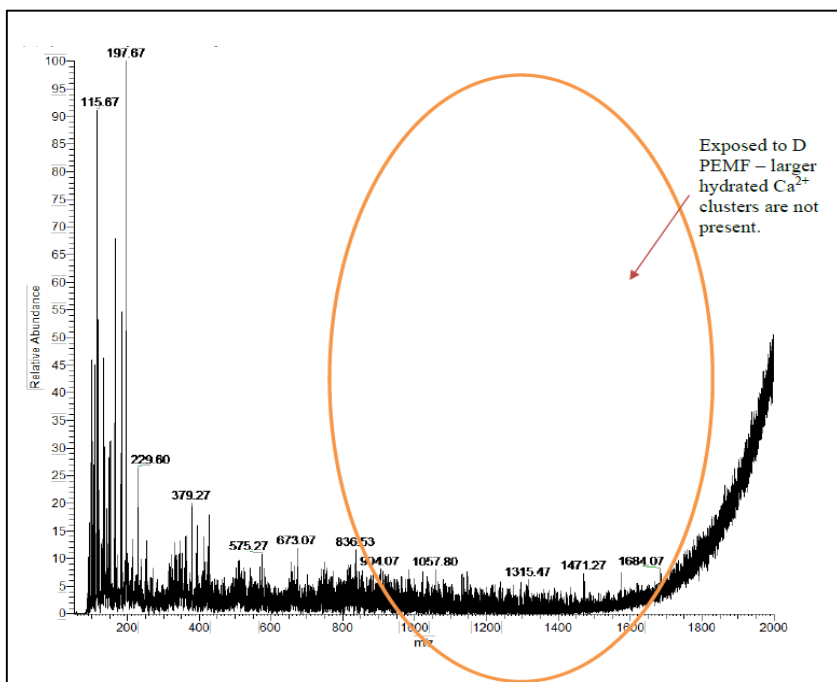


Figure 1-45: ESI-MS 5mM $\text{Ca}(\text{NO}_3)_2$ PEMF (10 minutes) Ca^{2+} spectra (Piyadasa et al., 2017)

Mechanism: PEMF induced changes in ionic hydration impacts nucleation

The Dolphin 3000 PEMF 180 minute exposure treatment facilitated faster and sharper absorbance at 2 minutes of the UV-Vis scans with the curve flattening at 22 minutes, compared to control absorbance peaking at 8 minutes and ongoing

nucleation at 30 minutes. This, in combination with the preliminary ESI-MS analysis exhibiting shifts in cluster profiles, and the correlated morphological changes in the CaCO_3 precipitates, culminated with this research team claiming, “*It is our contention that both of these factors (precipitation rate and crystal morphology) are expected to be influenced by nucleation processes that involve aqueous cationic and anionic clustering in solution*” (p.96, Piyadasa et al., 2017).

A Dolphin 3000 PEMF device was also incorporated in the research of Cho et al. (2003) to analyse the mitigation of scale formation in heat exchangers whilst monitoring fouling resistance in terms of heat fouling resistance and reported an approximate nine fold increase in thermodynamic efficiency compared to the control baseline due to device use over the course of 800 hours (see Figure 1-46).

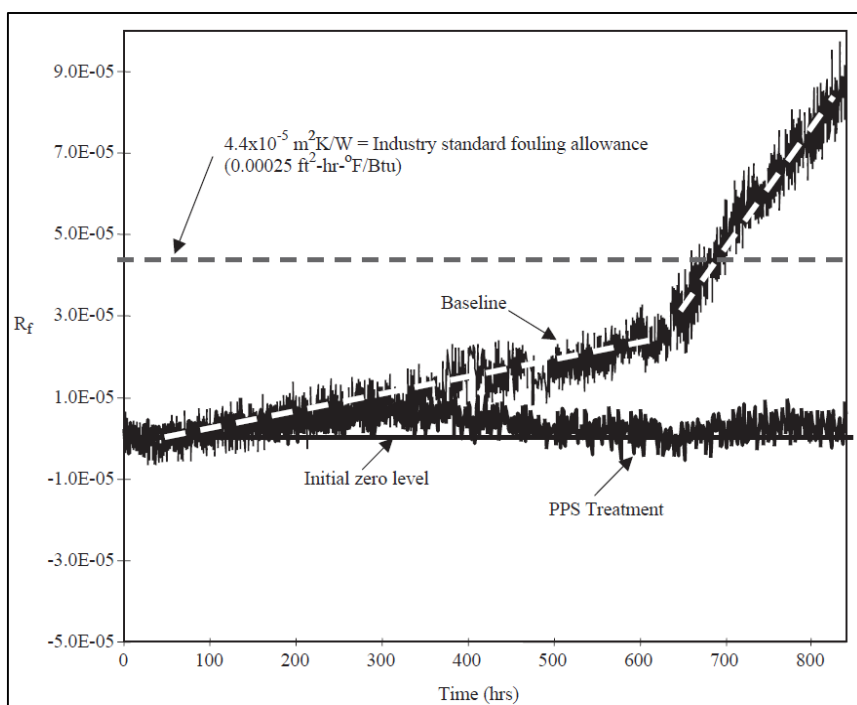


Figure 1-46: Dolphin 3000 vs control and scale inhibition over 800 hours (Cho et al., 2003)

Mechanism: PEMF exposure altered typical CaCO_3 ionic hydration and nucleation.

Domestic and industrial water regimens are not the only fields utilising use PEMF treatments as they are also employed in contemporary chemical practices. Peng, Du & Wang (2015) conducted research on cobalt oxalate synthesis ($\beta\text{-CoC}_2\text{O}_4 \cdot 2\text{H}_2\text{O}$) by subjecting component solutions of ammonium oxalate $(\text{NH}_4)_2\text{C}_2\text{O}_4 \cdot \text{H}_2\text{O}$ and

cobalt chloride (CoCl_2) to 30, 60 and 90 seconds of PEMF exposure (800 V/3Hz solenoidal fluctuation = 2.59 T to 4.42 T), then precipitating a product with a higher degree of sphericity and increased mechanical performance than had previously been identified via the traditional synthesis routes .

The group prepared 50mL of aqueous 0.66M CoCl_2 in a reaction vessel surrounded by a solenoidal PEMF generating coil immersed in a water bath, then carefully combined 100mL of 0.33M aqueous $(\text{NH}_4)_2\text{C}_2\text{O}_4 \cdot \text{H}_2\text{O}$ to the reaction precursors, and applied the 2.59 T to 4.42 T oscillating field once the ammonium oxalate addition was completed for periods of 30, 60 and 90 seconds, then maintained the reaction under constant stirring for 60 minutes at 40°C. The reactions were cooled for 10 minutes, and the precipitates were filtered, washed several times with deionised H_2O to remove impurities, and then placed in a vacuum desiccator at room temperatures.

Morphological analysis was then conducted utilising scanning electron microscopy (SEM) which identified the expected rod like characteristics in the control species, which was also noted in the 30 second PEMF exposure salt, however a previously unreported highly spherical $\beta\text{-CoC}_2\text{O}_4 \cdot 2\text{H}_2\text{O}$ morphology was identified in the 60 second exposure product, with a blend of spheroid and customary rod like aspects in the 90 second exposure analytes (Figure 1-47)

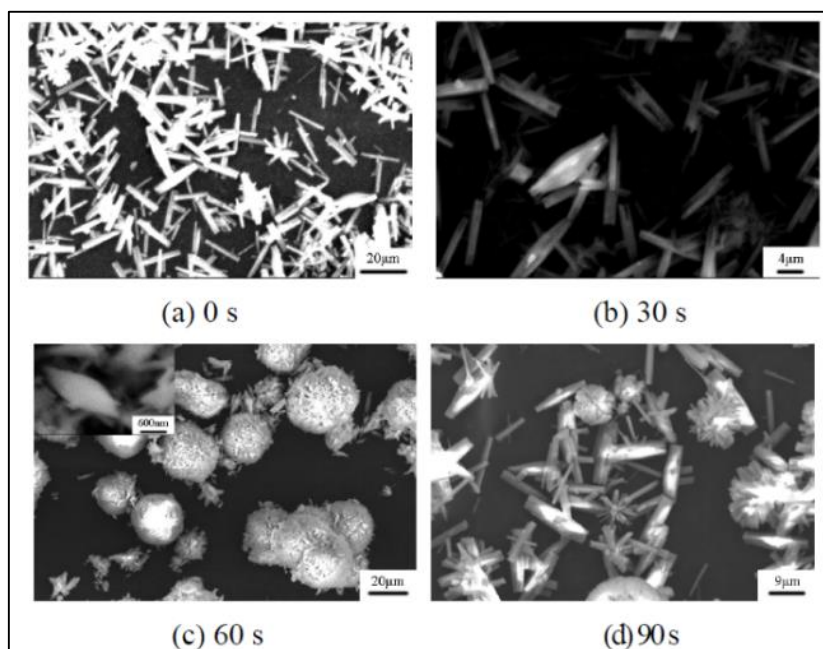


Figure 1-47: PEMF exposure time SEM $\beta\text{-CoC}_2\text{O}_4 \cdot 2\text{H}_2\text{O}$ morphology (Peng, Du and Wang, 2015)

X ray diffraction analysis was then undertaken on the β - $\text{CoC}_2\text{O}_4 \cdot 2\text{H}_2\text{O}$ control and 60 second PEMF samples, which returned matching diffraction indexation confirming that the two analytes were molecularly consistent with profiles of β - $\text{CoC}_2\text{O}_4 \cdot 2\text{H}_2\text{O}$ standards (Figure 1-48).

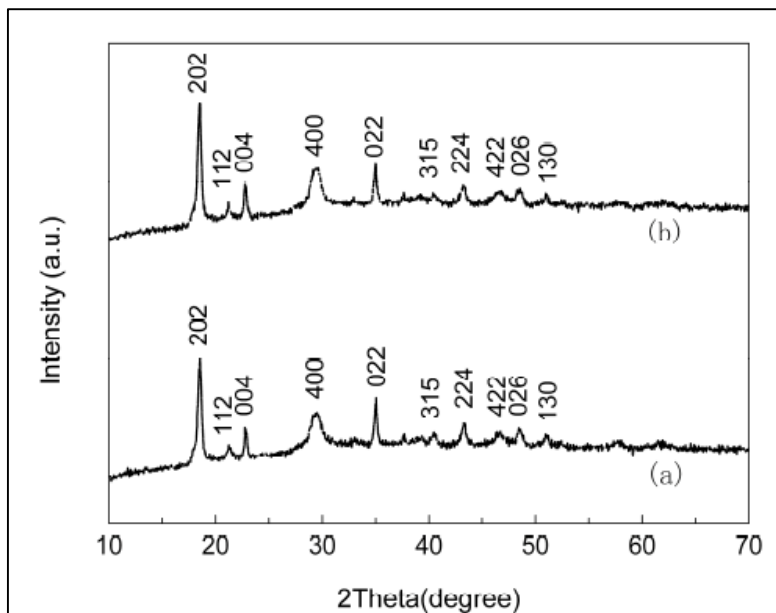


Figure 1-48: a) β - $\text{CoC}_2\text{O}_4 \cdot 2\text{H}_2\text{O}$ standard, and b) β - $\text{CoC}_2\text{O}_4 \cdot 2\text{H}_2\text{O}$ - PEMF XRD profiles.
(Peng, Du and Wang, 2015)

Mechanism: PEMF induced time related impacts on morphology

Peng and associate concluded that the PEMF exposure time response aspects resulting in variations in final morphology resulted from induced kinetic competition at crucial stages in the diffusion of ions and particles during anisotropic nucleation phases.

According to Campos and Ortiz (2020), recent estimates of potato farming and consumption reveal the global farmland use at 19,000,000 hectares, providing crops of 378,000,000 tonnes, ranking this vegetable third behind rice and wheat as the world's most important plant based food source. Research was undertaken by Ocieczek and Otremba (2019) with food storage integrity in mind, when they experimented with potato starch samples incorporating magnetic field drying treatments, motivated by the substances strategic significance as a source of human

nutrition, and therefore improved food storage practices, and to investigate how potato starch preservation could be improved with regard to its likely use as a food source for human space exploration outside of the earth geomagnetic field.

The potato starch samples utilised in the experiments was analysed for particle size and shape representation and the H₂O content of the experimental samples was calculated via laboratory convective thermal drying. The magnetic field for the exposure samples was facilitated by the placement of static neodymium magnets employed in a manner to elicit equidistant field gradients between 20 to 190mT, under selected 30 ± 1°C and 40 ± 1°C temperature conditions chosen as suitable parameters for desorption process under these conditions (see Figure 1-49).

The experimental method employed four hermetically sealed glass bottles containing 1 gram of potato starch for exposure, with four other identical controls placed on alternative shelves in the dryer, which were switched in a secondary series of experiments in order to preclude favourable positioning, the overall outcome being eight samples of exposure and control analytes at 30°C and 40°C respectively. The rate of change measurements of H₂O desorption kinetic were conducted at 90, 180 and 270 minutes, determined by the gravimetric method as the weight change in comparison to the weights prior to commencing oven drying, with complimentary H₂O vapor measurements in the drying chambers utilising a hygrometer.

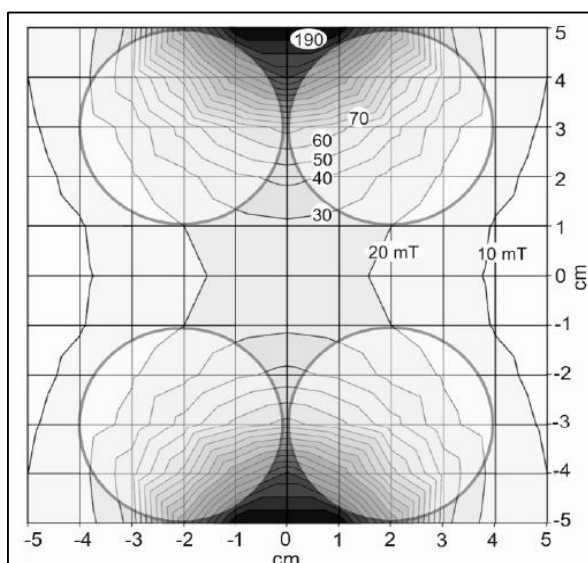


Figure 1-49: Starch desorption design and 20-190mT magnetic flux density gradient
(Ocieczek and Otremba, 2019)

The calculated results of the experiments afforded the following data (Table 1-22):

Table 1-22: Potato starch control vs magnetic exposure desorption				
	30°C @ 270min		40°C @ 270min	
Analyte	Control	Exposure	Control	Exposure
H ₂ O g/cm ⁻³ (\bar{x})	0.1646	0.1618	0.1353	0.1312
H ₂ O g/cm ⁻³ (σ)	0.0016	0.0012	0.0021	0.0029
F value (<0.001)		0.4905		0.3761
P Value (<0.05)		0.0015		0.0060
Oven H ₂ O g/cm ⁻³ (\bar{x} %)	35.93	2.23	15.50	0.95

The researchers concluded that magnetic field exposure impacted the kinetics of the drying process causing the starch particles to dehydrate faster at all measured intervals and regardless of the utilised temperatures.

Mechanism: Dynamic magnetic fields lower starch-H₂O bond energy

Ocieczek and Otremba hypothesised that there was an increase in the H₂O vapor pressures facilitated by the magnetic field which altered the thermodynamic state and increased the entropy of the system, by lowering and breaking the hydrogen bonding energies that are typically represented by the starch and H₂O interplay.

1.5.3. Proton transfer in magnetic fields

A team of petroleum engineers located in Iran, Hashemizadeh et al. (2018) commenced research with varying hydrochloric acid (HCl) concentrations in combination with a variety of static magnetic field strengths, differing flow rates and temperatures, then measured pH and retention time factors, with a view to maximising the performance and cost effectiveness of significant HCl use utilised in the acidification of hydrocarbons in crude oil and gas wells. They employed the “Taguchi Method” (p.216, Hashemizadeh et al., 2018), which according to Roy (2010), is a statistical methodology devised by Dr Genichi Taguchi in the 1980’s when working on optimising research and design optimisation at General Motors in the U.S.A. This concept focused on the design of experiments (DoE) incorporating

orthogonal arrays which each represent the smaller fractional components in experimental design to reveal the factors which can reduce variability and achieve optimal performance as “*signal to noise ratio (S/N)*” (p.221, Hashemizadeh et al., 2017), which is the culmination of optimal analytical performance predictions, utilising the following calculation of the variation in the arrays:

$$\frac{S}{N} = -10 \times \log (1 \div y_i^2 \div n)$$

y_i is the reduction in rate reaction

n is the number of experimental replications

This research team employed a variation of this DoE method, to effectively combined the data from 27 actual experiments to give the effective statistical data of what would have required 243 experiments, focusing on the higher percentage conclusions to maximize their experimental goals.

Table 1-23: 0.23T HCl variable molarity, flow, temperature, and pH analysis

Trial	(T)	HCl (M)	Flow 5 min (m/s)	Temp (°C)	pH/H ⁺ (min)	T/pH (±)	T/H ⁺ (±)	S/N
1	0.23	1.5	0.5	25	0	+ 0.046	- 10%	20.0000
2	0.23	1.5	0.5	25	30	+ 0.022	- 5%	13.9794
3	0.23	1.5	0.5	25	60	+ 0.022	- 5%	13.9794
4	0.23	3.0	1.0	35	0	+ 0.155	- 30%	29.5424
5	0.23	3.0	1.0	35	30	+ 0.108	- 22%	26.8485
6	0.23	3.0	1.0	35	60	+ 0.108	- 22%	26.8485
7	0.23	4.5	1.5	45	0	+ 0.102	- 21%	26.4444
8	0.23	4.5	1.5	45	30	+ 0.056	- 12%	21.5836
9	0.23	4.5	1.5	45	60	+ 0.046	- 10%	20.0000

The orthogonal arrays incorporating the following DoE are outlined in Table 1-24:

Table 1-24: Taguchi experimental design components					
Trial	\vec{B} (T)	Flow (m/s)	HCl (M)	Temp (°C)	pH analysis (min)
1-9	0.23	0.5, 1.0, 1.5	1.5, 3.0, 4.5	25, 35, 45	0, 30, 60
10-18	0.33	0.5, 1.0, 1.5	1.5, 3.0, 4.5	25, 35, 45	0, 30, 60
19-27	0.43	0.5, 1.0, 1.5	1.5, 3.0, 4.5	25, 35, 45	0, 30, 60

A selection of the experimental data components tabled above (Table 1-23), highlighting the S/N calculations were drawn from the combined experimental design contributions, and as can be deduced from the data, experiment 4 (bold) consisting of 3.0M HCl reagent that underwent 0.23T exposure @ 1.0m/s flow and 35°C afforded the highest S/N result is correlated with the best overall performance and mitigation of variance factors and was therefore deemed the best DoE for this series. These S/N calculations drawn from the Taguchi statistics derived from a total of 27 experiments, employed one way ANOVA to determine experimental component variation in the data and identify statistical significance (Table 1-25):

Table 1-25: Experimental design factors with DoE statistical significance					
Factor	DF	σ^2	F-value (= >2.49)	P-value (= <0.05)	SSQ
\vec{B} strength	2	448.26	41.77	<0.0001	896.52
Flow (m/s ⁻¹)	2	64.52	3.01*	0.0779*	64.52
HCl %	2	1356.96	63.22	<0.0001	1356.96
°C	2	136.52	6.36*	0.0093*	136.52
$\vec{B} \rightarrow$ pH/ H ⁺	2	560.96	26.14	<0.0001	560.96
Residual	16	10.73			171.70

* Experimental design factors deemed insignificant

The calculated significance of the DoE taken from the respective arrays that HCl concentration contributed 42% to optimal S/N, with magnetic field intensity contributing 28% to the maximal design factors. The overall contribution of post exposure pH and H⁺ analysis regarding the time lapse and magnetic exposure stability pertaining to pH, H⁺ and time was deemed to be an 18% contribution, the flow rate accounting for a very minimal 2% of the overall modelling, and the error value in the modelling was calculated at 6%.

The overall combination of experimental factors deduced that 3.0M HCl exposed to a 0.43T field under 1.5m/s^{-1} flow@ $25.0\text{ }^{\circ}\text{C}$ afforded the maximum response in S/N (32.4650), pH increase (0.237) and reduction of available H^{+} ions (42%) when analysed immediately after \vec{B} field exposure. They further calculated the temperature effects from the Taguchi arrays, which revealed a moderate performance decline from $25.0\text{ }^{\circ}\text{C}$ to $35.0\text{ }^{\circ}\text{C}$, and negligible differences between $35.0\text{ }^{\circ}\text{C}$ and $45.0\text{ }^{\circ}\text{C}$, discounting temperature within these ranges as a significant factor, along with flow rates. The \vec{B} field retention effects all showed peak readings immediately after exposures and declined over the course of 0 to 30 and 60 minutes of analysis.

Later experiments undertaken by Hashemizadeh and Ameri (2021) investigating 3.8M HCl corrosion with prepared N80 carbon steels ($62.8 \times 18.0 \times 3.7\text{ mm}$) incorporating the same 4 minute static magnetic “pre-treatment” exposures of the same field strength utilised in this research (0.3T), applied electrochemical, gravimetric and SEM analysis concluded that the mean gravimetric weight reduction and corrosion rates of the 0.3T 3.8M HCl/N80 sample had reduced corrosion after 6 hours of contact time. Furthermore, these phenomena were still strongly present 48 hours after 0.3T exposure (Table 1-26)

Table 1-26: 3.8M HCl and 0.3T N80 steel corrosion (6 hours/$21.0 \pm 0.1\text{ }^{\circ}\text{C}$)						
Analyte	3.8M HCl control			3.8M HCl (4min/0.3T)		
Time (hours)	0	24	48	0	24	48
Gravimetric reduction (mg ± 0.1)	289.6	289.6	289.6	19.5	50	65.4
Corrosion (mg/cm2/60min)	1.73	1.73	1.73	0.119	0.3	0.48
Reduction (%)				93.47	83.56	73.73

Mechanism: Lorentz Force lowers H^{+} transfer kinetics

The overall findings of this research hypothesised that the Lorentz Force was the contributor to the shift in acidification of HCl solutions in static magnetic fields, and that this has significant benefits in the kinetics of crude oil and gas well acidic

retardation practices, but the parameters in the methodology require fine tuning in order to maximise the effects, with aspects such as the strength of the acid, magnetic field, and charged particle velocities all contributing to the maximisation of the Lorentz Force process.

1.5.4. Hydrated ions and magnetic field computer simulations

Molecular dynamic simulations were conducted by Bin, Hai-Bo and Feng (2011), focusing on sodium (Na^+), magnesium (Mg^{2+}) and calcium (Ca^{2+}) cations correlated with chloride anions, focusing on the Intermolecular interactions of the ions and H_2O , focusing on the Lorentz Force (insert equation) deduced from intermolecular Coulombic electrostatic charge stabilities and Lennard-Jones potentials, which are based on the foundation of near range inter-ionic, inter atomic synergistic repulsions, median range attractions, and distant range neutrality, with the densities programmed for $0.62 \text{ mol}^{-1}/\text{L}$, then derived calculations for pair correlation functions $g_{ij}(r)$, to determine the distribution function (g) feasibility of an atom/ion (j) at a distance (r) of another atom/ion (i) in the simulation, and the mean squared displacements (MSD) as the estimated evaluation of the speed and trajectories of H_2O molecules and ions under standard Brownian and magnetic field exposure conditions, to determine the respective diffusion coefficients (D).

Mechanism: The simulated magnetic field induced cation pairing

The extrapolated calculations revealed that the 0.2T field simulations weakened the interactions between H_2O and cations and increased cation contact pairing as a result, with the diffusion coefficients of Na^+ , Mg^{2+} and Ca^{2+} increasing and decreasing in the case of the Cl^- anions.

Iranian computer scientists Moosavi and Gholizadeh (2014) utilised molecular dynamic simulations with a series of solvents of varying chemical classes, acetone (ketone), acetonitrile (nitrogen), toluene (aromatic), and n-hexane (alkane) at ambient temperatures and pressures with and without the presence of a 1.1T static

magnetic field, utilising density functional theory to establish structural components such as bond lengths and angles and atomic charges.

The researchers focused on Lorentz Force parameters for their flux density \vec{B} modelling $\vec{F}_B = q(\vec{V} \times \vec{B})$ but modified the equation to incorporate their established calculations for self-diffusion @ 298.15K/1.01325 bar as follows:

$$\vec{a} = \vec{a}_c + \frac{q}{m} (\vec{V} \times \vec{B})$$

\vec{a}_c is the control simulation particle acceleration

q is the particle charge

\vec{V} is particle velocity vector

m is the magnetic force divided by the particle mass

The simulated homogenous static field of 1.1T was distributed across the “z” direction of the simulation cell, to mimic the real world perpendicular aspects of the induced Lorentz Force and then ran their simulations.

The respective control and field ζ axis radial distribution function solvent pair correlations and molecular mobility analysis drawn from the MSD experiments were calculated, and the conclusions illustrated that OH hydrogen bonding in the 1.1T field is strengthened along the ζ axis on the C₃H₆O molecule pairs, the CH bonds on the C₂H₃N pairs shifted ~30% downfield and the CH pair distributions are ~40% higher in the C₇H₈ comparisons. It should also be noted that the OH binding strength under the field exhibited a significantly higher response the nitrogen bonding specifics in the C₂H₃N simulations.

The respective control and 1.1T solvent densities and self-diffusion constants were calculated from the data as tabled below in **Table 1-27**:

Table 1-27: MDS solvent control vs solvent (1.1T) diffusion coefficient and density				
Solvent	Acetone	Acetonitrile	n-Hexane	Toluene
Control D (m^2s^{-1})	4.8152×10^{-9}	1.3557×10^{-8}	4.3846×10^{-9}	3.2118×10^{-10}
1.1T D (m^2s^{-1})	1.3800×10^{-12}	6.8676×10^{-12}	6.8878×10^{-11}	4.1267×10^{-13}
Change D (m^2s^{-1})	4.8138×10^{-9}	1.3557×10^{-8}	4.3157×10^{-9}	3.2076×10^{-10}
Control ρ (g cm^{-3})	0.6731	0.4366	0.5547	0.9382
1.1T ρ (g cm^{-3})	0.9102	0.8475	0.6657	1.0337
Change ρ (g cm^{-3})	+ 0.2731 (22%)	+ 0.4109 (48%)	+ 0.1110 (17%)	+ 0.0955 (9%)

Mechanism: Lorentz Force increases hydrogen bonding energy

The Lorentz Force modelling of a 1.1T static field across a z axis strengthen the hydrogen bonding of the respective solvents by increasing electrostatic attractions and van der Waals interactions due magnetic field induced shifts in the radial distribution functions of the solvents.

Keyword search: *water ion magnetic susceptibility, pascal's constants, Wiedemann's Law of Magnetic Additivity, magnetic field redox, magnetic field nucleation, PEMF ion morphology, magnetic field starch, magnetic field water proton transfer, magnetic field hydronium proton transfer, magnetic field HCl, magnetic field ion H₂O simulation, magnetic field ion H₂O hydrogen bonds, magnetic field solvent hydrogen bonds.*

1.6. Magnetic water devices: Quackery and critiques.

Introduction

As previously outlined throughout sub chapters 1.1.1. through to 1.5.3. of the literature review, there have been a wide variety of static magnetic, electromagnetic, and dynamic magnetic exposure configurations and time dependent design protocols implemented in the research fields, with a corresponding assortment of hypothetical conclusions with varying levels of conviction and cynicism. This section of the thesis provides a brief overview of the fundamentals applied to aqueous static and electromagnetic field device configurations, and a section focusing on rebuttals to many of the alleged claims arising from these devices.

1.6.1. Domestic magnetic water devices and absurd claims

A wide range of domestic permanent magnetic devices accompanied by exotic claims have appeared on the market such as the “Aquafer” device, which is stated to eliminate hard scale, reduce chemical costs, and improve horticultural growth performance by effecting(insert drum roll)..... “wetter water” (www.dimewaterinc.com, n.d.). The suppliers claim that the magnetic field induces dramatic increases in proton disassociation that impact on Ca^{2+} and HCO_3^- nucleation kinetics which shapes softer charge nullified aragonite CaCO_3 salts which are pass through plumbing systems much easier. The overall kinetics combines respective H_2O flow rates with configurations of neodymium magnets that generate an alternating magnetic field, which gives the assumption from the design image that they are arrayed in diametric configurations, and it is claimed that this design generates an electric field that can retain aragonite morphology for 72 hours under stagnant conditions (www.dimewaterinc.com, n.d.)

Another horticultural magnetic water treatment product is the “*Superimploder*” (www.breakthru-technologies.com, n.d.) which combines a unique vortex flow design with static magnetic field exposure to combat water particulates (see Figure 1-50).

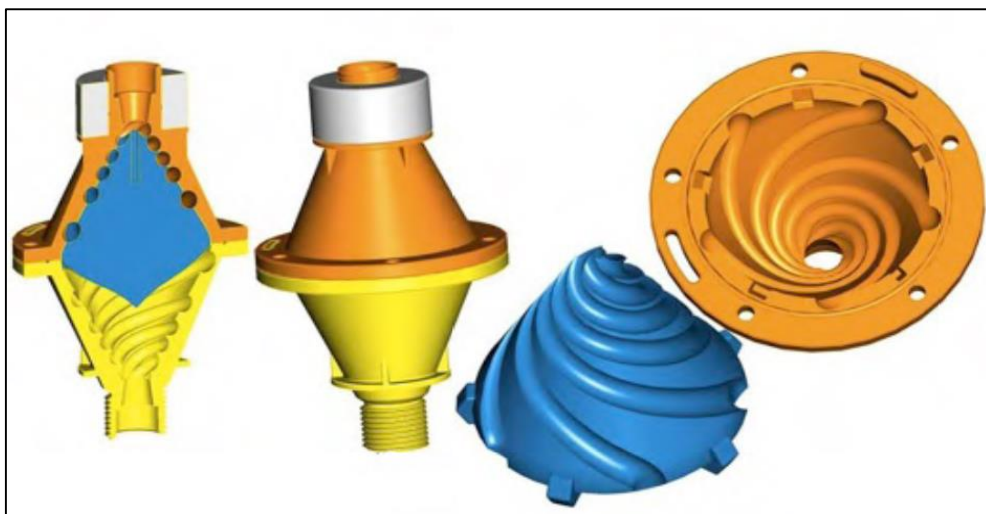


Figure 1-50: “Superimploder” vortex and magnetic water treatment device
www.breakthru-technologies.com, n.d.)

The Superimploder does indeed appear to be a magnificent wonder of scientific engineering. It consists of a “*fortron superplastic IMPLOSION NOZZLE*” (www.breakthru-technologies.com, n.d.) which is apparently designed on the premise of the multiplication of the Planck length ($l_p = 1.616225 \times 10^{-35} \text{m}$) by the Golden ratio ($\frac{1 + \sqrt{5}}{2}$) and this relationship’s correlation with the radii of hydrogen, which is claimed to be the reason for the hydrogen element’s existence (Author: *I am not making this up*). The device claims to incorporate “*phase conjugate dynamics*” (www.breakthru-technologies.com, n.d.) which apparently involves a hydrodynamic additive effect of quantum wave states, combined with “*phase conjugate magnetics*” (www.breakthru-technologies.com, n.d.), whereby the converging centripetal hydrodynamics facilitate increased molecular ordering and spin symmetry, resulting in “*independently validated*” (www.breakthru-technologies.com, n.d.) resulting in claims of up to 328% increases in plant growth, improved seed germination arising from the improved “*plasmic forces*” (www.breakthru-technologies.com, n.d.) of water

1.6.2. Critiques of magnetic field induced aqueous research

A scathing critique of these magnetic device applications was put forward by Robillard, Sharpe and Swistock (2001) stating comprehensively that “*There is*

virtually no valid scientific data to support any water treatment benefit from magnetic devices" (p.1, Robillard, Sharpe and Swistock, 2001), further adding that "*...permanent magnets have no effect on the hardness of water or the formation of scales on pipes*" (p.1, Robillard, Sharpe and Swistock, 2001), and concluding that "*... fraud plaintiffs throughout the United States are finding sympathetic courts as judgements against the sellers of electromagnetic treatment devices who use false product claims*" (p.2, 2001). The United States Water Quality Association (2001) assembled a "*magnetics task force*" (p.2, OC II, J.I.I. and OI, J., 2001) to investigate the published anecdotal evidence related to magnetic water treatment research spanning between 1952 and 2000, concluding that only 34 of 106 papers analysed met the task force scientific criteria protocols and of those 34 no consensus could be identified regarding the competency of MWT.

Timothy Keister (2008) delivered a scathing broadside at MWT device claims stating that "*exposure to electrical and/or magnetic fields has never been shown to affect the size of ions in solution*" (p.2, Keister, 2008), and with regard to CaCO₃ particulate claims that "*calcium and carbonate exist in water solution as dissolved ions, thus they are not in a particle form*" and "*..exposure of these ions to the low level magnetic, electrical or mechanical forces produced*" (p.2, Keister, 2008) as a result of exposure to non-chemical devices "*....will not alter their ionic state*" (p.2, Keister, 2008). Psychological research undertaken by Francis Beauvais in 2019 claimed that experimental claims of MWT memory effects in a biological setting were a result of psychological "*classical conditioning*" responses in researchers as "*experimenters straightaway expected a meaningful relationship*" (p.14, Beauvais, 2019)

Recent analysis undertaken by Andrianov and Orlov (2018) noting the lack of scientific consensus of the integrity or mechanisms related to CaCO₃ and MWT, incorporated a commercial industrial permanent magnetic device (Figure 1-51), consisting of a steel pipe housing cylindrical magnets in controlled experiments in a 180-litre circulating system consisting of a tap water over replicate exposure and control periods of 180 and 200 minutes. The devices recommended flow rate (0.9m³/60 mins) was selected in the methodology, and analytical monitoring for total salinity, calcium titration (EDTA), pH and alkalinity titration (HCl) were measured,

and the experimental outcome did “*not confirm the effect of magnetic treatment on calcium carbonate precipitate formation*” (p.1, Andrianov and Orlov, 2018).



Figure 1-51: MBC DN10 industrial static magnetic water treatment device
(Andrianov and Orlov, 2018)

The Lorentz Force with regard to MWT phenomena and static magnetic fields has been consistently invoked by scientists in the mechanism hypotheses of the research field, with Panczyk and Camp (2021) theorising that such claims were in contravention of the classical physics incorporated in Bohr-van Leeuwen theorem, which states that the mobility of charged particles at thermal equilibrium in a uniform magnetic field are independent of the effects of the magnetic field. The research focus investigated the rigor of Lorentz Force static magnetic field research claims by employing computer molecular dynamics simulation modelling with Na^+ ions in a H_2O environment under the influence of a 1T homogenous magnetic field.

The simulations were closely scrutinised for the static and dynamic aspects of Lorentz Force interactions with charged and partially charged species, and the outcome of the resulting data concluded that thermal and non-magnetic fluctuations at normal temperatures ranged up to “*eight orders of magnitude*” (p.9, Panczyk and Camp, 2021) higher respective kinetic contributions than the Lorentz Force in their modelling, concluding that the relatively minor residual variation of ion and H_2O kinetics could be explained by way of the models statistical fluctuation.

Keyword search: *Influence of magnetic fields aqueous calcium carbonate, magnetic water treatment scale, domestic magnetic water devices, electromagnetic fields, electromagnetic fields physics solenoid, pulsed electromagnetic field wave forms, , pulsed electromagnetic field sinusoidal wave forms, Dolphin 3000 pulsed*

electromagnetic, water treatment pulsed electromagnetic, magnetic water non-chemical devices, electromagnetic water memory, magnetic field water lorentz

1.7. Literature review summation

An extensive range of scientific literature has been outlined in sections 1.1.1. to 1.6.3. incorporating a wide variety of magnetic field applications with varying results and hypothetical conclusions, however the conspicuous conclusion drawn from the sum of these research projects is the variation in assigning major contributing factors and the lack of consensus in explaining identified phenomena, even with research of a similar nature. What consistent or differing roles do static and variable magnetic fields play in this research? What is the relevance of magnetic field strengths and oscillations? Are typical properties assigned to water, ionic and molecular hydration impacted by external magnetic fields outside of thermodynamic considerations?

It is with these questions in mind that discussions with this research team were undertaken to move away from the traditional magnetic field research areas focusing on ionic nucleation and their resulting morphology's, variables introduced by diverse aqueous solutes and their interrelationships, the complexities surrounding the cellular functions of living organisms, aqueous analyte flow rates, and magnetic field application variables. These deliberations arrived at investigating clock reactions as a good possible choice for magnetic field exposure research, noting that these are well researched and consistent experiments which could be employed to circumvent the complications arising from the aforementioned issues, and as excellent control and magnetic field exposure candidates of identical concentration and dilution in magnetically inert reaction vessels (borosilicate glass).

1.8. Clock reactions

Introduction

This research incorporates a variation of the clock reaction, as it's kinetic medium to investigate magnetic field exposures, which are now defined as classical series of

chemical experiments in reaction kinetics. The first reported finding of this classification of reactions is afforded to Hans Heinrich Landolt, whose historical importance is best summed up by Witts (1911), who recounted Landolt's obituary as follows, “*On the 15th of March 1910, died one of the oldest members of the present generation of chemists, the patriarch of physical chemistry, Hans Heinrich Landolt*” (p.1653, Witts, 1911). Landolt stumbled across what has become a cornerstone in chemistry kinetics education and research, the “*Landolt reaction*” (Landolt, 1886) whilst experimenting with a variety of concentrations and configurations of I₂, SO₂ and SO₃ based aqueous reagents, that progressed to interactions with iodic acid (HIO₃) and sulfurous acid (H₂SO₃) mixtures. During his progress with HIO₃ and H₂SO₃, he treated the reagents with additional starch, and observed that a “*striking phenomenon occurs*”, whereby the reaction was “*initially completely clear and....after the lapse of a certain time....became suddenly deep blue*”. His further experimental manipulations identified that these reactions could “*easily be determined by means of the clock*”, dependent upon the relationship between the “*relative weights of the two substances*”, the aqueous “*concentration of mixture*” and temperature, “*the rise of which accelerates the process*”, which all combined to determine the “*certainty with which the passage of time the reaction can be determined*” (pp. 1317-1365, Landolt, 1886, as translated by McNaughton, 1/2/2022)

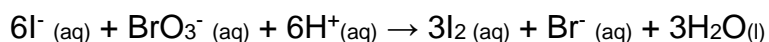
Ruekberg (2020) claims that the catalogue of clock reactions has grown significantly since Landolt’s discovery, with a range of differing chemical compositions incorporated in a variety of mechanisms, however the utilisation of the starch-iodine blue complexation is still considered the traditional “*skeleton mechanism*” (p.1688, Ruekberg, 2020) whereby iodides in the presence of an oxidiser form into iodine species, that are again converted back to iodides in the presence of a limiting reducing agent, until it becomes exhausted, the iodide forms iodine and polyiodide species and “*the iodine combines with starch to form a blue complex, the alarm, if you will, in the iodine-clock reactions*” (p.1688, Ruekberg, 2020).

1.8.1. The bromate-iodide clock reaction

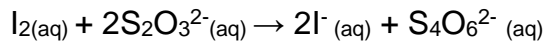
The scientific literature has presented varying hypotheses explaining the complicated mechanistic dynamics of the bromate-iodide clock reactions. Simoyi, Masvikeni, and Sikosana (1986) presented a 22 step reaction mechanism commencing with the nucleophilic attack by iodide ions on protonated bromate ions in aqueous solution, and then a complicated series of transitory hydrolysis and redox reactions take place. Chinake and Simoyi (1996) later presented a 17 step mechanism incorporating 6 reversible reaction steps, which was later opposed by Machado and Faria (2009), who identified a 22 step mechanism incorporating 6 reversible reaction steps accounting for oxohalogen species in aqueous clock reactions. Whilst the underlying complexities of transitory species generated and their relative rate constants are hotly debated, the core mechanisms involved in the redox reactions when incorporating sodium thiosulfate and iodide-starch complexation, are in general agreement, and are presented as the following example:

Solution A: aqueous sodium thiosulfate (excess), sodium thiosulfate and starch
Solution B: aqueous sodium bromate, hydrochloric acid (slight excess)

Reaction 1) Clear solutions A and B are blended, then Iodide ions in the presence of acidic bromate ions undergo oxidation to Iodine species in the slow step of the reaction:

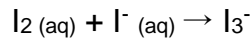


Reaction 2) The Iodine species undergo reduction by thiosulfate ions in the fast step of the reaction and the oxidised thiosulfate is consumed forming tetrathionate ions:



The redox cycle continues until the thiosulfate limiting reagent is consumed.

Reaction 3: The Iodine product of reaction 1 now binds with excess Iodide, forming triiodide ions:



Reaction 4: The triiodide species form a charge inclusion complex in the helical hydrophobic cavity of amylose, amylopectin's or α -cyclodextrins:

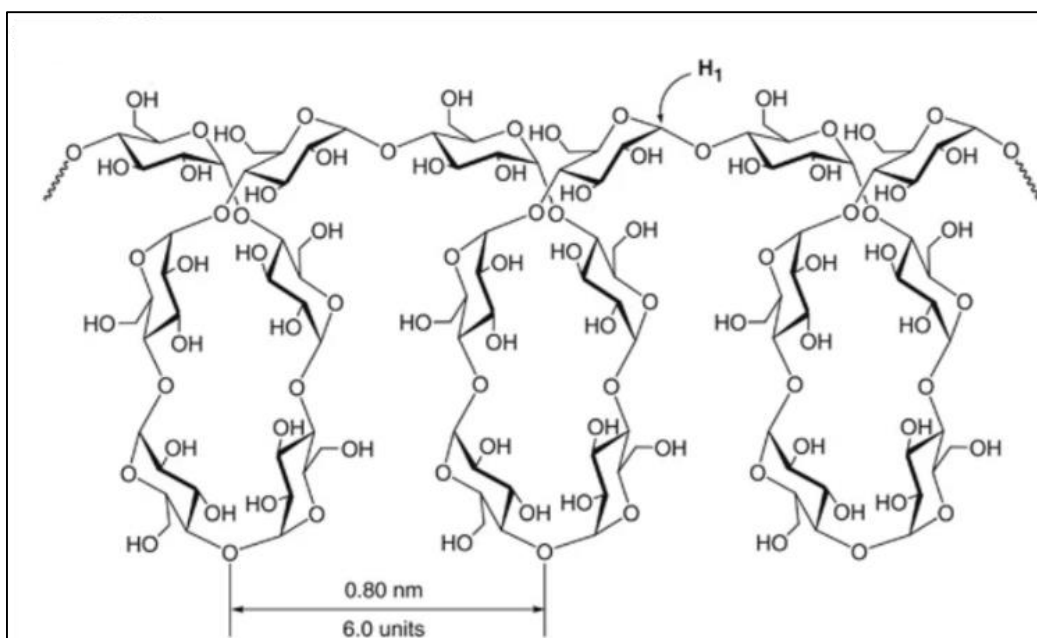


Figure 1-52: hydrated α -amylose helix molecular configuration (Nomura et al., 2011).

1.8.2. Properties of bromate-iodide reaction chemicals and ions

The reaction rate of these clock experiments are ultimately dependent upon relative concentrations, reaction temperature or the presence of a catalyst, and reliable mathematical models can be utilised to determine how these various factors encompassed in a chemical reaction. Information pertaining to the molecular and ionic components of this reaction is outlined for reference purposes in Tables 1-28 and 1-29.

Table 1-28: Bromate-iodide clock reaction chemical properties

Chemical	MW (g)	M.P. (°C)	H ₂ O Solubility (g/100mL/25 °C)	pH (25°C)	Magnetic susceptibility ($\chi \times 10^{-6} \text{ cm}^3 \text{ mol}^{-1}$)
Nal	149.89*	651*	184#	8-9.5*	- 57.0*
NaBrO ₃	150.89*	381*	39.4#	7.0#	- 44.2*
Na ₂ S ₂ O ₃ •5H ₂ O	248.19*	48*	20.9#	~7.0*	-
HCl	36.46*	NA	100%*	~0.1*	- 22.0*
(C ₆ H ₁₀ O ₅) _n	polymer	257 ^Δ	Nil ▲	5-7	- 44.2*
H ₂ O	18.02	0.00*	NA	7.0*	- 12.96▼
			▲ (C ₆ H ₁₀ O ₅) _n = 5g/100mL H ₂ O @90.0°C		

N.C.B.I., 2022, * Merck Index, 14th ed., 2006, ▲ Chem Supply SA083

* Landolt-Bornstein, n.d., ▼ Bain and Berry, 2008

Table 1-29: Bromate-iodide clock reaction ionic properties

Ion	Mass (Da)	Free Bonds	H donors	H acceptors	Polar area (Å ²)	χ_d ($\chi = 10^{-6} \text{ cm}^3 \text{ mol}^{-1}$)
Na ⁺	22.989#	0#	0#	0#	0#	- 6.8▼
H ₃ O ⁺	19.023#	0#	1#	0#	1#	-
Cl ⁻	35.453#	0#	0#	1#	0#	- 23.4▼
I ⁻	130.906#	0#	0#	1#	0#	- 50.6▼
I ₃ ⁻	380.713#	0#	0#	1#	0#	-
BrO ₃ ⁻	128.913#	0#	0#	3#	57#	- 40.0▼
S ₂ O ₃ ²⁻	112.129#	0#	0#	4#	104#	- 46.0▼
S ₄ O ₆ ²⁻	224.300#	3#	0#	6#	182#	-

N.C.B.I., 2022, ▼ Bain and Berry, 2008

1.8.3. Starch, amylose, and amylopectin

The works of Kearsley and Dziedzic (1995) along with Wu, Witt and Gilbert (2013) combine to inform that the hydrolytic cleavage of amylose forms chain intermediates, known as amylodextrins, thereby increasing reducing power relative to cleavage intervals as the number of aldehyde groups at the C1 cleavage sites are exposed, further noting that these shorter chains can still form triiodide complexes in the UV range until chains below 40 glucose polymer monomer assemblies emerge.

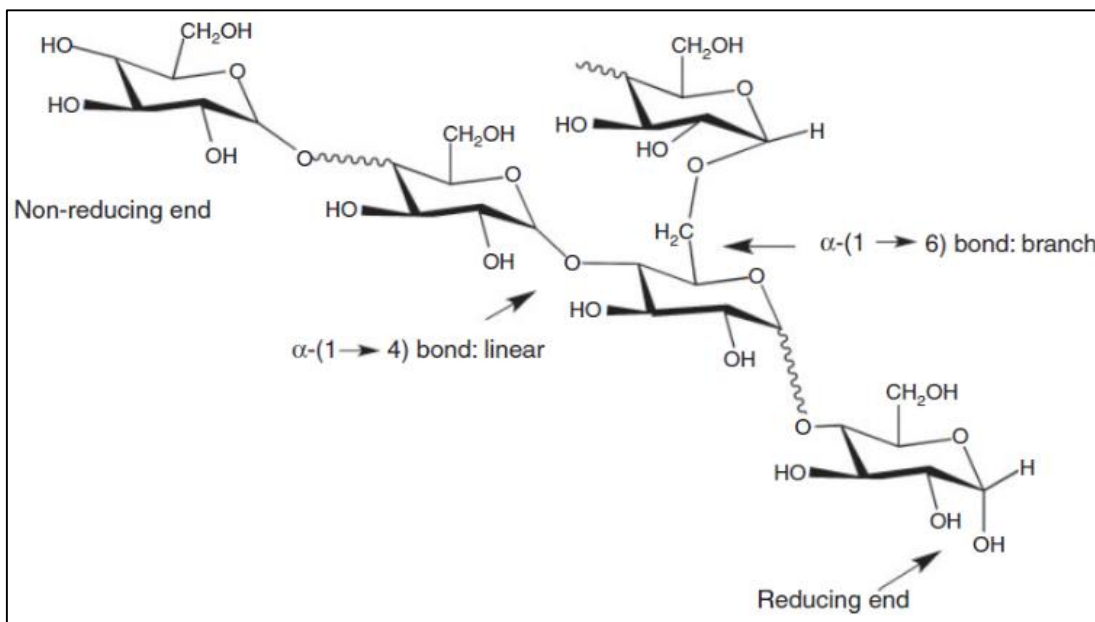


Figure 1-53: Linear (α 1→4) and branched (α 1→6) starch molecule (Wu, Witt and Gilbert, 2013)

The findings of Lee, Han and Lim (2009) are of interest, after they scrutinised the molecular configurations of Maize starches containing differing amylose and amylopectin ratios exposed to varying hydrolysis conditions between pH 5.0 and 10.0. This methodology employed size exclusion chromatography incorporating laser scattering and refractive index detection analysis, and identified that regardless of pH, the amylopectin generally retained a spherical geometry of unmodified chains throughout the pH range. Conversely, the specific volumes of amylose unit mass increased as pH scaled up from 5.0 to 10.0 with these researchers concluding that alkali could be a deprotonating agent that lowers chain associations, notably beyond pH 9.0.

According to Wang et al. (2017), a process known as retrogradation occurs when starch amylose and amylopectin are heated then slowly cooled, which alters the molecular structures. Furthermore, it is reported that amylose chains are typically single random or helical coiled configurations in amorphous solid starch granules which are dispersed in heated H₂O and form hydrogen bonded double helical arrangements between 40 to 70 glucose monomers in chain length upon cooling, and according to Wang (2020), the retrogradation of amylose “gradually loses its

ability to form a blue complex with iodine if double-helical associations occur between amylose chains on retrogradation” (p.97, Wang, 2020).

A further journey through the research literature of Qiao et al. (2016) and Chi et al, (2022) discloses that a Maize starch of similar amylose/amyllopectin ratio (23:77) to that typically associated with potato starch, was subjected to dilute alkaline solution hydrolysis (0.1% w/v), and analysis identified that the resulting starch hydrolytes exhibited a reduction in the alignment of double helices due to alkali ions penetrating and affecting inter helical H₂O hydrogen bonding network, leading to helical disassociation, which facilitated greater rates of amylose cleavage at higher populations of exposed chain sites. Computer simulations undertaken Immel and Lichtenthaler (2000) stating that the single helical structures have significantly elevated hydrophobicity in the helical cavity due to the higher consistency in glycosidic oxygen and methylene group distribution, and external hydrophilicity due to the distribution of glucosyl hydroxyl arrangements, which favours polyiodide inclusion complexation. Conversely, the double helix amylose arrangements are reportedly incapable of forming inclusion complexes and are less kinetically favorable due to the increased time required for helical disassociation to facilitate complexation (see Figure 1-54).

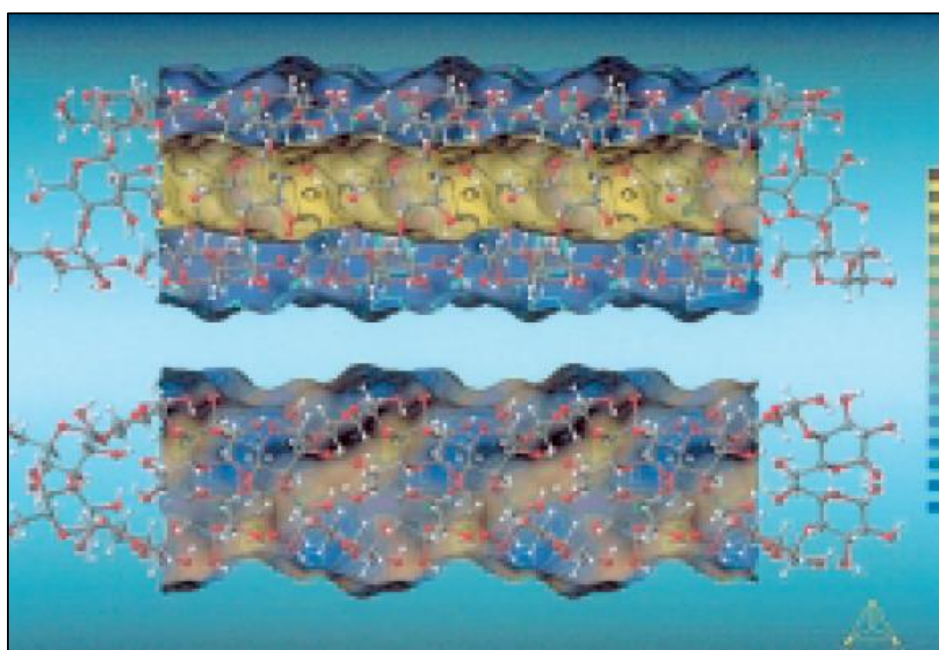


Figure 1-54: H₂O single (top) and double (bottom) helical amylose with respective hydrophilic (blue) and hydrophobic (yellow) intensities (Immel and Lichtenthaler, 2000)

Comments on sub chapter 1.8.

The bromate-iodide clock reaction can be utilised as a suitable candidate for investigating whether magnetic field exposures impact reaction kinetics with regard to the initiation of starch-triiodide complexation and the rate of reaction completion, providing consistent reactant concentrations, reaction dilution ratios and reaction temperatures were utilised in experimental and control analysis in order to specifically isolate the impact that magnetic fields may convey to the respective ionic and molecular components and their aqueous hydration characteristics.

It was now essential to investigate a proper analytical method to determine reaction kinetics relative to starch-iodide colour complexation emergence and reaction completion, by further scrutinizing an obvious and well researched candidate for precision colour absorbance analysis, UV-Vis spectrophotometry.

Keyword search: *Hans Heinrich Landolt, bromate iodine clock reaction, Iodine clock mechanism examination, starch hydrolysis, starch materials perspectives, amylose inclusion complexes, pH aqueous starches, Starch retrogradation, starch structure functionality food, amylose starch structure alkali, starch structure alkali temperature, amylose blue iodine complex*

1.9. UV-Vis Spectrophotometry

Introduction

Akash and Rehman (2020) extensively report that the kinetics of chemical reactions utilising UV-Vis spectrophotometry has been utilised to reliably measure temperature effects, velocity constants, reaction orders, concentration, and solvent effects for many decades. This method is advantageous due to low chemical consumption, the speed of analysis and the ease of the chemist-instrumental interaction.

1.9.1. UV-Vis Spectrophotometry and temperature

Yarborough, Haskin and Lambdin (1954) were early pioneers of UV-Vis spectrophotometry kinetic applications who set out to investigate the impacts of temperature in UV absorbance with regard to the integrity of research methodology after citing concerns in the literature pertaining to aromatics, dyes and retinoids, dating back to 1932. One series of experiments incorporated several solvents in combination with methanol and iso-octane in temperatures ranging between 5°C to 33°C in increasing increments of 2°C, to afford 15 independent temperature ranges.

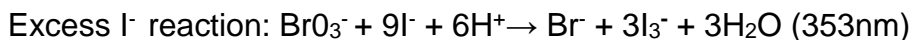
The outcome of this work identified that in general absorbance decreased linearly with temperature increase, and that temperature was a “*significant factor for certain aromatic hydrocarbons and some chelated aliphatic oxygenated compounds*” (p.1578, Yarborough, Haskin and Lambdin, 1954), with regard to absorbance integrity (see Table 1-30).

Table 1-30: Temperature impact on solvent UV Constants (5 - 33°C)				
	(M μ) @ 25.0°C		Constant Shift (\pm)(ϵ per 1°C)	
Diluent	Analyte	Analyte	Analyte	Analyte
	Methanol	Iso-octane	Methanol	Iso-octane
Benzene	254.4	254.8	0.0062	0.0062
Toluene	268.8	268.8	0.0086	0.0085
Aniline	284.0	287.0	0.0020	-
Acetone	274.0	270.0	0.0004	0.0009
Pyridine	257.0	256.0	0.0027	0.0014

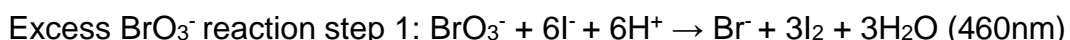
1.9.2. UV-Vis Spectrophotometry polyiodide and iodine analysis

Simoyi, Masvikeni and Sikosana (1986) undertook an extensive kinetics analysis incorporating UV-Vis spectroscopy with a variety of iodide and bromate stoichiometries, and identified that the observations of Randall (1910) and the

reaction mechanism was indeed correct when excess iodide was in the reaction, resulting in the generation of triiodide products identified at 353nm:



However, their research identified, that when an excess of bromate was present the stoichiometry of the reaction differed and iodine now replaced iodide as the product when analysing the kinetics of the isosbestic wavelength for I_2/I_3^- at 460nm, and applying the Randall mechanism:



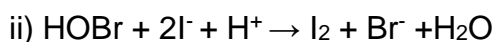
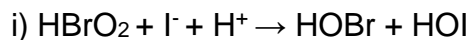
These researchers then monitored the spectra for bromine in the excess bromate reactions and further determined the kinetic stoichiometric relationship:



Further investigation of the kinetic reaction calculations confirmed a significant finding that step 2 of the excess bromate reaction could not commence until all of the iodide ions in the step 1 reaction had been exhausted, thereby confirming an oscillatory nature in this stoichiometric experiment. This team further concluded with a controversial claim of a different reaction mechanism:

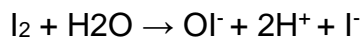


Or



The spectroscopic designation of the hypoiodite ion (OI^-) drew attention from others in the field, with Fonslick, Khan and Weiner (1989) undertaking the search for the elusive reaction mechanism by incorporating starch with iodine and potassium iodide

solutions and scanning the UV-Vis range between 190 to 740nm. They reported three peaks arising from aqueous iodine, triiodide and starch analytes, at 205nm (strongest ϵ), 285nm (middle ϵ), and 355nm (weakest ϵ), in an 8:2:1 ratio, noting that Moknach and Rusakova identified an increasing band at 355nm during UV-Vis analysis of the starch titration of I₂ analytes, which they had hypothesised to OI⁻ generation, and assigned 355nm accordingly, and that Drey in 1964 had further hypothesised the inclusion complex threshold by the following mechanism:



The research trio then proceeded investigating the reaction with other solvents characterised by oxygen molecules, acetone, ethanol, and isopropanol, which identified the three identical peaks observed in H₂O solvent experiments, but with a decreased intensity at the major 205nm peak. They then applied INDO CI calculations in their search for the OI⁻ species, an aspect of computer generated modelling utilised in the infancy of computational chemistry, concluding firstly that it was improbable that the band at 355nm was a result of OI⁻ ions in the reactions at neutral pH would exist as HOI species and calculated that only 0.02% of the free ions could be present, which would not explain the considerably abundant peak at 355nm, and that the observance of the 355nm peak, which gave the ϵ maximum in acetone solvent, as it would require a double carbocation mechanism to break of the carbon oxygen double bond to form OI⁻, and dismissed the existence of the species in this reaction, further adding that the peak at “*355 nm in the aqueous solution of iodine is not due to OI⁻ ions*” (p.3838, Fonslick, Khan and Weiner, 1989).

The researchers then set out to conduct computer simulations focusing on I₂ and various solvents, musing that the phenomena identified with iodine and solvents exhibiting oxygen molecules at 355nm could be the result of iodine polarisation, resulting in iodine complexes with oxygen present on the starch molecule. They configured an I₂-H₂O “axial” model to support their polarisation theory, calculating an I₂ charge shift of +0.1 at the O-I intercept and an increased negative charge of -0.4 at the distal iodine molecule, an increased H-O-H bond angle (108.5°), with an increase in the negative charge on the O molecule (-0.4) and an increase of +0.3 in the hydrogen atoms, with complementary absorbance maxima calculations at 181nm,

277nm and 365nm, noting that the 277nm and 365nm wavelengths fitted well to the experimental values of 285nm and 355nm, and also calculated at a 2:1 ϵ ratio.

Pursell and Pursell (2016) undertook rigorous analysis of the kinetics underlying the α -cyclodextrin and the triiodide inclusion mechanism by utilising varying concentrations of aqueous iodine and potassium iodide to induce triiodide species ($I_2 + I^- \rightleftharpoons I_3^-$) which were then titrated with aqueous α -cyclodextrin (α -CD) solutions and analysed via UV-Vis kinetic protocols.

Temperature control was rigorously maintained throughout the experiments ($\pm 0.2^\circ\text{C}$), and initial wavelength peaks for concentrations of were identified at 352nm for I_3^- ($20\mu\text{M } I_2 + 20\text{mM } I^-$), and 459nm for I_2 ($800\mu\text{M } I_2 + 50\text{mM } \text{HIO}_3$). The baseline measurement for $8\mu\text{M } I_2 \text{ H}_2\text{O} + 800\mu\text{M } I^- \text{ H}_2\text{O} = 3\mu\text{M } I_3^-$ for 38% conversion, and after the addition of $10\mu\text{M } \alpha\text{-CD}$ they noted that I_3^- absorbance had increased significantly and that the I_2 in the 450-550nm range had shifted considerably in to the I_3^- range (see Figure 1-56, dashed lines), concluding that as α -CD was introduced, it formed the $\alpha\text{-CD}\cdot I_3^-$ complex and kinetically shifts the reaction to further increase I_3^- ions in the solution.

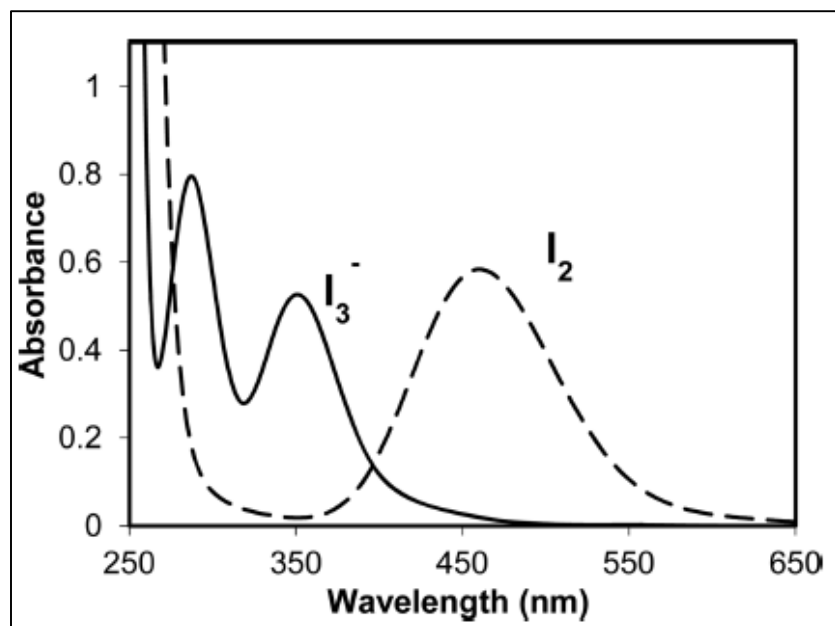
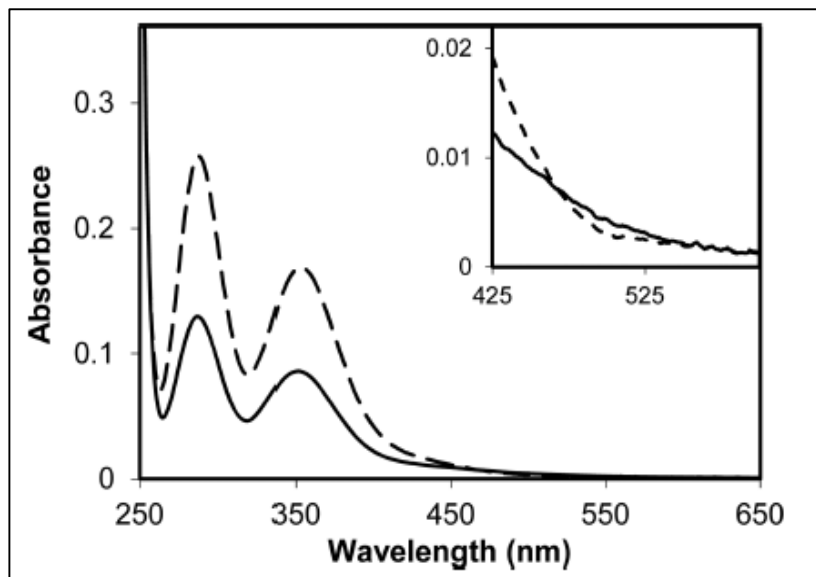
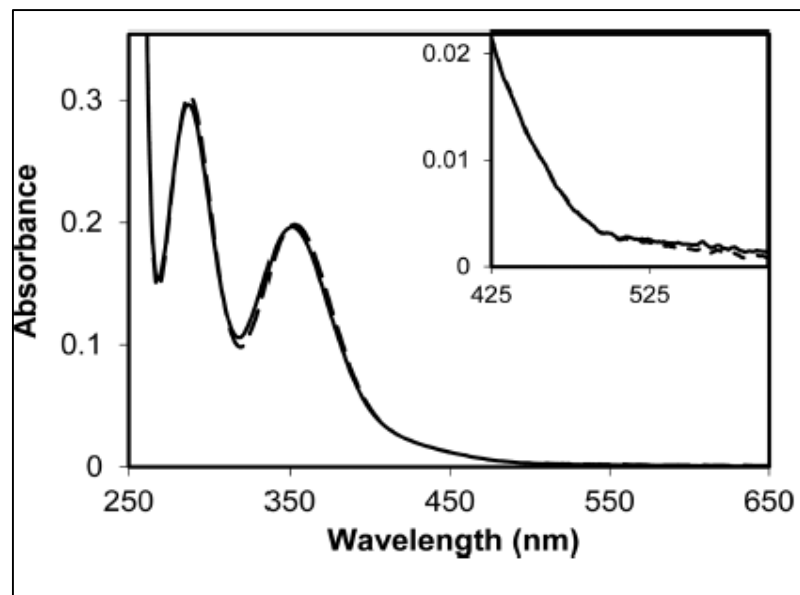


Figure 1-55: (left) UV-Vis absorbance for I_2 (459nm) and I_3^- (288 and 352nm)
(Pursell and Pursell, 2016)



**Figure 1-56: $\text{KI} + \text{I}_2 + \alpha\text{-CD} \rightarrow \text{I}_3^-$ (288 and 352nm) increase, and I_2 (459nm) decrease shift
(Pursell and Pursell, 2016)**

The research team then undertook experiments to push all of the I_2 present in the reaction to I_3^- species by increasing the ratio of from $\text{I}^- \times 100$ to $\text{I}^- \times 1000$, ($8\mu\text{M}$ I_2 $\text{H}_2\text{O} + 8\text{ mM I}^- \text{ H}_2\text{O}$) with $10\mu\text{M}$ $\alpha\text{-CD}$, and the resulting spectra identified an 86% conversion of I_2 to I_3^- (see Figure 1-56)



**Figure 1-57: UV-Vis absorbance $\alpha\text{-CD}\text{I}_3^-$ complex and I_3^- (288 and 352nm)
(Pursell and Pursell, 2016)**

The analysis of 1:1 stoichiometric experiments were then undertaken in order to identify respective I_2 , I^- and I_3^- kinetics, starting with reaction 1 $[I_3^-] K_{eq}[I_2]^2$ and inputs from the I_2 ($50\mu M$) and I^- ($50\mu M$) spectrophotometry measurements incorporating $5-50\mu M$ concentrations of α -CD titrant (see Figure 1-58). It was noted that dependable kinetic behaviour was exhibited at the isosbestic point and the calculated stoichiometric binding constant for α -CD• I_3^- as: $K_{eq} = 1.35 (\pm 0.005) \times 10^5 M^{-1}$ (room temperature), concluding that the molar absorption of isolated aqueous I_3^- and the aqueous α -CD• I_3^- complex were **virtually identical!**

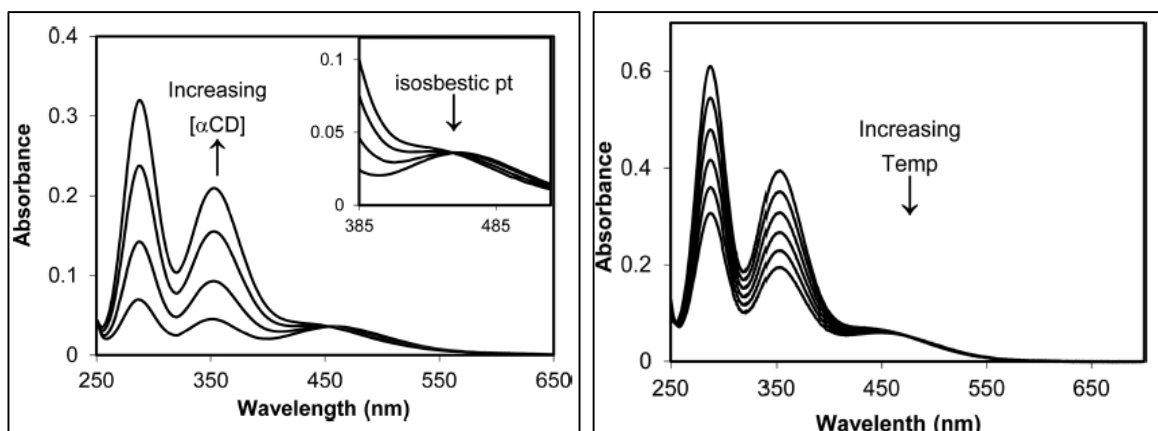


Figure 1-58 (left): UV-Vis absorbance α -CD• I_3^- complex stoichiometric analysis

**Figure 1-59 (right): UV-Vis absorbance α -CD• I_3^- complex temperature analysis
(Pursell and Pursell, 2016)**

Complimentary analyses and calculations determined the following α -CD binding constants for the three species at room temperature, which basically ruled out α -CD + I_2 and/or I^- involvement in the absorbance complexation spectra:

$$\alpha\text{-CD}\cdot I^- = 19 M^{-1}$$

$$\alpha\text{-CD}\cdot I_2 = 5.93 \pm 1.00 \times 10^3 M^{-1}$$

$$\alpha\text{-CD}\cdot I_3^- = 1.35 \times 10^5 M^{-1}$$

This excellent research concluded with a series of stoichiometric reactions ($50\mu M I_2 + 50\mu M I^- + 20\mu M \alpha$ -CD) at six temperatures between 15 to $40^\circ C$ and decreasing absorbance with increasing temperature (see Figure 1-59) calculating that the kinetics of the α -CD• I_3^- complex was also temperature dependent ($\Delta H = -31.0 \pm 0.9$ kJ/mol), concluding that they had “conclusively demonstrated” (p.2148, Pursell and

Pursell, 2016) that the increase of UV absorbance was not related to the generation of the α -CD·I₃⁻ complex under titration conditions, but was arose from the “*increased conversion of iodine to triiodide with added α -CD*”, and that the “*equilibrium binding constant is temperature dependent*” (p.2148, Pursell and Pursell, 2016).

Kireev and Shnyrev (2015) embarked on a UV-Vis spectrophotometric investigation pertaining to I₂, IO₃⁻, I⁻ and I₃⁻ species incorporating a variety of aqueous compositions with regard to incorporating UV-Vis spectrophotometry in the detection of radioactive iodine isotopes at nuclear fuel facilities. The iodine, iodate, iodide, and triiodide analytes were drawn from varying concentrations of aqueous I₂, KHO₃, KI, and I₂ + KI solutions respectively, then scanned between 180nm to 600nm (@+5nm), resulting in the data set out in Table 1-31.

Table 1-31: Iodine species UV-Vis (180-600nm) maximum absorbance spectra

Analyte	Major peak (nm)	ϵ (cm ² /mol)	Peak (nm)	ϵ (cm ² /mol)	Peak (nm)	ϵ (cm ² /mol)
IO ₃	Nil	Nil	180	2.91 x 10 ⁻¹⁷	240	2.16 x 10 ⁻¹⁸
I ⁻	< 180	1.40 x 10 ⁻¹⁶	226	5.04 x 10 ⁻¹⁷		
I ₂	203	7.80 x 10 ⁻¹⁷	461	2.91 x 10 ⁻¹⁸		
I ₃ ⁻	288	3.25 x 10 ⁻¹⁷	352	2.08 x 10 ⁻¹⁷		

The conclusions in this research stated the iodate spectra decreased linearly from 180nm over the scanning range, noting that the absorbance coefficient for 240nm had decreased by almost one order of magnitude, the iodide analysis detected a major absorption band below 180nm which sloped downward to bottom out at 210nm (1.47×10^{-17}), then exhibited a sharp second peak at 226nm which slowed sharply away again at 245 nm (6.77×10^{-18}). The iodine peak wavelength kinetics exhibited a sharp rise from the scanning baseline of 180nm (3.14×10^{-17}) to the major peak at 203nm (7.80×10^{-17}) which linearly declined at 225nm (2.55×10^{-17}), then exhibited a second peak at 461nm which was 30 times lower than the major peak, noting that I₂ bands have been cited in the literature above the experimental cut off range 600nm. The triiodide analysis noted that there was no absorbance of statistical value in the 180 to 240nm range (240nm = 9.32×10^{-20}), the major peak registering at 288nm (3.25×10^{-17}), sloping to 320nm (1.08×10^{-17}), then registering

a second peak at 352nm, which was consistent with the scientific literature. This study established that UV-Vis spectrophotometry in combination with the incorporation of laser emission pre-treatment could be utilised successfully in the online detection of iodine species in nuclear fuel analysis.

1.9.3. UV-Vis Spectrophotometry and iodide starch complexation

The incorporation of UV-Vis analysis with amylose and amylopectin starch arrangements has identified various affinities of differing complex formation, peak wavelengths and absorption profiles, according to Cole, Eggleston and Triplett (2017), who further noted that aqueous iodine affinity between amylose and amylopectin is 20:1 respectively, the isolated amylose-iodine peak absorbance range is between 605 to 650nm, and the isolated amylopectin-iodide peak absorbance exhibits a significant shift to the 540 to 560nm range (Tables 1-31 and 1-32)

Table 1-32: Various reported starch + I₂ H₂O UV-Vis absorbance (λ_{\max})		
λ_{\max} (nm)	Starch + I₂ H₂O complex	Research source
Vegetable starch sources		
510	Corn	Sakac et al., 2020
600	Corn	Cole et al., 2017
590	Rice	Sakac et al., 2020
632	Wheat	Sakac et al., 2020
632	Barley	Sakac et al., 2020
571	Potato	Sakac et al., 2020
600	Potato (Sasta 7.8)	Cole et al., 2017
600	Potato (Sasta 7.9)	Cole et al., 2017
600	Potato (GSI-17)	Cole et al., 2017
622	Potato	Moulay, 2013
700	Potato (C.S.R.)	Cole et al., 2017
700	Potato (GSI-16)	Cole et al., 2017

Table 1-33: Various reported starch + I₂ H₂O UV-Vis absorbance (λ_{\max})

λ_{\max} (nm)	Starch + I ₂ H ₂ O complex	Research source
Starch, amylose, amylopectin and α-cyclodextrin		
540	Amylopectin	Makhayeva et al., 2020
560	Amylopectin	Cole et al., 2017
625	Amylose (potato)	Horton, 1999
650	Amylose	Makhayeva et al., 2020
618	21% amylose, 79% amylopectin (potato)	Ayun et al., 2015
570	Starch	Raghu et al., 2018
615	Starch	Fonslick et al. 1989
615	Starch	Sulistyarti et al, 2015
694	Starch	Morley and Knurr, 2021
585	Starch	Garcia-Arrona et al, 2017
460-740	Starch	Yu et al., 1996
459	α -cyclodextrin	Pursell and Pursell, 2016

1.9.4. UV-Vis Spectrophotometry and bromate analysis

Bottled and communal drinking water supplies routinely incorporate chemicals and ozonolysis in their disinfection practices, and a major drawback of these protocols is the generation of bromate species from bromine present in water, particularly relating to ozone treatments, with the bromate ingestion associated to significant gastrointestinal illnesses, identified in upregulated renal and thyroid follicular tumorigenesis in rats and is recognised worldwide as a potential human carcinogen, as extensively outlined by Michalski and Łyko (2013). Major health regulatory bodies all over the world have set permissible bromate levels for drinking water below 10 μ g/L, with European authorities reducing the allowable maximum to 3 μ g/L for ozonolysis disinfection of bottled waters, which are standards that are still maintained in the present time.

The European Commission, Directorate General Joint Research Centre, Institute for Reference Materials and Measurements, undertook the International Evaluation Measurement Programme headed up by a panel of representatives Cordeiro et al.,

(2011) aimed at the analytical detection methods of bromate in water with the collaboration of 16 independent laboratories, who received aqueous analytes of treated and untreated drinking water, swimming pools samples and covertly spiked aqueous analytes with 10µg/L of bromate, in order to assist in the determination of the upcoming draft for the ISO/DIS 11206 standard analytical protocols, and concluded from the results incorporating various methodologies that the UV-Vis detection of triiodide at 352nm incorporating ion chromatography and acidic potassium iodide post derivatization analysis provided the best quantitative statistical assessment of the methods employed, citing RSD's of 3 to 6% that were significantly below the analytical baseline for detection. Michalski and Łyko (2013) later commented that the UV-Vis ion chromatography analysis for bromate detection was “*the most important method of bromate determination*” (p.101, Michalski and Łyko, 2013) with the international Standardisation Organisation (ISO), , The U.S.E.P.A. and the American Society for Testing and Materials (ASTM), incorporating this method in their regulatory analytical protocols, further commenting that the incorporation of Ion chromatography and UV-Vis triiodide (352nm) detection for bromate had contributed the best instrumental limit of detection (0.05µg/dm³).

Keyword search: *Essentials of pharmaceutical analysis, UV-Vis spectroscopy temperature, UV-Vis spectroscopy bromate-iodine, UV-Vis spectroscopy inclusion complexation triiodide, UV-Vis spectroscopy aqueous hypoiodite, UV-Vis spectroscopy iodine iodide triiodide, UV-Vis analytical evaluation starch, UV-Vis bromate analysis iodide, bromate drinking water analysis*

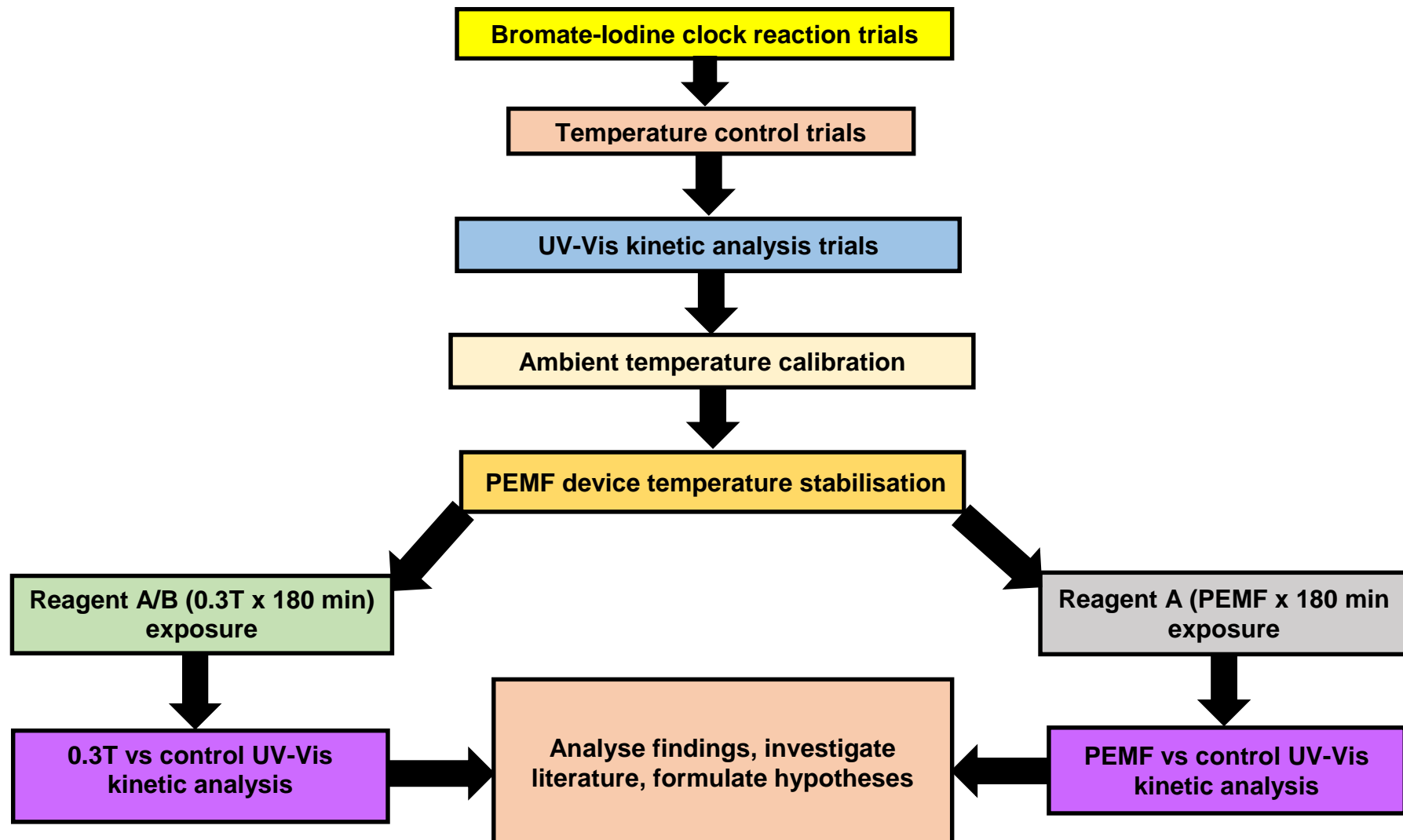
1.10. Research design and method modelling

The literature encompassing clock reactions and UV-Vis research pertaining to iodine, iodide, bromate and iodide-starch analysis encouraged a feasible pathway to research magnetic fields and reaction kinetics for experimental model trials and data analysis, however, close attention had to be afforded to consistency and precision pertaining to concentration, dilution, and temperature impacts with control and experimental replication. The thesis research facility had a Shimadzu UV-1900 spectrophotometer present, a pulsed electromagnetic water treatment device that

was utilised in prior published research, and a rare earth 0.3T cylindrical rod magnet that could be employed in static and dynamic magnetic field experiments with various bromate-iodide clock reaction reactant solutions, then clock reactions conducted under otherwise consistent replicant exposure and control protocols via UV-Vis kinetic analysis could be undertaken to identify reaction rate factors.

Significant work had to now be undertaken to devise reasonable reaction parameters, facilitating consistency in control and experimental replicant temperature consistency, magnetic exposure design, the suitability of UV-Vis spectrophotometer absorbance precision, kinetic software sensitivity and incremental outputs, as well as monitoring ambient temperature precision and correlation with real time UV-Vis analysis. Substantial work also had to be undertaken in order to mitigate temperature increase in a pulsed electromagnetic field device in order to neutralize any impact that temperature might play in influencing the modification of exposure analyte hydration characteristics in comparison to control replicates.

Chapter 2: Experimental Design and methodology



Chapter 2: Experimental Design and method trials

2.1. The development of the clock reaction methodology

2.1.1. Reactant compositions, concentrations, dilutions, and initial ambient temperature reaction time trials.

A series of initial bromate-iodine reaction precursor combinations, concentrations and dilutions were undertaken, under both static and mixing conditions, to identify agreeable reaction initiation and completion parameters under typical laboratory ambient conditions. The static and mixing conditions at the chosen concentration ratios and reaction dilutions exhibited little difference in the timing for starch-iodide complex emergence and reaction completion, so mixing was precluded from further experiments. The chemicals employed for these experiments are outlined as follows:

Chemicals

Sigma-Aldrich reagent plus Sodium Iodide ≥ 99% 100g

Sigma-Aldrich RT Sodium Bromate ≥ 99.5% 250g

Merck "Suprapur" Sodium Thiosulfate Pentahydrate (99.999% purity) 100g

Sigma-Aldrich Supelco "titripur" 0.1M Hydrochloric acid 1L

Chem Supply SA083-500 AR Starch (soluble) 500g

Milli Q water (Footscray Park campus)

A suitable combination of individual chemical concentrations and overall reaction dilution was identified, affording an approximate redox reaction time of 60-70 seconds prior to the commencement of the triiodide-starch complexation, and a further 80-90 seconds to reach completion.

The suitable concentrations and ratios were identified as follows:

Stock solutions

Analyte A: Aqueous NaI 0.004M, Na₂S₂O₃ 0.001M, 2% Starch

Analyte B: NaBrO₃ 0.006M, HCl 0.1M

Individual reactant dilutions solutions

Analyte A: NaI 4.00×10^{-2} mM, Na₂S₂O₃ 5.00×10^{-3} mM, Starch 2.00×10^{-2} mg

Analyte B: NaBrO₃ 1.20×10^{-1} mM, HCl 1.00 mM

Analyte A = 15 mL

Analyte B = 30 mL

Conclusion

Several sets of experiments with varying combinations of analyte concentrations and reaction dilutions were undertaken until a suitable set of combinations was identified at ambient laboratory temperatures, however, it was noted that there was still inconsistencies in reaction parameters arising with the levels of precision and repeatability in the reactions.

2.2. Clock reaction and temperature factors

It was ascertained after conducting multiple replicate experiments over several days in the concentration and dilution phase of the trials that the reactions were highly sensitive to temperature fluctuations encountered in the laboratory. Atmospheric laboratory temperature monitoring was undertaken, which confirmed these suspicions, and a generic laboratory water bath was incorporated for analyte temperature stabilisation to mitigate this issue.

2.2.1. Clock reaction and water bath trials

Multiple replicate clock reaction experiments were then further undertaken with the chosen A and B reagent compositions, concentrations, and overall reaction dilutions, by immersing respective vials of solutions A and B in generic laboratory water bath

located in a nearby laboratory storage room, and then conducting preliminary replicate visual analysis of the emergence and completion of initial blue complexation over time. This method of temperature stabilization unfortunately did not meet satisfactory requirements for experimental precision, and a discussion with the research team noted that a high precision thermostat controlled refrigerated Scavac water bath was at the Victoria University Hoppers Crossing campus, which was then obtained by laboratory support staff, and after several initial trials it was deemed worthy for continuing with these experiments.

Conclusion

A generic laboratory type thermostatically controlled water bath did not stabilise analytes and reaction temperature kinetics to the requisite precision.

2.2.2. Clock reaction and Scavac water bath trials

Instruments and perishables

Labogene Scavac SHC 2000 circulator (20-150°C working range, 0.1°C resolution, 0.01°C stability) incorporating LabGear-Chillsafe 5 litre water bath.

Gresinger G1700 digital thermometer (-200.0 to 450.0°C range), G1710 thermocouple (-70.0 to 250.0°C range, ± 0.01°C deviation: DIN EN ISO 9001:2015)
35 mL glass capped vials

Laboratory stopwatch timer

5 x 20 mL borosilicate reaction beakers.

Sartorius Proline 1000-5000 µL adjustable pipette.

Sartorius Proline 10-100 µL adjustable pipette.

Individual reactants

Analyte A (35ml*): NaI, Na₂S₂O₃, Starch (as per ratios and dilutions outlined in 2.2.1.)

Analyte B (35ml*): NaBrO₃, HCl (as per ratios and dilutions outlined in 2.2.1.)

Vial positioning and temperature integrity analysis

Initial analysis was conducted on the temperature integrity of the 3 x 30 mL MQ H₂O vial position placements in the water bath (see Figure 2-1 to 2-3), noting the water bath's thermostat temperature readout in combination with temperature measurements conducted utilizing a Gresinger G1700/1710 digital thermometer (certified ± 0.01 °C sensitivity), and all water bath vial placement positions exhibited stable correlating uniform temperature readings after more than 10 minutes of stabilized readings.



Figure 2-1: Scanvac water bath and reagent A/B temperature control method.

Following the vial placement temperature integrity experiments, the clock reaction reagents and MQ H₂O solutions were immersed in the water bath at set temperatures, with the MQ H₂O vial monitored for temperature stability with the Gresinger 1700/1710 digital thermometer until a desired uniform temperature had achieved equilibrium for a period of at least 10 minutes, and then replicate visual analysis was undertaken.



Figure 2-2: Gresinger G-1700 digital thermometer (± 0.01 °C sensitivity)



Figure 2-3: Reagent temperature control experimental design layout

Conclusion

The temperature thermostat readout on the Scavac SHC 2000 circulator was in reliable agreement with the digital readout of the Gresinger G1700/1710 digital thermometer, and a series of 5 x replicate reactions across a range of temperatures stabilised at 20, 22, 24 and 26°C were undertaken whilst visually scrutinizing for the emergence of the commencement of the blue complexation and reaction completion monitored by stopwatch. This series of trial experiments identified improved consistency in replicate temperature dependent reaction complexation and an identifiable linearity in the temperature curve. Scavac refrigerated water bath analyte A and B vial placement did not impact reaction kinetics.

2.3. Experimental UV-Vis kinetic analysis trials

This research initially set out at its inception to investigate analyte ion clustering phenomena with regard to control and magnetic field exposures, by incorporating electrospray mass spectrometry ionization as the designated instrumental analysis of choice, however pandemic restrictions upon training and instrument accessibility intervened, and alternative analytical methods were explored. During the initial reaction trials, it had been noted that various chemical component compositions and dilutions elicited differing times for the initial emergence of the blue complexation product, as well as the rate of complexation and reaction completion. The improved consistency in reaction kinetics observed in the latter refrigerated water bath temperature stabilised reactions also exhibited this phenomena, and with this in mind, further investigations regarding UV-Vis spectroscopic kinetic analysis were now undertaken, to see if this analytical method could conceivably be utilized with this research to measure the kinetic rate of the complexation with a view to analysing suitable complexation initiation and reaction completion parameters with greater precision and higher sensitivity.

The indispensable expertise of Larruceo “Larry” Bautista was recruited to assist in programming a Shimadzu UV 1900 instrument, then the experimental performance

of the Scanvac water bath temperature control of clock reactants, and UV-Vis spectrophotometric kinetic analysis were closely scrutinized.

2.3.1. UV-Vis Spectrophotometry application in this research

The preceding literature in chapter 1.9. informed of aspects to be considered in the UV-Vis analysis incorporated in this research. The potato starch utilised was of an unknown amylose and amylopectin ratio, stating the molecular formula of $(C_6H_{10}O_5)_n$, and a solubility of 50g/L H₂O @ 90°C (Chem Supply SA083-500), which raised questions about incorporating the λ_{max} wavelength measurements outlined in section 1.9.3., due to the wide variation in peak absorption and the unknown properties of our experimental starch. No literature from Chem Supply regarding the amylose/amylopectin ratios, or any UV-Vis analytical data pertaining to starch-iodide complexation λ_{max} wavelength could be located. These unknown factors, combined with the significant variability of UV-Vis peak wavelength in the literature, compelled a closer scrutinization for the wavelength detection method, noting the findings of Pursell and Pursell in 2016, that triiodide generation and starch triiodide complexation were identically interrelated and that this could combine to potentially provide two kinetic parameters at the same time.

Both the 288nm major triiodide peak and 352nm secondary peak were then researched, and after contemplating that most of the literature UV-Vis data was predominately associated with I₂ + I⁻ to generate I₃⁻, and in some instances also utilised various other chemicals not utilised in this research, it decided to focus BrO₃⁻ and I₃⁻ UV-Vis methodologies which identified the highest precision in UV-Vis detection at wavelength 352nm. Further investigation of carbonate UV-Vis analysis at 288nm uncovered that α-CD's and starches are reported to form complexes with dissolved CO₂ in their cavities (Horton, p.313, 1999), so based on this combination of factors, combined with the world standards best practice for bromate determination in drinking water, It was decided to opt for 352nm detection wavelength in the UV-Vis kinetics research that follows.

2.3.2. UV-Vis spectroscopy Kartell cuvette baseline calibration

The Shimadzu UV-1900 UV-Vis spectrophotometer was set at 352 nm in accordance with scientific literature specifications relating to triiodide and starch-triiodide complex absorbance (Cordeiro et al., 2011, Michalski and Łyko, 2013, Pursell and Pursell, 2016, Kireev and Shnyrev, 2015), and a baseline blank measurement was conducted over 190-1100nm was established with 2 x Kartell 01960-00 cuvettes containing 2.35 mL MQ H₂O. The disposable cuvettes were well behaved in the baseline calibration according to their designated calibration range (Kartell, 2019) and no background noise in the blank absorbance spectra was identified in the applicable wavelength range (see Figure 2-4).

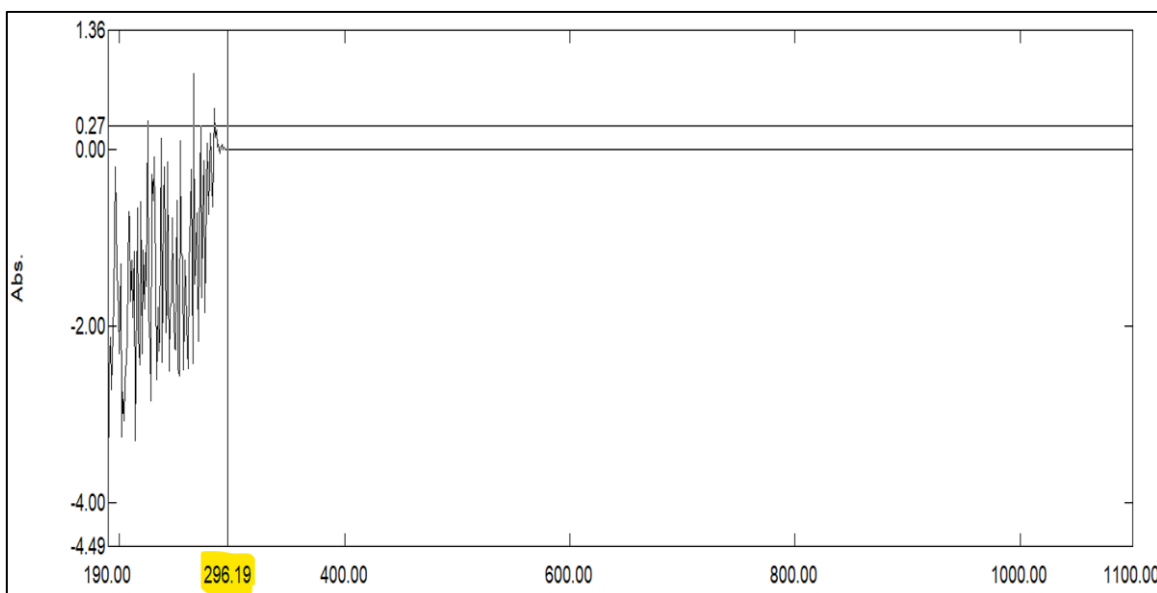


Figure 2-4: Shimadzu UV1900 Milli Q blank baseline spectra (352nm)

2.3.3. Scanvac temperature control and UV-Vis kinetic trials

Instruments and perishables

Shimadzu UV1900 spectrophotometer (serial no. A 12425601063)

Lab Solutions kinetic software (version 1.03)

Kartell 01960-00 4 clear side disposable polypropylene cuvettes.

Labogene Scavac SHC 2000 circulator (20-150°C working range, 0.1°C resolution, 0.01°C stability) incorporating LabGear-Chillsafe 5 litre water bath.

Gresinger G1700 digital thermometer (-200.0 to 450.0°C range), G1710 thermocouple (-70.0 to 250.0°C range, \pm 0.01°C deviation: DIN EN ISO 9001:2015)

Sartorius Proline 1000-5000 μ L adjustable pipette

Sartorius Proline 10-100 μ L adjustable pipette

Digital stopwatch (1 second increments)

UV-Vis analytes

Analyte A: 0.75mL (volume modified as per 2.1.1. concentrations)

Analyte B: 1.60mL (volume modified as per 2.1.1. concentrations)

UV-Vis cuvette reaction volume (2.35mL)

UV-Vis/Lab Solutions (1.03) kinetic software programmed parameters

Identification of the initial emergence of the triiodide species (I_3^-) at 352nm/0.001 cm^{-1} absorbance was programmed into the Shimadzu UV-1900 Lab Solutions kinetic software (version 1.03), and the rate of increased $I_3^- +$ starch complexation was set at one second increments until the increase in absorbance reached maximum at 4.000 cm^{-1} .

Method

- 1) When the desired reactant A and B analytes had achieved 10 or more minutes of sustained temperature equilibrium in the Scavac water bath/ Gresinger thermocouple temperature readings, 1.6 mL of solution B and 0.75 mL of solution A were carefully pipetted into new clean cuvettes in quick succession
- 2) the stopwatch timer was commenced as the 2nd solution was blended with the initial aliquot, and the reaction commenced.
- 3) The spectrophotometer lid was quickly closed, and kinetic absorbance measurement was immediately commenced at the instrument software interface.

4) Careful scrutiny was afforded to recording the instrument commencement time and calculate the time differential on the digital stopwatch, which was combined with the instrument kinetic data for true kinetic analyses.

2.3.4. Scanvac temperature control and UV-Vis kinetic results

Graphs were plotted from the respective temperature mean measurements, with respective replicate error displayed, and an excellent mean temperature - absorbance linearity was identified over this experimental range (Figure 2-5).

Table 2-1: Scanvac temperature control/ UV-Vis kinetic statistics								
Temp (°C)	352nm λ_{max} / seconds	\bar{X} (x5)	SEM (x5)	\tilde{x} (x5)	SD (x5)	95% C.I. (x5)	Upper 95% CI	Lower 95% CI
20-1	167	163.6	1.4	162	3.13	3.88	167.48	159.71
20-2	167							
20-3	167							
20-4	161							
20-5	162							
22-1	147	148.6	0.93	149	2.07	2.57	151.17	146.02
22-2	151							
22-3	146							
22-4	149							
22-5	150							
24-1	133	133.6	0.75	134	1.67	2.07	135.67	131.12
24-2	135							
24-3	134							
24-4	134							
24-5	131							
26-1	119	118.8	0.66	119	1.48	1.84	120.64	116.95
26-2	121							
26-3	117							
26-4	119							
26-5	118							

An expanded statistical analysis of these experiments is outlined in Table 2-1.

Water bath temperature controlled reaction analyte and UV-Vis absorbance kinetics (352nm)

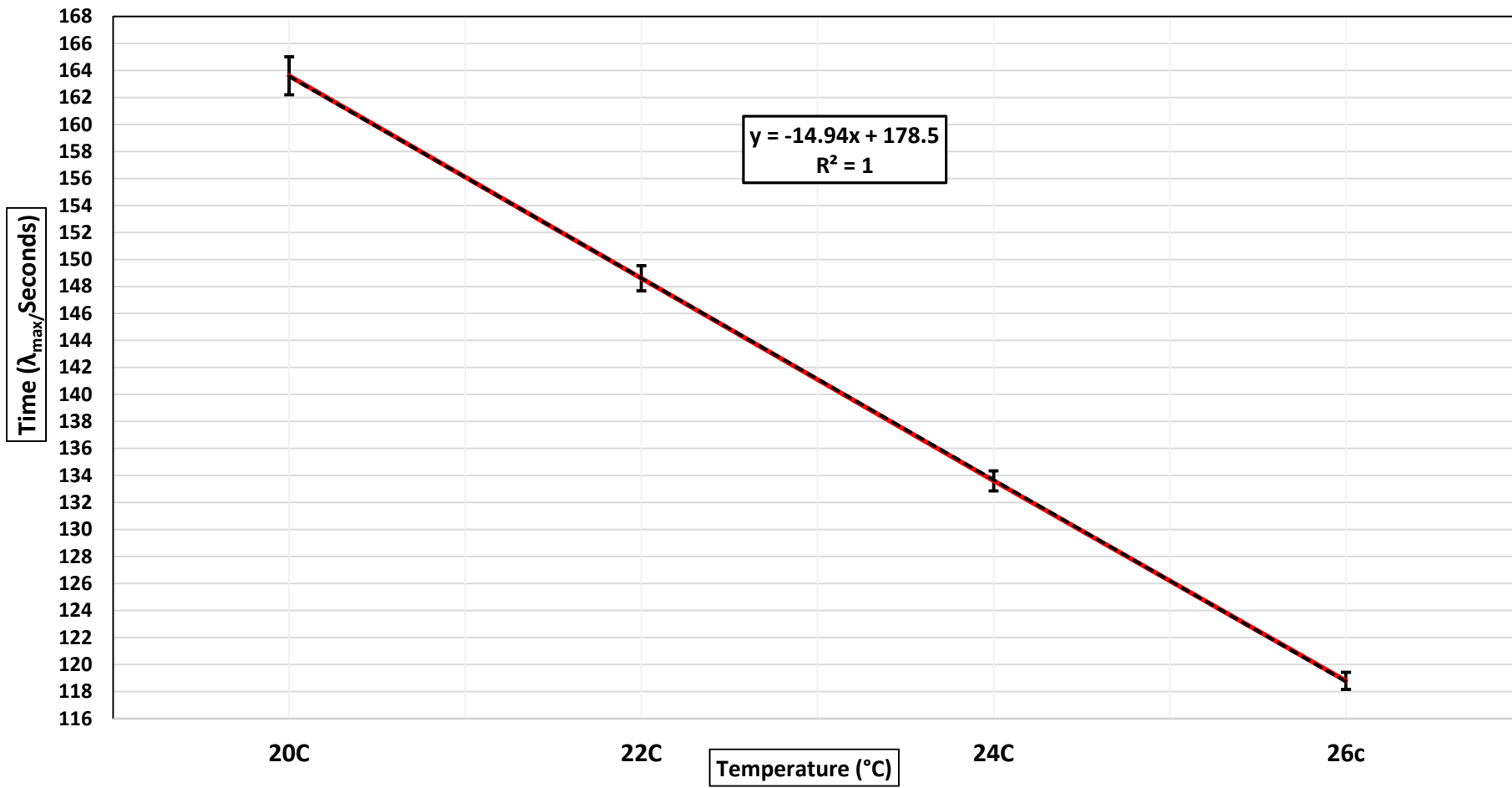


Figure 2-5: Water bath temperature controlled UV-Vis mean λ_{max} absorbance including standard error bars
(20.0°C, 22.0°C, 24.0°C, 26.0°C) x 5 replicates.

Conclusion

These experimental outcomes identified that the 20, 22, 24 and 26°C temperature stabilised analyte replicate reactions exhibited excellent UV-Vis kinetic sensitivity, consistency, and linearity, conferring high confidence in the Scanvac water bath and reaction temperature control stability. The UV-Vis triiodide-starch complexation absorbance kinetic methodology was also found to suitable for experimental analytical purposes, with the replicate standard error and standard deviation calculations improving by approximately 100% as UV-Vis analysis approached the typical laboratory ambient temperature range (25.0C°), and all independent λ_{max} /seconds measurements falling within the 95% confidence range.

2.4. Experimental ambient temperature measurement

Introduction

As previously outlined, the refrigerated Scanvac water bath delivered excellent results with analyte temperature stabilisation and UV-Vis kinetic absorbance replicability, however, this experimental set up was not viable isolating individual analytes with static or pulsed electromagnetic field exposures, due to the relatively small accessibility of the area of the water bath, and the very close proximity of control analytes. Therefore, a suitable experimental design and methodology would have to be devised in order to correlate laboratory ambient temperatures with static magnetic field exposure analytes and their respective control replicates.

2.4.1. The 0.3T rare earth magnet experimental design

A powerful rare earth rod magnet was incorporated 180-minute static magnetic field exposure with the respective reagents. Enquiries identified that the magnet was of a neodymium-iron-boron composition encased in a stainless-steel body that provides a 0.3 Tesla magnetic field at the outer North pole. The working stem of the device had a diameter of 25.4mm, and an overall length of 50mm from the protection shroud situated just above the magnetic south pole (Figure 2-6).



Figure 2-6: Alpha magnetics scientific 0.3T neodymium magnet device.

2.4.2. 0.3T magnet exposure and ambient temperature monitoring

It became evident at this point that in order to conduct magnetic exposure and control experiments at a suitable distance free from magnetic field interference that these reactions would have to be conducted at room temperature to facilitate virtually identical analyte temperature exposures and kinetic absorbance analyses.

The assistance of Miroslav Radev from the University Electrical Engineer department was enlisted for input to devise a method for monitoring analyte temperatures under ambient laboratory conditions, who forwarded a suggestion of employing a computer data logger with a suitable thermocouple. An investigation into thermocouple suitability was undertaken which identified that a type K 608-053 310 stainless steel (310SS) thermocouple could be utilized in aqueous ambient temperature monitoring. This thermocouple had a maximum working temperature range up to 1100°C and consisted of an austenitic 25/20 chromium/Nickel alloy with less than 0.1% carbon content (TC Measurement & Control, n.d.), affording high protection against oxidation. Furthermore, the performance integrity of 310SS alloys in the presence of external magnetic fields ascertained from ASSDA (2010), notes that grade 310 austenitic alloys are virtually impermeable to responses with external magnetic fields (Figure 2-7, yellow).

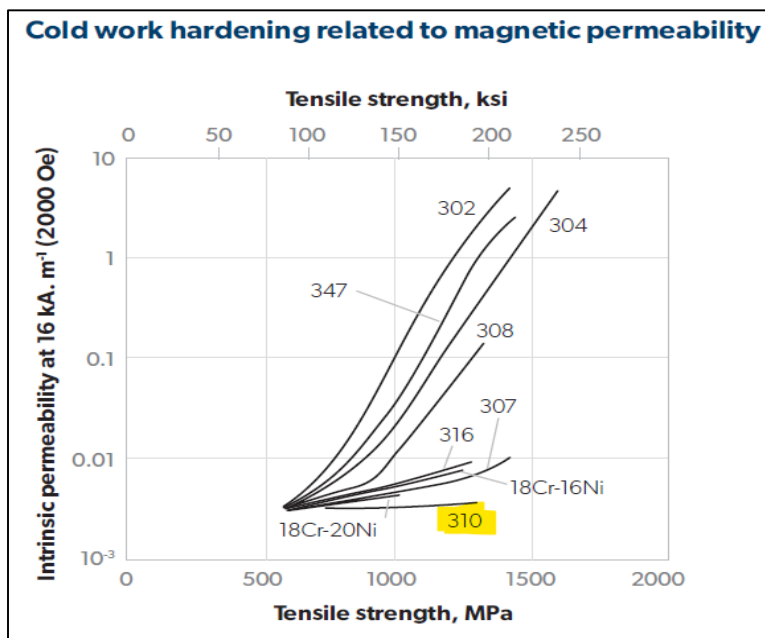


Figure 2-7: Stainless steel alloys and correlated magnetic field response (ASSDA, 2010)

The type K 608-053 310 SS thermocouple was wired in to the Keybright 34972A temperature data logger/computer system, then immersed in to an identical beaker with an identical volume of control analytes, which were placed next to the ambient temperature monitoring beaker, whilst the static magnet exposure analytes were place approximately 60-70 cms away in an area in the laboratory of virtually identical temperature, and then the computer software was set to log aqueous ambient temperatures on two second intervals prior to the commencement of magnet exposures, throughout the exposure times, and throughout the undertaking of control and exposure UV-Vis analysis.

Conclusion

Experimental trials were not deemed necessary for these factors, as both 0.3T magnet exposure analytes and control ambient solutions would both be in close laboratory proximity and considered to be of equivalent ambient temperature.

2.5. Investigating the Dolphin 3000 PEMF device

The Dolphin series 3000 technical manual (Clearwater Systems Corporation, 2008) describes the product as a pulsed electromagnetic field water treatment device which is designed for bacterial and ionic scale particulate control in domestic and industrial water supplies. The technology claims to remove the surface charges from particles suspensions in aqueous systems inducing them to “act as seeds for precipitation of dissolved minerals” (p.2, Clearwater Systems Corporation, 2008), which can be removed via filtration, and overcoming the issue hard scale adherence to irrigation system surfaces. Furthermore, the device claims that the generated “negative static” (p.4, Clearwater Systems Corporation, 2008) charged particles interact with bacterial membranes to encapsulate bacteria, and induce “electroporation” (p.4, Clearwater Systems Corporation, 2008) which erodes bacterial membranes and significantly limit their numbers. The device layout consists of an electrical signal generator which connects to a treatment module consisting of a solenoidal pulsed electromagnetic field inducing chamber, through which the irrigation pipework of the treated water supply flows and is exposed to an oscillating magnetic field.

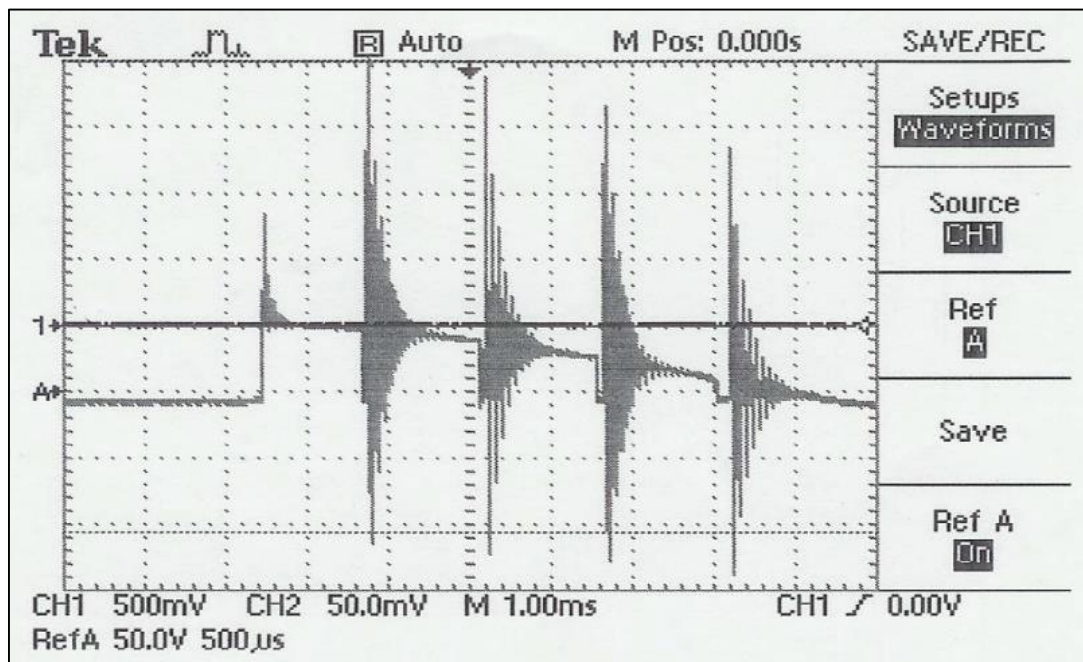


Figure 2-8 : Dolphin 3000 PEMF oscilloscope wave (Clearwater Systems Corporation, 2008)

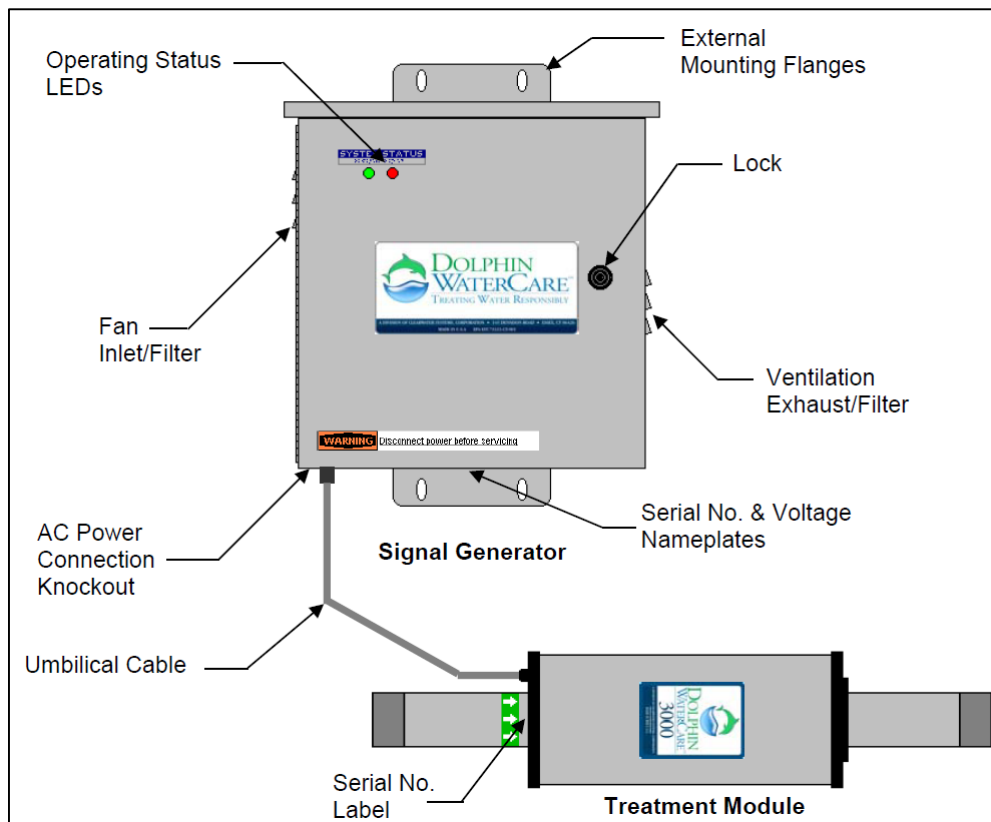


Figure 2-9: Dolphin 3000 electrical control box and connected PEMF reaction coil
 (Clearwater Systems Corporation, 2008)

Piyadasa (2017) report that the device utilises a 230V single phase AC current at 60Hz which generates a pulsed electromagnetic field through a cylindrical aperture 25.4mm in diameter of a treatment module 388mm in length which encloses the PEMF solenoid coil, imparting varying high frequency electric fields at 60 times per second, which peak and then dampens to negligible intensity over approximately 3 milliseconds in the overall MHz range. The same Dolphin 3000 PEMF device utilised in this research was accessed from the Hoppers Crossing campus and set up with a view to conduct initial experiments of respective reactant A and B “dry” runs of 180 minutes in the instrument, as outlined by Piyadasa et al. (2017) when they undertook identical exposure treatments with bacteria and calcium carbonate experiments over a period preceding 2017.

Unfortunately, difficulties were encountered straight away with the instrument shutting down constantly around 40 minutes in to experimental runs, and a reconfiguration of the experimental design with polypropylene tubing filled the PEMF coil and tubing assembly with approximately 600mL of cold tap water, consistent with

the “wet” experimental exposures conducted by Piyadasa et al. (2017), however the instrument shut downs at 40 - 60 minutes continued to persist.

2.5.1. The Dolphin 3000 PEMF device temperature analysis

The assistance of Miroslav Radev from the Victoria University Electrical Engineering Department was employed to assist with the overheating issue, and a thermal analysis of the device was conducted with approximately 300mL of cold tap water in the PEMF system, with thermocouples placed inside the aqueous coil housing and in the external ventilation area where the coil is located, in combination with infra-red measurements of the external coil housing, and the results of Miroslav’s investigation informed us that the device was indeed overheating (Table 2-2)

Table 2-2: Electrical engineers report of PEMF device thermal analysis		
Device on (mins)	Temperature (°C)	Measurement
0	19	Internal
8	29	Internal
15	41	Internal
23	59	Internal
29	66	Internal
29	50.3	IR external
40	77	Internal
43	80	Internal
46	82	Internal
46		Instrument shut down

Conclusion

It was now conclusively apparent that the device was not performing as it had at least 3 years earlier in the research of Piyadasa et al. (2017), and an assumption was put forward that this was most likely the result of dust accumulating in the ventilation housing of the coil. This could not be investigated without pulling the instrument apart and potentially causing permanent damage to the device and bringing this arm of the research to a halt.

2.5.2. The Dolphin 3000 PEMF device electrical engineer report

It was at this point that further analysis of the PEMF device electrical output was required, and Miroslav Radev was again consulted to conduct an examination of the devices electronic integrity and PEMF performance including the waveform outputs. The results of this report confirmed that no fault was identified in the control unit and the device was electronically performing in accordance with the operating specifications and data obtained from the patents with the exception of the overheating issue (see Figures 2-8 and 2-10). Further analysis of the coil voltage and waveform electrical signal derived from the operating manual also matched, with the engineer's report concluding that all other voltage and current measurements associated with the device control box correlated "also as per specs".

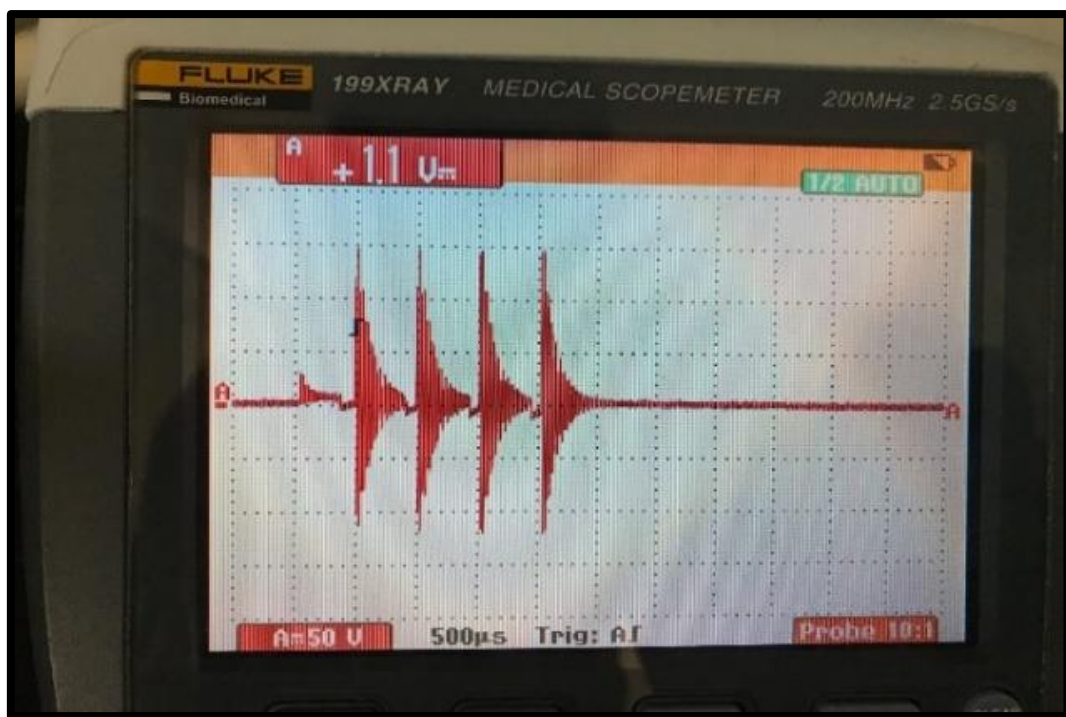


Figure 2-10: Electrical engineer oscilloscope report of Dolphin 3000 wave output.

Unfortunately, a true measurement of the electromagnetic field inside the instrument was never undertaken, as the COVID-19 pandemic again intervened and brought research to a halt, this time permanently. A magnetometer would have been required to measure the internal coil field, which was not available at the time, and the only other way the electromagnetic field could have been calculated is by destroying the

device treatment module to gain physical measurement of the solenoid coil specifications, however, some additional information about the device performance was obtained as an afterthought once the research was halted.

The available device electronic specifications were 230 volts at single phase and 50/60Hz, as outlined in the additional data of the Piyadasa thesis (2017), which commented that the device emits “*high frequency electric fields*” at “*60 times per second*” in the overall “*MHz range*”, which peak and then dampen to negligible intensity “*over approximately 3 milliseconds*”. Approximated calculations taken from the electrical engineer electrical reported that the single pulse phase output scale ranges from 500mV at the first pulse to 50mV at the final pulse in the cycle over the course of 11 oscillations at 3.6 μ s intervals, then the field “dampens” for 10 μ s before committing to the next pulse cycle. This contributes to an output frequency of 20KHz and consists of 20,000 dampening events per second, provided this is an uninterrupted phase cycle.

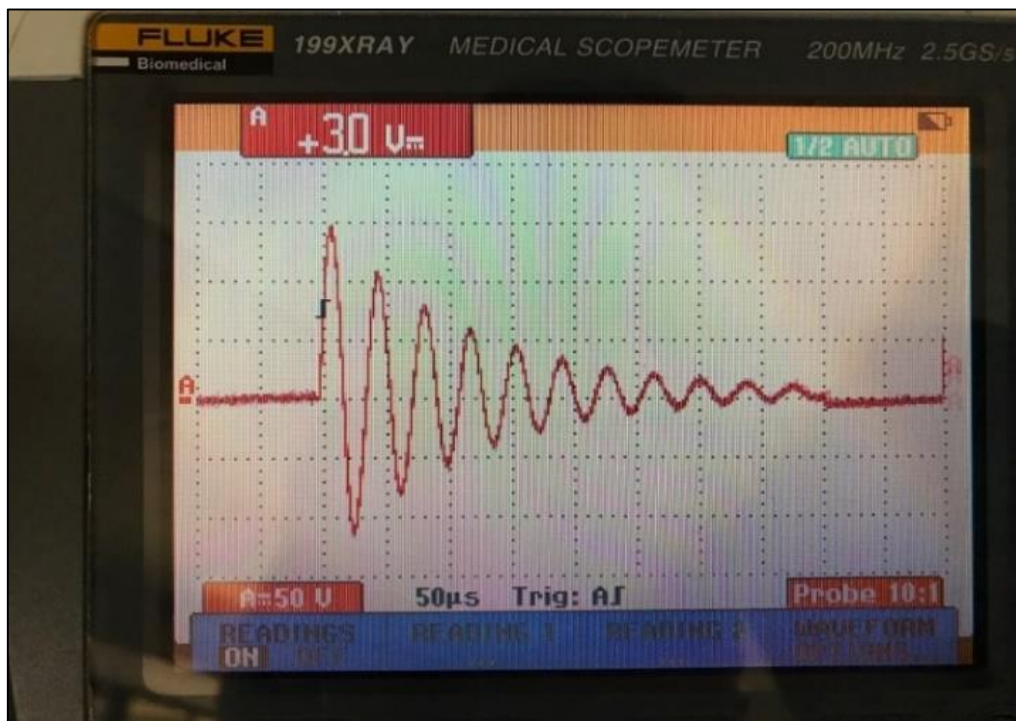


Figure 2-11: Electrical engineer oscilloscope report of Dolphin 3000 single pulse.

Conclusion

No further significant investigation of the Dolphin 3000 instrument overheating issues were undertaken, and an assumption for the device temperature issues was thought to be dust build up in the solenoid cooling vents during 3 years of dormancy.

2.5.3. Scinvac water bath and Dolphin 3000 PEMF trial

Some thought was required to devise a way to mitigate the PEMF device overheating issues, and an investigation of incorporating the Scinvac refrigerated water bath as a recirculating cooling system with the PEMF device was undertaken.

The Scinvac refrigerated water bath was employed as the Dolphin 3000 recirculating water system, and the Gresinger G1700/ G1710 digital thermometer and thermocouple combination were again employed to measure recirculating water bath temperature fluctuation and Scinvac thermostat precision.

Conclusion

The resulting temperature control trials proved fruitful and in combination with the Gresinger 1700 digital thermometer readings, the refrigerated water bath system recirculating cooled water through the PEMF coil as it was running, with no more than 0.1°C variation in temperature response identified between the Scinvac thermostat and Gresinger thermocouple measurements (Figure 2-12). The incorporation of the Scinvac water bath provided excellent thermal control for a period of 210 minutes with manually adjusted temperature variations of little more than 0.5°C noted throughout these trials, after adjustments for the initial temperature jump in the first 5-10 minutes of commencement of PEMF generation. This excellent outcome allowed the possibility to continue pursuing this arm of the research.

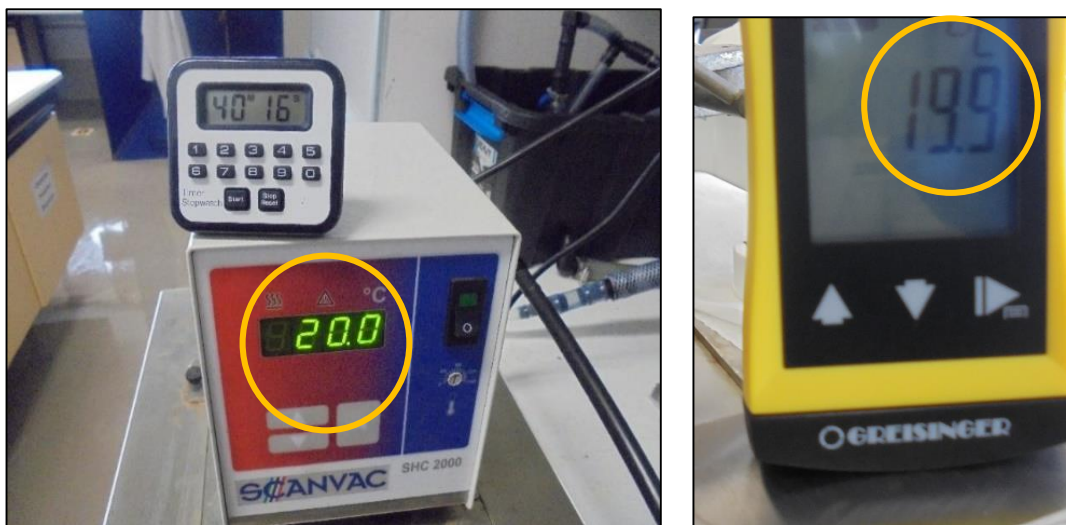


Figure 2-12: Scanvac water bath and Dolphin 3000 temperature control calibration

2.5.4. Dolphin 3000 PEMF thermocouple and reaction vessel design

Satisfied that the device output was performing consistently, and the heat stabilisation of the water bath was suitable for mitigating PEMF induced temperatures fluctuations, the research focus shifted to insulating the reactant temperature inside the PEMF device during 180 minutes of exposure, and maintaining these temperatures in close correlation with laboratory aqueous ambient temperature measurements. 55mL round bottom borosilicate glass vials with chemical resistant GL14 caps were obtained, which were 200mm in length and 22mm in diameter to serve as the reaction vessels inside the PEMF device coil aperture, then an investigation of a suitable thermocouple for the methodology with regard to the suitability with exposures to the respective chemical constituents in the A and B reagents was undertaken. An extensive investigation of the literature identified that the chemical compatibility of the type K 608-053 310 stainless steel (310SS) thermocouple, utilized in the ambient temperature control, was difficult to source with regards to references for 310SS alloys, however, Shurflo (2003) claimed that 310SS exhibited a higher rating of chemical resistance than 304SS alloys which were classified as grade A compatibility for iodide and thiosulfate ions, as well as starch solutions. An unfortunate finding was that 310SS, like most SS alloys was not suitable for HCl exposure, and therefore real time PEMF exposure temperature monitoring for analyte B solutions, and therefore PEMF exposure for these analytes was shelved for the time being.

The thermocouple and reaction vessel configuration was devised (Figures 2-13 and 2-14) to monitor real time reaction temperatures by incorporating a GL14 cap with a diaphragm typically employed in LC applications, and fixing the thermocouple inside the reaction vessel where it was located centrally in the analyte, making sure it did not make contact with the reaction vessel walls.



Figure 2-13: Reaction vessel, thermocouple and GL14 cap design.

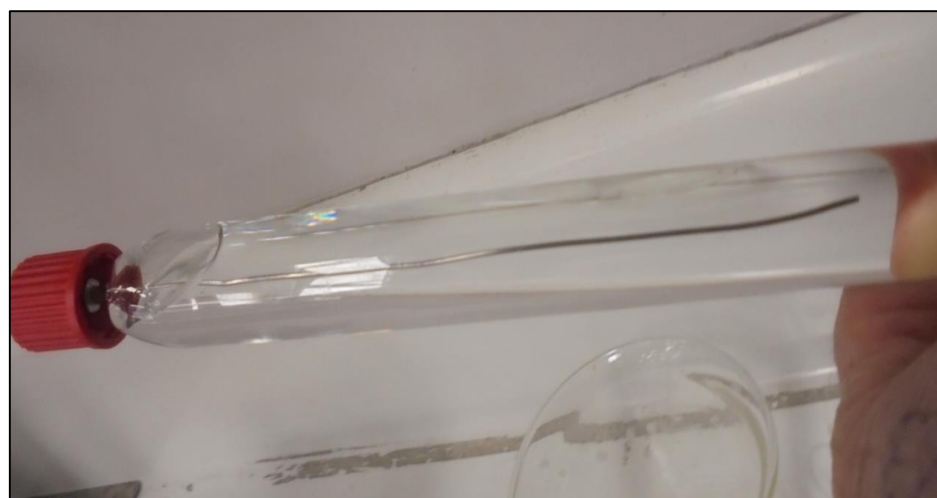


Figure 2-14: Sealed reaction vessel/thermocouple and Reagent A.

2.5.5. Dolphin 3000-thermocouple-irrigation system design trial

The trial design of the thermocouple-reaction vessel and Scanvac recirculating water system afforded a flow area of 3.4mm after the reaction vessel was inserted to the correct position in the PEMF aperture. The incorporation of a polypropylene Y piece

coupling with a rubber septum to seal the thermocouple feedback wire through the irrigation system was devised, whereby the wire would snake from the reaction vessel, through the recirculating water system, and exit out through the septum, and was then hard wire connected to the Keybright data logger (Figures 2-15 and 2-16).

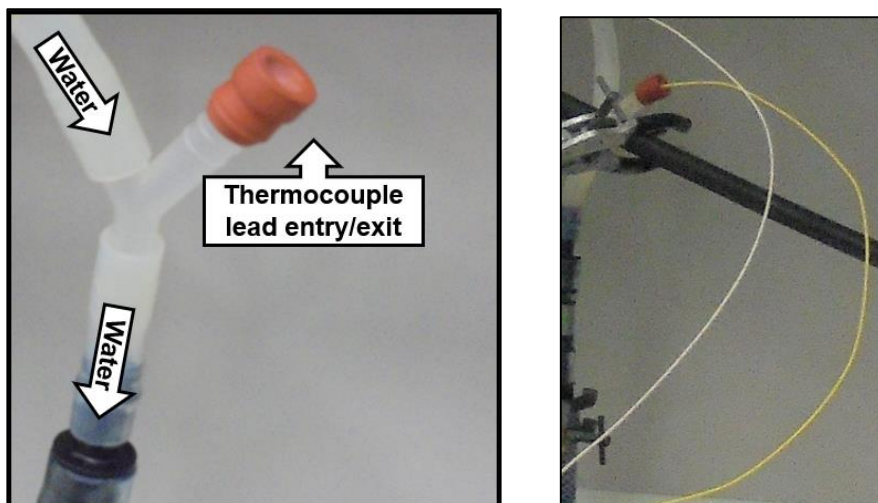


Figure 2-15: (left) Scanvac water bath irrigation hose and Y piece, (right) Y piece/thermocouple lead (yellow) to data logger.

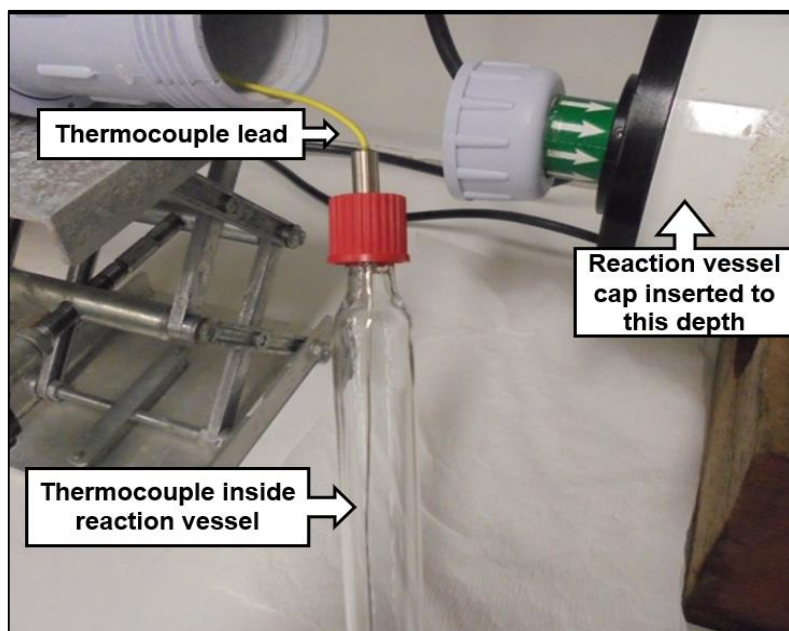


Figure 2-16: Overall thermocouple/reaction vessel configuration.

The Dolphin 3000 PEMF device and Scanvac refrigerated water bath irrigation system was configured as outlined in the photograph below (Figure 2-17).

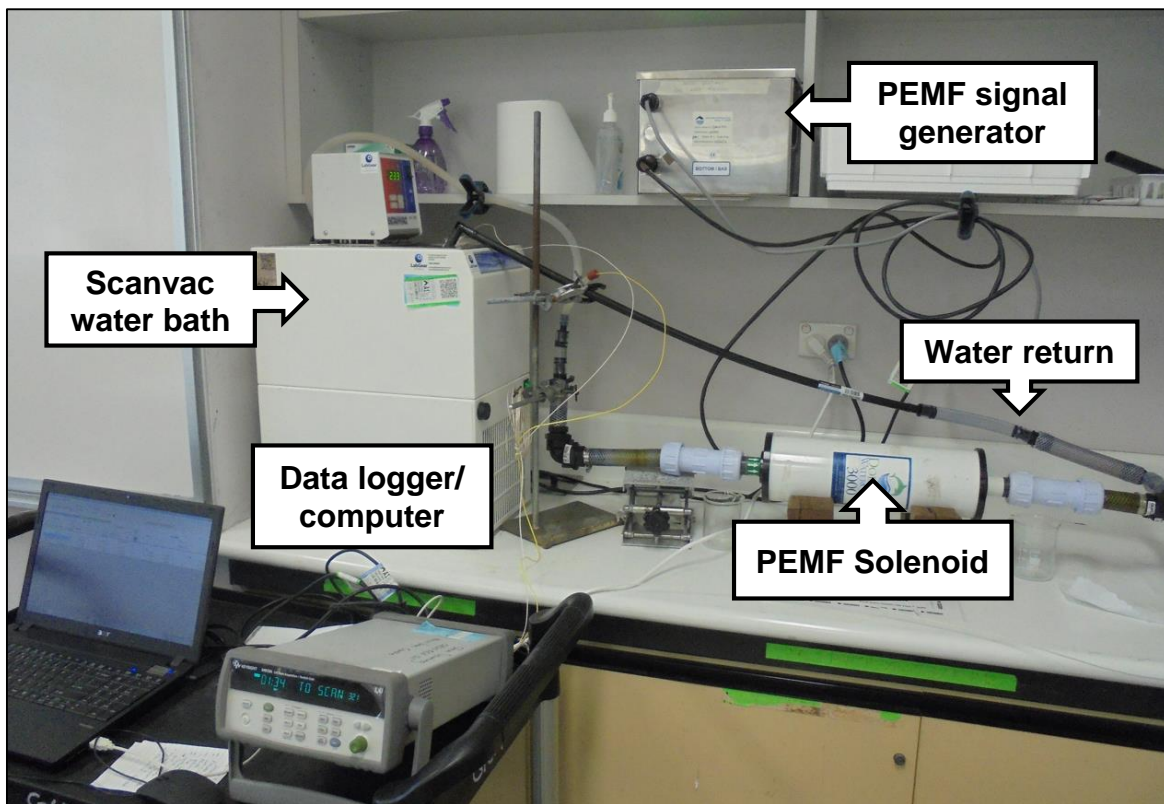


Figure 2-17: Dolphin 300/Scanvac/data logger overall experimental design layout.

2.5.6. The thermocouple/PEMF/Scanvac water bath trial

The Scanvac refrigerated water bath was filled with approximately 6 L of water in total and adjusted with manual observation of the Milli Q ambient temperature data readout situated nearby, which informed the requisite manual adjustment of the refrigeration setting on the water bath from the information relayed to the data logger from the thermocouple reaction vessel undergoing PEMF exposure. These initial trials were conducted with Milli Q as the reaction vessel analyte, and the data logger temperature readouts were set at 10 second increments. The reaction vessel was filled with Milli Q H₂O with the thermocouple inserted and centrally located, the cap securely sealed, and the reaction vessel was then inserted in the PEMF coil aperture at the position where the PEMF field was measured to have the strongest output (Figure 2-18).

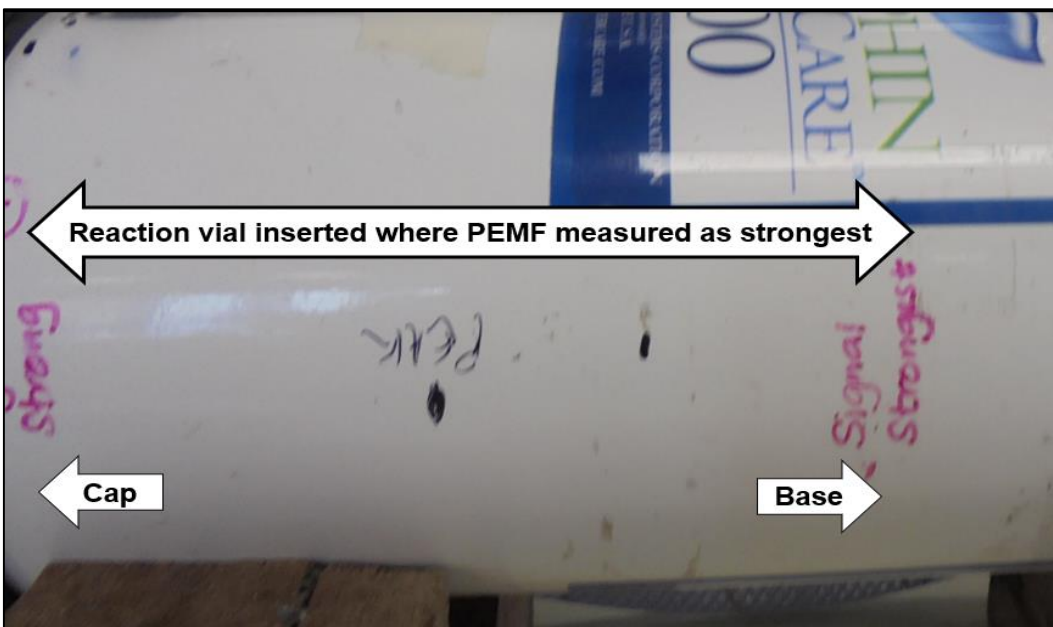


Figure 2-18: Dolphin 3000 PEMF coil reaction vessel insertion area

The hose connections of the PEMF device and irrigation system were then securely fastened, the water bath circulation pump was turned on, and the water bath temperature was adjusted over the course of approximately 5 minutes to closely stabilize with the ambient temperature measurements. The Dolphin 3000 PEMF was then switched on and 180 minutes of OEMF exposure was initiated with the Milli Q trial analytes whilst ambient and PEMF instrument temperature feedbacks were closely scrutinized and manually adjusted necessary.

Table 2-3: PEMF - water bath/thermocouple temperature control trial (16/3/21)

Operation (mins)	Time	Thermocouple (°C)		Variation (°C)
		PEMF	Ambient	
0	13:01:54	23.768	20.386	3.382
4	13:05:54	20.290	19.230	1.060
9	13:10:54	19.655	19.266	0.389
14	13:15:54	19.856	19.450	0.406
19	13:20:54	19.932	19.495	0.437
24	13:25:54	20.043	19.512	0.531
29	13:30:54	20.093	19.553	0.540
34	13:35:54	20.112	19.540	0.572
39	13:40:54	20.094	19.488	0.606
44	13:45:54	20.050	19.461	0.589
49	13:50:54	20.115	19.466	0.649
54	13:55:54	20.043	19.512	0.531
59	14:00:54	20.093	19.553	0.540
89	14:30:54	20.127	19.374	0.753
119	15:00:54	20.147	19.323	0.824
149	15:30:54	20.174	19.254	0.920
180	16:01:44	20.192	19.242	0.950

Conclusion

The previously identified overheating issues with the PEMF device with approximately 300mL of water acting as an insulator, identified a rise in operating temperature of 10°C after 10 minutes of operation, and an overall 63 °C increase after 46 minutes of operation which resulted in device shutdown.

The PEMF/Scavac temperature mitigation trial outcomes provided excellent results, displaying a variation between reaction vessel and ambient thermocouple measurements of approximately 0.50°C after 60 minutes. No further manual water bath adjustments were executed for the next 120 minutes of the total 180 minute trial run. A minimal further increase of approximately 0.4 °C in ambient – PEMF device temperature ratio was detected between 60 and 180 minutes, giving high

confidence in this experimental trial design in the knowledge temperature control could be improved with familiarisation with the experimental method.

2.6. Experimental 0.3T magnet design trial

The North pole at the tip of the magnetic rod would be encased in clean 25 mL beakers designated for each analyte, to protect the magnet and analytes from direct contact, then immersed in individually designated analyte A and B 100 mL beakers filled with 30mL of the respective analytes. The insertion of the rod magnet displaced the analyte to encase up to approximately the 10 mL markings on the 25 mL beakers leaving a space of approximately 20mL between the base of the 25 mL and 100mL bases of the beakers (Figure 2-19).



Figure 2-19: 0.3T static magnet and reagent exposure experimental method.

2.6.1. Experimental 0.3T static magnet exposure/control trials

The respective A and B static magnet control analytes were placed next to the Milli Q H₂O temperature calibration analyte during this period which were all situated withing approximately 60-70 cms of the exposure experiments, ensuring that no residual temperature variation was encountered, and when the static magnet was correctly immersed and centrally positioned in the individual A and B analytes in the manner

as represented above, the time was recorded and the 0.3T magnetic field exposure period was undertaken for a precise duration of 180 minutes.

2.6.2. An approximation of the 0.3T magnetic flux density

The magnetic field strength of the 0.3T experimental rod magnet can be calculated as follows (see Figures 2-20):

- 1) The magnet suppliers and colleagues informed that the experimental magnet had a flux density at the north face of 0.3T (3000 Gauss).
- 2) The calculation of the flux density (\vec{B}) at the z gradient is as follows:

$$\vec{B} = \frac{Br}{2} (D + z \div \sqrt{R^2 + [D + z]^2} - z \div \sqrt{R^2 + z^2})$$

Br is the field remanence

z is the distance from the magnetic surface at the center of the axis

D is the effective length of the magnetic cylinder

R is the radius at the magnetic surface

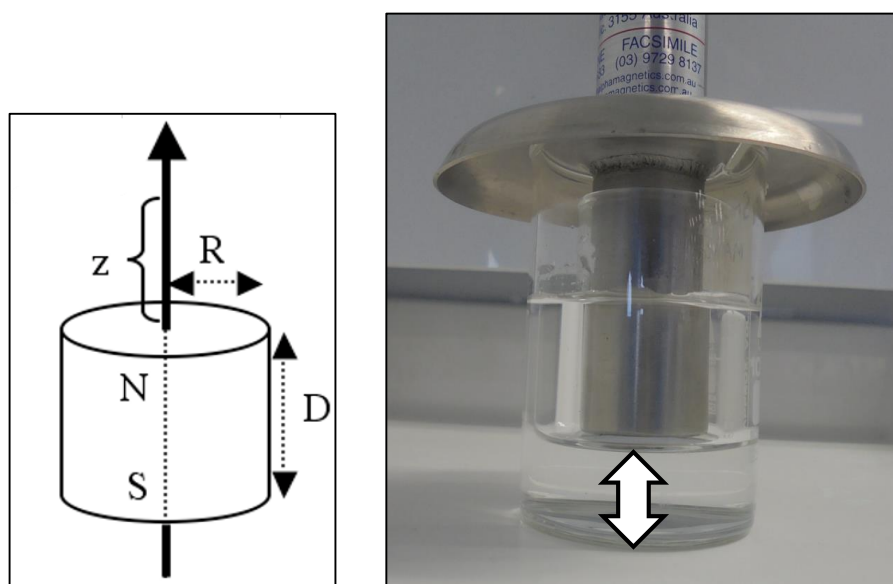


Figure 2-20: (left) Static rod magnet Z gradient calculation factors (www.Supermagnete.de, n.d.), (right) Approximate magnetic Z gradient in the 0.3T rod magnet experimental design.

Software calculations were derived based upon the properties of an N45 neodymium magnet, utilized in the experimental device, but was damped to 0.3T, due to the configuration of the stainless-steel housing. The approximated magnetic field in the ζ direction of the static magnet exposure experiments to be $\sim 0.3\text{T}$ at the glass sheath analyte* contact point which decreases to 0.036T at an approximated base depth of 16.5mm:-

* Possible glass interference with magnetic flux density not calculated.

Conclusion

In the absence of better magnetic field detection equipment, there was reasonable confidence that the experimental design was achieved that would bring the entire area of the subjected analyte in to contact with the 0.3T static magnetic field contact, as it through the ζ gradient and extend back through the analyte in the beaker shroud-exposure beaker area to the magnetic south pole located at the external magnet shroud.

2.7. Summary of trial experiments

The experimental research design and method adjustments ultimately resulted in good confidence in the trial outcomes with regards to desirable chemical concentrations and reaction dilution parameters relative to reaction time, temperature stabilisation and monitoring of the magnetic exposure and control analytes, as well as a suitable method for analytical evaluation encompassing a requisite kinetic application and sensitivity. Data relating to flow characteristics were not required as the analytes were relatively stationary under magnetic exposure, but unfortunately, accurate measurements of the experimental magnetic fields were not able to be facilitated. It was now deemed that adequate model testing and data analysis protocols had been undertaken and experimental research investigating the phenomena of static and PEMF magnetic exposure upon ionic and molecular analytes incorporating UV-Vis kinetic analysis could now proceed in order to determine whether these exposures impacted reaction rate factors.

Chapter 3: Experimental research

3.1. Analyte A/B (0.3T x 180 min) exposure methodology

Chemicals

As outlined in section 2.1.1.

Instruments and perishables

Alpha magnetics neodymium-iron-boron permanent magnet (0.3T).

Keybright 34972A temperature data logger/computer system.

1 x type K 608-053 310 stainless steel thermocouple.

1 x 100 mL new Borosilicate glass beaker (for Milli Q ambient H₂O)

1 x 100 mL new Borosilicate glass exposure beaker (1 + 1 for analyte A/B exposure)

1 x 25 mL new borosilicate glass sheath beaker (1 + 1 for analyte A/B exposure)

Sartorius Proline 1000-5000 µL adjustable pipette.

Sartorius Proline 10-100 µL adjustable pipette.

Reagent concentrations and volumes

Reagent A/B 0.3T exposure volume (30 mL)

Reagent A*: volume modified as per 2.1.1. concentrations

Reagent B*: volume modified as per 2.1.1. concentrations

* Milli Q H₂O was the reaction solvent

Thermocouple ambient temperature monitoring solution (60mL): Milli Q H₂O

0.3T magnet exposure methodology

As outlined in section 2.6.

3.2. 0.3T magnet control analyte preparation

Chemicals

As outlined in section 2.1.1.

Instruments and perishables

Keybright 34972A temperature data logger/computer system.

1 x type K 608-053 310 stainless steel thermocouple.

1 x 100 mL new Borosilicate glass beaker (for 60 mL ambient temp Milli Q H₂O)

2 x 100 mL new Borosilicate glass beakers (for control A/B analytes)

Sartorius Proline 1000-5000 µL adjustable pipette.

Sartorius Proline 10-100 µL adjustable pipette.

Reagent concentrations and volumes

As outlined in 3.1.

Thermocouple ambient temperature monitoring solution (60mL): Milli Q H₂O

3.3. Magnet (0.3T x 180 min.)/control UV-Vis methodology

0.3T magnet exposure UV-Vis kinetic methodology

Once the 180-minute magnetic exposure time had lapsed, the magnet was carefully withdrawn from the reagents, and the magnetic exposure reagents were incorporated with their complimentary reaction analytes for 5 x replicate UV-Vis kinetic analysis.

The corresponding 5 x replicate control experiments were conducted under identical protocols.

UV-Vis analytes

As outlined in 2.3.3.

Method

- 1) The Shimadzu UV-1900 instrument was turned on.
- 2) The instrument software for baseline measurements over 190-1100nm was selected.

2 x clean new Kartell 01960-00 cuvettes were inserted into the instrument, and 1 x 2.35 mL aliquots of Milli Q H₂O was carefully pipetted into each cuvette.

- 3) Baseline blank measurements were then conducted over the 190-1100nm range to obtain the appropriate response applicable to the working range of this analyte and class of cuvettes.
- 4) Once baseline was deemed satisfactory, the front cuvette containing 2.35mL Milli Q H₂O was removed, and the Lab Solutions kinetic software (version 1.03) was selected, then set to scan for 352nm at second by second increments.
- 5) Clean new Kartell 01960-00 cuvettes were then inserted in the instrument and the respective exposure-control and control-control A and B analytes were blended by first carefully pipetting 1.6 mL of solution B into new clean cuvettes, then 0.75 mL of the corresponding analyte A was then carefully pipetted into the same cuvettes in quick succession
- 6) The stopwatch timer was immediately commenced as the 2nd solution was blended with the initial aliquot.
- 7) The spectrophotometer lid was then quickly closed, and kinetic absorbance scanning measurements were immediately commenced at the instruments Lab Solutions kinetic software interface.

- 8) Careful scrutiny was afforded to recording the instrument commencement time and calculate the time differential on the digital stopwatch, which was combined with the final instrument kinetic data for true kinetic reaction analyses.
- 8) UV-Vis analysis ambient temperature measurements were also taken from the readings at the Keybright temperature data logger and thermocouple immersed in the 60mL Milli Q H₂O temperature analyte within 30 seconds of the commencement of UV-Vis kinetic scanning.
- 9) Analyte A or B (0.3T x 180 mins) exposure + A or B control, and Analyte A + B control UV-Vis kinetic analysis were each conducted for 5 x replicates under identical protocols.

3.4. Analyte A (0.3T x 180 min.) vs control UV-Vis data

The statistical analysis of the replicate (3 x 5) analyte A 0.3T magnet exposure UV-Vis kinetic displacement measurements were conducted between a period spanning 45 to 130 minutes post magnetic exposures, and UV-Vis analysis for the individual replicate sets were conducted within a time span of 24, 27 and 47 minutes from start to finish.

The statistical analysis of the replicate (3 x 5) corresponding A + B control analyte reaction UV-Vis kinetic displacement measurements were conducted in combination with the correlating magnet B measurements over a span of 62, 67 and 72 minutes for the total corresponding 3 x 10 measurements.

The comparative temperature for magnet A exposure and control UV-Vis Kinetic analysis 3 x 5 replicate sets exhibited little variation with spreads of 0.02°C, 0.09°C and 0.16°C

Table 3-1: Analyte A (0.3T x 180 min. x 15) and control (x 15) UV-Vis displacement kinetics and temperatures		
Data (x15)	Magnet A (seconds)	Control (seconds)
Initial λ (0.001cm)	67	68
λ_{max} (4.000cm)	157	158
λ duration	90	90
UV-Vis Kinetic analysis temperature		
Data (x15)	Magnet A ($^{\circ}$C)	Control ($^{\circ}$C)
Range	20.85-22.02	20.86-21.90
\bar{X}	21.26	21.26
\tilde{x}	21.12	21.12

3.5. Analyte B (0.3T x 180 min.) vs control UV-Vis data

The statistical analysis of the replicate (3 x 5) analyte B 0.3T magnet exposure UV-Vis kinetic displacement measurements for the individual replicate sets were conducted within a time span of 26, 38 and 46 minutes from start to finish.

The statistical analysis of the replicate (3 x 5) corresponding A + B control analyte reaction UV-Vis kinetic displacement measurements were conducted in combination with the correlating magnet B measurements over a span of 51, 54 and 54 minutes for the total corresponding 3 x 10 measurements.

The comparative temperature for magnet B exposure and control UV-Vis kinetic analysis 3 x 5 replicate sets exhibited little variation with spreads of 0.22 $^{\circ}$ C, 0.14 $^{\circ}$ C and 0.21 $^{\circ}$ C.

Table 3-2: Analyte B (0.3T x 180 min. x 15) and control (x 15) UV-Vis displacement kinetics and temperatures		
Data (x15)	Magnet B (seconds)	Control (seconds)
Initial λ (0.001cm)	75	73
λ_{max} (4.000cm)	172	169
λ duration	97	96
UV-Vis Kinetic analysis temperature		
Data (x15)	Magnet B (°C)	Control (°C)
Range	20.14-20.99	19.90-21.04
\bar{X}	20.55	20.54
\tilde{x}	20.38	20.41

3.6. Analyte A (PEMF/180 min) exposure methodology

Chemicals

As outlined in section 2.1.1.

Instruments and perishables

Dolphin 3000 PEMF water device

Keybright 34972A temperature data logger/computer system

2 x type K 608-053 310 stainless steel thermocouples

1 x 55 mL new Borosilicate glass beaker w/GL 14 cap

4 x 100mL beakers

Shimadzu UV1900 spectrophotometer (serial no. A 12425601063)

Lab Solutions kinetic software (version 1.03)

Kartell 01960-00 4 clear side disposable polypropylene cuvettes.

Sartorius Proline 1000-5000 μ L adjustable pipette

Sartorius Proline 10-100 μ L adjustable pipette

Digital stopwatch (1 second increments)

PEMF exposure and control reagent concentrations and volumes

Analyte A PEMF (50 mL): (volume modified as per 2.1.1. concentrations)

Analyte A control (50 mL): As above

Analyte B solution (60 mL): (volume modified as per 2.1.1. concentrations)

Thermocouple ambient temperature monitoring solution (60mL): Milli Q H₂O

Method

- 1) The data logger was switched on and the ambient temperature thermocouple was lowered in to the 60mL Milli Q ambient temperature solution and monitoring of ambient laboratory temperature was given time to equilibrate.
- 2) A volume of 50 mL of reagent A was carefully placed in the PEMF reaction vial, then securely fastened with the GL14 cap thermocouple assembly assuring the thermocouple was centrally located in the reagent and not touching the sides of the vessel.
- 3) The reaction vessel was then carefully placed inside the PEMF coil aperture at the position where the PEMF field was measured to have the strongest output.
- 4) The hose connections of the PEMF device and irrigation system were securely fastened, the water circulation pump was turned on and over the course of 5-10 minutes the water bath temperature was adjusted to closely match the ambient temperature measurements.
- 5) When a close correlation between the recirculating water bath and ambient temperature measurements had been identified, the Dolphin 3000 PEMF device was turned on and the instrument start time was noted.

- 6) A period of 180 minutes of PEMF exposure was undertaken whilst closely monitoring and manually calibrating the temperature readouts from the reaction vial with the ambient thermocouple temperature measurements.
- 7) As the 180 minute period of PEMF exposure lapsed, the PEMF device was turned off and the recirculating water was left running for approximately 10 more minutes in order to cool the solenoid for drainage
- 8) Once the solenoid had cooled, the water bath pump was turned off, the water bath system drained, and the reaction vial was immediately removed from the device and left to sit at room temperature for a further 20-30 minutes.
- 9) To avoid external contamination from the irrigation water was avoided, the external area of the reaction vessel underwent two rinses with pure Milli Q H₂O followed by subsequent drying with “Kimi wipes”.
- 10) The reaction vessel lid was carefully unscrewed, the thermocouple removed, and the external thread of the reaction vessel carefully wiped dry again with fresh Kimi wipes
- 11) The PEMF exposure analyte was then carefully decanted into a clean dedicated beaker for UV-Vis analysis.
- 12) During the PEMF exposure treatments the control A & B reagents were positioned at room temperature next to the Milli Q/thermocouple ambient temperature monitoring solution.

3.7. Analyte A (PEMF x 180 min x 5)/control UV-Vis methodology

The Analyte A (PEMF x 180 min x 5) and control (x5) UV-Vis kinetic analysis was conducted under the identical concentrations, reaction dilutions and UV-Vis methodology as that outlined in section 3.1.

3.7.1. Analyte A (PEMF x 180 min) exposure temperature control

The Dolphin 3000 PEMF instrument temperature was well stabilized by the Scanvac refrigerated water bath with manual monitoring and calibration. The peak variation in PEMF and ambient temperatures ranging between 0.72°C and 1.48°C were all brought under 0.5°C in the first 0-8 minutes and stabilized at ≤ 0.2°C in the first 0-30 minutes of the experiments.

Table 3-3: Analyte A (PEMF x 180 min.) & post PEMF temperature calibration (°C)

Replicate set	PEMF/ambient temp calibration (± °C/ 0-180 mins)	Post - PEMF/ambient temp (± °C at 180 mins)
1 x 5	PEMF + 0.72	PEMF + 0.01
2 x 5	PEMF + 0.77	PEMF + 0.01
3 x 5	PEMF + 0.79	PEMF + 0.08
4 x 5	PEMF + 1.48	PEMF + 0.15

3.7.2. Analyte A (PEMF x 180 min) vs control UV-Vis kinetic data

The statistical analysis of the replicate (4 x 5) analyte A PEMF exposure vs control UV-Vis kinetic displacement measurements were conducted between a period spanning 60 to 200 minutes post PEM exposures. Consideration was given to post – PEMF exposure temperature and the commencement of UV-Vis kinetic analysis to fully ensure that PEMF exposure analytes have equilibrated with ambient temperature control analytes.

The statistical analysis of the replicate (4 x 5) analyte A PEMF exposure UV-Vis kinetic displacement measurements for the individual replicate sets were conducted within a time span of 47, 53, 67 and 63 minutes from start to finish.

The statistical analysis of the replicate (3 x 5) corresponding A + B control analyte reaction UV-Vis kinetic displacement measurements were conducted in combination with the correlating magnet B measurements over a span of 95, 77, 78 and 74 minutes for the total corresponding 3 x 10 measurements.

The comparative temperature for magnet B exposure and control UV-Vis kinetic analysis 3 x 5 replicate sets exhibited little variation with spreads of 0.07°C, 0.38°C, 0.06°C and 0.07°C

Table 3-4: Analyte A (PEMF) and (0.3T) and respective control series UV-Vis absorbance commencement, λ_{\max} and displacement duration		
Data (x15)	PEMF A (seconds)	Control (seconds)
Initial λ (0.001cm)	69	70
λ_{\max} (4.000cm)	158	159
λ duration	89	89
UV-Vis Kinetic analysis temperature		
Data (x15)	PEMF A (°C)	Control (°C)
Range	20.93-21.17	20.86-21.15
\bar{X}	21.06	21.03
\tilde{x}	21.10	21.08

3.8. ICP-MS analysis of thermocouple/analyte integrity

At a later date after these clock reaction experiments had been finalised, similar experiments with Na₂CO₃ and Ca(NO₃)₂ analytes researching CaCO₃ kinetics under similar arrangements were conducted, and it was noted that Ca(NO₃)₂ had a good although lowered compatibility rating (B) compared with iodide, thiosulfate and starch (A). ICP analysis was undertaken on two independent sets of Ca(NO₃)₂) control and 180-minute PEMF exposure analytes of stronger concentrations (0.8M) than that utilised with reactant A analytes, to scrutinise whether impurities leached from the type K 608-053 310 stainless steel thermocouple had introduced metal ions in to the reactant A analytes and imparted either an unexpected catalytic effect, or interfered with absorbance measurements. This analysis identified no measurable chromium or nickel ions at the instrumental baseline limit of 1 ppm (see Table 3-5 below).

Table 3-5: ICP-MS Ca(NO₃)₂ (PEMF x 180 min.) and control Cr and Ni analysis				
Factor	Ca(NO₃)₂ analytes			
	PEMF-1	Control-1	PEMF-2	Control-2
Concentration	8mM	8mM	8mM	8mM
Cr scan 1 (ppm)	-1.96	-1.96	-1.97	-1.97
Cr scan 2 (ppm)	-1.97	-1.96	-1.97	-1.97
Cr scan 3 (ppm)	-1.97	-1.96	-1.97	-1.97
Cr (ppm)	-1.97	-1.96	-1.97	-1.97
Cr RSD (ppm)	0.03	0.07	0.03	0.03
Ni scan 1 (ppm)	-1.40	-1.39	-1.40	-1.41
Ni scan 2 (ppm)	-1.40	-1.39	-1.40	-1.41
Ni scan 3 (ppm)	-1.40	-1.39	-1.40	-1.41
Ni (ppm)	-1.40	-1.39	-1.40	-1.41
Ni RSD (ppm)	0.13	0.02	0.13	0.05
Cr wavelength	267.716			
Ni wavelength	231.604			

Chapter 4: Results and Discussion

4.1. Extrapolation of Scavac water bath UV-Vis analysis

The 20.0 to 26.0°C water bath temperature control clock reaction absorbance (λ_{\max}) which displayed excellent linearity and sensitivity has been extrapolated for purposes in this results section (Figure 4-1). The calculated mean, upper and lower 95% confidence intervals have been determined to correlate temperature and UV-Vis analysis integrity with the static magnet, PEMF exposure, and their respective control measurements. The representative temperature ranges and correlating statistics of interest are in bold text on the left-hand side of Table 4-1.

Table 4-1: Extrapolated temperature control (λ_{\max}) UV-Vis upper/lower 95% C.I.

\bar{X} (°C)	\bar{X} (sec)	Upper 95% (°C/sec)	Lower 95% (°C/sec)
19.8	165.1	169.1	161.1
19.9	164.3	168.3	160.4
20.0	163.6	167.5	159.7
20.1	162.7	166.7	159.0
20.2	162.1	165.9	158.3
20.3	161.3	165.0	157.6
20.4	160.6	164.2	157.0
20.5	159.9	163.4	156.3
20.6	159.1	162.6	155.6
20.7	158.3	161.7	154.9
20.8	157.7	160.9	154.2
20.9	156.8	160.1	153.5
21.0	156.1	159.3	152.9
21.1	155.3	158.4	152.2
21.2	154.5	157.6	151.5
21.3	153.8	156.8	150.8
21.4	153.1	156.0	150.1
21.5	152.8	155.1	149.4
21.6	151.5	154.3	148.7
21.7	150.8	153.5	148.1
21.8	150.1	152.7	147.4
21.9	149.3	151.8	146.7
22.0	148.5	151.0	146.0
22.1	147.8	150.2	145.3
22.2	147.0	149.4	144.6

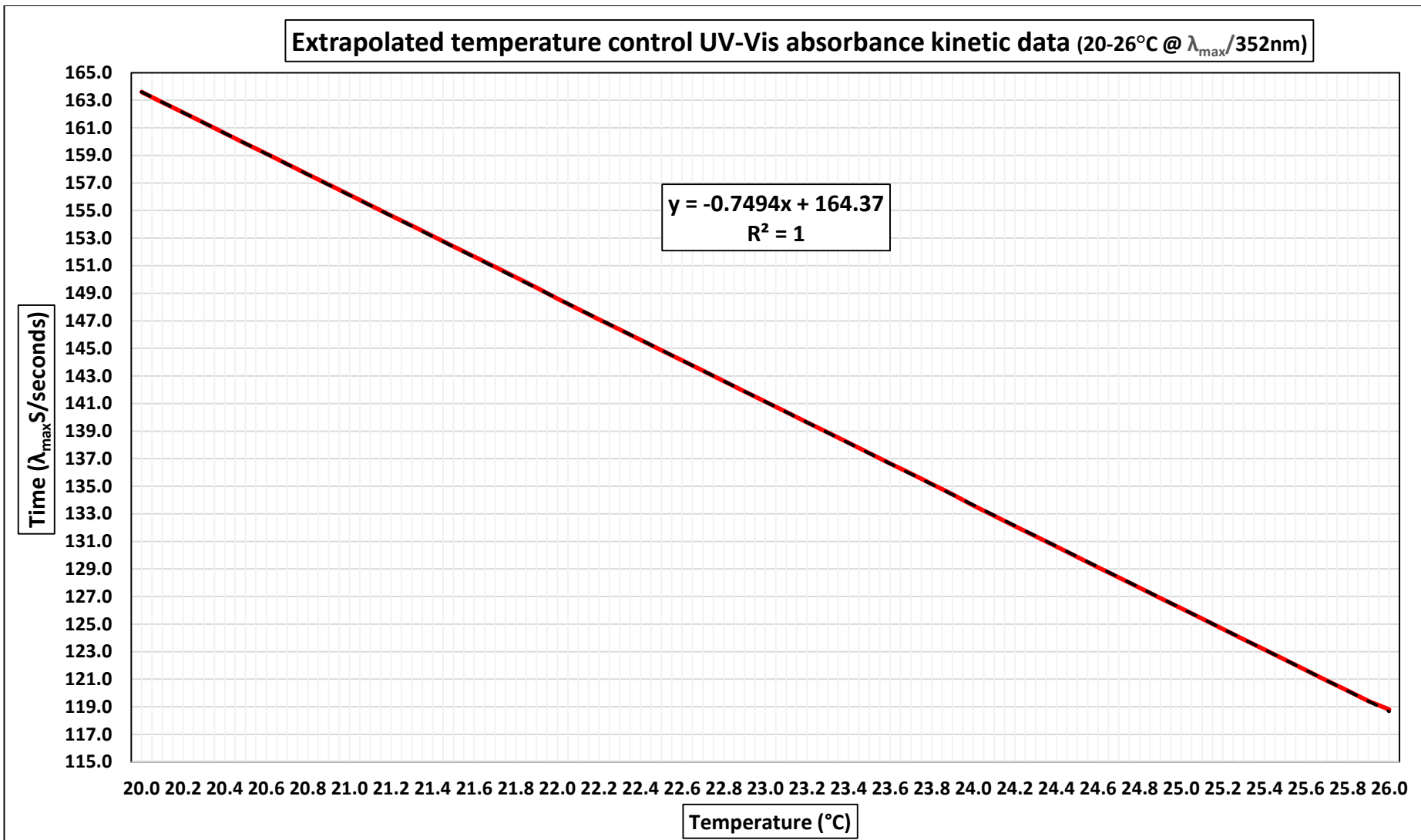


Figure 4-1: Extrapolation of Figure 2-5 temperature-controlled UV-Vis mean λ_{\max} absorbance (20.0°C, 22.0°C, 24.0°C, 26.0°C x 5 replicates) incorporating calculated 0.2°C gradient intervals.

4.2. Analyte A (0.3T) vs control UV-Vis kinetic results

The statistical kinetic calculations revealed that the initial increase in kinetic absorbance displacement, peak and duration was basically identical, however, despite these identical reaction rate profiles, a closer inspection of the respective kinetic rates (see Figure 4-2) identified that the magnetic exposure analytes exhibited higher kinetic absorbance differential commencing at 95 seconds, and peaking at 136 seconds by an absorbance factor of 0.224 equating to an 11.75% increase comparative to the control kinetic rate at 136 seconds, prior to the respective kinetic rates merging again at 148 seconds. However, this overall result must be deemed as a non-significant finding as there was standard error overlap between 0.3T magnet A exposure and corresponding control replicate reaction sets throughout the entirety of the aforementioned differential kinetic displacement absorbance curves (Figure 4-1)

The respective temperature range and mean, and λ_{\max} for the data sets were analysed against an extrapolated breakdown of the mean, upper and lower 95% limit data taken from the temperature control absorbance kinetics to identify how well these results matched sensitivity and linearity in that data set, and it was identified that the respective (0.3T x 180 min.) analyte A and control kinetic ranges fell within the mean and upper 95% ($\lambda_{\max}/\text{sec.}$) range of the extrapolated data.

Table 4-2: Analyte A (0.3T x 180 min. x 15) and control (x 15) temperature control statistical comparison correlated with λ_{\max} and temperature

	Analyte A (0.3T)			Control A		
	$\lambda_{\max}/\text{sec.}$	\bar{X} (°C)	Range	$\lambda_{\max}/\text{sec.}$	\bar{X} (°C)	Range
Experimental	157	21.26	20.8-22.0	158	21.26	20.8-21.9
Temp control/UV-Vis kinetic correlations*						
146-152	(°C)			Sec.		
			Sec.	(°C)	Sec.	Sec.
95% Lower	21.28	157.6	151-162	20.25	157.6	147-154
Mean	20.75	154.5	148-158	20.75	154.5	149-158
95% Upper	20.40	152	146-152	21.15	152	152-162

* Data extracted from Table 4-1.

Respective displacement kinetics for (0.3T x 180 min.) analyte A (x 15) and Control (x 15) series

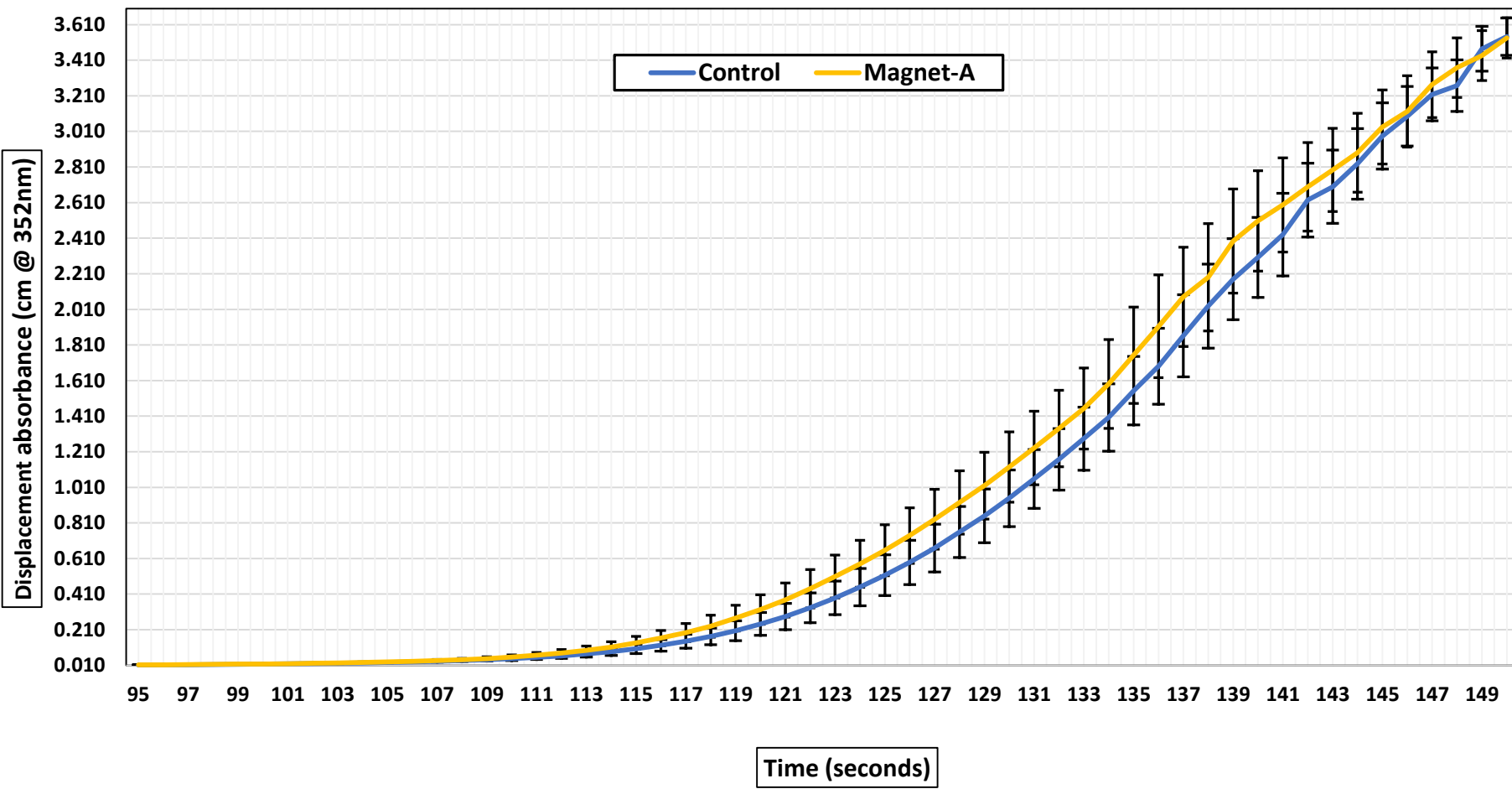


Figure 4-2: Differential replicate (x 15) analyte A (0.3T x 180 mins) displacement and replicate (x 15) control displacement (at 95 - 150 sec) incorporating overlapping experimental standard error bars.

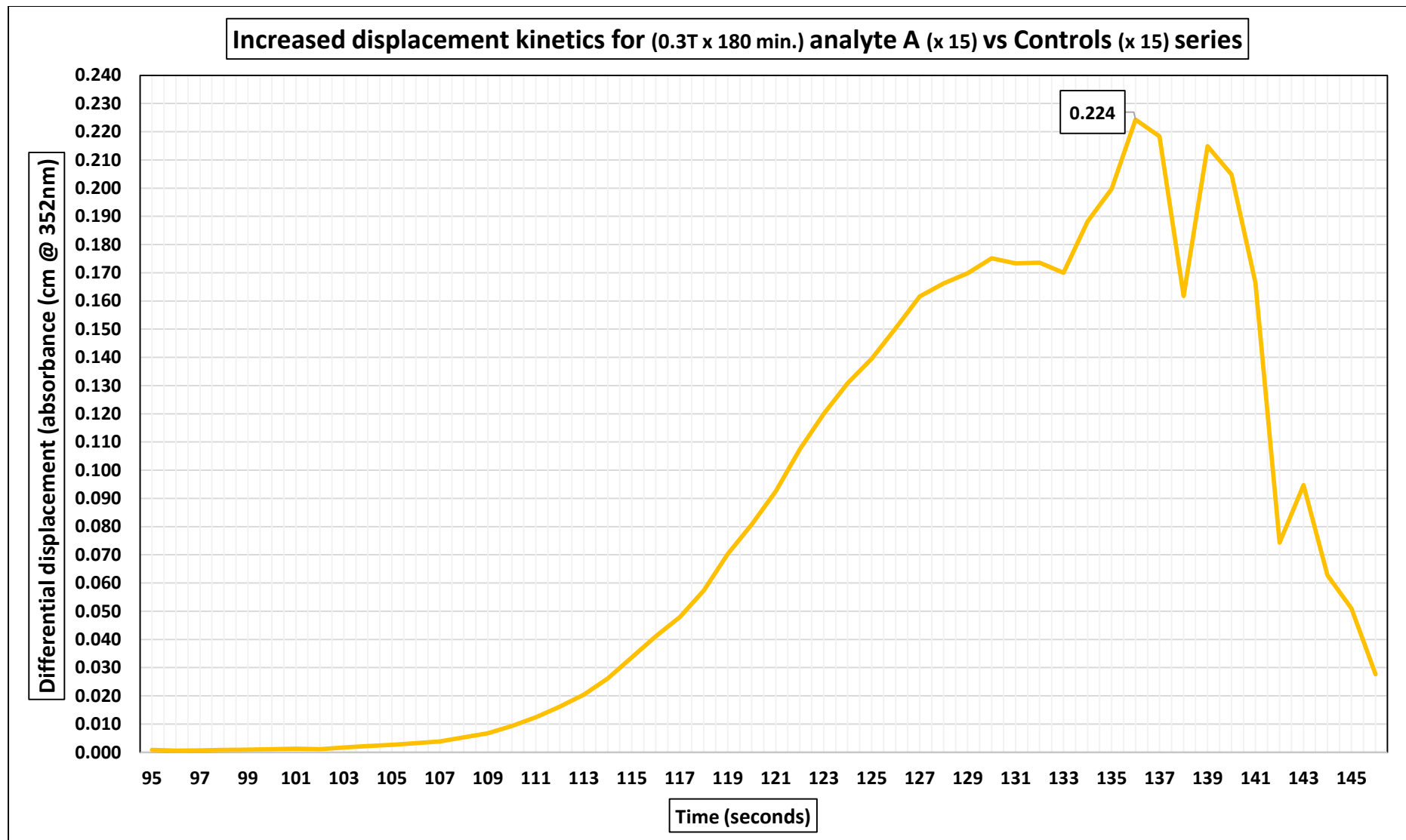


Figure 4-3: Increased differential analyte A (0.3T x 180 mins) series displacement in comparison to control series displacement (95 - 146 sec)

4.3. Analyte B (0.3T) vs control UV-Vis kinetic results

The statistical analysis of the 15 replicate control and analyte B 0.3T magnet exposure UV-Vis kinetic displacement measurements revealed a minimal variation in the comparative statistical range, mean and median readings of the respective data sets, and the statistical kinetic calculations revealed that the initial increase in kinetic absorbance displacements, peaks and duration again revealed little variation.

A deeper look at the data revealed an interesting observation, which was that the control analytes exhibited higher differential absorbance kinetics on this occasion, despite relatively well agreed overall absorbance commencement and duration profiles commencing at 95 seconds and peaking at 151-152 seconds. This increased control displacement absorbance factor peaked at 0.284 at 151-152 seconds, equating to an 11.85% increase comparative to the Magnet B exposed kinetic rate at 151-152 seconds, prior to the respective displacement curves merging again at 171-172 seconds.

However, as identified in the reactant A magnet and control absorbance series, the error overlap was again present throughout the displacement increase in the respective reactant B magnet and control differential displacement curves.

The second interesting observation is that the maximum differential increases closely correlated to the overall differential displacement percentage identified in the Magnet A vs control data (11.75% vs 11.85%), except with a reversal of kinetic displacement between the 0.3T magnet exposed analytes and the respective control series.

The respective temperature range and mean, and λ_{\max} for the data sets was analysed against an extrapolated breakdown of the mean, upper and lower 95% limit data taken from the temperature control absorbance kinetics to identify how well these results matched with the good sensitivity and linearity in that data set, and it was identified that the respective (0.3T x 180 min.) analyte B and control kinetic statistics ($\lambda_{\max}/\text{sec.}$) both fell well outside of the extrapolated ranges (Table 4-3).

Table 4-3: Analyte B (0.3T x 180 min. x 15) and control (x 15) and temperature control statistical comparison correlated with λ_{\max} and temperature						
	Magnet B			Control B		
	$\lambda_{\max}/\text{sec.}$	\bar{X} ($^{\circ}\text{C}$)	Range	$\lambda_{\max}/\text{sec.}$	\bar{X} ($^{\circ}\text{C}$)	Range
Experimental	172	20.55	20.14-20.99	169	20.54	19.90-21.14
Temp control/UV-Vis kinetic correlations*						
	Magnet B			Control B		
C.I.	($^{\circ}\text{C}$)	Sec.	Sec.	($^{\circ}\text{C}$)	Sec.	Sec.
95% Lower	-	163	153-159	-	163	152-160
\bar{X}	-	159.5	155-160	-	159	159-164
95% Upper	-	155.2	160-166	19.8	155	158-168

* Data extracted from Table 4-1.

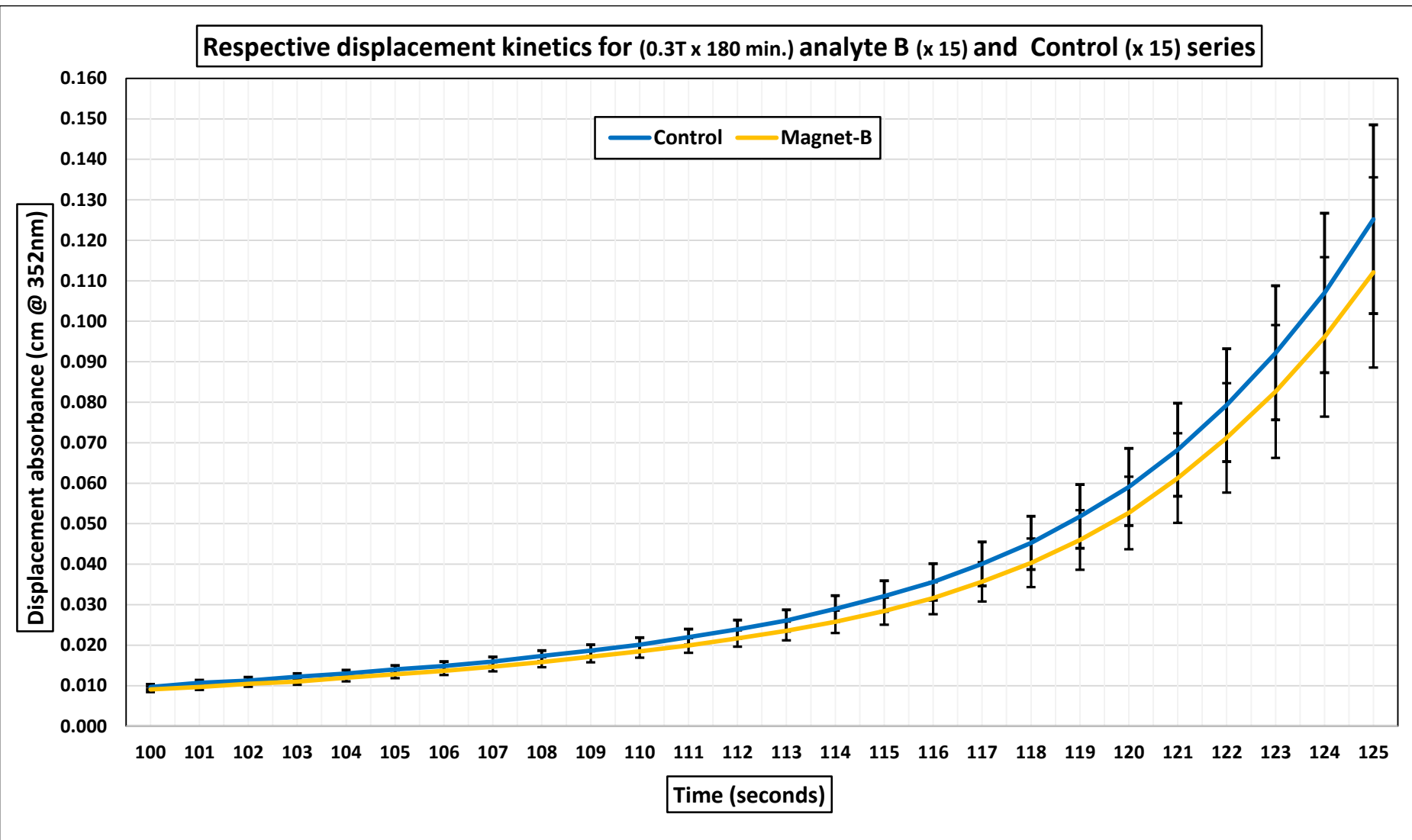


Figure 4-4: Differential replicate (x 15) analyte B (0.3T x 180 mins) displacement and replicate (x 15) control displacement (at 100 – 125 sec) incorporating overlapping experimental standard error bars.

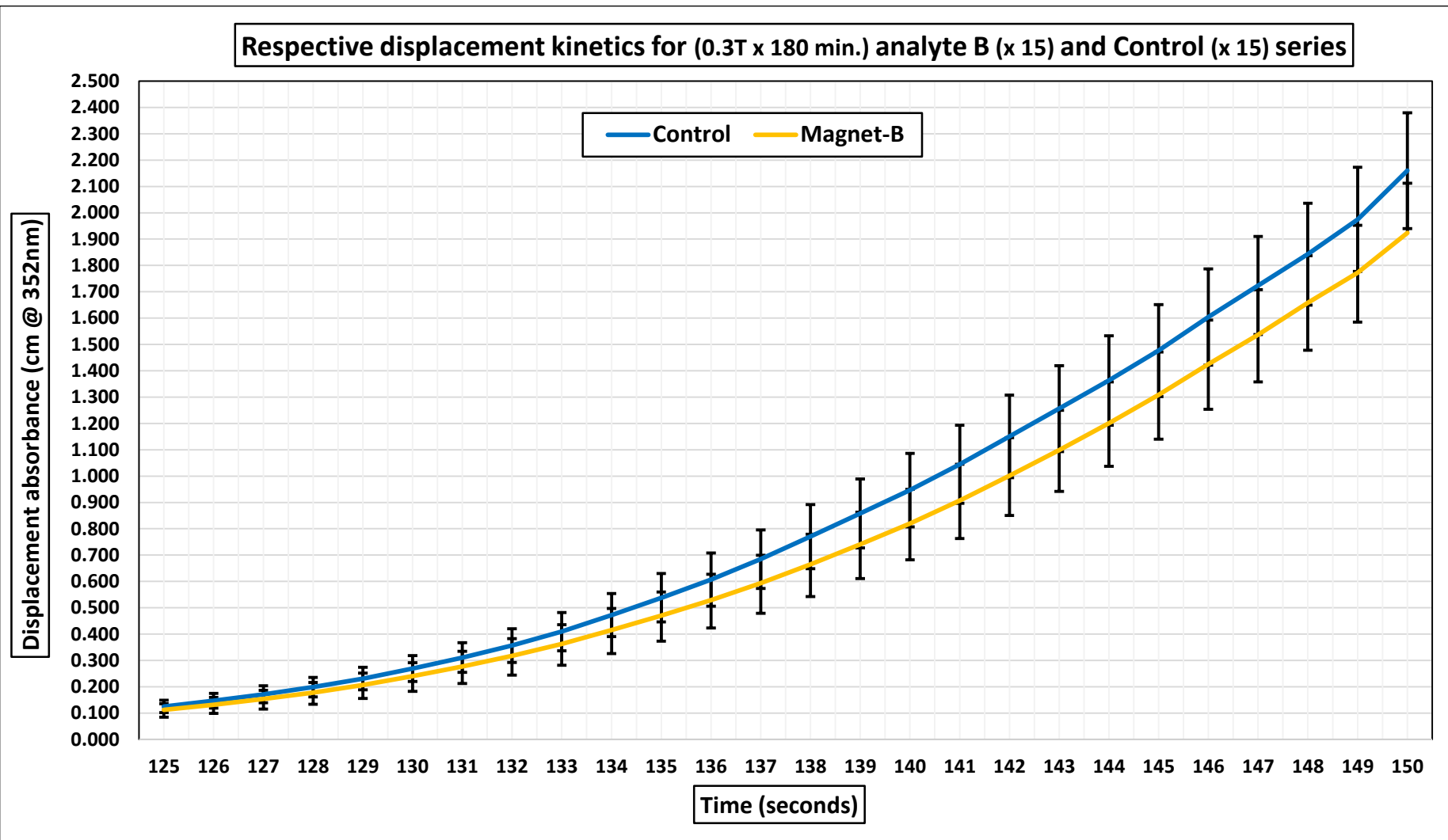


Figure 4-5: Differential replicate (x 15) analyte B (0.3T x 180 mins) displacement and replicate (x 15) control displacement (at 125 – 150 sec) incorporating overlapping experimental standard error bars.

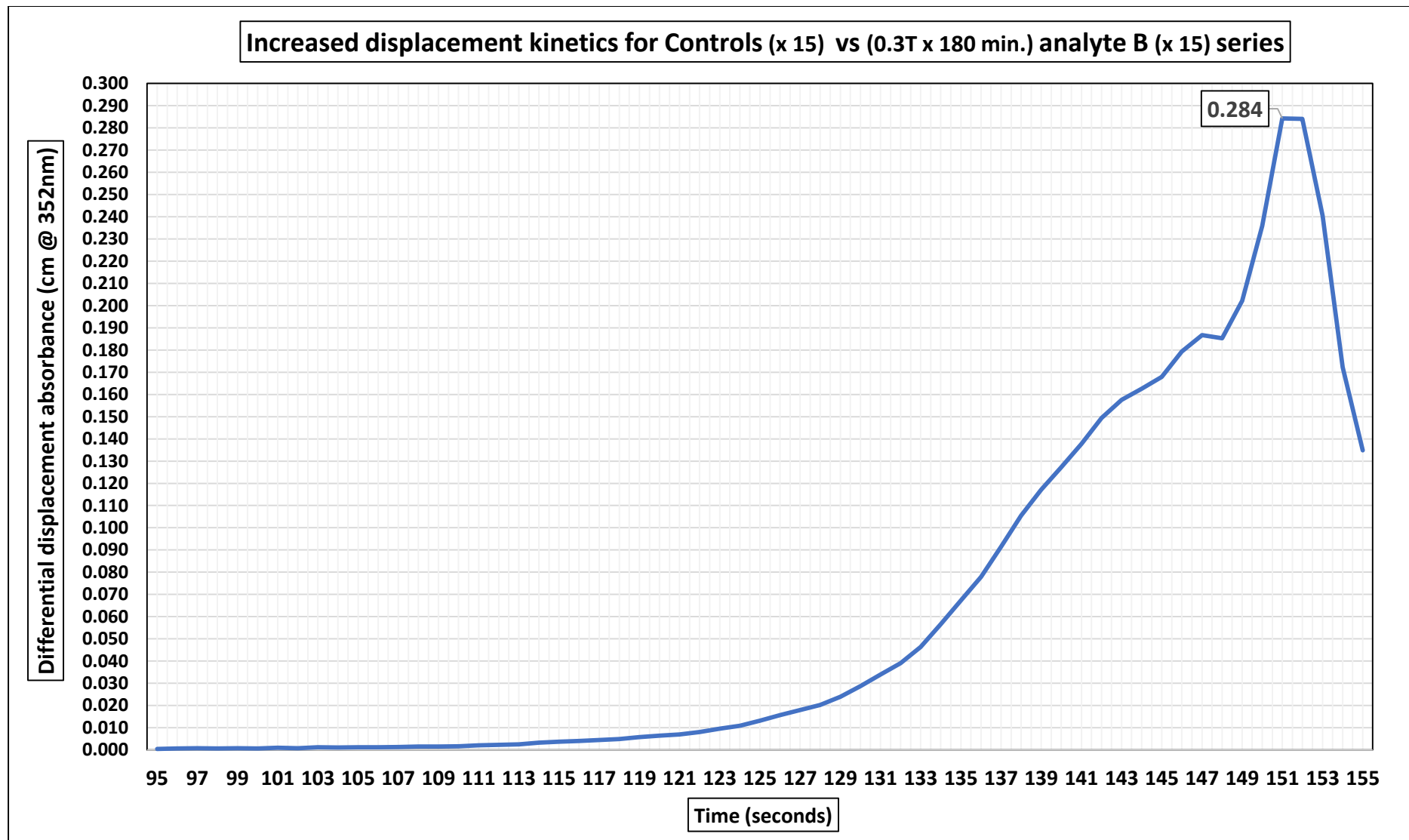


Figure 4-6: Increased differential to control series displacement in comparison to analyte B (0.3T x 180 mins) series displacement (95 - 152 sec)

4.4. Analyte A/B (0.3T) and temperature discussion

As pointed out previously, the maximum magnet exposure differential increases were in close correlation, but in reverse absorbance kinetic differential profiles. A third interesting observation was that the comparative respective correlating magnet A-control and magnet B-control replicate series exhibited notable variation UV-Vis absorbance kinetic rate data.

Table 4-4: Analyte A/ B (0.3T) and control series analysis				
Measurement	UV-Vis kinetic displacement and temperature (x 15)			
352nm/seconds	Analyte A	Analyte B	A control	B control
1st λ (0.001cm)	67	75	68	73
λ_{max} (4.000 cm)	157	172	158	169
λ duration	90	97	90	96
Temp (°C)				
UV-Vis range	20.85-22.02	20.14-20.99	20.86-21.90	19.90-21.04
UV-Vis \bar{X}	21.26	20.55	21.26	20.54
UV-Vis \tilde{x}	21.12	20.38	21.12	20.41

As can be identified from that data above, the magnet A and control A kinetic rates and temperatures were in good agreement with the data extrapolated from temperature controlled kinetic statistics, and furthermore, the difference in kinetic displacement in the magnet and control A data comparisons at 136 seconds identifies a correlated 16 second increase in the reaction rate at a temperature of 25.8°C, some 4.5°C above the temperature mean taken at the times of UV-Vis analysis, and 4.9°C above the replicate mean based upon reaction times.

These measurements were also considerably above the maximum temperature recorded in the entire reactant A magnet exposure data set (22.02°C = +3.6 °C), and the differential also exhibited a higher kinetic rate than the overall than the displacement profile extrapolated from the 22.0 °C at 136 seconds (0.224 vs 0.139) which was some 0.74°C higher in temperature than the Magnet A data set mean.

Table 4-5: Analyte A (0.3T x 180 min.) and temperature-controlled differential kinetic rate comparison (100-136 seconds)

UV-Vis displacement (Seconds)	Analyte A (0.3T) Displacement (352 nm) ($\bar{X} = 21.26^{\circ}\text{C}$) #	Temperature control Displacement (352 nm) (22.0°C data set) *	Displacement variation (\pm) (352 nm)
100	0.001	0.001	-
104	0.002	0.002	-
108	0.005	0.003	~
112	0.016	0.006	0.010
116	0.041	0.015	0.026
120	0.081	0.035	0.046
124	0.131	0.067	0.066
128	0.166	0.104	0.062
132	0.174	0.132	0.052
136	0.224	0.137	0.087

Data extracted from analyte A (0.3T x 180 min. x 15) differential displacement as observed in Figure 4-2 between 100-136 seconds,

* Data extracted from Table 4-1

Based on these findings in isolation, it can be hypothesized with some confidence that this increased kinetic differential is outside a margin for error, particularly considering the analyte A (0.3T x 180 min. x 15) median temperature (21.26°C) and overall temperature range of the 3 x 5 replicate analysis (20.85 – 22.02°C), in comparison to the displacement kinetics observed with the temperature controlled series at 22.00°C, because logic would concede that the lower temperature set should have exhibited complimentary slower kinetics. However, the overlap in the 95% C.I of the analyte A (0.3T x 180 min. x 15) series with its correlating control series (x 15) still needs to be taken in to account. The analyte B (0.3T x 180 min. x 15) and its correlating control B series (x 15) significantly contradicted similar temperature controlled kinetic correlations for that respective data.

A critical examination of the variation in temperature at the time UV-Vis kinetic analysis in the static magnet reactions identified that reactant A and B exhibited opposing differential profiles relative to their respective control series, but this alone does not inform of anything other than the random chance arising from the flipping of

a coin, as it is expected that any given treatment and reference data set would randomly favor one or the other when replicate kinetic absorbance evaluations of a Brownian and thermal motion dependent solute reaction. This position is further reinforced when perpetual error overlap is identified throughout both analyte 0.3T magnet exposure replicate and respective control sets.

Table 4-6: Analyte A/ B (0.3T x 180 min.) and control comparisons			
Factor	A – 0.3T (x 15)	B – 0.3T (x 15)	A/B variation
Initial λ (0.001 cm) (sec)	67	75	8
λ_{max} (4.000 cm) (sec)	157	172	15
$I_3^-/starch$ time (sec)	90	97	7
(0.3T) UV-Vis (°C)	20.85 – 22.02	20.14 – 20.99	\pm 0.29 - 1.03
Control UV-Vis (°C)	20.86 – 21.90	19.90 – 21.04	\pm 0.96 - 0.86
0.3T vs control (°C)	1.17 vs 1.04	0.85 vs 1.14	\pm 0.32 - 0.10
Spread differential (°C)	0.13	0.29	\pm 0.16
0.3T UV-Vis \bar{X} (°C)	21.26	20.55	\pm 0.71
Control UV-Vis \bar{X} (°C)	21.26	20.54	\pm 0.72
0.3T vs control \bar{X} (°C)	Nil	0.01	\pm 0.01
0.3T (x 15) vs Control (x 15) differential displacement			
Factor	Analyte A 0.3T vs control	Analyte B 0.3T vs control	
Maximum (cm)	+ 0.268	- 0.284	
Maximum (%)	+ 14.00%	- 11.45%	
Error overlap	Consistent	Consistent	

4.5. Analyte A (PEMF) vs control UV-Vis kinetic results

The temperature correlations for the respective PEMF-A and control UV-Vis kinetic analyses exhibited very minor variation over the measurement ranges (20.93 - 21.17°C vs 20.86 - 21.15°C) supported a minuscule shift in the respective temperature analysis mean of 0.03°C which would not impact rate kinetics at a 0.1 second level, according to the temperature controlled kinetic correlations.

The PEMF-A differential data exhibited a good linear increase in reaction rate, with a minor fluctuation at 142 seconds, then 146 seconds prior to the differential increase maximizing between 148 and 149 seconds, however, this is to be expected as both data sets approached maximum absorbance within the final 10 seconds and the largest exponential increases in absorbance were occurring. The PEMF-A analyte reactants became exhausted as this set of reactions reached completion, as the control kinetic rate was reaching peak intervals of displacement.

The respective PEMF-“A” and control temperature ranges were in good agreement with the calculated temperature controlled kinetic statistics with both just outside the mean correlating λ_{max} and inside the upper 95% limit. Likewise, the PEMF-A analytes were inside the upper 95% limit based on the temperature mean data set, bordering on the temperature control mean range, whilst the control A analytes fell fractionally outside these respective ranges. The overall respective temperature ranges of UV-Vis analysis agreed with both the mean and upper 95% limits of the temperature control data (see Table 4-7 **bold**).

Table 4-7: Analyte A (PEMF x 180 min. x 20) and control (x 20) and temperature control kinetic statistical data comparisons*						
	PEMF-A			Control-A		
Experimental	$\lambda_{max}/sec.$	\bar{X} (°C)	Range (°C)	$\lambda_{max}/sec.$	\bar{X} (°C)	Range (°C)
	158	21.06	20.9-21.2	159	21.03	20.9-21.2
Analyte A PEMF and Control (x 20)/Temp controlled UV-Vis data correlations*						
Temp Control	(°C)	Sec.	Sec.	(°C)	Sec.	Sec.
95% Lower	20.2-3	152-3	152-154	20.1	154	152-154
\bar{X}	21.2	159-60	158-160	21.1	160	<159.9
95% Upper	21.1	158-9	157-160	21.0	160	157-60

* Data extracted from Table 4-1

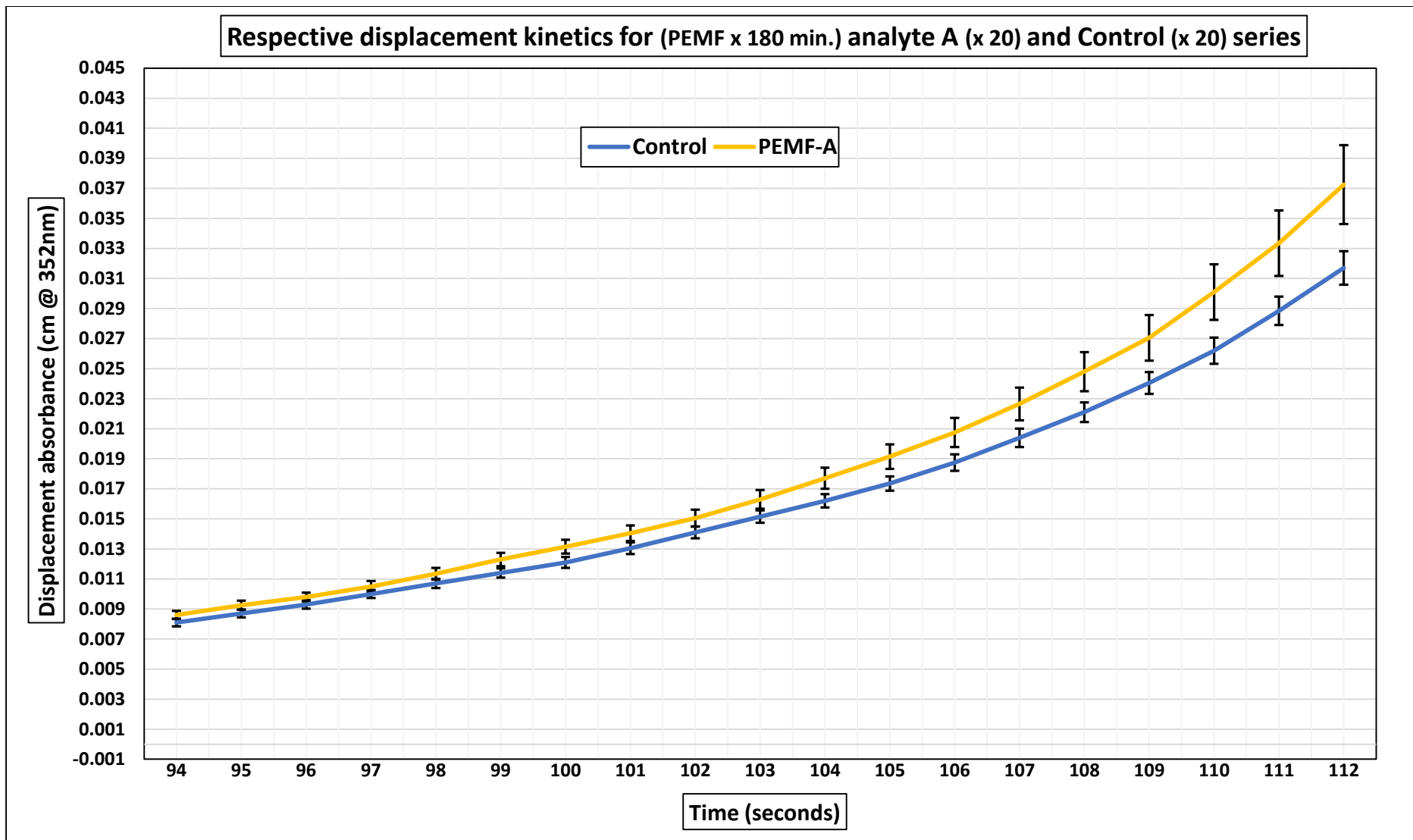


Figure 4-7: Differential replicate (x 20) analyte A (PEMF x 180 mins) displacement and replicate (x 20) control displacement (at 94 – 112 sec) incorporating experimental standard error bars.

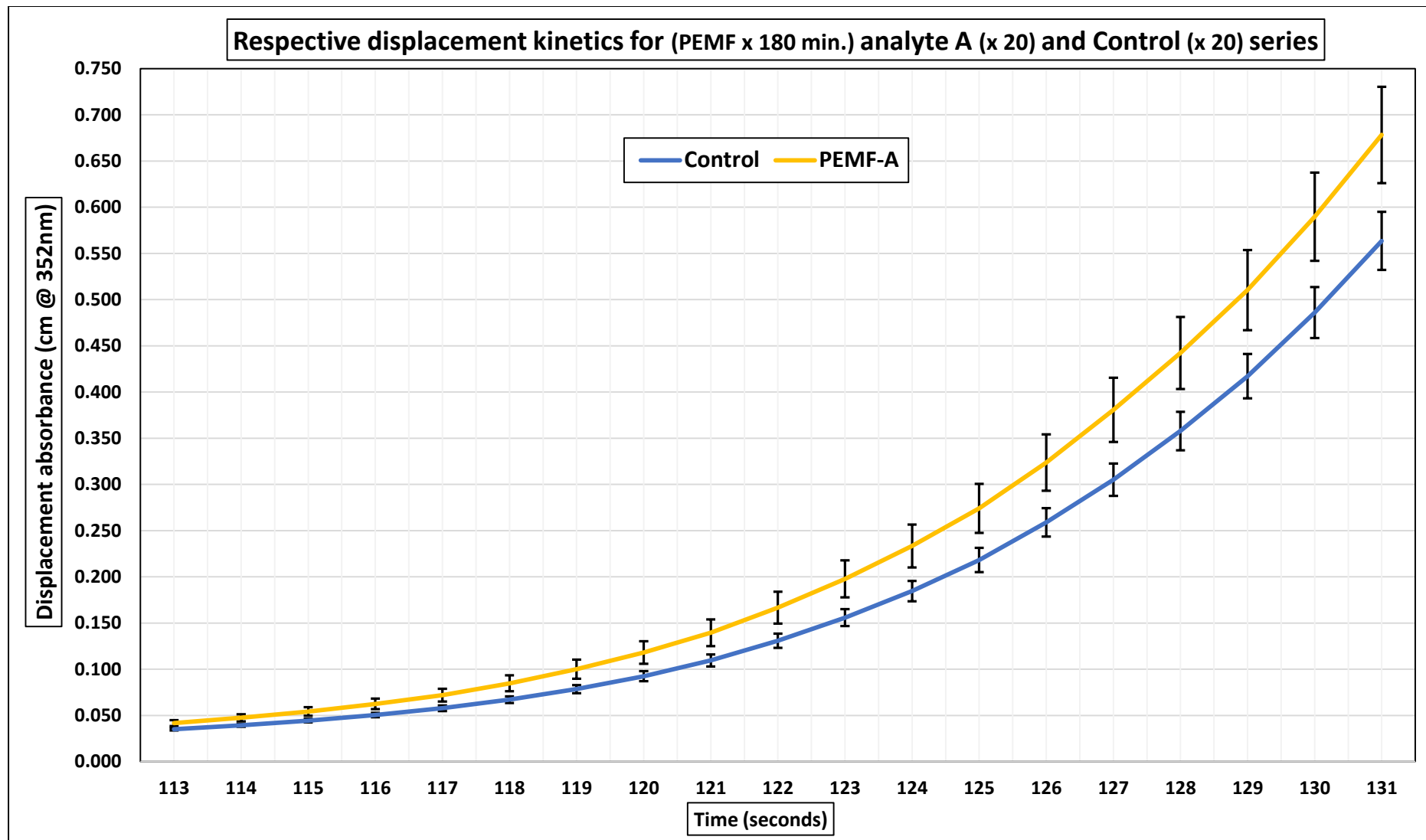


Figure 4-8: Differential replicate (x 20) analyte A (PEMF x 180 mins) displacement and replicate (x 20) control displacement (at 113 – 131 sec) incorporating experimental standard error bars.

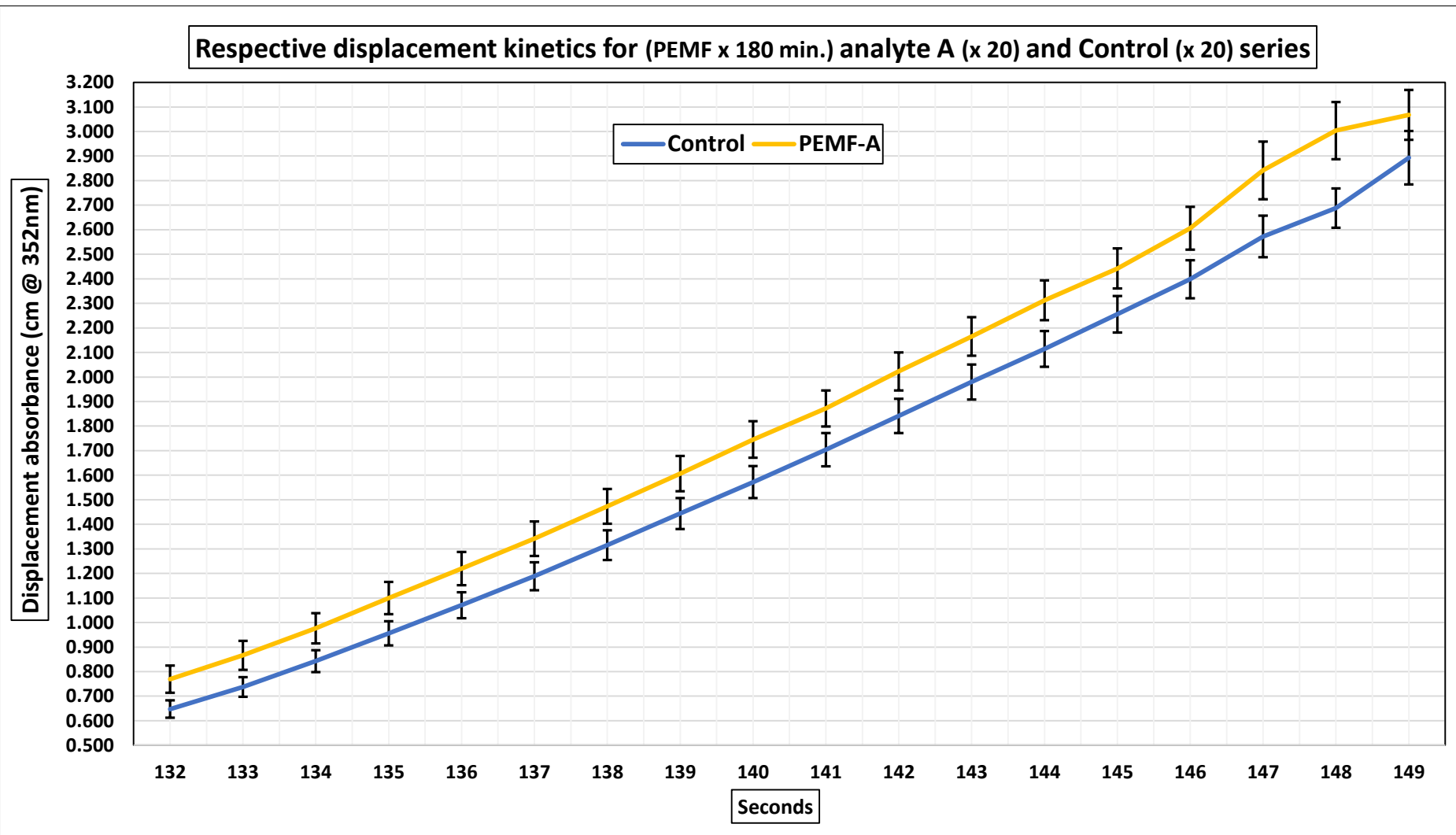


Figure 4-9: Differential replicate (x 20) analyte A (PEMF x 180 mins) displacement and replicate (x 20) control displacement (at 132 – 149 sec) incorporating experimental standard error bars.

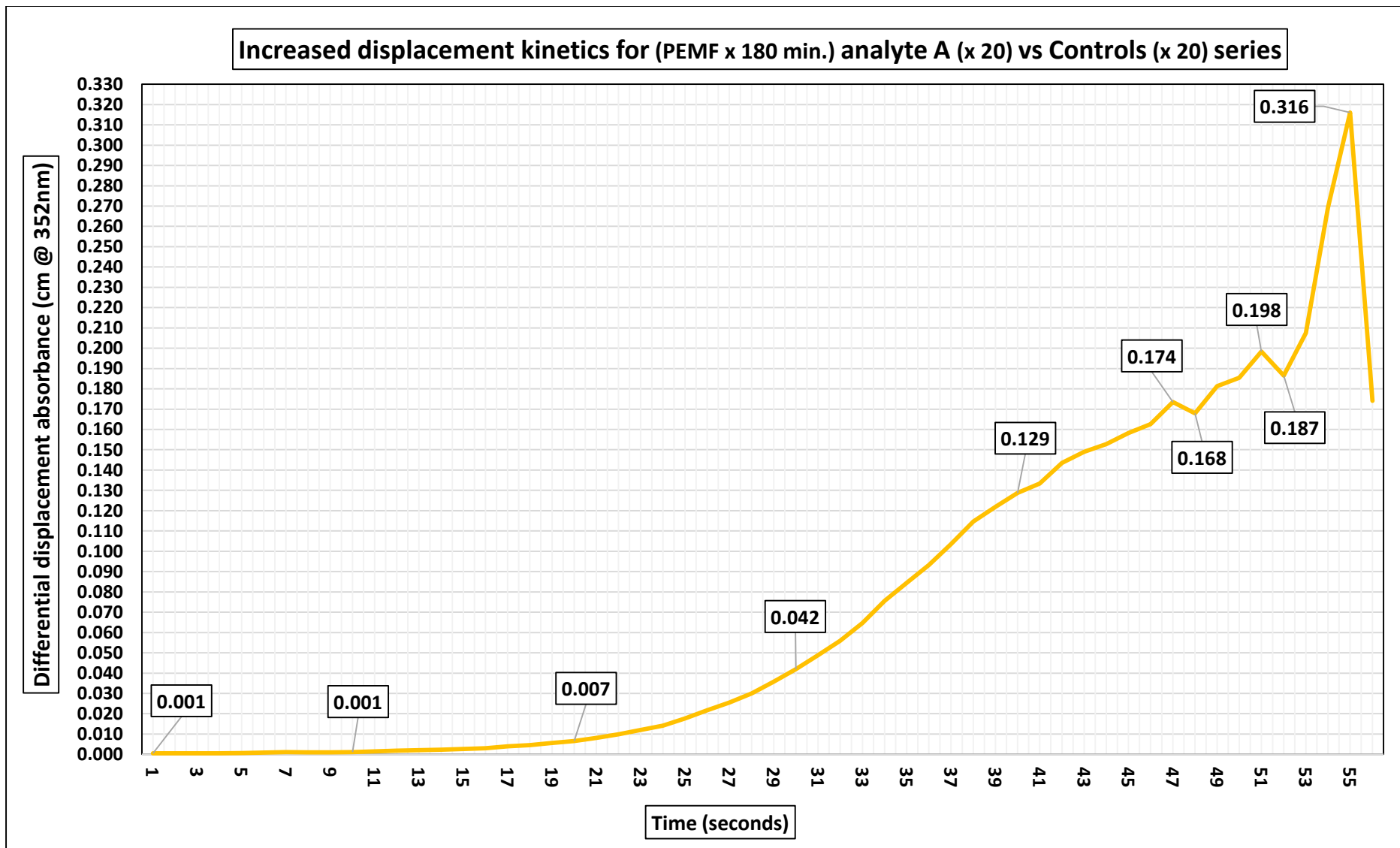


Figure 4-10: Increased differential analyte A (0.3T x 180 mins) series displacement in comparison to control series displacement (94 - 149 sec)

4.6. Analyte A (PEMF and 0.3T magnet) discussion

The first thing of note identified from this PEMF series of experiments was how closely the exposure and control kinetic rate factors of initiation, cessation and duration correlated with each other, and with the related reactant “A” and control replicate data.

Table 4-8: Analyte A (PEMF) and (0.3T) and respective control series UV-Vis absorbance commencement, λ_{\max} and displacement duration			
Data set	Initial λ (0.001cm)	λ_{\max} (4.000cm)	λ duration
PEMF-A	69	158	89
PEMF control	70	159	89
Magnet-A	67	157	90
Magnet-A control	68	158	90

The outcomes of the reactant “A” exposure and control comparisons also identified an increase in PEMF-“A” kinetic differential, as was identified in the 0.3T magnet-“A” v control experiments, with the exception that the exposure vs control differential kinetic increase was sustained for longer (Figure 4-2: 0.3T @ 41 seconds vs Figure 4-9: PEMF @ 54 seconds)

4.7. Atmospheric gasses and this research

Whilst it is a reasonable conclusion that temperature range and variability and correlated aqueous thermal kinetic variation can explain the ambiguous outcomes in the 0.3T permanent magnet experiments, there are some theoretical musings that could explain a notable point of interest in the experimental data, being the increased kinetic rate differential in the reactant A analyte exposed to the permanent magnet and the pulsed electromagnetic field, comparative to their respective controls. A review of the mechanistic aspects tabled in this paper with regard to magnetic fields, H₂O and ionic solutions outlines many theoretical mechanisms incorporating the interplay between the magnetic field with existing dissolved or field generated absorption and diffusion of atmospheric gasses, with the aqueous ionic

investigations hypothesise alterations of ion hydration and hydrogen bonding, cationic impacts relative to ionic charges, Lorentz Force impacts on diffusion and radical “*spin mixing*” as previously discussed (Colic and Morse, 1999, Valee et al., 1999, Lee et al., 2013, Shcherbakov et. al, 2020, Pan et al., 2019)

The impacts of the absorption of atmospheric gasses cannot be precluded from the research, and multiple weeks of experiments in CaCO_3 kinetics incorporating Na_2CO_3 and $\text{Ca}(\text{NO}_3)_2$ precursors, the integrity of which were ultimately undermined when it was deemed that atmospheric absorbed CO_2 significantly impacted the experiments, rendering them useless even when the fresh stock solutions were tightly sealed, and atmospheric absorption exposure time was minimised.

It is not expected that anything to that extent occurred with the clock experiments, however the reactant A and B magnet and control analytes were open to the atmosphere during exposure, and consequently during UV-Vis analysis atmospheric mitigation protocols were not undertaken. A point of note is that PEMF-A analytes were quickly placed in the reaction vessel, from the sealed stock solutions, and tightly secured for PEMF exposure for at least 180 minutes in comparison to controls, and prior to UV-Vis analysis, thereby limiting atmospheric gas absorption exposure time in these experiments, and possibly inducing atmospheric gas diffusion in the closed reaction vessel headspace. This may be a factor as to why error overlap with the corresponding controls did not emerge in these experiments during the increased absorbance kinetic differential phase.

4.8. The Piyadasa hypothesis

The Piyadasa research relating to brief ESI-MS analysis noted a decrease in cationic hydrated cluster size and put forward a mechanism that an experimentally observed increase in CaCO_3 turbidity and absorbance nucleation kinetics emerging from precursor analytes that underwent PEMF exposure with the Dolphin 3000 device. A first observation being that the major peaks in the Ca^{2+} spectra of the 5mM analyte exposed to PEMF treatment are still present, with the 2nd major peak increasing by 14-15% in relative abundance. However, there does not appear to be any significant

shifts outside 1400-1700 m/z range. Conversely, the 5mM control monovalent Na⁺ ion hydration clustering has clearly been impacted to a greater degree by PEMF exposure, with significantly higher ratios of smaller clustering identified in these spectra (see Figures 1-42 to 1-45).

These outcomes would appear to be consistent with several computer simulations analysing hydration energy and entropy focusing on aqueous ionic models, such as that conducted by Saha and Mukherjee in 2016 (page 96) which calculated the translational and rotational entropy's ($T\Delta S$) of H₂O in the 1st and 2nd hydration shells related to various hydrated ionic species, including sodium and calcium cations (see Table 1-13). As can be seen in this modelling, the Ca²⁺ (H₂O)_n thermodynamic kinetics exhibit ~16% less translational entropy in the 1st hydration shell whilst maintaining comparable 1st shell rotational entropy with Na⁺ (H₂O)_n kinetics. Likewise, the 2nd shell translational entropy is basically identical relative to (H₂O)_n configurations, but approximately 35% more H₂O molecules are to some extent fixed in the rotational state of the Ca²⁺ cation over this 50ns scan. This analysis also conducted calculations of various hydrated anions and noted that the H₂O entropy exhibited in divalent anions was similar to that identified in monovalent cation entropy kinetics.

The literature would also suggest that there's a kinetic trade-off in Ca²⁺ and CO₃²⁻ ionic pairing reaction rates when the supramolecular H₂O environments and respective ionic hydration are altered by magnetic field interactions, and the notion of increased aqueous ionic reaction kinetics related to PEMF and SMF exposure also needs to take in to account a significant volume of research literature consensus relating to strengthened H₂O intra cluster binding energies at the expense of inter cluster kinetics, supported by MSD modelling and multiple reports of lowered diffusion, and increased viscosity, surface tension, cohesion and evaporation, with the combined impacts this would have on nucleation kinetics as previously tabled (Toledo et. al, 2008, Gutierrez-Mejia and Ruiz-Suarez, 2012, Moosavi and Gholizadeh, 2014, D'Emilia et. al, 2015, Usanov et al., 2016, Chirkova et. al, 2019).

Question

When the cationic and anionic hydration characteristics of the Piyadasa and reactant A precursors are considered, is there a strong correlation in the UV-Vis absorbance kinetics which would support the altered ion cluster hydration hypothesis?

The Piyadasa hypothesis and this research

It is feasible to question whether hydrated anions undergoing identical treatment would not also exhibit considerable hydration structure deformation and take in to account that thiosulfate and carbonate ions and their complementary reaction anions nitrate and iodide, exhibit similar comparative ratios of charge, diffusion coefficients and hydrodynamic radius, as identified in Table 1-11 (page 94).

The ionic analytes utilised in this research were all monovalent sodium cationic salts, so a conclusion drawn from this almost identical PEMF exposure and control kinetic rate emergence correlations, that if the PEMF exposure induced higher populations of smaller Na^+ ion hydration clusters, then this did not appear to play any part in the iodide and thiosulfate redox mechanisms outlined in steps 1 and 2 of the clock reaction sequence.

This particular research focused not only on the triiodide – starch complex, but the generation of triiodide ions in isolation utilising UV-Vis analysis at 352nm, and these outcomes would not support a mechanism that iodide and iodide complexation kinetics were increased due to PEMF induced shifts in anionic hydration arrangements or lability, and it is likely counterintuitive to consider a kinetic increase would only emerge after the initial redox mechanisms in steps 1 and 2 of the reaction had concluded, as any cluster alteration charge related phenomena of the triiodide complexation would have also impacted the kinetic rate of $\text{S}_2\text{O}_3^{2-}$ consumption.

It appears to be increasingly likely that the starch molecule under PEMF exposure, and possibly with permanent magnet exposure, is the main player in driving the identified increased reactant A differential kinetics. In conclusion to this section, this research would not dismiss the Piyadasa hypothesis, but in comparison with this

work, it appears that at least regarding salt nucleation, either the charge of the cationic species (Ca^{2+}), concentration (5mM + 5mM vs 30mM + 15mM) and/or precursor chemical properties (ionic salts vs ionic salts + starch molecules) played some role in those reported outcomes.

4.9. Analyte A magnetic susceptibility factors

Focusing on the magnetic aspects of H_2O and the respective ionic species present in reactant A, the diamagnetic susceptibilities set out in Table 1-18 (page 105), a conclusion can be drawn that if increased diamagnetic repulsion in the 0.3T and PEMF magnetic field exposure A analytes instigated higher ionic diffusion kinetics via Lorentz force factors, and/or reconfigurations of hydration cluster and contact ion binding energies, then this would have also been revealed in the oxidation of iodide in the presence of acidic bromate ions, and to some extent in the following reduction of formed iodine by thiosulfate ions would have also been noted. The UV-Vis absorbance kinetic data does not support this.

The similarities in reaction kinetics of both reactant A magnetic exposure methods in comparison to each other, and with their virtually aligned corresponding control kinetic data at the point of reaction initiation, would reinforce the view that magnetic field induced ionic hydration aspects were not responsible for the observations revealed in absorbance, at least as far as the aforementioned redox steps 1 and 2 of this reaction are concerned.

This motivates further investigation for increased kinetics at step 3, triiodide complexation, or step 4, the kinetic enhancement of the triiodide-starch inclusion, or perhaps a combination of both reactions.

4.10. ICP-MS analysis of PEMF thermocouple/analyte results

This ICP-MS analysis identified no measurable chromium or nickel ions at the instrumental threshold baseline limit of 1 ppm.

Chapter 5: Conclusions

5.1. Factors to consider for analyte A PEMF and static magnet differential kinetics

An interesting starting point can be drawn from works in several different fields, which have been covered in the literature review, commencing with the observations of analytes under flow through a static magnetic field affording $0.7\text{--}0.9\text{T m}^{-2}$ that focused on the impacts on electron exchange in various chemicals including glucose, as outlined previously on page 110 by Bozic, Lipus and Kokol (2008).

The electrode oxidation-reduction potential (ORP) measurements impacted alkaline aqueous glucose solutions, with this group hypothesising a possible mechanism arising from **aqueous alkaline and magnetic field induced “distortions” in the hydrogen bonded hydration shells associated with OH groups lining the glucose molecule** increasing reduction potentials. It is interesting to note that the glucose molecule has some similarity to the starch molecule employed in the reactant A composition of this research (see Figure 5-1).

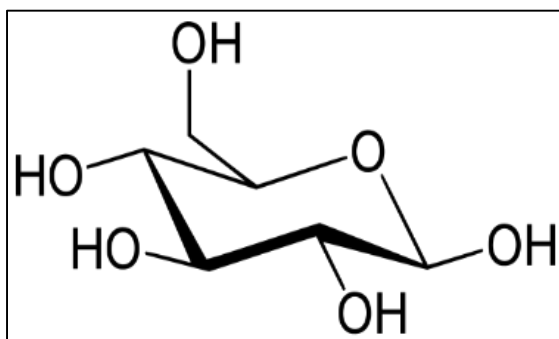


Figure 5-1: The glucose molecule (Bozic, Lipus and Kokol, 2008)

Question

If magnetic field exposure to aqueous alkali salts and glucose impacted respective redox potentials, then could it also impart an effect on polymers containing glucose linkages?

It is well understood that the polysaccharide assemblages in potato starch, are amylose with its α 1→4 straight chained linkages of glucose units, and the larger amylopectin's which are amylose branched structures at α 1→6 linkages spaced approximately at 30 glucose molecule intervals. Whilst amylose and amylopectin are not classified as reducing sugars such as glucose, these polymeric chains do exhibit C2, C3 and C6 hydroxyl functional groups which can undergo substitution reactions. (refer to Figure 1-53, page 136).

If we refer back to pages 136-137 it was noted that Kearsley and Dziedzic (1995), and Wu, Witt and Gilbert (2013) reported that **the “hydrolytic cleavage of amylose forms chain intermediates”**, known as amylodextrins, results in increasing reducing power relative to cleavage intervals as the number of aldehyde groups at the C1 cleavage sites are exposed, further noting that **these shorter chains can form triiodide complexes in the UV range** until chain lengths below 40 glucose polymer monomer assemblies emerge.

It is at this point that a series of experiments outlined by Lee, Han and Lim (2009) on page 137 are of interest, when subjecting differing amylose and amylopectin starch compositions to varying hydrolysis conditions between pH 5.0 and 10.0., and identified that regardless of pH, amylopectin generally retained a spherical geometry of unmodified chains throughout the pH testing range. Conversely, the specific volumes of **amylose unit mass increased as pH scaled up from pH5.0 to 10.0** with these researchers concluding that **alkali could be a deprotonating agent that lowers chain associations.**

We can recall that Wang et al. (2017) on page 137 commented on a process known as **retrogradation which occurs when starch amylose and amylopectin are heated then slowly cooled, altering their molecular structure and intermolecular interactions.** Furthermore, it was also reported that **amylose chains** are typically single random or helical coiled configurations in amorphous solid starch granules, that are **dispersed when heated H₂O and then reform as hydrogen bonded double helical arrangements between 40 to 70 glucose monomers in chain length upon cooling.** Wang (2020) also informed on the same page, that **amylose retrogradation causes the molecule to “gradually lose its ability to form a blue**

complex with iodine if double-helical associations occur between amylose chains on retrogradation”

I would now return to the computer simulations undertaken Immel and Lichtenhaler (2000), previously outlined on page 138, stating that the **single helical structures have significantly elevated hydrophobicity in the helical cavity** due to the higher consistency in glycosidic oxygen and methylene group distribution.....which **favours polyiodide inclusion complexation**. Conversely, this research declared that **double helix amylose** arrangements are reportedly **incapable of forming inclusion complexes**, and are less kinetically favorable for inclusion completion due to the increased time required for helical disassociation (see Figure 1-53).

Question

If exposure to magnetic fields can alter the electron exchange in monosaccharides, the heating and cooling of starch solutions can alter amorphous structure which regulate inclusion kinetics, and alkali conditions could facilitate polysaccharide cleavage, then could these three factors in combination at least facilitate the disassociation of the comparatively weakly bound double helix retrogradation induced associations of starch molecules?

A further recall of the literature review discloses that a Maize starch of similar amylose/amyopectin ratio (23:77) to that typically associated with potato starch, as outlined on page 138, by Qiao et al. (2016) and Chi et al, (2022) stating that exposure of aqueous starch to aqueous alkali exhibited **a reduction in the alignment of double helices** due to alkali ions penetrating and affecting inter helical H₂O hydrogen bonding network, **leading to double helical disassociation**, with further analysis confirming **greater rates of amylose cleavage and higher populations of exposed chain sites.**

A review of the clock reaction analyte A precursors utilised in this work informs that ambient temperature aqueous Na₂S₂O₃•5H₂O solution exhibits neutral pH, NaI is alkaline in the range of 8- 9.5, and that potato starch in solution is mildly acidic (6.5) according to Kim and Huber (2013). Unfortunately, pH analytical equipment was

sought out during the research, but could not be made available, therefore no measurements accompany this work, so based upon the literature, chemical concentration, and composition, it is assumed for the purposes of providing mechanistic explanations that the overall reactant A analyte was mildly alkaline in nature.

5.1.1. Analyte A (PEMF and 0.3T) exposure: Hypothetical mechanisms.

Hypothesis 1

The aforementioned research outlined in sub chapter 5.1. and the results identified in chapter 4 enables a conceivable hypothesis that alkaline starch solutions subjected to static magnetic fields induce higher rates of hydrolytic cleavage (*Bozic, Lipus and Kokol, 2008*), which ultimately facilitate higher populations of complexation monomer chains (*Kearsley and Dziedzic, 1995, and Wu, Witt and Gilber, 2013*) resulting in increased complexation kinetic rates with polyiodide species (*Immel and Lichtenthaler, 2000, and Wang, 2020*).

Hypothesis 2

Further correlations with the established literature and this research gives rise to the feasibility that static magnetic field exposure with starches in alkali aqueous solutions can increase deprotonation of amylose double helical associations (*Lee, Han and Lim, 2009, Qiao et al., 2016 and Chi et al, 2022*), resulting in higher populations of single helical structures being available to form I₃⁻ and α-amylase helical complexes, thereby resulting in the increased kinetic complexation response (*Immel and Lichtenthaler, 2000, and Wang, 2020*).

Hypothesis 3

The excellent work research of Pursell and Pursell (2016), as outlined in pages 143-146, is worthy of further consideration with the experimental results in this thesis. The Pursell team utilised aqueous α-cyclodextrin, a molecule very similar to the

aqueous amylose starch utilised in this research, which focused on α -cyclodextrin-iodide complexation, incorporating UV-Vis analysis at the identical wavelength utilised in this research (352nm). Their results noted that as aqueous α -cyclodextrin concentration was increased with aqueous solutions of $I_2 + I^-$ in titration experiments, the rate of generated I_3^- products increased accordingly by significant levels (38% - 86%).

It is therefore proposed that the magnetic exposures of analyte A in this research may have resulted in the increase in $I_2 + I^- \rightarrow I_3^-$ of generation after the $Na_2S_2O_3$ clock reaction limiting reagent has been depleted, which is in turn assisted by mechanisms detailing an increase in available single amylose helices, as outlined in hypotheses 1 and 2, thereby shifting the reaction kinetics favourably towards a higher generation of I_3^- and an accompanying increase in triiodide-starch complexation (Pursell and Pursell, 2016).

5.1.2. Analyte A and magnetic field exposure: Conclusion

In summing up, these results reveal that there was no significant data to support the premise that a (0.3T x 180 min) static magnet exposure of reagent A impacted the rate of the triiodide-starch complexation in comparison with the complimentary control reactions, due to error overlap during absorbance differential kinetic displacement. A significant result was obtained from the (PEMF x 180 min) exposures of reagent A, which exhibited an increased rate for triiodide-starch complexation in comparison with the complimentary control reactions, which was outside the evaluated levels for error.

Comment

Variation in exposure and corresponding control UV-Vis analysis temperature may also explain these different outcomes, noting the Pursell team's experiments additionally identifying that the $I_3^- \cdot \alpha$ -cyclodextrin binding constant was temperature dependent (-31.0 ± 0.9 kJ/mol), which may go some way to explaining the kinetic differential error overlap identified in the 0.3T Magnet A and control series due to a broader temperature range at the times of UV-Vis kinetic analysis, and a significantly

narrower range in the respective PEMF treatment and control UV-Vis temperature spreads by a factor of approximately 1:4 (Table 5-1 **bold**).

Table 5-1: Analyte A (0.3T) and (PEMF) UV-Vis analysis and temperature		
Factor	Analyte A 0.3T /180 min	Analyte A PEMF/180 min
UV-Vis range (°C)	20.85 – 22.02	20.93 – 21.17°C
Difference (°C)	1.17°C	0.24°C
Control UV-Vis range (°C)	20.86 – 21.90°C	20.86 – 21.15°C
Difference (°C)	1.04°C	0.29°C

Another feasible explanation for the variation in the static magnet and PEMF displacement profiles could arise from aspects related to the Lorentz Force, which was beyond the reach of this present research.

Further research is required to better reinforce or dismiss these findings.

5.2. Analyte B (0.3T) UV-Vis kinetic analysis

As pointed out earlier in this section, a correlation with temperatures may be the simple explanation for the variation in the kinetic initiation and duration of starch-triiodide complexation with the 0.3T magnet exposure and control experiments. It is possible that the associated outcomes of variable displacement differential findings could simply be the result of random outcomes.

5.2.1. Temperature alignments of Analyte B and Control kinetics

A deeper investigation of the reactant B and 180 minute 0.3T magnet exposure was undertaken with a focus on exposure and control analytes that had minor temperature variance $\pm 0.2^\circ\text{C}$ at the time of conducting UV-Vis analysis, and an interesting trend was revealed.

A total of 22 possible combinations of exposure and control $\pm 0.2^\circ\text{C}$ range comparisons were taken from 66% of the available data sets, with calculations of the

various combinations revealing that only a single correlation was in disagreement with the overall findings tabled in the experimental section (Table 5-2, red). The remaining 21 possible combinations were either ineffectual or in agreement with the observational outcomes in the overall 0.3T exposure and control differential displacement kinetics, and correlated with the overall differential displacement trend that revealed lowered kinetic displacement in the analyte B 0.3T exposures in comparison with corresponding control replicate UV-Vis analyses.

Once again, this reveals the sensitivity of temperature range when utilising this instrumental analysis for this type of reaction.

Table 5-2: Analyte B (0.3T x 180 min) and control $\pm 0.2^{\circ}\text{C}$ UV-Vis data						
Analyte	UV-Vis temp ($^{\circ}\text{C}$)	λ_{max} seconds	Analyte	UV-Vis temp ($^{\circ}\text{C}$)	λ_{max} seconds	Control (\pm seconds)
Magnet 1	20.31	169	Control 1	20.29	168	+1,
Magnet 3	20.33	171	Control 3	20.31	165	+4, +6
Magnet 4	20.34	166	Control 4	20.32	166	+3, +5, 0
Magnet 5	20.35	165	Control 5	20.33	165	+4, +6, +1, 0, 0
Magnet 2	20.35	165	Control 2	20.37	165	0, 0
Magnet 4	20.47	162	Control 4	20.45	164	-2
Magnet 5	20.51	163	Control 5	20.53	163	0
Magnet 3	20.97	157	Control 1	20.99	153	+4, +1, +1
Magnet 4	20.98	154	Control 3	20.99	152	+5, +2, +2
Magnet 5	20.99	154	Control 5	21.01	151	+3

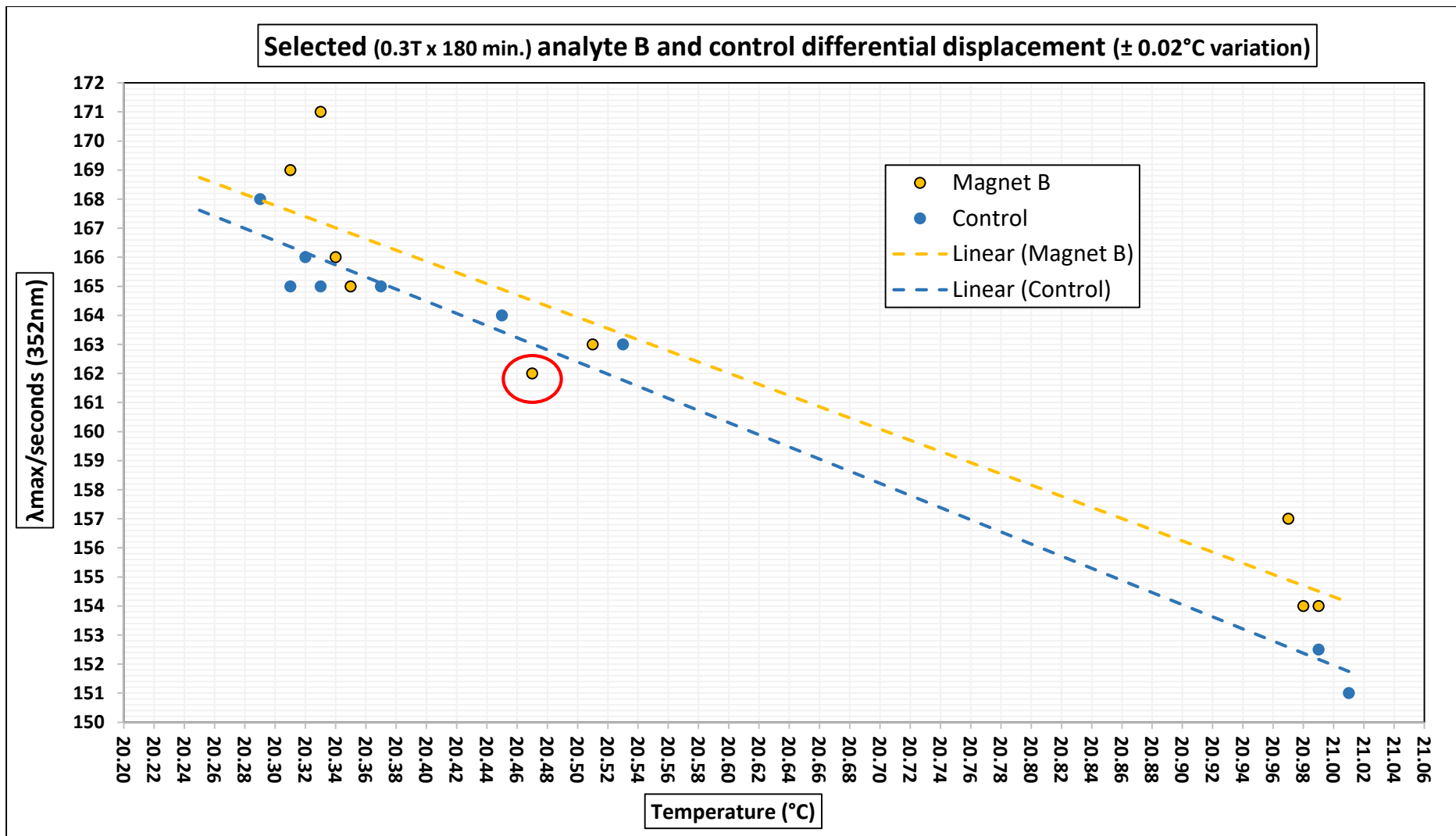


Figure 5-2: Analyte B 0.3T magnet (180 minute) vs control UV-Vis absorbance at $\pm 0.02^\circ\text{C}$ variation.

A focus will now shift to H₂O kinetics under magnetic field exposure to develop a mechanistic hypothesis with and without the hydronium proton in its various configurations.

5.2.2. H₂O cluster geometry and hydrogen bond energy revisited

As outlined in the literature review on page 68 by Liu, Wang and Ho (2011), computer simulation calculations of hydrogen bond energies related to (H₂O)₂₋₃₀ clusters arranged in various geometries pointed out that **H₂O structure dictated kinetically favorable strength and disassociation fragmentation**. A broad selection of the reviewed research also reported consistent findings that the **magnetic field gradient impacted intramolecular H₂O clustering resulting in decreased H₂O diffusion and mobility** (Toledo et. al, 2008, Gutierrez-Mejia and Ruiz-Suarez, 2012, Moosavi and Gholizadeh, 2014, D'Emilia et. al, 2015, Usanov et al., 2016, Chirkova et. al, 2019, Toledo and Ramalho, 2021)

Comment

A consensus drawn from these combined H₂O and magnetic field computer simulation conclusions is that H₂O_n cluster hydrogen bonding favours monomer disassociations, respective to intra cluster population and geometry, and the external magnetic field applied to H₂O_n arrangements alters monomer fragmentation relative to intra cluster population, geometry and the atomic coordinate relative to the applied magnetic field z gradient.

5.2.3. H₃O⁺ and H₂O proton transfer revisited

The literature review recalls on page 98 that Tachikawa (2017) claimed from his simulations that “**proton transfer was strongly dependent on cluster size**”, which was dependent upon a **unique collaboration of neighboring H₂O acceptor molecules, and correlating stabilisation to promote the required energy barrier to facilitate further proton transfer** along the bulk water environment. Fischer and Gunlycke (2019) further commented on page 98-99, that even when proton transfer

cooperation among immediate neighboring H₂O molecules occurred, **this predominately resulted in proton transfer reversal, largely dictated by the existing (H₂O)_n makeup of further neighboring H₂O clusters.**

Recent density functional theory–quantum chemical cluster model (DFT-CM) computer simulations on page 99 presented by Dong and Bi (2019) revealed an even more elaborate three dimensional proton transfer mechanism, whereby **opportunistic cavities in bulk H₂O are essential to facilitate a rotation channel and accompanying translocation and rotation of hydrogen bonds of H₂O molecules in the cavity** are required to for the diffusion of the hydronium ion through the bulk H₂O. Perez de Tudela and Marx (2020) informed on pages 99-100 of the temperature dependency of HCl and H₂O ionization, and identified that the collaboration of 6 x H₂O molecules were required at room temperature to facilitate HCl disassociation, with van der Loop et al. (2017) further stating on page 100 that **HCl proton diffusion rates decreased significantly dynamic magnetic field exposure due to the decrease in H₂O reorientation rate in the presence of the applied magnetic field**, and that a collaboration of 15 H₂O in bulk water were required to induce proton transfer.

Comment

The combined conclusions elicited from these sources is that whether or not H⁺ proton transfer occurs by either a Grotthuss, rotation or cavitation mechanism, an intricate interplay of H₂O molecular cluster binding energy and secondary H₂O localisation collaborations are required to stabilize the energy to facilitate proton transfer rates in order to mitigate reverse proton rattling.

5.2.4. HCl and proton transfer under magnetic field exposure

As previously presented in the magnetic field and ions section, (Hashemizadeh et al., 2018) conducted a range of experiments of differing HCl concentrations (1.5, 3.0 and 4.5M) static magnetic field strengths (0.23T, 0.33T and 0.43T), flow rates and temperatures (25.0-45.0°C) was undertaken, which noted a **consistent rise in pH measurements** conducted **0, 30 and 60 minutes after the experimental magnetic**

field exposures, concluding that **proton transfer had somehow been mitigated by exposure to magnetic fields.**

5.2.5. Factors to consider for analyte B magnet differential kinetics

There was error overlap in the displacement differentials and the absorbance profiles did not fit well with the temperature control kinetic profiles. As pointed out previously in this paper, the impact of thermal kinetics competing with any magnetic phenomena is far greater, as was shown out in this research when control and exposure UV-Vis analysis temperature was not correlated to a high level of precision. However, it is noted that when data was selected according to a minor temperature variation of $\pm 0.2\text{C}$ at the time of undertaking UV-Vis analysis, an interesting trend in supporting the overall calculated differential kinetic rate was identified by a ratio of 15 to 1 in favor of the trend, with 6 neutral results.

A significant correlation was also identified when the minor variation temperature data was further scrutinised, and it is again noted that the analyte B ($0.3\text{T} \times 180$) differential kinetics were also inversely associated with both the analyte A PEMF and ($0.3\text{T} \times 180$) differential kinetics sets that did not incorporate HCl exposed in the 0.3T static magnetic field.

Therefore, the following hypotheses are proposed:

5.2.6. Analyte B (0.3T) exposure: Hypothetical mechanisms

Hypothesis 1

The analyte B ($0.3\text{T} \times 180$ min.) static magnet exposure impacted on the kinetics of non-protonated H_2O hydrogen bond fragmentation entropy thermodynamics (Liu, Wang and Ho, 2011), and increased or decreased intra cluster bond energies specific to respective cluster population and molecular coordination's relative to the magnetic field ζ gradient in comparison with unexposed control analytes (Moosavi and Gholizadeh, 2014), thereby lowering H_2O diffusion and proton transfer (Toledo

et. al, 2008, Gutierrez-Mejia and Ruiz-Suarez, 2012, Moosavi and Gholizadeh, 2014, D'Emilia et. al, 2015, Usanov et al., 2016, Chirkova et. al, 2019, Toledo and Ramalho, 2021).

Hypothesis 2 (i-iv)

The magnetic field reduced proton transfer rates to variable degrees relative to z magnetic gradient, and due to one or all of the following mechanisms:

- i) Mitigating $(H_2O)_n$ bulk water cluster arrangements required for proton transfer (Tachikawa, 2017)
- ii) Increasing neighbouring $(H_2O)_n$ arrangements that favored “proton rattling” and slower proton transfer(Fischer and Gunlycke, 2019)
- iii) Mitigating $(H_2O)_n$ cavitation and/or collaborative channel H_2O hydrogen bond arrangements to facilitate typical proton diffusion (Dong and Bi, 2019).
- iv) Decreased HCl proton diffusion due to a decrease in $(H_2O)_{15}$ reorientation in the magnetic field (van der Loop et al., 2017).

Hypothesis 3

The analyte B (0.3T x 180 min) magnetic exposure may have induced shifts in Na^+ , Cl^- and BrO_3^- hydration or this may be an additional factor.

5.2.7. Analyte B magnetic field exposure: Conclusion

The results reveal that there was no significant data to support the premise that a (0.3T x 180 min) static magnet exposure with reagent B impacted the rate of the triiodide/starch complexation.

5.3. Analyte A/B (0.3T x 180 min) magnet exposure vs control displacement differentials

As previously noted the 0.3T analyte A and analyte B kinetic analyses identified differing differential displacement relative to their respective control experiments.

5.3.1. Analyte A/B magnetic field exposure displacement differentials: Conclusion

Aside from the conclusions put forward, the error overlap in differential kinetics over the entire analyte A and B 0.3T exposure and corresponding control replicate range may be either:

- i) A result of the variation in temperatures at the time of UV-Vis analytical measurement.
- ii) A result of variation in analyte A and B molecular residence time respective to the magnetic ζ gradient due to typical thermal factors.
- iii) The result of random kinetic events undergoing no impact from the static magnetic field.

Further research of higher experimental precision is required

Comment

There is an abundance of controversial research related to magnetic field exposures and the “memory effect”, this research will not cover this in any great detail other than reporting that none of the magnetic exposure and complimentary control analytical research was conducted whilst under the influence of an introduced magnetic field, but the research did identify phenomena in analytes that were analysed between 30 and 200 minutes after magnetic exposures.

Chapter 6: Future Research

It became clearer as time progressed that what is generally viewed as a high school level chemistry experiment took on exponential levels of complexity when an external magnetic field is introduced and then a detailed scrutinization of the identified phenomena is required.

Clearly, the first step forward in further researching this series of experiments is in gaining better magnetic field data to provide better kinetic calculations, and this was unfortunately another derailment arising from the COVID-19 pandemic. The next step forward in further evolving this work is to isolate the individual chemical components and subject them individually to otherwise corresponding magnetic field exposure and analytic determinations. High levels of temperature precision are required for the integrity of the overall clock reaction UV-Vis kinetic analysis, but this would not necessarily be the case when examining individual chemical components.

The UV-Vis analysis could also have been a lot more detailed, if time permitted, and this needs further research.

A discussion regarding a thermocouple ambient temperature feedback loop in the Keybright data logger-computer system to provide automated instrument temperature control of higher precision in the Dolphin 3000 device, was conducted with the Footscray Park campus electrical engineers, who informed that this is a relatively simple undertaking to improve the experimental design.

The ability to access Helmholtz coil type instrumentation for future research would also significantly mitigate the temperature related aspects when dealing with the Dolphin 3000 device and allow for high precision magnetic field adjustment to research field strength frequency, gradient and voltage related aspects.

Research utilizing electrospray ionization mass spectroscopy (ESI-MS) utilizing highly purified analytical grade H₂O and D₂O can be employed with iodine and iodide under the magnetic field protocols utilised in this research to identify impacts on

hydration and polyiodide generation ($I_2 + I^- \rightarrow I_3^-$). The same instrumental analysis can also be utilised with combinations of bromate ions in the presence of HCl, in combination with and without Iodide and thiosulfate ions. The cluster hydration of amylose, amylopectin and starch would also be an area for investigation.

Scanning Electron Microscope (SEM) analysis of amylose, amylopectin, starch, and a variety of cyclodextrins impacted by external magnetic fields is also worthy of serious investigation, particularly as starches and cyclodextrins are being incorporated as complexes for drug delivery in greater abundance. The hypothesis of amylose helical dissociation in the presence of static and dynamic fields also needs to be further investigated, and the SEM analysis of starch-polyiodide complexation should also be considered for research.

The UV-Vis analysis conducted in this research has only made a brief glimpse of the myriad of factors that are yet to be evaluated, such as the impact of magnetic fields and generated polyiodide (I^-_n) species scanning, as well as the hydrated ionic absorbance profiles of all the ionic species utilised in this work and generated by the overall reaction.

Nuclear Magnetic Resonance (NMR) analysis of H_2O and D_2O exposed in magnetic fields is also an area of research interest in order to examine if the typical thermodynamics of ortho to para ratio of hydrogen atom spin is impacted by magnetic fields, thereby opening up new areas of research for quantum chemistry.

Future experiments would also incorporate pH and electrical conductivity measurements, and a variety of ion selective electrodes can be incorporated for monovalent, bivalent, and trivalent analysis of ionic species exposed with magnetic fields.

The availability of a more advanced tunable EMF device would no doubt open up the investigation to all of the aforementioned proposals exponentially

References

1. Akash, M.S.H. and Rehman, K., 2020. *Essentials of pharmaceutical analysis* (pp. 173-184). Singapore: Springer.
2. Al Helal, A., Soames, A., Gubner, R., Iglauer, S. and Barifcani, A., 2018. Influence of magnetic fields on calcium carbonate scaling in aqueous solutions at 150° C and 1 bar. *Journal of colloid and interface science*, 509, pp.472-484.
3. Alotaibi G., and Bukhari M., 2021. Factors Influencing Bacterial Biofilm Formation and Development, *American Journal of Biomedical Science & Research*, 12(6), pp. 617-626.
4. Amjad, Z. and Demadis, K.D. eds., 2015. *Mineral scales and deposits: scientific and technological approaches*. Elsevier.
5. Andrianov, A. and Orlov, E., 2018. The assessment of magnetic water treatment on formation calcium scale on reverse osmosis membranes. In *MATEC Web of Conferences* (Vol. 178, p. 09001). EDP Sciences.
6. Artemov, V. G., Volkov, A. A., & Sysoev, N. N., 2015. Autoionization of water: does it really occur? *arXiv preprint arXiv:1508.00126*.
7. Artemov V. G., Volkov, Jr. A. A., Sysoev, N. N. and Volkov, A. A., 2016. On Autoionization and pH of Liquid Water, *Doklady Physics*, Vol. 61, No. 1, pp. 1–4.
8. Australian Stainless Steel Development Association, n.d., Magnetic Effects of Stainless Steel, ASSDA Technical FAQ 3, <https://www.assda.asn.au/technical-info/technical-faqs/magnetic-effects-of-stainless-steels>, (accessed 23/2/21)

9. Ayun, Q., Sulistyarti, H. and Atikah, A., 2015. Development of Spectrophotometry Method for Iodide Determination Based on I₂-Starch Complex Formation with Hypochlorite as oxidator. *The Journal of Pure and Applied Chemistry Research*, 4(2), p.53.,
<https://search.proquest.com/openview/4a7607a2a027e935c3f6ebc8ea0f9034/1?pq-origsite=gscholar&cbl=2047998>, (accessed 2/1/22)
10. Bain, G.A. and Berry, J.F., 2008. Diamagnetic corrections and Pascal's constants. *Journal of Chemical Education*, 85(4), p.532,
<https://pubs.acs.org/doi/abs/10.1021/ed085p532>, (accessed 14/7/21)
11. Beauvais, F., 2018. Benveniste's Experiments Explained by a Non-Conventional Experimenter Effect. *Medicines*, 5(2), p.28., <https://www.mdpi.com/277342>, (accessed 21/9/21)
12. Bharagava, R.N. and Saxena, G., 2020. *Bioremediation of Industrial Waste for Environmental Safety: Volume II: Biological Agents and Methods for Industrial Waste Management*. Springer Nature Singapore Pty Ltd.
13. Bin, G.U.O., HAN, H.B. and Feng, C.H.A.I., 2011. Influence of magnetic field on microstructural and dynamic properties of sodium, magnesium and calcium ions. *Transactions of Nonferrous Metals Society of China*, 21, pp.s494-s498.
14. Bohme, D.K., Mackay, G.I. and Tanner, S.D., 1979. An experimental study of the gas-phase kinetics of reactions with hydrated hydronium (1+) ions (n= 1-3) at 298 K. *Journal of the American Chemical Society*, 101(14), pp.3724-3730.,
<https://pubs.acs.org/doi/pdf/10.1021/ja00508a003>, (accessed 20/2/22)
15. Bormashenko, E., 2019. Moses effect: Physics and applications. *Advances in colloid and interface science*, 269, pp.1-6.
16. Božič, M., Lipus, L. and Kokol, V., 2008. Magnetic field effects on redox potential of reduction and oxidation agents. *Croatica Chemica Acta*, 81(3), pp.413-421.

17. Campos, H. and Ortiz, O., 2020. *The potato crop: its agricultural, nutritional and social contribution to humankind*. Springer Nature.
18. Castor-Villegas, V.M., Guevara-Vela, J.M., Vallejo Narváez, W.E., Martín Pendás, Á., Rocha-Rinza, T., Fernández-Alarcón, A., 2020, On the strength of hydrogen bonding within water clusters on the coordination limit. *Journal of Computer Chemistry*. No. 2, Vol. 41, pp. 2266– 2277.
19. Chem Supply, n.d., Potato Starch, SA083-500G, <https://shop.chemsupply.com.au/documents/SA083.pdf>, (accessed 9/4/21)
20. Chi, C., He, Y., Jiao, W., Wang, H. and Tan, X., 2022. Hierarchical structural transformation of corn starch in NaOH solution at room temperature. *Industrial Crops and Products*, 178, p.114672.
21. Chirkova, V.Y., Sharlaeva, E.A. and Stas, I.E., 2019. Changes in cohesive and adhesive characteristics of water as a result of electromagnetic influence. *Proceedings of Universities. Applied Chemistry and Biotechnology*, 9(2), pp.222-231.
22. Chinake, C.R. and Simoyi, R.H., 1996. Kinetics and Mechanism of the Complex Bromate– Iodine Reaction. *The Journal of Physical Chemistry*, 100(5), pp.1643-1656
23. Cho, Y.I., Lee, S., Kim, W. and Suh, S., 2003. Physical water treatment for the mitigation of mineral fouling in cooling-tower water applications.
24. Clearwater Systems Corporation., 2008. *Technical Manual, Dolphin series 3000*. Essex, CT 064262008, http://origin-faq.profase.com/resources/sites/PROFACE/content/live/FAQS/170000/FA170215/en_US/IOM%203000%20Dolphin%20Watercare.pdf, (accessed 16/5/21)

25. Cole, M., Eggleston, G. and Triplett, A., 2017. Analytical evaluation of current starch methods used in the international sugar industry: Part I. *Food chemistry*, 228, pp.226-235.,
<https://www.sciencedirect.com/science/article/pii/S030881461730167X>, (accessed 2/1/22)
26. Colic, M. and Morse, D., 1999. The elusive mechanism of the magnetic 'memory' of water. *Colloids and Surfaces A: Physicochemical and Engineering Aspects*, 154(1-2), pp.167-174.
27. Collins, K.D., 2019. The behavior of ions in water is controlled by their water affinity. *Quarterly reviews of biophysics*, 52.
28. Cordeiro, Fernando, Piotr Robouch, Maria Beatriz de la Calle, Håkan Emteborg, Jean Charoud-Got, Franz Schmitz, and Collaborators: Bauer KH Bogenschuetz G Broeckx S Brunton J Caille N De Borba B Désiré Djoukeng J Garche A Harihara Subramanian N Hoffmann A Kim JR Läubli M Michalski R Röhrig KH Schumacher B Waals K Winzek P., 2011. "Determination of dissolved bromate in drinking water by ion chromatography and post column reaction: interlaboratory study." *Journal of AOAC International* 94, no. 5: 1592-1600.,
<https://academic.oup.com/jaoac/article-abstract/94/5/1592/5655408>, (accessed 7/1/22)
29. Dahms, F., Costard, R., Pines, E., Fingerhut, B. P., Nibbering, E. T. J., Elsaesser, T., 2016. The Hydrated Excess Proton in the Zundel Cation $H_5O_2^+$: The Role of Ultrafast Solvent Fluctuations, *Angew. Chem. Int. Ed.*, 55, 10600
30. Dane, J.H., Topp, G.C. and Campbell, G.S., 2002. *Methods of soil analysis*. Soil Science Society of America.
31. Dembic, Z., 2015. *The cytokines of the immune system: the role of cytokines in disease related to immune response*. Academic Press.

32. D'Emilia, E., Giuliani, L., Lisi, A., Ledda, M., Grimaldi, S., Montagnier, L. and Liboff, A.R., 2015. Lorentz force in water: Evidence that hydronium cyclotron resonance enhances polymorphism. *Electromagnetic Biology and Medicine*, 34(4), pp.370-375.
33. D'Emilia, E., Ledda, M., Foletti, A., Lisi, A., Giuliani, L., Grimaldi, S. and Liboff, A.R., 2017. Weak-field H₃O⁺ ion cyclotron resonance alters water refractive index. *Electromagnetic Biology and Medicine*, 36(1), pp.55-62.
34. Díaz-Tinoco, M., Romero, J., Ortiz, J.V., Reyes, A. and Flores-Moreno, R., 2013. A generalized any-particle propagator theory: Prediction of proton affinities and acidity properties with the proton propagator. *The Journal of Chemical Physics*, 138(19), p.194108.
35. Dobersek, D. and Goricanec, D., 2014. An experimentally evaluated magnetic device's efficiency for water-scale reduction on electric heaters. *Energy*, 77, pp.271-278.
36. Dong, S., and Shuping Bi. 2019. "The solvation effect on the rattling behaviour of the hydrated excess proton in water." *Physical Chemistry Chemical Physics*, 21, no. 40, pp. 22385-22389.
37. El-Esawi, M., Arthaut, L.D., Jourdan, N., d'Harlingue, A., Link, J., Martino, C.F. and Ahmad, M., 2017. Blue-light induced biosynthesis of ROS contributes to the signaling mechanism of Arabidopsis cryptochrome. *Scientific Reports*, 7(1), pp.1-9.
38. El-Shamy, A.M., Abdo, A., Gad, E.A., Gado, A.A. and El-Kashef, E., 2021. The consequence of magnetic field on the parameters of brackish water in batch and continuous flow system. *Bulletin of the National Research Centre*, 45(1), pp.1-13.
39. Esteso, M.A., Ribeiro, A.C.F., George, S.C., Abraham, A.R. and Haghi, A.K. eds., 2021. *Optical and Molecular Physics: Theoretical Principles and Experimental Methods*. CRC Press.

40. FAO and UNEP. 2021. Global assessment of soil pollution - Summary for policy makers. Rome, FAO., <https://www.fao.org/documents/card/en/c/b4894en/>, (accessed 11/11/21)
41. Fathi, A., Mohamed, T., Claude, G., Maurin, G. and Mohamed, B.A., 2006. Effect of a magnetic water treatment on homogeneous and heterogeneous precipitation of calcium carbonate. *Water research*, 40(10), pp.1941-1950.
42. Fischer, S.A. and Gunlycke, D., 2019. Analysis of correlated dynamics in the Grotthuss mechanism of proton diffusion. *The Journal of Physical Chemistry B*, 123(26), pp.5536-5544.
43. Fonslick, J., Khan, A. and Weiner, B., 1989. On the question of hypoiodite ion formation in the aqueous solution of iodine: theoretical and experimental study of H₂OI₂ complex. *The Journal of Physical Chemistry*, 93(9), pp.3836-3838.
44. Fujii, A. and Mizuse, K., 2013. Infrared spectroscopic studies on hydrogen-bonded water networks in gas phase clusters. *International Reviews in Physical Chemistry*, 32(2), pp.266-307.
45. Gabrielli, C., Jaouhari, R., Maurin, G. and Keddam, M., 2001. Magnetic water treatment for scale prevention. *Water Research*, 35(13), pp.3249-3259.
46. Gallaher R., 1947. Abram Tuston Hay, *The Pampelist*, No 28, pp. 193-206., [https://resources.ohiohistory.org/ohj/browse/displaypages.php?display\[\]=%0056&display\[\]=%404&display\[\]=%441](https://resources.ohiohistory.org/ohj/browse/displaypages.php?display[]=%0056&display[]=%404&display[]=%441), (accessed 27/7/21)
47. Garcia-Arrona, R., Arranz, M., Bordagaray, A. and Millán, E., 2017. Practical activity for development and validation of a simple UV-spectroscopic method for iodate determination in table salt. *J. Lab. Chem. Educ*, 5, pp.26-31.
48. Gatard, V., Deseure, J. and Chatenet, M., 2020. Use of magnetic fields in electrochemistry: a selected review. *Current Opinion in Electrochemistry*, 23, pp.96-105.

49. Gebauer, D., Volk, A. and Colfen, H., 2008. Stable prenucleation calcium carbonate clusters. *Science*, 322(5909), pp.1819-1822.
50. Gesundheit B, Ben-David E, Posen Y, Ellis R, Wollmann G, Schneider EM, Aigner K, Brauns L, Nesselhut T, Ackva I, Weisslein C and Thaller A, 2020. Effective Treatment of Glioblastoma Multiforme with Oncolytic Virotherapy: A Case-Series. *Frontiers in Oncology*, No. 10:702
51. Grehl, S., Viola, H.M., Fuller-Carter, P.I., Carter, K.W., Dunlop, S.A., Hool, L.C., Sherrard, R.M. and Rodger, J., 2015. Cellular and molecular changes to cortical neurons following low intensity repetitive magnetic stimulation at different frequencies. *Brain stimulation*, 8(1), pp.114-123.
52. Gutiérrez-Mejía, F. and Ruiz-Suarez, J.C., 2012. AC magnetic susceptibility at medium frequencies suggests a paramagnetic behaviour of pure water. *Journal of magnetism and magnetic materials*, 324(6), pp.1129-1132.
53. Hashemizadeh, A., Ameri, M.J., Aminshahidy, B. and Gholizadeh, M., 2018. Influence and application of an external variable magnetic field on the aqueous HCl solution behavior: experimental study and modelling using the taguchi method. *Applied Chemistry for Engineering*, 29(2), pp.215-224.
54. Hashemizadeh, A. and Ameri, M.J., 2021. Toward a mechanistic understanding of the magnetic field effect on N-80 carbon steel corrosion in aqueous HCl solution. *Anti-Corrosion Methods and Materials*,
<https://www.emerald.com/insight/content/doi/10.1108/ACMM-10-2020-2389>,
(accessed 17/2/22)
55. Helm, L. and Merbach, A.E., 2019. The periodic table and kinetics?. *CHIMIA International Journal for Chemistry*, 73(3), pp.179-184.
56. Horton, D., 1999. *Advances in Carbohydrate Chemistry and Biochemistry: Cumulative Subject and Author Indexes, and Tables of Contents*. Academic Press.

57. Horton, T.M., Jenkins, G., Pati, D., Zhang, L., Dolan, M.E., Ribes-Zamora, A., Bertuch, A.A., Blaney, S.M., Delaney, S.L., Hegde, M. and Berg, S.L., 2009. Poly (ADP-ribose) polymerase inhibitor ABT-888 potentiates the cytotoxic activity of temozolomide in leukemia cells: influence of mismatch repair status and O6-methylguanine-DNA methyltransferase activity. *Molecular cancer therapeutics*, 8(8), pp.2232-2242.
58. IB Chemistry Web, n.d. Halide ionic radii,
<https://www.ibchem.com/IB16/05.22.htm>, (accessed 21/8/21)
59. Ignatov, I. and Mosin, O., 2014. Basic concepts of magnetic water treatment. *European journal of molecular biotechnology*, 4, pp.72-85.
60. Ikeda, T. and Sueoka, K., 1970. Determination of Magnetic Moments of Copper Ions in Water by the Viscometer Method. *Bulletin of the Chemical Society of Japan*, 43(5), pp.1273-1275.
61. Immel, S. and Lichtenthaler, F.W., 2000. The hydrophobic topographies of amylose and its blue iodine complex. *Starch-Stärke*, 52(1), pp.1-8.
62. Index, M., 2006. Chemistry Constant Companion, Now with a New Addition, Ed 14Th, USA: Merck & Co.
63. Jalali, A., Zafari, J., Jouni, F.J., Abdolmaleki, P., Shirazi, F.H. and Khodayar, M.J., 2019. Combination of static magnetic field and Cisplatin in order to reduce drug resistance in cancer cell lines. *International Journal of Radiation Biology*, 95(8), pp.1194-1201.
64. Jones, G. and Dole, M., 1929. The viscosity of aqueous solutions of strong electrolytes with special reference to barium chloride. *Journal of the American Chemical Society*, 51(10), pp.2950-2964.

65. Kartell Labware, 2019., Disposable cuvettes, p.100,
<https://www.kartelllabware.com/m/docs/files/kartell-labware-ita-eng-fra-2019-2-low.pdf>, (accessed 14-11-2021)
66. Kearsley, M.W. and Dziedzic, S.Z. eds., 1995. *Handbook of starch hydrolysis products and their derivatives*. Springer Science & Business Media.
67. Keister, T., 2008. Non chemical devices: Thirty years of myth busting. *Water Conditioning & Purification*, 490, pp.11-12.,
<https://web.archive.org/web/20120417131247/http://www.wcponline.com/pdf/0804Keister.pdf>, (accessed 3-11-21)
68. Kidwai, M., Ahmad, I.Z. and Chakrabarty, D., 2020. Class III peroxidase: An indispensable enzyme for biotic/abiotic stress tolerance and a potent candidate for crop improvement. *Plant cell reports*, 39(11), pp.1381-1393.
(<https://link.springer.com/article/10.1007/s00299-020-02588-y>)
69. Kilaj, A., Gao, H., Rösch, D., Rivero, U., Küpper, J. and Willitsch, S., 2018. Observation of different reactivities of para and ortho-water towards trapped diazenylium ions. *Nature communications*, 9(1), pp.1-7.
70. Kim, J.Y. and Huber, K.C., 2013. Heat–moisture treatment under mildly acidic conditions alters potato starch physicochemical properties and digestibility. *Carbohydrate polymers*, 98(2), pp.1245-1255.
71. Kireev, S.V. and Shnyrev, S.L., 2015. Study of molecular iodine, iodate ions, iodide ions, and triiodide ions solutions absorption in the UV and visible light spectral bands. *Laser Physics*, 25(7), p.075602.,
<https://iopscience.iop.org/article/10.1088/1054-660X/25/7/075602/meta>, (accessed 28/12/21)

72. Kirov, M.V., Fanourgakis, G.S. and Xantheas, S.S., 2008. Identifying the most stable networks in polyhedral water clusters. *Chemical Physics Letters*, 461(4-6), pp.180-188.
73. Kirstein, A., Schmid, T.E. and Combs, S.E., 2020. The role of miRNA for the treatment of MGMT unmethylated glioblastoma multiforme. *Cancers*, 12(5), p.1099.
74. Klimov V., 2019. *From Basic to Clinical Immunology*, Springer Nature, Switzerland AG
75. Kubik, S., 2019. *Supramolecular Chemistry in Water*. 10.1002/9783527814923.
76. Kuchel, P.W., Chapman, B.E., Bubb, W.A., Hansen, P.E., Durrant, C.J. and Hertzberg, M.P., 2003. Magnetic susceptibility: solutions, emulsions, and cells. *Concepts in Magnetic Resonance Part A: An Educational Journal*, 18(1), pp.56-7
77. Kusakina, J. and Dodd, A.N., 2012. Phosphorylation in the plant circadian system. *Trends in plant science*, 17(10), pp.575-583.
78. Landler L, Keays D.A., 2018. Cryptochrome: The magnetosensor with a sinister side? *PLoS Biol* 16(10): e3000018. <https://doi.org/10.1371/journal.pbio.3000018>, (accessed 8/7/21)
79. Landolt, H., 1886. Ueber die Zeitdauer der Reaction zwischen Jodsäure und schwefliger Säure. *Berichte der deutschen chemischen Gesellschaft*, 19(1), pp.1317-1365.,
https://scholar.archive.org/work/ez3kow3mubhylmfopj7sscwwzi/access/ia_file/crossref-pre-1909-scholarly-works/10.1002%252Fcber.188501802220.zip/10.1002%252Fcber.188601901293.pdf, (accessed 14/11/22)
80. Landolt-Bornstein, n.d., University of Texas Libraries,
<https://guides.lib.utexas.edu/chemistry/landoltbornstein>, (accessed 13/12/21)

81. Latva, M., Inkkinen, J., Rämö, J., Kaunisto, T., Mäkinen, R., Ahonen, M., Matilainen, J. and Pehkonen, S., 2016. Studies on the magnetic water treatment in new pilot scale drinking water system and in old existing real-life water system. *Journal of Water Process Engineering*, 9, pp.215-224.
82. Łebkowska, M., Rutkowska-Narożniak, A., Pajor, E., Tabernacka, A. and Załęska-Radziwiłł, M., 2018. Impact of a static magnetic field on biodegradation of wastewater compounds and bacteria recombination. *Environmental Science and Pollution Research*, 25(23), pp.22571-22583.
83. Lee, J.H., Han, J.A. and Lim, S.T., 2009. Effect of pH on aqueous structure of maize starches analyzed by HPSEC-MALLS-RI system. *Food Hydrocolloids*, 23(7), pp.1935-1939,
<https://www.sciencedirect.com/science/article/pii/S0268005X08002932>,
(accessed 15/2/22)
84. Lee, S.H., Jeon, S.I., Kim, Y.S. and Lee, S.K., 2013. Changes in the electrical conductivity, infrared absorption, and surface tension of partially-degassed and magnetically-treated water. *Journal of Molecular Liquids*, 187, pp.230-237
85. Li, Y.H. and Chen, Y.J., 2021. The effect of magnetic field on the dynamics of gas bubbles in water electrolysis. *Scientific reports*, 11(1), pp.1-12.
86. Lippert, B., 1999. Chemistry and biochemistry of a leading anticancer drug. *Verlag Helvetica Chimica Acta, Zürich*.
87. Liu, H., Liu, B., Zhao, C., Pepper, M. and Lin, C., 2011. The action mechanisms of plant cryptochromes. *Trends in plant science*, 16(12), pp.684-691.
88. Liu, X., Lu, W.C., Wang, C.Z. and Ho, K.M., 2011. Energetic and fragmentation stability of water clusters (H_2O) n, n= 2–30. *Chemical Physics Letters*, 508(4-6), pp.270-275.

89. Liu, X., Zarfel, G., van der Weijden, R., Loiskandl, W., Bitschnau, B., Dinkla, I.J., Fuchs, E.C. and Paulitsch-Fuchs, A.H., 2021. Density-dependent microbial calcium carbonate precipitation by drinking water bacteria via amino acid metabolism and biosorption. *Water Research*, 202, p.117444.
90. Luo, X., Zhang, H. and Zhang, J., 2021. The influence of a static magnetic field on a Chlorella vulgaris-Bacillus licheniformis consortium and its sewage treatment effect. *Journal of Environmental Management*, 295, p.112969.
91. Machado, P.B. and Faria, R.B., 2009. Modeling the Complex Bromate– Iodine Reaction. *The Journal of Physical Chemistry A*, 113(18), pp.5338-5341.
92. Mahardiono, N.A., Fakhrurroja, H., Luvita, V. and Cahyaningsih, S., 2016. The Pulse Electromagnetic Fields Effect on pH and Heavy Metal of Water, *International Proceedings of Chemical, Biological and Environment Engineering*, V94.1, http://www.ipcbee.com/vol94/rp0020_ICWT2016-W0005.pdf. (accessed 28/11/22)
93. Maity, A., Maithani, S., Pal, A. and Pradhan, M., 2021. High resolution spectroscopic probing of ortho and para nuclear-spin isomers of heavy water in the gas phase. *Chemical Physics*, 541, p.111041.
94. Makhayeva, D.N., Irmukhametova, G.S. and Khutoryanskiy, V.V., 2020. Polymeric iodophors: preparation, properties, and biomedical applications. *Review journal of chemistry*, 10(1), pp.40-57., <https://link.springer.com/article/10.1134/S2079978020010033>, (accessed 2/1/22)
95. Marcus, Y., 2015. *Ions in Solution and their Solvation*. John Wiley & Sons.
96. Meier, B., Mamone, S., Concistrè, M., Alonso-Valdesueiro, J., Krachmalnicoff, A., Whitby, R.J. and Levitt, M.H., 2015. Electrical detection of ortho–para conversion in fullerene-encapsulated water. *Nature Communications*, 6(1), pp.1-4.

97. Michalski, R. and Łyko, A., 2013. Bromate determination: state of the art. *Critical Reviews in Analytical Chemistry*, 43(2), pp.100-122.,
<https://www.tandfonline.com/doi/abs/10.1080/10408347.2012.747792>, (accessed 7/1/22)
98. Mishra, S., Marzio, M.D., Giovanardi, R. and Tassinari, F., 2020. Magnetoelectrochemistry and asymmetric electrochemical reactions. *Magnetochemistry*, 6(1), p.1.
99. Mogi, I. and Watanabe, K., 2011. Chiral recognition of amino acids by magnetoelectrodeposited Cu film electrodes. *International Journal of Electrochemistry*, 2011.
100. Monzon, L.M. and Coey, J.M.D., 2014. Magnetic fields in electrochemistry: The Kelvin force. A mini-review. *Electrochemistry Communications*, 42, pp.42-45.
101. Moosavi, F. and Gholizadeh, M., 2014. Magnetic effects on the solvent properties investigated by molecular dynamics simulation. *Journal of Magnetism and Magnetic Materials*, 354, pp.239-247.
102. Morley, S.E. and Knurr, B.J., 2021. Probing the Role of the Solvation Shell for the Iodine–Starch Complex Using Millifluidic Devices. *Journal of Solution Chemistry*, 50(6), pp.833-850.
103. Moulay, S., 2013. Molecular iodine/polymer complexes. *Journal of Polymer Engineering*, 33(5), pp.389-443.
104. Myerson, A., Erdemir, D., & Lee, A. (Eds.). (2019). *Handbook of Industrial Crystallization* (3rd ed.). Cambridge: Cambridge University Press.
doi:10.1017/9781139026949
105. National Center for Biotechnology Information (2022). PubChem Compound Summary for CID 24445, Bromic acid.
<https://pubchem.ncbi.nlm.nih.gov/compound/Bromic-acid>. (accessed 23/1/22)

106. National Center for Biotechnology Information (2022). PubChem Compound Summary for CID 312, Chloride ion.
<https://pubchem.ncbi.nlm.nih.gov/compound/Chloride-ion>. (accessed 23/1/22)
107. National Center for Biotechnology Information, 2022. PubChem Compound Summary for CID 30165, Iodide ion.
<https://pubchem.ncbi.nlm.nih.gov/compound/Iodide-ion>. (accessed 23/1/22)
108. National Center for Biotechnology Information, 2022. PubChem Compound Summary for CID 123332, Oxonium. Retrieved March 7, 2022 from
<https://pubchem.ncbi.nlm.nih.gov/compound/Oxonium>.
109. National Center for Biotechnology Information, 2022. PubChem Compound Summary for CID 923, Sodium ion.
<https://pubchem.ncbi.nlm.nih.gov/compound/Sodium-ion>. (accessed 23/1/22)
110. National Center for Biotechnology Information, 2022. PubChem Compound Summary for CID 23668195, Sodium bromate.
<https://pubchem.ncbi.nlm.nih.gov/compound/Sodium-bromate>. (accessed 23/1/22)
111. National Center for Biotechnology Information, 2022. PubChem Compound Summary for CID 5238, Sodium iodide.
<https://pubchem.ncbi.nlm.nih.gov/compound/Sodium-iodide>. (accessed 23/1/22)
112. National Center for Biotechnology Information, 2022. PubChem Compound Summary for CID 61475, Sodium thiosulfate pentahydrate.
<https://pubchem.ncbi.nlm.nih.gov/compound/Sodium-thiosulfate-pentahydrate>. (accessed 23/1/22)
113. National Center for Biotechnology Information, 2022. PubChem Compound Summary for CID 4657547, Tetrathionate.
<https://pubchem.ncbi.nlm.nih.gov/compound/Tetrathionate>. (accessed 23/1/22)

114. National Center for Biotechnology Information, 2022. PubChem Compound Summary for CID 1084, Thiosulfate ion.
<https://pubchem.ncbi.nlm.nih.gov/compound/Thiosulfate-ion>. (accessed 23/1/22)
115. National Center for Biotechnology Information, 2022. PubChem Compound Summary for CID 105054, Triiodide Ion.
<https://pubchem.ncbi.nlm.nih.gov/compound/Triiodide-Ion>. (accessed 23/1/22)
116. Niu, H., Bian, C., Long, A., Wang, Z., Cao, M. and Luo, J., 2021. Impacts of root pruning and magnetized water irrigation on the phytoremediation efficiency of *Celosia argentea*. *Ecotoxicology and Environmental Safety*, 211, p.111963.
117. Nomura, S., Kyutoku, T., Shimomura, N. Kaneko, Y., Kadokawa, J-I., 2011. Preparation of inclusion complexes composed of amylose and biodegradable poly(glycolic acid-co-ε-caprolactone) by vine-twining polymerization and their lipase-catalyzed hydrolysis behavior. *Polymer Journal*, 43, pp. 971–977
118. Novoselova, E.G., Novikov, V.V., Lunin, S.M., Glushkova, O.V., Novoselova, T.V., Parfenyuk, S.B., Novoselov, S.V., Khrenov, M.O. and Fesenko, E.E., 2019. Effects of low-level combined static and weak low-frequency alternating magnetic fields on cytokine production and tumor development in mice. *Electromagnetic Biology and Medicine*, 38(1), pp.74-83.
119. OC II, J.I.I. and OI, J., 2001. *Water Quality Association Magnetics Task Force.*,
<http://www.premierwatermn.com/documents/WQA-Magnetics-Task-Force-Report-2001.pdf>, (accessed 18/1/2022)
120. Ocieczek, A. and Otremba, Z., 2019. Effect of a magnetic field on water desorption from the surface of potato starch. *Acta Agrophysica*, 26(3), pp.43-55.

121. Oliveira, R.A.D.C., de Andrade, A.S., Imparato, D.O., de Lima, J.G.S., de Almeida, R.V.M., Lima, J.P.M.S., Pasquali, M.A.D.B. and Dalmolin, R.J.S., 2019. Analysis of *Arabidopsis thaliana* redox gene network indicates evolutionary expansion of class III peroxidase in plants. *Scientific reports*, 9(1), pp.1-9. (<https://www.nature.com/articles/s41598-019-52299-y>)
122. Palayam, M., Ganapathy, J., Guercio, A.M. Tal, L., Deck, S., Shabek, N., 2021. Structural insights into photoactivation of plant Cryptochrome-2, *Communications Biology*, 4, No. 28, pp. 1-9. <https://www.nature.com/articles/s42003-020-01531-x>, (accessed 11/9/21)
123. Pan, H., Jiang, X., Wang, X., Wang, Q., Wang, M. and Shen, Y., 2019. Effective magnetic field regulation of the radical pair spin states in electrocatalytic CO₂ reduction. *The Journal of Physical Chemistry Letters*, 11(1), pp.48-53.
124. Panczyk, T. and Camp, P.J., 2021. Lorentz forces induced by a static magnetic field have negligible effects on results from classical molecular dynamics simulations of aqueous solutions. *Journal of Molecular Liquids*, 330, p.115701., <https://www.sciencedirect.com/science/article/pii/S0167732221004268>, (accessed 1/2/22)
125. Pasi, F., Fassina, L., Mognaschi, M.E., Lupo, G., Corbella, F., Nano, R. and Capelli, E., 2016. Pulsed electromagnetic field with temozolomide can elicit an epigenetic pro-apoptotic effect on glioblastoma T98G cells. *Anticancer research*, 36(11), pp.5821-5826.
126. Paul, S., Kiryutin, A.S., Guo, J., Ivanov, K.L., Matysik, J., Yurkovskaya, A.V. and Wang, X., 2017. Magnetic field effect in natural cryptochrome explored with model compound. *Scientific reports*, 7(1), pp.1-10.
127. Peng, S.J., Du, H.L. and Wang, B., 2015. Synthesis of Spherical and Fine Cobalt Powders from Cobalt Oxalate. In *Advanced Materials Research* (Vol. 1088, pp. 300-304). Trans Tech Publications Ltd.

128. Pérez de Tudela, R. and Marx, D., 2020. Generating Excess Protons in Microsolvated Acid Clusters under Ambient Conditions: An Issue of Configurational Entropy versus Internal Energy. *Chemistry—A European Journal*, 26(52), pp.11955-11959. <https://chemistry-europe.onlinelibrary.wiley.com/doi/abs/10.1002/chem.202000864>, (accessed 17/2/22)
129. Pershin, S.M. and Bunkin, A.F., 2009. Temperature evolution of the relative concentration of the H₂O ortho/para spin isomers in water studied by four-photon laser spectroscopy. *Laser physics*, 19(7), pp.1410-1414.
130. Picarro Inc., Cavity Ring Down Spectroscopy (CRDS),
<https://www.picarro.com/company/technology/crds>, (accessed 16/12/21)
131. Piyadasa, C., Yeager, T.R., Gray, S.R., Stewart, M.B., Ridgway, H.F., Pelekani, C. and Orbell, J.D., 2017. The influence of electromagnetic fields from two commercially available water-treatment devices on calcium carbonate precipitation. *Environmental Science: Water Research & Technology*, 3(3), pp.566-572.
132. Piyadasa, C., 2017. *Effects of commercially available pulsed electromagnetic field devices on bacterial viability and calcium carbonate precipitation* (Doctoral dissertation, Victoria University).
133. Pooam, M., Arthaut, L.D., Burdick, D., Link, J., Martino, C.F. and Ahmad, M., 2019. Magnetic sensitivity mediated by the *Arabidopsis* blue-light receptor cryptochrome occurs during flavin reoxidation in the dark. *Planta*, 249(2), pp.319-332.
134. Putro, T.S., & Endarko, 2016. The influence of electron discharge and magnetic field on calcium carbonate (CaCO₃) precipitation. *AIP Conference Proceedings* 1725, 020067 (2016)

135. Pursell, J.L. and Pursell, C.J., 2016. Host–guest inclusion complexation of α-cyclodextrin and triiodide examined using UV–Vis spectrophotometry. *The Journal of Physical Chemistry A*, 120(13), pp.2144-2149., <https://pubs.acs.org/doi/abs/10.1021/acs.jpca.6b00982>, (accessed 21/4/21)
136. Qiao, D., Yu, L., Liu, H., Zou, W., Xie, F., Simon, G., Petinakis, E., Shen, Z. and Chen, L., 2016. Insights into the hierarchical structure and digestion rate of alkali-modulated starches with different amylose contents. *Carbohydrate Polymers*, 144, pp.271-281.
137. Rageh, M.M., El-Garhy, M.R. and Mohamad, E.A., 2020. Magnetic fields enhance the anti-tumor efficacy of low dose Cisplatin and reduce the nephrotoxicity. *Naunyn-Schmiedeberg's Archives of Pharmacology*, 393(8), pp.1475-1485.
138. Raghu, N., Kale, A., Raj, A., Aggarwal, P. and Chauhan, S., 2018. Mechanical and thermal properties of wood fibers reinforced poly (lactic acid)/thermoplasticized starch composites. *Journal of Applied Polymer Science*, 135(15).
139. Rebello, S., Sivaprasad, M.S., Anoopkumar, A.N., Jayakrishnan, L., Aneesh, E.M., Narisetty, V., Sindhu, R., Binod, P., Pugazhendhi, A. and Pandey, A., 2021. Cleaner technologies to combat heavy metal toxicity. *Journal of Environmental Management*, 296, p.113231.
140. Robillard, P.D., Sharpe, W.E., Swistock, E.R., *Magnetic Water Treatment Devices*, 2001, <http://www.mwqa.com/wp-content/uploads/2016/09/magnetic-water-treatment-devices.pdf>, (accessed 19/1/2022)
141. Roy, R.K., 2010. *A primer on the Taguchi method*. Society of Manufacturing Engineers.

142. Ruekberg, B., 2020. A Closer Examination of the Mechanism of the Hydrogen Peroxide Iodine-Clock Reaction with Respect to the Role of Hypoiodite Species. *Journal of Chemical Education*, 97(6), pp.1688-1693., <https://pubs.acs.org/doi/abs/10.1021/acs.jchemed.9b00006>, (accessed 7/11/2021)
143. Saha, D. and Mukherjee, A., 2016. Impact of ions on individual water entropy. *The Journal of Physical Chemistry B*, 120(30), pp.7471-7479., <https://pubs.acs.org/doi/abs/10.1021/acs.jpcb.6b04033>, (accessed 20/2/2022)
144. Sakač, N., Karnaš, M., Dobša, J., Jozanović, M., Gvozdić, V., Kovač-Andrić, E., Sakač, M.K. and Šarkanj, B., 2020. Application of spectrophotometric fingerprint in cluster analysis for starch origin determination. *Food Technology and Biotechnology*, 58(1), p.5., <https://www.ncbi.nlm.nih.gov/pmc/articles/pmc7365342/>, (accessed 2/1/22)
145. Sarker, Md. Monzer & Hossen, Tamanna, 2013. MAGNETIC TREATMENT OF WATER FOR INDUSTRIAL USE IN BANGLADESH, *Proceedings of the International Conference on Engineering Research, Innovation and Education*. ICERIE 2013, 11–13 January, SUST, Sylhet, Bangladesh
146. Schwab M., 2011. *Encyclopaedia of Cancer*, Springer, Berlin, Heidelberg, https://link.springer.com/referenceworkentry/10.1007/978-3-642-16483-5_1189, (accessed 19/11/21)
147. Shcherbakov, I.A., Baimler, I.V., Gudkov, S.V., Lyakhov, G.A., Mikhailova, G.N., Pustovoy, V.I., Sarimov, R.M., Simakin, A.V. and Troitsky, A.V., 2020, August. Influence of a constant magnetic field on some properties of water solutions. In *Doklady Physics* (Vol. 65, No. 8, pp. 273-275). Pleiades Publishing.
148. Sherrard, R.M., Morellini, N., Jourdan, N., El-Esawi, M., Arthaut, L.D., Niessner, C., Rouyer, F., Klarsfeld, A., Doulazmi, M., Witczak, J. and d'Harlingue, A., 2018. Low-intensity electromagnetic fields induce human cryptochrome to modulate intracellular reactive oxygen species. *PLoS biology*, 16(10), p.e2006229. Strie

149. Shinde, S.D., Jain, P.G., Cheke, R.S., Surana, S.J. and Gunjegaonkar, S.M., 2021. Abrogation of Cisplatin-induced nephrotoxicity in rats and HEK-293 cell lines by formononetin: in vivo and in vitro study. *Comparative Clinical Pathology*, 30(4), pp.617-625.)
150. Shu-Li Lin, Yi-Tsai Su, Sheng-Wei Feng, Wei-Jen Chang, Kan-Hsin Fan & Haw-Ming Huang, 2019. Enhancement of natural killer cell cytotoxicity by using static magnetic field to increase their viability, *Electromagnetic Biology and Medicine*, 38:2, 131-142
151. Shurflo, Chemical Compatibility Chart, 2003,
<https://www.arrid.com.au/pdf/Pump/Shurflo/Shurflo%20Chemical%20Chart.pdf>,
(accessed 27/3/21)
152. Simonič, M. and Urbanci, D., 2017. Alternating magnetic field influence on scaling in pump diffusers. *Journal of Cleaner Production*, 156, pp.445-450.
153. Simoyi, R.H., Masvikeni, P. and Sikosana, A., 1986. Complex kinetics in the bromate-iodide reaction: a clock reaction mechanism. *The Journal of Physical Chemistry*, 90(17), pp.4126-4131.
154. Stefanutti, E., 2017. *Structural and dynamical studies on confined water* (Doctoral dissertation, Université Pierre et Marie Curie-Paris VI; Università degli studi Roma Tre). English.
155. Sulistyarti, H., Fardiyah, Q. and Febriyanti, S., 2015. A simple and safe spectrophotometric method for iodide determination. *Makara Journal of Science*, 19(2), p.1., <https://scholarhub.ui.ac.id/science/vol19/iss2/1/>, (accessed 2/1/22)
156. Tachikawa, H., 2017. Proton Transfer Rates in Ionized Hydrogen Chloride-Water Clusters: A Direct Ab Initio Molecular Dynamics Study. *The Journal of Physical Chemistry A*, 121(28), pp.5237-5244.,
<https://pubs.acs.org/doi/abs/10.1021/acs.jpca.7b05112>, (accessed 14/2/22)

157. TC Measurement & Control Pty Ltd, *Maximum Operating Temperature Guide for Mineral Insulated Thermocouples*,
<https://www.tcaus.com.au/thermocouples/thermocouple-sheath-materials.html>,
(accessed 20/3/21)
158. Thakur, I.S., and Medhi, K., 2019. Nitrification and denitrification processes for mitigation of nitrous oxide from wastewater treatment plants for biovalorization: Challenges and opportunities. *Bioresource technology*, 282, pp.502-513
159. Thornley, P. and Adams, P. eds., 2017. *Greenhouse Gas Balances of Bioenergy Systems*. Academic Press.
160. Toledo, E.J. and Ramalho, T.C., 2021. Controversies about hydrogen bonds in water molecules on the influence of high magnetic fields: implications on structural and electronic parameters. *Molecular Simulation*, 47(14), pp.1159-1167.
161. Toledo, E.J., Ramalho, T.C. and Magriotis, Z.M., 2008. Influence of magnetic field on physical–chemical properties of the liquid water: Insights from experimental and theoretical models. *Journal of Molecular Structure*, 888(1-3), pp.409-415.
162. Tweedy, S.E., Rodríguez Benítez, A., Narayan, A.R., Zimmerman, P.M., Brooks III, C.L. and Wymore, T., 2019. Hydroxyl radical-coupled electron-transfer mechanism of flavin-dependent hydroxylases. *The Journal of Physical Chemistry B*, 123(38), pp.8065-8073.
163. Usanov, A.D., Ulyanov, S.S., Ilyukhina, N.S. and Usanov, D.A., 2016. Monitoring of changes in cluster structures in water under AC magnetic field. *Optics and Spectroscopy*, 120(1), pp.82-85.
164. Valenzuela, R., 1993. Inductance spectroscopy. In *Advanced Topics in Materials Science and Engineering* (pp. 187-194). Springer, Boston, MA.

165. Vallée, P., Lafait, J., Legrand, L., Mentré, P., Monod, M.O. and Thomas, Y., 2005. Effects of pulsed low-frequency electromagnetic fields on water characterized by light scattering techniques: role of bubbles. *Langmuir*, 21(6), pp.2293-2299., <https://pubs.acs.org/doi/abs/10.1021/la047916u>, (accessed 4/7/21)
166. van der Loop, T.H., Ottosson, N., Vad, T., Sager, W.F., Bakker, H.J. and Woutersen, S., 2017. Communication: Slow proton-charge diffusion in nanoconfined water. *The journal of chemical physics*, 146(13), p.131101. <https://aip.scitation.org/doi/abs/10.1063/1.4979714>, (accessed 4/1/22)
167. van der Lubbe, S.C. and Fonseca Guerra, C., 2019. The nature of hydrogen bonds: A delineation of the role of different energy components on hydrogen bond strengths and lengths. *Chemistry—An Asian Journal*, 14(16), pp.2760-2769.
168. Vanderstraeten, J., Gailly, P. and Malkemper, E.P., 2018. Low-light dependence of the magnetic field effect on cryptochromes: Possible relevance to plant ecology. *Frontiers in plant science*, 9, p.121.
169. Vermeiren, T., 1958. Magnetic Treatment of Liquids for Scale and Corrosion Prevention, *Corrosion Technology*, July, pp. 215-219.
170. Veselinović, D. and Velikić, Z., 2016. The pH measurement with glass electrode in an electromagnetic field. *Journal of the Serbian Chemical Society*, 81(12), pp.1407-1414.
171. Wang, B., Jiang, W., Dai, X., Gao, Y., Wang, Z. and Zhang, R.Q., 2016. Molecular orbital analysis of the hydrogen bonded water dimer. *Scientific reports*, 6(1), pp.1-7.
172. Wang, S. ed., 2020. *Starch Structure, Functionality and Application in Foods*. Springer.

173. Wang, S., Li, C., Copeland, L., Niu, Q. and Wang, S., 2015. Starch retrogradation: A comprehensive review. *Comprehensive Reviews in Food Science and Food Safety*, 14(5), pp.568-585..
<https://ift.onlinelibrary.wiley.com/doi/abs/10.1111/1541-4337.12143>, (accessed 28/2/22)
174. Witt, O. N. 1911. "Obituary notices: Friedrich Konrad Beilstein, 1838–1906; Emil Erlenmeyer, 1825–1909; Rudolph Fittig, 1835–1910; Hans Heinrich Landolt, 1831–1910; Nikolai Alexandrovitsch Menschutkin, 1842–1907; Sir Walter Palmer, Bart., 1858–1910.", *Journal of the Chemical Society, Transactions* 99: 1646-1668., <https://pubs.rsc.org/en/content/articlepdf/1911/ct/ct9119901646>, (accessed 10/1/22)
175. Wu, J., Shangguan, H., Fu, T., Chen, J., Tang, J., Zeng, R.J., Ye, W. and Zhou, S., 2021. Alternating magnetic field mitigates N₂O emission during the aerobic composting of chicken manure. *Journal of Hazardous Materials*, 406, p.124329.
176. Wu, A.C., Witt, T. and Gilbert, R.G., 2013. Characterization methods for starch-based materials: State of the art and perspectives. *Australian Journal of Chemistry*, 66(12), pp.1550-1563.
177. Xu, D., Ji, H., Ren, H., Geng, J., Li, K. and Xu, K., 2020. Inhibition effect of magnetic field on nitrous oxide emission from sequencing batch reactor treating domestic wastewater at low temperature. *Journal of Environmental Sciences*, 87, pp.205-212.
178. Yarborough, V.A., Haskin, J.F. and Lambdin, W.J., 1954. Temperature dependence of absorbance in ultraviolet spectra of organic molecules. *Analytical Chemistry*, 26(10), pp.1576-1578.,
<https://pubs.acs.org/doi/pdf/10.1021/ac60094a012>, (accessed 26/1/22)

179. Yu, H.M., Chen, S.T., Suree, P., Nuansri, R. and Wang, K.T., 1996. Effect of microwave irradiation on acid-catalyzed hydrolysis of starch. *The Journal of Organic Chemistry*, 61(26), pp.9608-9609,
<https://scholars.lib.ntu.edu.tw/bitstream/123456789/143753/1/24.pdf>, (accessed 2/1/22)
180. Zhao, K., Zhang, P., Wang, B., Tian, Y., Xue, S. and Cong, Y., 2021. Preparation of electric-and magnetic-activated water and its influence on the workability and mechanical properties of cement mortar. *Sustainability*, 13(8), p.4546